LABORATORY SIMULATIONS OF SOLAR PROMINENCES

Thesis by

J. Freddy Hansen

In Partial Fulfillment of the Requirements

for the Degree of

Doctor of Philosophy

California Institute of Technology

Pasadena, California

2001

(Defended May 24, 2001)

This thesis is dedicated to my mother.

Acknowledgments

The preparation of this thesis has benefitted from my interaction with several persons. First and foremost, I would like to thank my thesis advisor, Professor Paul Bellan; without his support, this thesis would not exist. During my first year at Caltech, Paul taught me plasma physics one-on-one, patiently, three hours per week. Toward the end of the year, it was clear that our scientific interests intersected, and soon the solar experiment was under intense development. Throughout my time at Caltech, Paul's advice and friendship have been invaluable, and for this he has my sincere gratitude.

I would also like to thank my fellow graduate students - Steven Sanders, Jimmy Yee, Steven Pracko, and Carlos Romero - and post-doc Scott Hsu for valuable advice and many a helping hand in the labs. Jimmy, thank you also for our numerous discussions on prominences, spheromaks, plasma physics in general, and the great world of science beyond.

Without Frank Cosso, our technician and miracle worker, life in the labs can be tricky some days. Frank, thanks for all the gadgets, the repairs, and your help.

Finally, I would like to extend my gratitude to those of you - too many to mention here - who provided valuable insights and comments at Caltech seminars as well as my presentations at conferences both near and far. Thank you.

This work was supported by the US Department of Energy grant DE-FG03-97ER5438.

Abstract

A solar prominence is a large, arch-shaped structure of magnetized hydrogen plasma protruding from the surface of the sun. From shifts in spectral lines, observers estimate typical prominence temperatures of 4300-8500 K, densities of 10^{16}-10^{17} m^{-3}, and magnetic fields of 0.4-2 mT. The typical length scale is 10^{7}-10^{8} m. Through careful scaling of terms in the two-fluid electron equation of motion, we have designed an experiment that should reproduce the essential physics of solar prominences. Our experiment has typical temperatures of about 50000 K, densities on the order of 10^{19} m^{-3}, magnetic fields of 100-500 mT, and a length scale of about 0.1 m. The advantages of having a prominence-like plasma conveniently located in a laboratory, rather than over 100 million kilometers away, include the following:

- Observations of the prominence from a vantage point of choice.
- Stereographic observation to better discern the three-dimensional shape of the prominence.
- In situ measurements of physical properties such as magnetic fields, electric potentials, densities and temperatures.
- Control of parameters that govern the creation and evolution of the prominence.

The topology and dynamics of solar prominences have been of great interest for several decades. While intrinsically interesting, solar prominences are also believed to produce magnetic clouds which can destroy sensitive spacecraft electronics or cause costly damage

to power-grid components when passing by Earth. Thus, it is important to better understand the physical phenomena behind these events.

Our experimental solar device is mounted on a large vacuum chamber. The solar device consists of a horseshoe magnet that provides a bias magnetic field from one prominence footpoint to the other. A gas valve injects hydrogen at the footpoints. As the hydrogen expands into the vacuum chamber, a high-voltage capacitor is connected between the two footpoints. The high voltage breaks down the hydrogen gas. The plasma forms along the arching magnetic field lines of the horseshoe magnet. The laboratory prominence is much smaller (footpoint distance 0.1 m) than the vacuum chamber (1.4 m diameter, 2 m long) so that one vacuum chamber wall acts as the solar surface while the other walls are too far away to influence the experiment.

Still photographs obtained from two high-speed cameras in a stereographic configuration have been combined to make three-dimensional movies of the evolution of the plasma. The plasmas resemble actual solar prominences, and evolve in a reproducible sequence through three stages. First, initial breakdown forms a main current channel consisting of several bright and dark strands of plasma. Second, as helicity is injected by ramping up the current flowing through the plasma from one footpoint to the other, the strands twist around each other. Third, the entire plasma takes on a helical structure and expands outward. The three-dimensional structure of the plasma has a handedness consistent with the sign of the injected helicity. Photographs taken from a top view show S-shaped and reverse S-shaped plasmas for the two different polarities of the horseshoe magnetic field, in accordance with observations of sigmoids on the southern and northern hemispheres of the Sun.

We have investigated plasma behavior using various boundary conditions and demonstrated several phenomena of importance to solar prominences. First, prominence eruption has been slowed or completely inhibited by a vacuum arcade field, or strapping field. It has been conjectured that the eruption of a solar prominence can be inhibited if a much larger scale, arched magnetic field straddles the prominence and effectively straps it down. We found that it is neither magnetic pressure nor magnetic field line tension in the strapping field that inhibits prominence eruption, as predicted in earlier models. Rather it is a $\mathbf{J} \times \mathbf{B}$-force between the current in the prominence and the strapping field. The strapping field magnitude required to completely inhibit prominence eruption is in good agreement with a theoretical model which takes into account the full three-dimensional magnetic topology.

Second, the interaction between two side-by-side prominences of equal or opposite helicity has been studied. In the co-helicity case, helicity is transferred from one prominence to the other, increasing the instability of the receiving prominence. In the counter-helicity case, there is evidence of reconnection and magnetic flux destruction causing increased instability in both prominences. X-ray production is larger by an order of magnitude in the counter-helicity case than in the co-helicity case.

Third, aspects of prominence shapes are explained by the force-free state equation $\nabla \times \mathbf{B} = \alpha \mathbf{B}$. This supports the suggestion that solar prominences are in Woltjer-Taylor states.

Contents

List of Figures

List of Tables

Preface

The premise of this work is that certain solar phenomena, in particular solar prominences, can be simulated in laboratory experiments. The advantages of simulating prominences and prominence eruptions in the laboratory are many. A laboratory experiment is reproducible, it occurs at desired times, and parameters for various quantities such as currents, magnetic fields, and length scales can be controlled. In the laboratory one can choose the viewing angle of the prominence and use in situ measurements to determine its properties. Experimental results presented here give valuable insight into the evolution of solar prominences, including how strapping fields can inhibit prominence eruption, how two interacting solar prominences can affect each other, and how aspects of prominence shapes can be explained by the force-free state equation $\nabla \times \mathbf{B} = \alpha \mathbf{B}$.

The organization of this thesis is chronological. The most important scientific results will be found in the last two out of five chapters.

Chapter 1 provides background information on solar prominences and laboratory spheromaks. Details of both types of plasmas are presented, and similarities between them are highlighted. An analysis of the forces dominating the respective plasmas suggests that solar prominences can be simulated with spheromak-like plasmas in the laboratory.

Chapter 2 describes the design process of the solar prominence experiment. The design and testing of the various experimental subsystems have been an important and substantial part of this thesis project. Subsequent chapters will refer to particular sections or figures in this chapter as required.

Chapter 3 describes experiments with the first generation solar device. The most important finding of this chapter is that we can explain both prominence S-shapes and an observed plasma bifurcation using the force-free state equation $\nabla \times \mathbf{B} = \alpha \mathbf{B}$, lending strong support to the conjecture that prominences are in Woltjer-Taylor states.

Chapter 4 describes experiments with a second generation device. The most important result of this chapter is that a strapping field can inhibit the eruption of a prominence. The strapping field is a large scale vacuum magnetic field that straddles a prominence. We show quantitatively that prominence eruption is inhibited due to a $\mathbf{J} \times \mathbf{B}$-force between strapping field and the prominence toroidal current.

Chapter 5 describes experiments with a device capable of creating two prominences side by side. The most important result of this chapter is that interaction between two prominences can cause one or both prominences to erupt sooner and at a higher velocity than a single prominence would. This can happen with two side-by-side prominences with opposite sign helicity (counter-helicity) via the destruction of toroidal magnetic flux, or with two side-by-side prominences with same sign helicity (co-helicity) due to helicity transfer from one prominence to the other.

Appendix A contains mathematical and physical formulae. The formulae are well known, but have been included since readers might find it useful to have them readily available. Appendix B describes the testing or monitoring of certain subsystems used in the solar prominence experiment. These were not considered to be of general interest, but are made available for reference purposes.

Chapter 1 Background

This chapter provides background information on solar prominences and laboratory spheromaks. These two types of plasmas are compared, and important similarities are emphasized. The main points of this chapter are as follows:

- Both solar prominences and laboratory spheromaks are governed by $\nabla \times \mathbf{B} = \alpha \mathbf{B}$.
- From a comparison of forces acting on solar prominence and laboratory spheromak plasmas, we conclude that a spheromak-like laboratory plasma, with correct boundary conditions, will capture the essential physics of a solar prominence.
- The three interpretations of the scalar α, namely ratio of magnetic energy to helicity, current per magnetic flux, and an inverse length scale, are presented. We will use α in this and subsequent chapters to explain some properties of solar prominences.
- A multitude of terms exist to describe and subdivide solar prominences. We suggest that all prominences share the same physics, and therefore that the division of prominences into subgroups is an artificial categorization.

1.1 Solar prominences

1.1.1 Historical nomenclature

Solar astronomers refer to arch-shaped structures on the surface of the Sun as "prominences" and have traditionally divided these into subgroups depending on observed properties such as morphology, spectrum, or relation to other solar activity (e.g., flares). Subgroups of prominences have received imaginative names such as active, quiescent [1][2], eruptive, sunspot, tornado [3][4], electromagnetic, irregular [5][6], normal, polar, mov-

ing, spot [7][8], short-lived, long-lived, intermediate, and ascending [9] prominences. Astronomers have also used the terms clouds, filaments, stems, plumes, horns, cyclones, flames, jets, sheafs, spikes [1][2], surges, spicules [7][8], sprays, loops, coronal rain, polar cap filaments, and sunspot zone filaments [9] to describe prominences. It might appear that there are a great many different types of solar prominences. This is however not the case. Note, for instance, that a single prominence can be associated with different subgroups at different times, e.g., an active prominence can become an eruptive prominence [4]. This reduces the number of true subgroups significantly. Non-temporal reductions are also possible, e.g., filaments that appear dark against the disk of the Sun are the same as prominences that appear bright above the solar limb [10][11], all prominences consist of magnetized plasma and should be considered "electromagnetic," etc. It is possible that even the most elementary division of prominences into only two subgroups, quiescent and active [1], does not describe two phenomenologically different plasmas. Rather, all prominences share the same physics and share the same regimes of certain important parameters, and the division of prominences into subgroups is merely an artificial categorization.

1.1.2 Prominence characteristics

All prominences are large, arch-shaped plasma structures protruding from the surface of the Sun [12][13]. Figure 1 shows an example of a prominence. A pair of sunspots often act as footpoints for the prominence. When observed from above, i.e., against the disk of the Sun, a prominence often shows a characteristic S-shape (sigmoid). Examples of sigmoids are shown in Figure 2. Prominences on the northern hemisphere of the Sun have predominantly reverse S-shapes, while forward S-shapes dominate on the southern hemisphere [14]. The handedness (or chirality) of prominences has been shown to be predominantly right handed

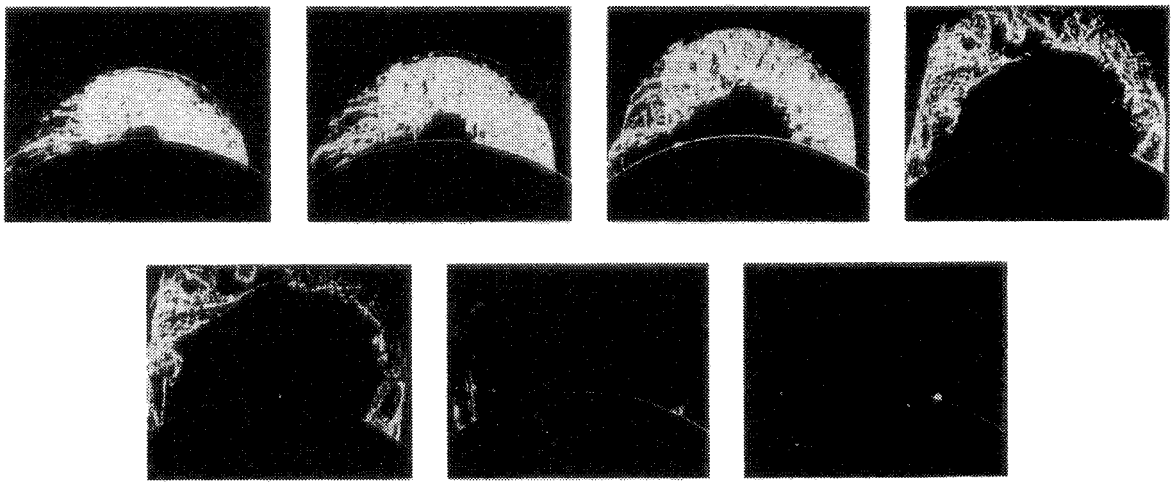

Figure 1: Erupting prominence photographed from Climax station of the High Altitude Observatory, Boulder, Colorado, on June 4, 1946.

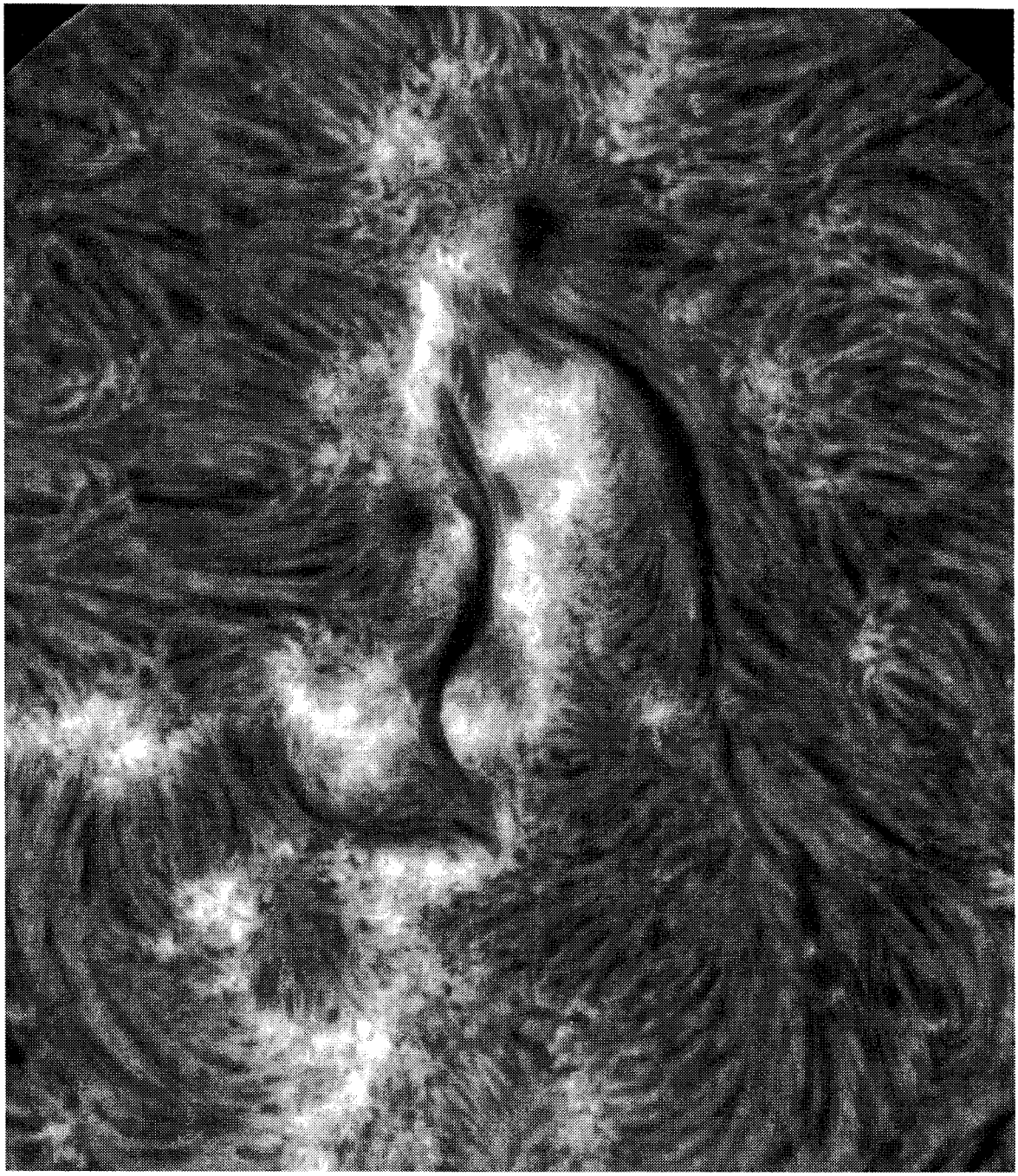

Figure 2: S-shaped prominences and sunspots (from the archive of the Ottawa River Solar Observatory, Herzberg Inst. of Astrophysics, National Research Council of Canada).

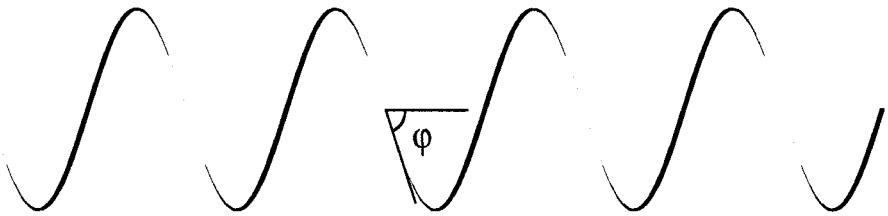

Figure 3: Explanation of handedness (chirality). Assuming the lighter portions of this helix (such as where the angle is indicated) to be in the background, while the heavier portions are in the foreground, then this is a left-handed helix. The angle is the complement to the pitch angle of the helix and will be discussed in Chapter 3.

(or positive) in the southern hemisphere of the Sun, and left handed (or negative) in the northern hemisphere [15][14] [16][17]. The concept of handedness is explained in Figure 3.

Prominences can be regarded as being dominated by magnetic forces, with the plasma frozen to magnetic field lines. This is because prominences have low β's and high Lundquist numbers. β is the ratio of plasma thermal to magnetic pressure (150), and the Lundquist number (137) is the ratio of the diffusive time scale to the convective (Alfvén) time scale, i.e., a measure of how well a magnetic field is frozen to the plasma. The β of a solar prominence is small, on the order of 10^{-3}-10^{-1}. The Lundquist number is large, reported to be as high as 10^{14} [18][19]. Being magnetically dominated, a prominence equilibrium is approximately a force-free state [20], where the currents are parallel to the magnetic fields, $\mathbf{J} = \alpha'\mathbf{B}$, so that the magnetic force $\mathbf{J} \times \mathbf{B}$ is negligible. This is an important quality of a solar prominence that we will return to later. The scalar α' may be non-uniform, $\alpha' = \alpha'(\mathbf{r})$ [21].

1.1.3 Physical parameters

Measurements of physical parameters (temperature, density, and magnetic field strength) of solar prominences have been conducted by numerous research groups throughout the

world. However, until a spacecraft is sent to the Sun, these measurements will be exclusively in the form of observations of spectral lines. The temperature of a solar prominence can be obtained by observing the Doppler broadening $\Delta\lambda_D$ of a spectral line λ_0:

$$\Delta\lambda_D = \frac{\lambda_0}{c}\sqrt{\frac{2k_BT}{m} + \xi_t^2} \tag{1}$$

where T is the temperature of the plasma and m is the mass of the radiating atom. Astronomical "micro-turbulence" introduces a non-thermal velocity component ξ_t that contributes to the Doppler broadening in a similar way as does the thermal velocity $v_0 = \sqrt{2k_BT/m}$. In general, extraction of temperature therefore requires data from two spectral lines of different elements.

The Stark effect is the splitting of a spectral line due to an electric field and the subsequent frequency shift of these lines. Often the individual lines cannot be resolved, hence one speaks of Stark broadening. The microscopic electric field in the vicinity of each ion depends on plasma pressure and density, so the prominence density can be estimated from Stark broadening. Another method used to determine densities is to look at density-dependent ratios of spectral line magnitudes.

The Zeeman effect is the splitting of a spectral line due to an imposed magnetic field. The magnetic field strength in prominences is too weak to produce a Zeeman splitting that is directly measurable, but taking advantage of the fact that the different lines have different polarizations, field strengths can still be estimated. The best estimates of prominence magnetic field strengths are obtained using the Hanle effect, which is similar to the Zeeman effect but originates in resonance polarization between a polarized photon flux and the emitted photons from atoms excited by this flux.

Typical values reported for the "central part" of the prominence [12] are as follows: the temperature is 4300-8500 K and the density is 10^{16}-$10^{17}\,\mathrm{m}^{-3}$. The "edges" of the prominence (i.e., plasma closer to the solar corona) have been reported as slightly hotter and thinner, although there is some controversy regarding these results [12]. The length scale of a solar prominence is 10^{7}-10^{8} m, and the magnetic field strength is 0.4-2 mT in either the central part or at the edges. The magnetic field strength has been the subject of some discussion due to a quantity known as the filling factor; because magnetic field measurements are done as an average over an area on the Sun that is larger than individual magnetic flux tubes, one can argue that larger magnetic fields localized over smaller areas can yield the same measured, average magnetic field as a non-localized, weaker magnetic field [12].

For purposes of comparing a solar prominence to a laboratory plasma (cf 1.3), we will use the values for the central part of the prominence: $T = 8500\,\mathrm{K}$, and $n = 1 \times 10^{16}\,\mathrm{m}^{-3}$. We will pick an average length scale of $L \simeq 10^{(7+8)/2}\,\mathrm{m} \approx 3 \times 10^{7}\,\mathrm{m}$. From the ideal gas law the pressure is calculated as $p \simeq 1 \times 10^{-3}\,\mathrm{Pa}$. From a weighted average over a histogram of magnetic field values, the magnetic field is obtained as $B \simeq 8 \times 10^{-4}\,\mathrm{T}$ [12].

1.1.4 Magnetic clouds

Prominences can remain on the surface of the Sun for days (quiescent prominences), but occasionally lose equilibrium and erupt. The eruption takes place in a few minutes and can eject up to 10^{12} kg of hydrogen into the solar wind. This is believed to be associated with a larger scale phenomenon called a coronal mass ejection [22]. Spacecraft observations of magnetic disturbances to Earth's magnetic field, some eighty hours after prominence eruptions, have linked prominences to magnetic clouds. An erupting prominence spawns a continuously expanding magnetic cloud that travels outward from the Sun. By the time a

magnetic cloud has reached 1 AU from the Sun (the Sun to Earth distance), it has expanded to a diameter of about 0.25 AU [23]. Magnetic fields of clouds intercepting Earth's magnetosphere have been measured by spacecraft; magnetic clouds are in force-free states [23], and the handedness of the clouds corresponds to the handedness of the associated prominences, such that S-shaped prominences yield clouds with positive helicity, and vice versa [24]. The magnetic clouds were also shown to be in Woltjer-Taylor states having an axisymmetric Bessel function solution [25], a concept that will be explained in the following section.

1.2 Spheromaks

We shall now discuss a laboratory plasma known as a spheromak. At first this matter will seem unrelated to solar prominences, but we will show that laboratory spheromaks and solar prominences share important features.

This section often refers to the two directions on the surface of a torus; the toroidal direction *circles* the hole of the torus, while the poloidal direction passes *through* the hole.

1.2.1 Analysis of the reverse field pinch

A curious plasma behavior was observed in the 1950's and 1960's in fusion research with a device called a toroidal Z-pinch. An initially turbulent plasma would, regardless of initial conditions, settle into a specific state where the toroidal magnetic field reversed direction in the vicinity of the plasma surface. An analysis by Taylor [26] of this device, later renamed reverse field pinch (RFP), explained the magnetic field reversal. The analysis begins with an assumption that magnetic turbulence dissipates magnetic energy (139) while keeping the magnetic helicity (140) constant. The basis of the assumption is that turbulence would cause microscopic changes in magnetic topology, dissipating energy while keeping the

total number of microscopic flux linkages constant. To show mathematically that magnetic energy $W = \int B^2/(2\mu_0)\, d^3r$ (139) decays faster than magnetic helicity $K = \int \mathbf{A}\cdot\mathbf{B}d^3r$ (140), we need to show the relation between magnetic turbulence and the time derivative of magnetic energy and helicity, respectively. Start with the time derivative of magnetic helicity

$$\begin{aligned}\frac{\partial}{\partial t}\int_V \mathbf{A}\cdot\mathbf{B}d^3r &= -2\int_V \mathbf{E}\cdot\mathbf{B}d^3r = -2\int_V (\eta\mathbf{J}-\mathbf{U}\times\mathbf{B})\cdot\mathbf{B}d^3r = \\ &= -2\int_V \eta\mathbf{J}\cdot\mathbf{B}d^3r = -2\int_V \frac{\eta}{\mu_0}(\nabla\times\mathbf{B})\cdot\mathbf{B}d^3r \qquad (2)\end{aligned}$$

where we have used Ohm's law (149) and Ampère's law. Compare this to the time derivative of magnetic energy

$$\frac{\partial W}{\partial t} = \frac{\partial}{\partial t}\int_V \frac{B^2}{2\mu_0}d^3r. \qquad (3)$$

To evaluate Equation (3), start by regarding the two expressions obtained from dotting Maxwell's first and second equations with $\mathbf{B}$ and $\mathbf{E}$ respectively:

$$(\nabla\times\mathbf{E})\cdot\mathbf{B} = -\frac{\partial\mathbf{B}}{\partial t}\cdot\mathbf{B} = \frac{\partial}{\partial t}\left(-\frac{B^2}{2}\right) \qquad (4)$$

$$(\nabla\times\mathbf{B})\cdot\mathbf{E} = \mu_0\mathbf{J}\cdot\mathbf{E}. \qquad (5)$$

Subtract (4) from (5):

$$\mathbf{E}\cdot\nabla\times\mathbf{B} - \mathbf{B}\cdot\nabla\times\mathbf{E} = \mu_0\mathbf{J}\cdot\mathbf{E} + \frac{\partial}{\partial t}\frac{B^2}{2}. \qquad (6)$$

The left side above is recognized as $\nabla\cdot(\mathbf{E}\times\mathbf{B})$ from a vector identity. Divide by μ_0 to obtain

$$\frac{\partial}{\partial t}\frac{B^2}{2\mu_0} + \nabla\cdot\left(\frac{\mathbf{E}\times\mathbf{B}}{\mu_0}\right) = -\mathbf{J}\cdot\mathbf{E}. \qquad (7)$$

We are not interested in radiative losses through the surface S, so the term containing the Poynting vector $\sim \mathbf{E}\times\mathbf{B}$ (radiation through S using the divergence theorem) is dropped,

giving the time derivative of magnetic energy

$$\begin{aligned}\frac{\partial}{\partial t}\int_V \frac{B^2}{2\mu_0}d^3r &= -\int_V \mathbf{J}\cdot\mathbf{E}d^3r = -\int_V \mathbf{J}\cdot(\eta\mathbf{J}-\mathbf{U}\times\mathbf{B})\,d^3r = \\ &= -\int_V \eta J^2 d^3r + \int_V \mathbf{J}\cdot\mathbf{U}\times\mathbf{B}d^3r \end{aligned} \tag{8}$$

where the last term is recognized as changes in the kinetic energy, since

$$\mathbf{U}\cdot\mathbf{J}\times\mathbf{B} = \rho\mathbf{U}\cdot\frac{\partial\mathbf{U}}{\partial t} = \frac{\partial}{\partial t}\frac{\rho U^2}{2} \tag{9}$$

for constant ρ.

We are interested in decay due to magnetic turbulence on a small length scale, $1/k$. The decay of magnetic energy is proportional $(\nabla\times\mathbf{B})^2 \sim k^2\mathbf{B}^2$, while the decay of magnetic helicity is proportional to $\nabla\times\mathbf{B} \sim k\mathbf{B}$, so the magnetic energy decays faster. A simpler argument can be made from dimensional analysis [27]; magnetic energy scales as B^2L^3, whereas magnetic helicity scales as B^2L^4. Thus, the smaller the linear length scale L over which a dissipative phenomenon occurs, the greater the ratio between magnetic energy decay and magnetic helicity decay (the ratio being L^{-1}). Magnetic turbulence and reconnection are intrinsically small scale phenomena and thus essentially dissipate magnetic energy while preserving magnetic helicity.

In a non-dissipative plasma, both magnetic helicity and magnetic energy are conserved, while the magnetic energy in a plasma with fine scale dissipation decays faster than the helicity. However, the magnetic energy cannot decay to zero, as that would require $B = 0$ which in turn would yield zero magnetic helicity. Rather, for a given magnetic helicity, the magnetic energy decays to some minimum value. Woltjer applied a variational

principle [28][29] to the problem, minimizing the energy subject to constant helicity:

$$\delta W + \lambda \delta K = 0 \tag{10}$$

where λ is a Lagrangian multiplier. Here, δW is the variation in magnetic energy and δK the variation in magnetic helicity due to a variation $\delta \mathbf{B}$ in the magnetic field (along with the variation $\delta \mathbf{A}$ in the field's vector potential). We have

$$\delta W = \frac{2\mathbf{B}\cdot\delta\mathbf{B}}{2\mu_0} \tag{11}$$

and

$$\delta K = \delta\mathbf{A}\cdot\mathbf{B} + \mathbf{A}\cdot\delta\mathbf{B} \tag{12}$$

ignoring second order terms in $\delta \mathbf{B}$ and $\delta \mathbf{A}$. Using the definition of $\mathbf{A}$, along with a vector identity, we further have

$$\mathbf{B}\cdot\delta\mathbf{B} = \mathbf{B}\cdot\nabla\times\delta\mathbf{A} = \nabla\cdot(\delta\mathbf{A}\times\mathbf{B}) + \delta\mathbf{A}\cdot(\nabla\times\mathbf{B}) \tag{13}$$

and

$$\mathbf{A}\cdot\delta\mathbf{B} = \mathbf{A}\cdot\nabla\times\delta\mathbf{A} = \nabla\cdot(\delta\mathbf{A}\times\mathbf{A}) + \delta\mathbf{A}\cdot(\nabla\times\mathbf{A}) = \nabla\cdot(\delta\mathbf{A}\times\mathbf{A}) + \delta\mathbf{A}\cdot\mathbf{B}. \tag{14}$$

Substitute in $\delta W + \lambda\delta K = 0$, use the divergence theorem and the fact that magnetic field lines define the outer boundary of the plasma to obtain

$$\frac{1}{\mu_0}\left(\oint_S \underbrace{\delta\mathbf{A}\times\mathbf{B}\cdot d\mathbf{S}}_{=0} + \int_V \delta\mathbf{A}\cdot(\nabla\times\mathbf{B})\,d^3r\right) +$$

$$+ \quad \lambda\left(\oint_S \underbrace{\delta\mathbf{A}\times\mathbf{A}\cdot d\mathbf{S}}_{=0} + 2\int_V \delta\mathbf{A}\cdot\mathbf{B}d^3r\right) = 0. \tag{15}$$

The surface terms vanish because $\delta\mathbf{A} = 0$ on the surface (since $\mathbf{A} + \delta\mathbf{A}$ must satisfy the same boundary conditions as $\mathbf{A}$). Thus,

$$\int_V \delta\mathbf{A}\cdot(\nabla\times\mathbf{B} + 2\lambda\mu_0\mathbf{B})\,d^3r = 0. \tag{16}$$

Now define $\alpha = -2\lambda\mu_0$ and note that $\delta\mathbf{A}$ is arbitrary, and we find that

$$\nabla \times \mathbf{B} = \alpha\mathbf{B}. \tag{17}$$

This is similar to an eigenvalue equation, and Taylor showed that, for the geometry of the RFP, the "eigenstates" of the equation have axisymmetric Bessel function solutions [26] (cf 3.3.3). Taylor thus solved the problem with the mysterious field reversal of the RFP, as the field reversal some distance from the plasma surface corresponds to the first root of the zeroth order Bessel function $J_0(\alpha r)$. Solutions to Equation (17) are hence called Taylor states, or Woltjer-Taylor states. Since $\nabla \times \mathbf{B} = \mu_0\mathbf{J}$ from Maxwell's equations, the Taylor states are force-free states where $\mathbf{J}$ is parallel to $\mathbf{B}$, or $\mathbf{J} = \alpha'\mathbf{B}$ with $\alpha' = \alpha/\mu_0$. This is similar to the prominence equilibrium (cf 1.1.2), and (spherical) Bessel function solutions have been suggested to apply to solar plasmas [30].

1.2.2 Simply connected geometry

Some years later, Taylor's approach to plasma equilibrium was extended to spherical geometry [31]. The major difference in this geometry is that there is no externally driven current through a hole in the plasma, i.e., the plasma is simply connected. This is unlike an RFP (or tokamaks and stellarators - more familiar plasma devices) which is toroidal, or doughnut shaped, and in which an external coil passes current through the hole of the doughnut. The solution to the force-free state equation (17) in spherical geometry, a spherical Bessel function solution, was named spheromak [31].

In the past couple of decades, spheromaks have been the object of great interest in plasma laboratories around the world [27]. Because of their simple geometry, their lack of external coils linking the plasma, and their absence of a toroidal magnetic field at the wall, spheromaks are regarded as a possible alternative to tokamaks for confining plasma

for nuclear fusion. Spheromaks do not necessarily need to be spherical; they can be of any shape as long as they are simply connected. Spheromaks have been created by a variety of methods, among them coaxial magnetized plasma guns, $z - \theta$ pinches, and inductive sources. Spheromaks have also been produced in a large range of temperatures, densities, magnetic energies, and time and length scales, a testament to the robustness of Taylor's theory that a plasma with a given helicity will relax to a minimum energy state regardless of initial conditions. We thus expect spheromaks to be a common state that might be found in nature. We also note that helicity has been shown to be conserved during spheromak formation over a wide range of plasma parameters [32][33].

1.2.3 Spheromak formation techniques

Before leaving the topic of spheromaks, we will look more closely at the coaxial magnetized plasma gun technique and some interesting results stemming from experiments using this technique [34][35] [32][36]. In this method, spheromaks are created via the following steps. First, an external magnetic field B_{pol} is created in the gun by discharging a capacitor into the coil of an electromagnet. This process takes place on a time scale much slower than the plasma dynamics, so that the field, often referred to as the bias field, can be regarded as constant. When the bias field is at a desired value, gas is injected into the region between two annular, cylindrical electrodes. With the gas in place, the voltage of another capacitor is applied between the two electrodes to break down the gas and form a plasma. After break-down, the capacitor will discharge through the plasma, building up a current I and an associated magnetic field B_θ, as well as injecting helicity into the plasma. $\mathbf{J} \times \mathbf{B}$-forces push the plasma down the electrode gap into a flux conserving container. Reconnection of

the bias field allows the plasma to form closed flux surfaces and obtain the characteristic simply-connected geometry of the spheromak configuration.

Note that the magnetic pressures from B_{pol} and B_θ are effective over approximately the same area, so that the condition for the spheromak to break through B_{pol}, out of the plasma gun and into the flux conserving container, is

$$B_\theta > B_{pol}. \tag{18}$$

From Maxwell's equations (Ampère's law) we find that

$$B_\theta = \frac{\mu_0 I}{2\pi r} \tag{19}$$

and further that the external magnetic field is associated with a poloidal flux through the inner electrode area $A \simeq \pi r^2$:

$$\Phi = B_{pol} A \simeq B_{pol} \pi r^2. \tag{20}$$

Combining Equations (18-20), the condition for spheromak formation is obtained as

$$\frac{\mu_0 I}{\Phi} > \frac{2}{r}, \tag{21}$$

which has been verified experimentally [32].

Compare this result with the expression for α obtained from integrating the force-free state equation (17) over the inner electrode area:

$$\alpha_{elec} = \frac{\int_A \mu_0 \mathbf{J} \cdot d\mathbf{S}}{\int_A \mathbf{B} \cdot d\mathbf{S}} = \frac{\mu_0 I}{\Phi}. \tag{22}$$

Thus α has been noted to have a three-fold role [37]:

1. α is related to the ratio of magnetic energy to magnetic helicity. To show this, manipulate the expression for magnetic energy

$$\begin{aligned} W &= \int_V \frac{B^2}{2\mu_0} d^3r = \frac{1}{2\mu_0}\int_V \mathbf{B}\cdot\nabla\times\mathbf{A} d^3r = \\ &= \frac{1}{2\mu_0}\int_V (\nabla\cdot(\mathbf{A}\times\mathbf{B}) + \mathbf{A}\cdot\nabla\times\mathbf{B})\, d^3r. \end{aligned} \tag{23}$$

Then introduce an arbitrary gauge potential f to find that

$$\begin{aligned} \int_V \nabla\cdot(\mathbf{A}\times\mathbf{B})\, d^3r &= \int_V \nabla\cdot(\mathbf{A}\times\nabla f)\, d^3r = \int_V \nabla f\cdot\mathbf{B} d^3r = \\ &= \int_V \nabla\cdot(f\mathbf{B})\, d^3r = \int_S f\mathbf{B}\cdot d\mathbf{S} = 0 \end{aligned} \tag{24}$$

since $\mathbf{B}\cdot d\mathbf{S} = 0$ on S for an isolated configuration. Thus,

$$\frac{W}{K} = \frac{1}{2\mu_0}\frac{\int \mathbf{A}\cdot\nabla\times\mathbf{B} d^3r}{\int \mathbf{A}\cdot\mathbf{B}\mathrm{d}^3r} = \frac{1}{2\mu_0}\frac{\int \mathbf{A}\cdot\alpha_{energy}\mathbf{B} d^3r}{\int \mathbf{A}\cdot\mathbf{B}\mathrm{d}^3r} = \frac{\alpha_{energy}}{2\mu_0}. \tag{25}$$

2. α is related to current per magnetic flux.

$$\alpha_{elec} = \frac{\mu_0 I}{\Phi}. \tag{26}$$

3. α is an inverse length scale, e.g., for the coaxial magnetized plasma gun

$$\alpha_{geom} = \frac{2}{r}. \tag{27}$$

With helicity a conserved quantity, energy becomes proportional to α. A system relaxing to a minimum energy state will thus relax to a configuration with smallest allowed α, and consequently to the largest allowed size, since α is the inverse length scale. This would explain why the relatively small plasmoid spewed out by an erupting prominence (length scale 10^7-10^8 m) expands to a much larger magnetic cloud (length scale 10^{10}-10^{11} m).

1.3 Motivation behind solar prominence experiment

As noted, both solar prominences and spheromaks are characterized by force-free states in which currents and magnetic fields are parallel, or $\mathbf{J} = \alpha'(r)\,\mathbf{B}$. Magnetic helicity plays an important role in the evolution of both prominences and spheromaks: both will, by Taylor's theory, find minimum energy states given their helicity. Some conjecture [23] that solar prominences spawn spheromak-like (simply connected in Woltjer-Taylor states) magnetic clouds. Given these similarities, it is reasonable to ask if one can recreate a solar prominence in the laboratory, using technology similar to that utilized for spheromak experiments [33] [38][39], but with modified boundary conditions appropriate to prominences.

1.3.1 Arguments against similarities between solar prominences and laboratory experiments

There is a large difference in magnitude between the physical parameters of a solar prominence and a laboratory spheromak. However, in some areas of physics, e.g., fluid dynamics, phenomena can be scaled in such ways that the relative importance of parameters remains the same. We need to scale down the size of a solar prominence (to make it fit in the laboratory), while scaling other parameters in such a way that the relevant physics is preserved, and the question is whether this can be done.

A possible argument used against the relevance of laboratory experiments to solar phenomena is the large difference in an important dimensionless number called the Lundquist number. The Lundquist number (137) relates the resistive diffusive time scale to the convective (Alfvén) time scale. We will now calculate the Lundquist numbers for a solar prominence and a spheromak, respectively.

Using the averages of solar prominence parameters calculated above (see 1.1.3), we find typical thermal energies of $k_B T \simeq 0.7\,\mathrm{eV}$, Debye length $\lambda_D = \sqrt{\varepsilon_0 k_B T_\sigma / n_{0\sigma} q_\sigma^2} \simeq 6 \times 10^{-5}\,\mathrm{m}$, impact parameter $b_{\pi/2} = q_e^2 / 4\pi\varepsilon_0 \mu v_0^2 \simeq 7 \times 10^{-10}\,\mathrm{m}$ (163), Spitzer resistivity $\eta = 6 \times 10^1\,\Omega\,\mathrm{m\,K^{3/2}}\,T^{-3/2} \ln\left(\lambda_D / b_{\pi/2}\right) \simeq 9 \times 10^{-4}\,\Omega$ (166), and a characteristic Alfvén velocity $v_A = B/\sqrt{\mu_0 n_i m_i} \simeq 2 \times 10^5\,\mathrm{m\,/\,s}$ (115). Finally, the Lundquist number is $S \simeq 8 \times 10^9$.

A representative laboratory spheromak has a density of $10^{20}\,\mathrm{m^{-3}}$, thermal energies of $5\,\mathrm{eV}$, magnetic field of $0.5\,\mathrm{T}$, and a length scale of $0.1\,\mathrm{m}$. From this we calculate a Debye length $\lambda_D \simeq 2 \times 10^{-6}\,\mathrm{m}$, impact parameter $b_{\pi/2} \simeq 1 \times 10^{-10}\,\mathrm{m}$, Spitzer resistivity $\eta \simeq 4 \times 10^{-5}\,\Omega$, and a characteristic Alfvén velocity $v_A \simeq 1 \times 10^6\,\mathrm{m\,/\,s}$. The Lundquist number for a typical spheromak is $S \simeq 3 \times 10^3$, which is much less than the Lundquist number for the typical solar prominence. (Under special circumstances, very hot laboratory spheromaks with Lundquist numbers on the order of 10^7 have been created [36].)

This difference in Lundquist numbers would appear to be a significant difference between the solar prominence and the spheromak-like lab plasma, as in the solar case events on the resistive diffusive time scale evolve $\sim 10^{10}$ times slower than the Alfvén time scale, while in the laboratory the ratio is only $\sim 10^3$. However, we will now show why the difference in Lundquist numbers is not important.

1.3.2 Two-fluid induction equation

The difference in Lundquist numbers in solar prominences and in lab-plasmas is a problem only when looking at the resistive MHD analysis of the situation. It is important to remember that MHD (145-148) is a simplification of the two fluid theory that treats electrons and ions separately. (Two fluid theory is in turn a simplification of the more correct

Vlasov equation.) In two fluid theory, the mechanisms acting to change the velocity of electrons are the Lorentz forces, the hydrostatic pressure, and electron-ion collisions (157-166). Thus, the electron fluid equation of motion (essentially Newton's second law) can be written as

$$\underbrace{m_e \frac{d\mathbf{u}_e}{dt}}_{\text{inertia}} = -\underbrace{q_e\left(\mathbf{E}+\mathbf{u}_e\times\mathbf{B}\right)}_{\text{Lorentz}} - \underbrace{\frac{1}{n_e}\nabla P_e}_{\text{hydrostatic}} - \underbrace{\nu_{ei} m_e\left(\mathbf{u}_e-\mathbf{u}_i\right)}_{\text{collisional}}. \tag{28}$$

In the collisional term, the collision frequency ν_{ei} between electrons and ions is equivalent to a resistivity η (166):

$$\nu_{ei} = \frac{n_e q_e^2}{m_e}\eta \tag{29}$$

while the difference between electron and ion velocities can be expressed as a current density

$$\mathbf{J} = -n_e q_e\left(\mathbf{u}_e-\mathbf{u}_i\right). \tag{30}$$

Further note that, as ions are much heavier than electrons, $\mathbf{u}_i \simeq \mathbf{U}$, where $\mathbf{U}$ is the center of mass velocity, so that the electron velocity in the Lorentz term can be expressed as

$$\mathbf{u}_e \simeq \mathbf{U} - \frac{\mathbf{J}}{n_e q_e}. \tag{31}$$

On the left-hand side of Equation (28), motion perpendicular to the magnetic field can be ignored as this will consist of gyro motion, while we are interested in phenomena on much longer time scales than the ion cyclotron period (and consequently very much longer than the electron cyclotron period). As the lighter electrons accelerate more readily along the magnetic field than the heavier ions,

$$\frac{d}{dt}\left(\frac{\mathbf{J}_\parallel}{n_e q_e}\right) = -\left(\frac{d\mathbf{u}_{e\parallel}}{dt} - \frac{d\mathbf{u}_{i\parallel}}{dt}\right) \simeq -\frac{d\mathbf{u}_{e\parallel}}{dt}. \tag{32}$$

Combining Equations (28-32) we obtain

$$\underbrace{-\frac{m_e}{q_e}\frac{d}{dt}\left(\frac{\mathbf{J}_\parallel}{n_e}\right)}_{\text{inertia}} = -q_e\left(\underbrace{\mathbf{E}+\mathbf{U}\times\mathbf{B}-\eta\mathbf{J}}_{\text{MHD Ohm's law}}\underbrace{-\frac{1}{n_e q_e}\mathbf{J}\times\mathbf{B}}_{\text{Hall}}\right)\underbrace{-\frac{1}{n_e}\nabla P_e}_{\text{hydrostatic}} \tag{33}$$

where we recognize the MHD Ohm's law (149). Note that the MHD Ohm's law is obtained from two fluid theory by dropping the electron inertial term, the Hall term, and the hydrostatic pressure term. The electric field $\mathbf{E}$ can be eliminated from the equation by taking the curl and using Faraday's law. We then get the induction equation

$$\underbrace{-\frac{m_e}{q_e^2}\nabla\times\left(\frac{d}{dt}\left(\frac{\mathbf{J}_\parallel}{n_e}\right)\right)}_{\text{inertia}} = \underbrace{\frac{\partial\mathbf{B}}{\partial t}-\nabla\times(\mathbf{U}\times\mathbf{B})+\nabla\times\eta\mathbf{J}}_{\text{MHD induction equation}}+\underbrace{\nabla\times\left(\frac{\mathbf{J}\times\mathbf{B}}{n_e q_e}\right)}_{\text{Hall}}+ \underbrace{-\frac{1}{q_e}\nabla\left(\frac{1}{n_e}\right)\times\nabla P_e}_{\text{hydrostatic}} \tag{34}$$

where we have also divided all terms by q_e.

Next consider the order of magnitude of each term for a characteristic magnetic field B_0, a characteristic density n_0, and a characteristic length scale L. Introduce dimensionless quantities of order unity $\overline{\mathbf{B}}=\mathbf{B}/B_0$, $\overline{n}=n_e/n_0$, $\overline{\nabla}=L\nabla$, $\overline{\mathbf{U}}=\mathbf{U}/v_A$, and $\overline{t}=t/t_A$, where $v_A=B_0/\sqrt{\mu_0 n_0 m_i}$ (115) is the Alfvén velocity, and $t_A=L/v_A$ is the Alfvén time. For all instances of the current density $\mathbf{J}$, use Ampère's law $\nabla\times\mathbf{B}=\mu_0\mathbf{J}$, and multiply each term with t_A/B_0 so that the first two terms of the MHD induction equation will be of order unity.

Begin with the MHD induction equation:

$$\frac{t_A}{B_0}\left(\frac{\partial\mathbf{B}}{\partial t}-\nabla\times(\mathbf{U}\times\mathbf{B})+\nabla\times\eta\mathbf{J}\right)=\frac{\partial\overline{\mathbf{B}}}{\partial\overline{t}}-\overline{\nabla}\times\left(\overline{\mathbf{U}}\times\overline{\mathbf{B}}\right)+\overline{\nabla}\times\underbrace{\frac{t_A}{B_0}\frac{\eta B_0}{L^2\mu_0}}_{=\frac{\eta}{v_A L\mu_0}\equiv S^{-1}}\overline{\nabla}\times\overline{\mathbf{B}}. \tag{35}$$

Per definition of the Lundquist number S (137), the resistive term $\nabla\times\eta\mathbf{J}$ is verified to be of order S^{-1} when the conductive term $\nabla\times(\mathbf{U}\times\mathbf{B})$ is of order unity.

Continue with the Hall term:

$$\begin{aligned}\frac{t_A}{B_0}\left(\nabla\times\left(\frac{\mathbf{J}\times\mathbf{B}}{n_e q_e}\right)\right) &= \frac{t_A}{B_0}\frac{B_0^2}{\mu_0 L^2 n_0 q_e}\left(\overline{\nabla}\times\left(\frac{\left(\overline{\nabla}\times\overline{\mathbf{B}}\right)\times\overline{\mathbf{B}}}{\overline{n}}\right)\right) = \\ &= \frac{B_0}{\mu_0 v_A L n_0 q_e}\left(\overline{\nabla}\times\left(\frac{\left(\overline{\nabla}\times\overline{\mathbf{B}}\right)\times\overline{\mathbf{B}}}{\overline{n}}\right)\right) \qquad (36)\end{aligned}$$

where the only non-unity factor is

$$\frac{B_0}{\mu_0 v_A L n_0 q_e} = \frac{B_0\sqrt{\mu_0 n_0 m_i}}{\mu_0 B_0 L n_0 q_e} = \frac{1}{L}\underbrace{\frac{1}{\sqrt{\mu_0}}\frac{1}{\sqrt{\varepsilon_0}}}_{=c}\underbrace{\sqrt{\varepsilon_0}\sqrt{\frac{m_i}{n_0 q_e^2}}}_{=1/\omega_{pi}} = \frac{c}{\omega_{pi}L} \qquad (37)$$

where ω_{pi} is the ion plasma frequency (151).

Similarly for the hydrostatic pressure term:

$$\begin{aligned}\frac{t_A}{B_0 q_e}\left(\nabla\left(\frac{1}{n_e}\right)\times\nabla P_e\right) &= \frac{t_A}{B_0 q_e}\frac{B_0^2}{L^2 n_0 \mu_0}\left(\overline{\nabla}\left(\frac{1}{\overline{n}}\right)\times\overline{\nabla}\beta_e\right) = \\ &= \frac{c}{\omega_{pi}L}\left(\overline{\nabla}\left(\frac{1}{\overline{n}}\right)\times\overline{\nabla}\beta_e\right) \qquad (38)\end{aligned}$$

using Equation (37), and where $\beta_e = 2\mu_0 P_e/B_0^2$ (150).

And finally the electron inertial term

$$\begin{aligned}\frac{t_A}{B_0 q_e}\left(\frac{m_e}{q_e}\nabla\times\left(\frac{d}{dt}\left(\frac{\mathbf{J}_\parallel}{n_e}\right)\right)\right) &= \frac{t_A m_e}{B_0 q_e^2}\frac{B_0}{L^2 t_A \mu_0 n_0}\overline{\nabla}\times\left(\frac{d}{d\bar{t}}\left(\frac{\overline{\nabla}\times\overline{\mathbf{B}}}{\overline{n}}\right)\right) = \\ &= \underbrace{\frac{m_e}{q_e^2 n_0}}_{1/\omega_{pe}^2}\varepsilon_0\frac{1}{\varepsilon_0}\underbrace{\frac{1}{\mu_0}}_{c^2}\frac{1}{L^2}\overline{\nabla}\times\left(\frac{d}{d\bar{t}}\left(\frac{\overline{\nabla}\times\overline{\mathbf{B}}}{\overline{n}}\right)\right) = \\ &= \frac{c^2}{\omega_{pe}^2 L^2}\overline{\nabla}\times\left(\frac{d}{d\bar{t}}\left(\frac{\overline{\nabla}\times\overline{\mathbf{B}}}{\overline{n}}\right)\right) \qquad (39)\end{aligned}$$

where ω_{pe} is the electron plasma frequency (151).

In summary,

$$- \underbrace{\frac{c^2}{\omega_{pe}^2 L^2}\overline{\nabla}\times\left(\frac{d}{d\bar{t}}\left(\frac{\overline{\nabla}\times\overline{\mathbf{B}}}{\overline{n}}\right)\right)}_{\text{electron inertia}} = \underbrace{\frac{\partial\overline{\mathbf{B}}}{\partial\bar{t}} - \overline{\nabla}\times\left(\overline{\mathbf{U}}\times\overline{\mathbf{B}}\right) + \frac{1}{S}\overline{\nabla}\times\overline{\nabla}\times\overline{\mathbf{B}}}_{\text{MHD induction}} +$$

$$+ \underbrace{\frac{c}{\omega_{pi}L}\overline{\nabla}\times\left(\frac{\left(\overline{\nabla}\times\overline{\mathbf{B}}\right)\times\overline{\mathbf{B}}}{\overline{n}}\right)}_{\text{Hall}} - \underbrace{\frac{c}{\omega_{pi}L}\overline{\nabla}\left(\frac{1}{\overline{n}}\right)\times\overline{\nabla}\beta_e}_{\text{hydrostatic}}. \tag{40}$$

When the first two terms of the MHD induction equation are of order unity, then the resistive term is of order S^{-1}, the Hall term is of order $c/\left(\omega_{pi}L\right)$, the hydrostatic pressure term is of order $\beta_e c/\left(\omega_{pi}L\right)$, and the electron inertial term is of order $c^2/\left(\omega_{pe}^2L^2\right)$. Depending on the plasma parameters S, ω_p, β, and L, the terms that are ignored in normal MHD analysis - the Hall term, the electron inertial term, and sometimes the hydrostatic pressure term - could play an important role in some cases. Numerous papers have discussed the importance of these terms, particularly the Hall term. The Hall term has been used in an experiment to drive DC currents in the rotamak device [40][41]. The electron inertial term has been shown experimentally to be the basis of shear Alfvén resonance cones [42]. The pressure term has been shown to produce very large (10^2 T) magnetic fields in intense laser experiments [43].

Now, for a typical solar prominence (cf 1.1.3) we find that $\omega_{pi} \simeq 1 \times 10^8\,\mathrm{rad/s}$, $\omega_{pe} \simeq 6 \times 10^9\,\mathrm{rad/s}$, and $\beta_e \simeq 5 \times 10^{-3}$. Thus, when the first two terms of the MHD induction equation are of order unity, the resistive term is of order 1×10^{-10}, the Hall term is of order 7×10^{-8}, the hydrostatic pressure term is of order 3×10^{-10}, and the electron inertial term is of order 3×10^{-18}.

For a typical spheromak (cf 1.3.1) we find that $\omega_{pi} \simeq 1 \times 10^{10}\,\mathrm{rad/s}$, $\omega_{pe} \simeq 6 \times 10^{11}\,\mathrm{rad/s}$, and $\beta_e \simeq 8 \times 10^{-4}$. When the first two terms of the MHD induction equation are of order unity, then the resistive term is of order 3×10^{-4}, the Hall term is of order

	Solar prominence	**Lab spheromak**
T [K]	8.5×10^3	6×10^4
$k_B T$ [eV]	0.7	5
L [m]	3×10^7	1×10^{-1}
n [m^{-3}]	1×10^{16}	1×10^{20}
p [Pa]	1×10^{-3}	8×10^1
B [T]	8×10^{-4}	5×10^{-1}
λ_D [m]	6×10^{-5}	2×10^{-6}
$b_{\pi/2}$ [m]	7×10^{-10}	1×10^{-10}
v_A [m/s]	2×10^5	1×10^6
t_A [s]	2×10^2	9×10^{-8}
S	8×10^9	3×10^3
t_R [s]	1×10^{12}	3×10^{-4}
ω_{pi} [rad/s]	1×10^8	1×10^{10}
ω_{pe} [rad/s]	6×10^9	6×10^{11}
β_e	5×10^{-3}	8×10^{-4}
η [Ωm]	9×10^{-4}	4×10^{-5}
S^{-1}	1×10^{-10}	3×10^{-4}
$c/(\omega_{pi} L)$	7×10^{-8}	2×10^{-1}
$\beta_e c/(\omega_{pi} L)$	3×10^{-10}	2×10^{-4}
$c^2/(\omega_{pe}^2 L^2)$	3×10^{-18}	3×10^{-5}

Table 1: Temperature, density, length scale, magnetic field strength, and quantities derived from these for a typical solar prominence and a typical laboratory spheromak.

2×10^{-1}, the hydrostatic pressure term is of order 2×10^{-4}, and the electron inertial term is of order 3×10^{-5}. All parameters have been summarized in Table 1. Note that for both the solar prominence and the lab spheromak, the Hall term is larger than the resistive term. This means that the exact magnitude of the resistive term, proportional to the inverse Lundquist number, is irrelevant. Non-MHD aspects of the field evolution will depend primarily on the Hall term. Also, for both the prominence and the spheromak, the order of the terms from largest to smallest is essentially the same. From this we conclude that a spheromak-like laboratory plasma, with correct boundary conditions, will capture the essential physics of a solar prominence.

1.3.3 Gravitational effects on a solar prominence

Finally we would like to add a note regarding the effect of gravity. Historically there has been much concern about what holds a prominence up against the gravitational forces of the Sun [12]. More recent results indicate that magnetic forces on the Sun dominate gravity [25]. In fact, because of magnetic forces which tend to push a prominence upward, instead of asking what holds a prominence up, one should ask what holds it down. We shall return to that question in Chapter 4.

Chapter 2 Design of solar prominence experiment

This chapter describes the design process of the solar prominence experiment. The design and testing of the various experimental subsystems have been an important and substantial part of this thesis project. Subsequent chapters will refer to particular sections or figures in this chapter as required.

The general idea of the experimental design is to use a vacuum chamber wall to represent the solar surface, place a horseshoe magnet behind this wall to create the appropriate magnetic field, and then send a current through a plasma from one footpoint of the magnetic field to the other, i.e., from one pole of the horseshoe magnet to the other.

As described in the previous chapter, we utilize technologies previously used to create laboratory spheromaks. There are three different technologies, or subsystems, used for three different steps in the plasma creation and evolution, namely, 1) bias magnetic field creation, 2) gas injection, and 3) gas breakdown and current ramp-up. We will describe the requirements and design of each sub-system, as well as describe briefly supporting equipment. We have developed several generations of the solar prominence experiment based on the principles discussed here. Parameters given in this chapter relate to the first generation solar device (Mark I). Chapters 4 and 5 will present parameters for later generations if different from what is given here.

2.1 Vacuum system

2.1.1 Vacuum chamber

Before beginning a detailed discussion on the design of the solar device's three main subsystems, we now describe the vacuum system that will contain the device. A vacuum chamber was specifically designed (by P.M. Bellan) for the purpose of this experiment. The vacuum chamber is made out of stainless steel, and consists of one cylinder and two end domes. The cylinder is 1.6 m (64 in) long and 1.4 m (54 in) in diameter. The end domes have a radius of 1.4 m (54 in) and are mounted with eight 12.7 mm (0.5 in) diameter bolts each on either side of the cylinder. Each dome has a vacuum seal consisting of two concentric o-rings. The cylinder and the two end domes give the vacuum chamber an overall length of $\sim$ 2.0 m and a volume of $\sim$ 2.7 m^3 (ignoring the ports described below). The walls of both cylinder and end domes are 12.7 mm (0.5 in) thick. The vacuum chamber is equipped with a custom-made stand, bolted to the laboratory floor such that the center point of each end dome is located 1.7 m above the floor. The cylinder is fitted with one 355.6 mm (14 in) vacuum port located midway between the end domes, facing the floor, two sets of five 254 mm (10 in) ports located equidistant on either side of the cylinder 1708 mm above the floor, as well as forty-three 69.9 mm (2.75 in) ports located at various locations. One end dome was fitted with three 254 mm ports and four 69.9 mm ports, the other with five 254 mm ports and four 49.9 mm ports. A schematic of the vacuum chamber with all eighteen 254 mm ports numbered is shown in Figure 4.

The solar device mounts on the middle of the three 254 mm ports on one of the end domes (port #17 in Figure 4), with the end dome wall acting as the solar surface, and the

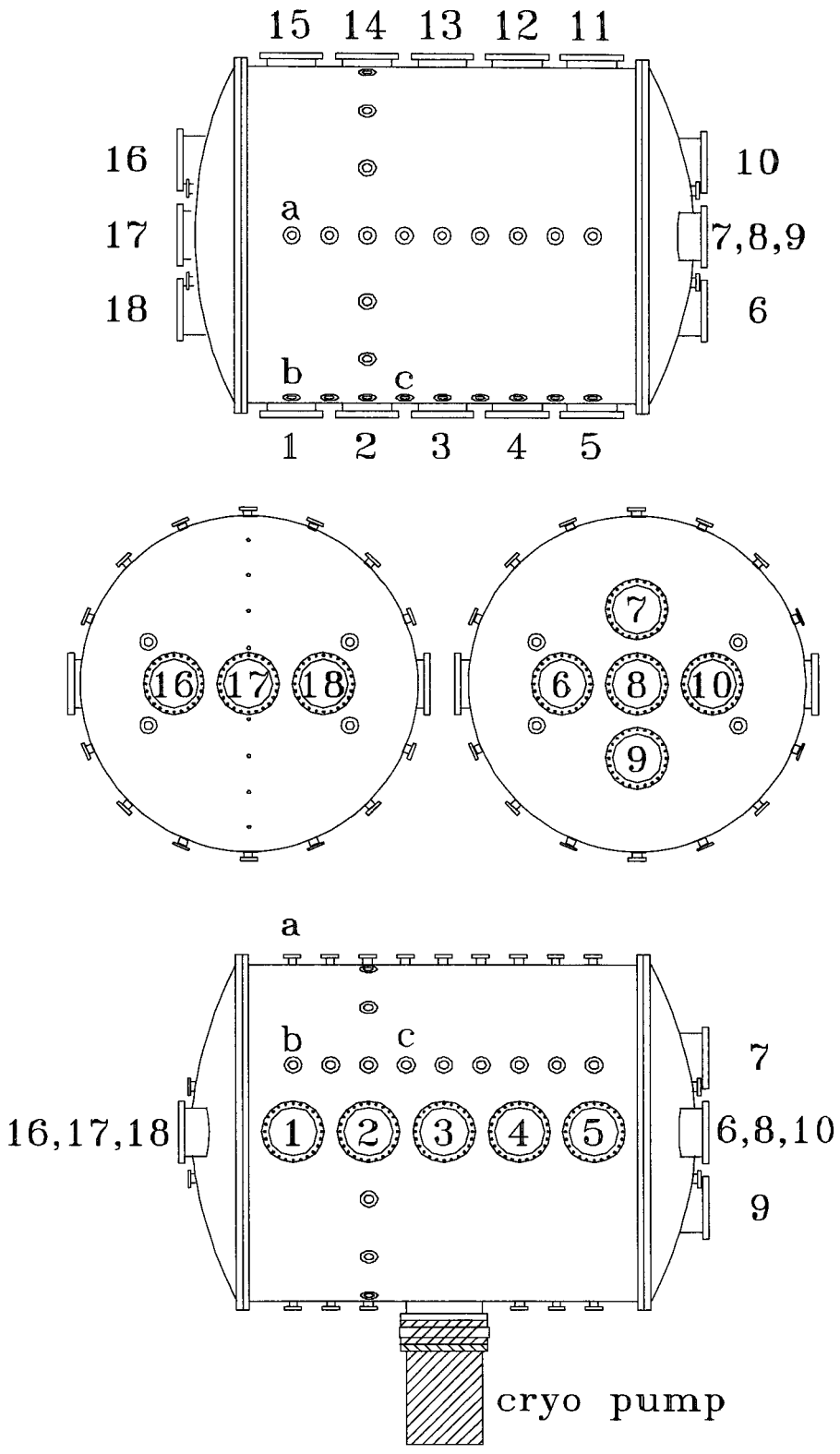

Figure 4: Vacuum chamber viewed from above, either end dome, and from the side.

other vacuum chamber walls sufficiently far away to leave essentially a half infinite space "above" the device.

2.1.2 Vacuum pumps

The 355.6 mm (14 in) port on the vacuum chamber's belly was equipped with a pneumatically operated gate valve and the expander of an APD Cryogenics liquid helium cryo pump model HC-8C (cf Figure 4). The compressor of the pump was located on the floor beneath the vacuum chamber. The compressor provides the expander with liquid helium and receives heated helium gas for refrigeration in a closed cycle. The heat generated in this process is removed through a cooling water system. A cryo diode monitors the temperature inside the expander; the temperature is shown on a liquid crystal display on a nearby lab rack and an automatic circuit can close the gate valve if the temperature becomes too high. This protects the pump in case a small leak in the vacuum chamber overwhelms the pump over time, or in case a more catastrophic leak were to occur. Similarly, an automatic closure of the gate valve ensures that a rough vacuum will be maintained inside the vacuum chamber if the cryo pump should fail or cease operation due to power failure or lack of cooling water.

One of the 69.9 mm ports is equipped with a small gate valve and a vacuum hose to a Varian liquid nitrogen cryo pump. This pump has two cryogenic stages, each filled with Zeolite to provide a large area of gas absorption, as well as a built-in first stage mechanical pump. The Varian pump is used to "rough" the chamber down (obtain a rough vacuum of about 2-4 Pa). The pump was equipped with a thermocouple gauge so that the pressure could be monitored.

Finally, a Tribodyn molecular drag pump was located beneath the vacuum chamber to provide a convenient pump capability for small volumes. The Tribodyn pump is used to pump down gas feed lines and volumes used for diagnostics that can be mounted on and removed from the vacuum chamber while the chamber is under vacuum. The Tribodyn pump is also used as a roughing pump for the APD cryo pump.

With this set of pumps, an oil-free vacuum chamber environment is guaranteed. A clean vacuum chamber is necessary, as earlier experiments with spheromaks have been critically dependent on cleanliness of vacuum chamber walls and spheromak gun electrodes [36][38].

2.2 Subsystem I: Current drive

If we regard a solar prominence as one half of a torus, then we will call the direction along the torus the toroidal direction. This is the direction along the prominence from one footpoint to the other. We will begin the discussion of the three main subsystems of the solar device by looking at the one that drives the toroidal current I_{tor} through the plasma. When operating the solar device (cf 3.2.1), this is the third subsystem to engage, after a bias magnetic field has been created (cf 2.4) and gas has been injected (cf 2.3) to the region of the magnetic field. A spheromak experiment based on the magnetized plasma gun technique (cf 1.2.3) used 59 μF capacitors, switched by an ignitron and connected by low-inductance cables, to achieve currents on the order of 10^5 A on time scales of tens of microseconds [39]. This time scale falls between our estimates for the Alfvén time scale, $t_A = L/v_A \simeq 0.1\,\mu$s, and the resistive diffusive time scale, $t_R = St_A \simeq 300\,\mu$s, as desired (cf 1.3). Thus we would like a similarly designed current drive for our solar prominence experiment. We used a single Aerovox 59 μF capacitor (henceforth called main capacitor)

and designed the current drive around this capacitor, starting with the circuitry needed to release the stored-up energy of the capacitor into a set of coaxial cables.

2.2.1 Ignitron

An ignitron is a device typically used to switch large currents. It consists of a cylinder partially filled with mercury and two major terminals - one at either end of the cylinder. The ignitron must be mounted vertically, so that the mercury inside collects in a pool at the bottom. When so oriented, the ignitron can withstand large voltages (tens of kilovolts) between the two major terminals. To make the ignitron conductive, a voltage pulse is applied to a third terminal, connected to a metal tip pointed toward and just above the surface of the mercury pool. When a voltage pulse is applied to this tip, a small arc forms between the tip and the mercury, causing mercury plasma to rapidly fill the volume above the mercury pool. If the ignitron is part of a high voltage/high current circuit, the ignitron will then close the circuit and stay closed until both voltage and current have dropped below some threshold values.

We used a General Electric ignitron model GL-7703 with a mercury ionization time of $< 0.5\,\mu$s, a maximum voltage stand-off of 25 kV, and a maximum peak current of 100 kA. The internal inductance of this ignitron is 20 nH.

2.2.2 Ignitron activation circuits

To provide a voltage pulse to activate the ignitron, we built a circuit consisting of a $2.0\,\mu$F capacitor, a transformer with a 2.5:1 turn ratio, and a krytron switch. A krytron is a four terminal (cathode, grid, anode, and keep alive), gas-filled, cold cathode switching tube with a β-emitting radioactive source (^{63}Ni) providing initial seed electrons ($\sim 2 \times 10^5$ Bq). We used an EG&G krytron model KN-6B with a response delay of < 30 ns and a rise time of

$< 1\,\mathrm{ns}$. When the krytron is activated, the $1.2\,\mathrm{kV}$ trigger capacitor voltage is applied to the primary side of the transformer, which steps up the voltage to $3.0\,\mathrm{kV}$ on the secondary side. The trigger terminal of the ignitron is the load of the transformer, and the ignitron is thus activated for at least as long as the transformer provides a high voltage/high current. In our case the trigger circuit provides a $5\,\mu\mathrm{s}$ current pulse with a peak of $\sim 2\,\mathrm{kA}$.

Other support circuits include a small DC power supply that charges the $2.0\,\mu\mathrm{F}$ trigger circuit capacitor to $1.2\,\mathrm{kV}$, a fiber-optic to TTL converter with amplifier that triggers a Motorola SCR (Silicon Controlled Rectifier) that in turn (via a smaller "trigger transformer") triggers the krytron. A fiber-optic trigger input is used to avoid a ground-loop. The activation sequence of the current drive subsystem can be summarized as:

$$
\begin{aligned}
&\rightarrow \boxed{\text{fiber-optic to TTL converter}} \rightarrow \boxed{\text{amplifier}} \underset{5\,\mathrm{V}}{\rightarrow} \boxed{\text{small ``trigger transformer''}} \underset{15\,\mathrm{V}}{\rightarrow} \\
&\rightarrow \boxed{\text{SCR}} \rightarrow \boxed{\text{capacitor}} \underset{10\,\mathrm{V}}{\rightarrow} \boxed{\text{big ``trigger transformer''}} \underset{150\,\mathrm{V}}{\rightarrow} \boxed{\text{krytron}} \rightarrow \\
&\rightarrow \boxed{2.0\,\mu\mathrm{F}\text{ capacitor}} \underset{1.2\,\mathrm{kV}}{\rightarrow} \boxed{\text{2.5:1 transformer}} \underset{3.0\,\mathrm{kV}}{\rightarrow} \boxed{\text{ignitron}} \rightarrow \\
&\rightarrow \boxed{\text{main capacitor}} \overset{\text{low inductance}}{\underset{\leq 12\,\mathrm{kV}\ \text{(before breakdown)}}{\rightarrow}} \boxed{\text{solar device}} \rightarrow \boxed{I_{tor}\text{ in plasma}}
\end{aligned}
$$

2.2.3 Low inductance circuit

From the point of view of the electrical circuit that includes the plasma, the plasma behaves like an inductor with inductance $2W_B/I_{tor}^2$, where W_B is the magnetic energy and I_{tor} is the current passing through the plasma. We would like to maximize the amount of stored energy in the capacitor that is converted into magnetic energy in the plasma. (The stored energy is $W_C = \frac{1}{2}CV_0^2$, where C is the capacitance and V_0 the charging voltage.) Thus, the inductance of the remainder of the circuit between capacitor and plasma device should be

minimized. For this purpose we obtained four Belden low-inductance coaxial cables model YK-98 (2 m long, 13 mm diameter).

A low inductance connection from the main capacitor to the coaxial cables was designed by P.M. Bellan. The low inductance connection consists of a copper sheet ground plane connected to the ground side of the capacitor (by four bolts, one in each corner of the capacitor's top rectangular surface), and a copper cylinder housing the ignitron. The other ends of the coaxial cables were connected in pairs to four brass blocks, which in turn were welded to two 3.81 cm (1.5 in) diameter iron cylinders - the legs of the horseshoe magnet (cf 2.4.3). The diameter of the iron cylinders was chosen among conveniently available diameters of iron rod, after an evaluation of the magnetic circuit (cf 2.4). As the ends of the iron cylinders would act as electrodes, each cylinder was capped by a 6.35 mm (0.25 in) thick tantalum disk. Tantalum is a highly refractory metal [44][45][46] and served to reduce plasma erosion of the electrodes [47]. In this fashion, a system with minimum inductance, from capacitor to horseshoe magnet, was obtained.

2.2.4 Charging supply and other supporting equipment

A Kaiser Systems charging supply model LS1500 was connected via a Ross Engineering relay (15 kV stand-off) to the main capacitor. The supply has the capability to charge the capacitor to 15 kV. Two high power 300 Ω carbon resistors were connected via another Ross relay (12 kV stand-off) to the capacitor, to provide a way of discharging it in an emergency.

The main capacitor and related equipment (the ignitron, the krytron circuitry, the charging supply, the emergency resistors, and the Ross relays) were placed in a cabinet featuring a transparent Plexiglas front for direct verification of the state of the Ross relays.

The entire cabinet was powered through the 12 kV relay. A circuit board with 86 resistors was installed to act as a finely tuned voltage divider to measure the voltage on the capacitor. A control panel was installed with the necessary electronics for the following controls: a main power switch that engages the 12 kV relay and powers the cabinet (the capacitor energy is automatically dumped to the emergency resistors if power fails or the main power is switched off), a knob to select the end-of-charge voltage on the main capacitor (each 0.6 units on knob corresponds to 1 kV), a push-button to engage the charging supply, and finally an emergency button to stop the charging sequence. The control panel also included a light emitting diode (LED) display to show the voltage on the main capacitor, as well as six LEDs to indicate power on to the charging supply, end-of-charge voltage achieved, and various fault conditions (cf Figure 5).

Once assembled, the current drive subsystem was powered on and tested. The main capacitor was charged to increasingly higher voltages (starting at 5.5 kV) and discharged through a resistive-inductive dummy load. The test was finished with several (>10) discharges at 10.3 kV, and the system performed flawlessly.

2.2.5 Plasma formation

While the main purpose of the current drive subsystem is to drive a current through the plasma from one footpoint to the next, another design goal was to let this system have the secondary function of breaking down gas to form a plasma. If successful, there would be no need to construct a separate system for that purpose alone. Normally, a gas breaks down when subjected to a sufficiently large electric field. Before presenting the conditions necessary for breakdown, the process of ionization should be described briefly.

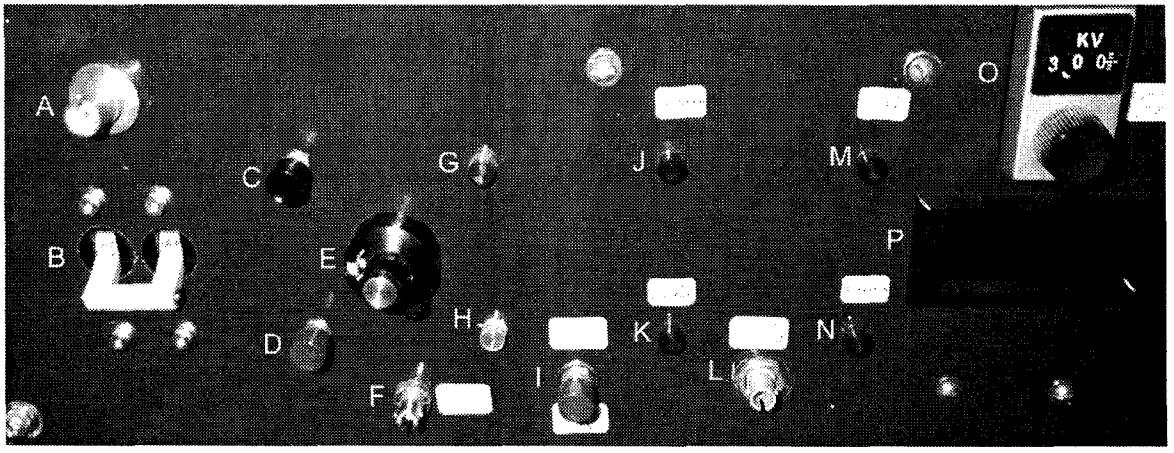

Figure 5: Main control panel. A) Output from Rogowski coil monitoring current from main capacitor (not initially installed, cf 4.1.6). B) Main power switch. C) Push-button to start charge-up sequence. D) Emergency push-button to stop charge-up sequence in progress. E) Knob to select end-of-charge voltage. F) Fiber-optic input to trigger the krytron switch. G) LED indicating power on to charging supply. H) LED indicating end-of-charge voltage on the main capacitor. I) Push-button to temporarily disengage main ground from entire cabinet for 7 s (not initially installed, cf B.2.1). J) LED indicating abnormal temperature in charging supply. K) LED indicating over-voltage on the main capacitor. L) Fiber-optic trigger output (not initially installed, cf 4.1.6). M) LED indicating that the main capacitor has become disconnected from the charging supply, or that the leads from the charging supply have become short- or open-circuited. N) LED indicating that the charging supply interlock has been activated. O) Knob to select at what voltage on the main capacitor a trigger is sent out on L), essentially the discharge voltage (not initially installed, cf 4.1.6). P) LED display indicating voltage on the main capacitor.

Ionization processes are often divided into three classes [48]. α-processes describe the mechanisms by which initial seed electrons are produced. These electrons are needed for avalanche effects and other processes to occur. In the case of laboratory devices, such as spheromak guns or our solar device, initial seed electrons are often provided by photo-ionization at the cathode, i.e., an incoming photon knocks an electron out of its orbit around a metal atom in the cathode (the photoelectric effect). Another example of an α-process would be a radioactive isotope that is producing electrons directly through radioactive decay (cf 2.2.2).

When seed electrons are accelerated to sufficiently large velocities by the electric field between the anode and the cathode, collisions between the electrons and neutral atoms yield secondary electrons and ions. This is referred to as a β-process.

Finally, the γ-processes are those associated with ions (produced by a β-process) smashing into the cathode and producing more electrons. It is clear that ionization of a gas depends on several factors, such as gas species and density [49], the type of metal [49][50] and the surface texture of the electrodes [49][50], geometric factors including the anode-cathode distance [49], and whether or not the electric field is alternating (RF) or constant (DC) [51][52][49].

Paschen's law gives the electric field strength needed for breakdown to occur in a given gas at a given pressure between two parallel electrodes [53][48][27]. This is not the geometry our experiment (a better estimate might be to use a model for a Townsend discharge through a long tube, or in our case a magnetic flux tube [50]), but the law still provides a reasonable estimate for when breakdown can be expected. Paschen's law can be derived in a straightforward manner from elementary scattering theory [27], and the voltage

Gas	B [VPa^{-1}m^{-1}]	C [Pa^{-1}m^{-1}]
He	25.5	0.49
H_2	104	0.88
Ar	135	1.96
Air	274	2.42

Table 2: Breakdown coefficients for various gases assuming typical electrode materials and surface textures.

V needed for breakdown to occur is obtained as:

$$V > \frac{Bpd}{\ln(Cpd)} \tag{41}$$

where p is the gas pressure, d is the electrode separation, and B and C are coefficients that can be estimated theoretically but in practice are assigned empirical values. Values [53][27] for B and C for various gases are given in Table 2, assuming typical electrode materials and surface textures. While operation with a variety of gases is an interesting undertaking, the gas we will use principally is hydrogen. Paschen's law for hydrogen, using the coefficients from Table 2, is plotted in Figure 6. The minimum voltage required to ionize hydrogen is $\simeq 322\,\mathrm{V}$ and occurs at a pressure-distance product of $\simeq 3.1\,\mathrm{Pa\,m}$. To the left of this point, breakdown becomes increasingly difficult as the gas gets thinner and thinner. Eventually the gas is so thin that initial seed electrons created by α-processes can travel the entire distance d without colliding with neutral gas atoms, thus never starting any β-processes. When the pressure-distance product is less than $\simeq 1.1\,\mathrm{Pa\,m}$, the hydrogen gas is so thin that breakdown cannot occur at any voltage. To the right of the minimum voltage point, breakdown becomes increasingly difficult as the gas gets denser and denser. The higher the density, the more often electrons collide with neutrals, and eventually the collisions occur so frequently that the kinetic energy of the electrons is insufficient for β-

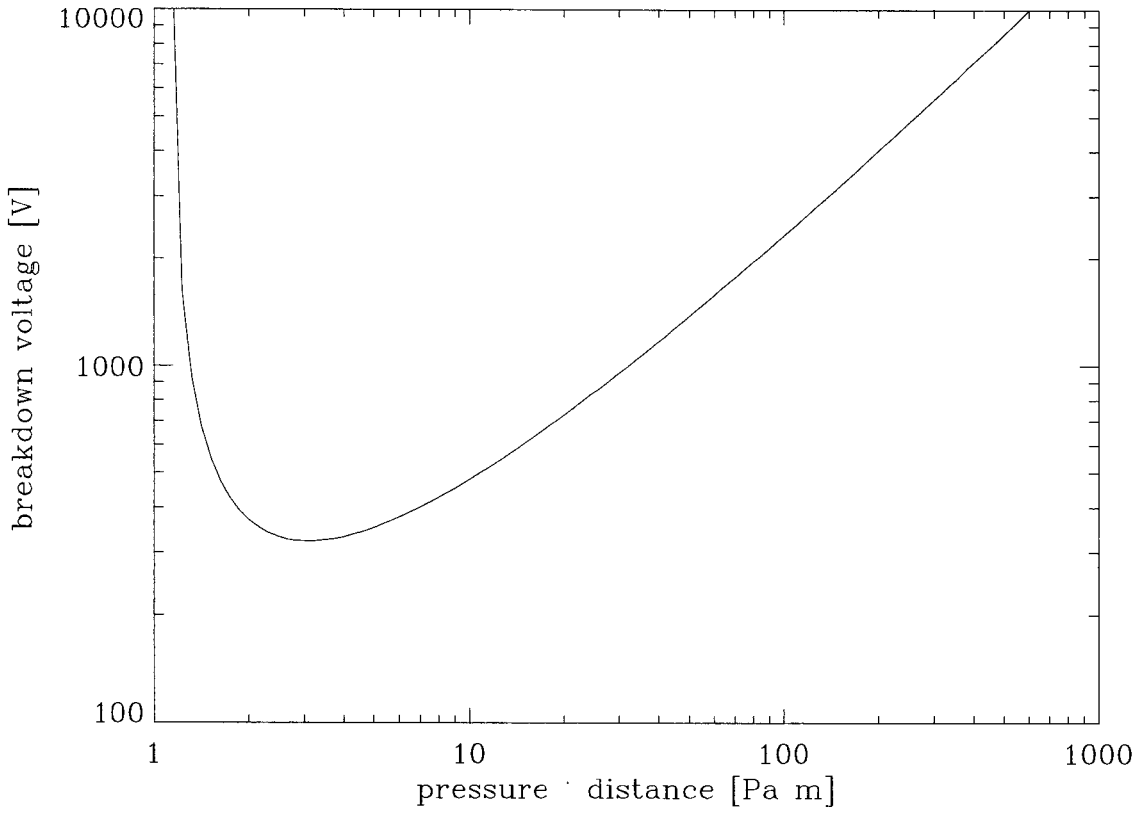

Figure 6: Breakdown voltage of molecular hydrogen as a function of pressure times distance.

processes to occur. However, one can always find a voltage at which breakdown will occur, no matter how dense the gas is.

With the equipment described above (see 2.2.4), up to 12 kV can provided for gas ionization (the limit is set by the 12 kV relay). However, to give ourselves some maneuvering room, it is desirable to have a guaranteed ionization at about half that voltage. At 6 kV, hydrogen breaks down between $\simeq 1.2\,\mathrm{Pa\,m}$ to $\simeq 320\,\mathrm{Pa\,m}$ (cf Figure 6), and we will keep this in mind at the next step of our design process.

Before continuing to the design of the gas injection subsystem, we would like to remark that this part of the experiment presumably has no analogy on the solar surface; prominences have not been observed to form as a result of gas breakdown in regions with large electric fields, but rather form from the emergence of magnetic flux ropes from the solar photosphere [54]. This does not invalidate our experiment; once the laboratory plasma has formed, it is unimportant how it got there.

2.3 Subsystem II: Gas injection

Gas allowed to expand into vacuum travels at a speed roughly equal to the speed of sound in that gas. Thus, in order to localize hydrogen gas to only the desired region of the vacuum chamber, a gas valve that remains open $\leq 100\,\mu\mathrm{s}$ is desirable. A special, electromagnetically operated gas valve [55], a type which has been used in spheromak experiments based on the coaxial magnetized plasma gun technique [33][27][39], would be suitable for this purpose. Such a gas valve consists of a gas line, or channel, blocked by a metal disk resting against an o-ring. High gas pressure, often several atmospheres, on one side of the disk presses the disk against the o-ring, creating a seal from the other side of the disk, which is at vacuum. A spring provides some additional force on the disk, mainly to keep the disk

against the o-ring while the system is not in use and there is no gas pressure differential. A few turns of wire form an electromagnet, aligned with the disk, on the other (vacuum) side of the o-ring. To operate the gas valve, a voltage pulse is applied to the electromagnet. This creates a magnetic field that seeks to penetrate the metal disk, resulting in an image current forming within the disk itself. This image current, antiparallel to the current in the electromagnet, creates a repelling force that moves the disk off the o-ring, allowing gas to stream past the disk into the vacuum side. As ohmic resistance in the disk attenuates the image current (thus allowing the magnetic field to penetrate the disk), the gas pressure and the spring force the disk back onto the o-ring, stopping the gas flow.

2.3.1 Order of magnitude analysis

From the Paschen's law analysis (cf 2.2.5), the desired pressure-distance product, in the region where the plasma is to form, is $\simeq 1.2\,\mathrm{Pa\,m}$ to $\simeq 320\,\mathrm{Pa\,m}$. The solar device must fit on a 254 mm port (cf 2.1.1). The anode-cathode distance must be somewhat less than the inside diameter, 20 cm, of the port. However, breakdown is not likely to occur on a straight line between the electrodes; the electrodes will also act as magnetic poles, so breakdown will occur along horseshoe-shaped magnetic field lines arcing between anode and cathode. As the exact shape of the magnetic field is not yet known, our best guess for the anode-cathode distance is the vacuum port size, or 20 cm. This gives a desired pressure in the range 5.8 Pa to 1600 Pa to successfully ionize the hydrogen gas. The optimum pressure is around 10-100 Pa.

We can now conduct an order of magnitude analysis to estimate the desired number of turns in the electromagnet and what size capacitor bank is needed to pulse the magnet. Start this analysis by estimating the volume of the region where the plasma forms to be about

ten liters, or $10^{-2}\,\mathrm{m}^3$. For practical reasons, a gas valve size on the order of centimeters is desired, so the gas volume in the valve, that is allowed to pass by the metal disk, is about $1\,\mathrm{cm}^3$. Thus, the gas feed pressure should be approximately 10^5-10^6 Pa (or 1-10 times atmospheric pressure). With an area of about $1\,\mathrm{cm}^2$ enclosed by the o-ring, this results in a force on the disk of 10^2-$10^3\,\mathrm{N}$, which must be overcome by the repelling force between the current in the wires and its image current in the metal disk. The force between two circular, concentric currents is given by Equation (123), where, in our case, the separation $d \simeq 1\,\mathrm{cm}$ and the electromagnet area is about $10\,\mathrm{cm}^2$ so that $a_1 = a_2 \simeq \sqrt{10/\pi}\,\mathrm{cm}$. Thus, the required current times turns product is on the order of $10^3\,\mathrm{A}$ to move the disk from the o-ring. Such a large current can be provide by a capacitor bank discharging through the electromagnet. A convenient charging voltage for a capacitor bank is on the order of $10^2\,\mathrm{V}$. From the theory of LRC-circuits (cf A.2.5), the desired resistance of our electromagnet is $R = 0.1\,\Omega$. With a characteristic time $t_{L/R} = L/R \simeq 100\,\mu\mathrm{s}$, the desired inductance is $L \simeq 10^{-5}\,\mathrm{H}$. If the electromagnet is made up of a single turn of wire, its inductance would be $L_{\text{one turn}} \simeq 10^{-7}\,\mathrm{H}$ (128), assuming a wire diameter on the order of $1\,\mathrm{mm}$. As the inductance scales with the square of the number of turns, $L \sim n^2$, a coil of wire with about 10 turns is needed. Assuming that $\sim 10\%$ of the stored energy $\frac{1}{2}CV^2$ in the capacitor bank converts to magnetic energy $\frac{1}{2}LI^2$, then $C \simeq 10^{-4}\,\mathrm{F}$.

2.3.2 Completed gas valve

A prototype gas valve and then the gas valve to be used in the experiment were designed (by P.M. Bellan) based on the above analysis and then tested. The interested reader will find detailed information on this in Appendix B.1. A $400\,\mu\mathrm{F}$ capacitor bank (maximum voltage $V_{valve} = 700\,\mathrm{V}$) was used for regular operation of the gas valve. Pulsing the gas

valve with this supply and using hydrogen, we found the following empirical formula for the amount of hydrogen let into the chamber:

$$\begin{aligned} m_{inj} \;\simeq\; & V_{valve} \cdot (p_{valve} \cdot 0.019\,\mu\mathrm{g}\,/\,(\mathrm{V\,MPa}) + 0.0070\,\mu\mathrm{g}\,/\,\mathrm{V}) + \\ & - (p_{valve} \cdot 6.3\,\mu\mathrm{g}\,/\,\mathrm{MPa} + 2.1\,\mu\mathrm{g}) \end{aligned} \tag{42}$$

where m_{inj} is the mass of injected hydrogen gas, V_{valve} is the voltage on the 400 μF capacitor bank of the pulsing supply, and p_{valve} is the pressure in the gas line that feeds the valve. This formula was established using gas line pressures between 0.34 MPa (34 psi over-pressure) and 0.79 MPa (100 psi over-pressure) and for pulse voltages up to 450 V, and is accurate to within 10%. It is likely to be accurate also for higher voltages and larger pressures. For smaller pressures there will eventually be some non-linearity when the restoring force of the spring becomes comparable to the restoring force of the gas pressure. Note that voltages less than $\sim$ 320 V will not open the gas valve (will lead to $m_{inj} < 0$ using the empirical formula).

2.4 Subsystem III: Toroidal magnetic field

The subsystem that drives a current along the prominence in the toroidal direction has already been described (cf 2.2). There is also a magnetic field in the toroidal direction, B_{tor}. On the Sun, this magnetic field is created by processes (the solar dynamo) beneath the solar surface. For our purposes, the details of these processes are irrelevant, but we must nevertheless provide a toroidal magnetic field by some means. We chose to use a horseshoe electromagnet consisting of an iron core and two coils. This section presents the reasons for our choice and details the design process.

2.4.1 Order of magnitude analysis

Just as we did for the gas injection subsystem, we shall now conduct an order of magnitude analysis to determine the desired toroidal magnetic field strength. The current that will pass through the plasma in the toroidal direction is $\sim 10^5$ A (cf 2.2). Using this number in Equation (21), the toroidal magnetic field flux density, $\Phi \simeq \mu_0 Ir/2$, can be calculated. For this calculation the length r must be estimated. It should be the radius of the area over which we seek the magnetic flux density, i.e., the minor radius of our (half) torus-like prominence. Obviously, the prominence minor radius cannot be larger than major radius, which will be $\lesssim 10\,\mathrm{cm}$ because the inside of a 254 mm vacuum port is $\approx 10\,\mathrm{cm}$. Furthermore, when a current is flowing along a plasma, the plasma cross-section will be "pinched" down - the larger the current, the smaller the cross-sectional area. This is called the pinch effect and comes from the fact that parallel currents attract each other. Consequently, it is reasonable to assume that the minor radius will be some fraction of the major radius, and so we estimate $r \simeq 1\,\mathrm{cm}$. The desired magnetic flux density is then calculated to be $\Phi \simeq 1$ mWb. This corresponds to a required magnetic field strength of $B_{tor} \simeq 2\,\mathrm{T}$, a fairly strong field.

Permanent magnets could possibly provide a field of this magnitude, but are unsuitable as we would like to be able to vary the magnetic field strength from one discharge to the next, to study the effect on the plasma. Electromagnets (coils) can accomplish the task, but because of their size they would have to be some distance away from the electrodes, which would require unrealistically large capacitor banks to drive large currents through the coils. A solution to this problem is to introduce a magnetic circuit composed of a material that essentially conducts magnetic fields. When this type of material is subjected to an external magnetic field $\mathbf{B}_0$ (from the coils), the material becomes magnetized so that

the total magnetic field at any point is the sum of the original field $\mathbf{B}_0$ and the field from the magnetized material $\mathbf{B}_m$. From the point of view of designing our solar device, using a circuit of magnetized material introduces some mathematical complexities which will be discussed next.

2.4.2 Mathematical treatment of magnetized material

A magnetized material can be thought of as a collection of magnetic dipoles with dipole moments $\mathbf{m}_k$. The definition of a magnetic dipole moment (138) gives us the vector potential corresponding to the magnetization vector

$$\mathbf{A}_m = \frac{\mu_0}{4\pi}\int_V \frac{\mathbf{M}\times(\mathbf{r}_i - \mathbf{r}_j)}{r^3} dv' \tag{43}$$

where the integration is over the volume V of the magnetized material, and $\mathbf{r}_i - \mathbf{r}_j$ is the vector from the infinitesimal volume dv' in the material to the point where we want to know $\mathbf{A}_m$. Thus, the total magnetic field in any point can now be written as

$$\mathbf{B} = \mathbf{B}_0 + \mathbf{B}_m = \mathbf{B}_0 + \nabla\times\mathbf{A}_m = \mathbf{B}_0 + \frac{\mu_0}{4\pi}\int_V \nabla\times\left(\frac{\mathbf{M}\times(\mathbf{r}_i - \mathbf{r}_j)}{r_{ij}^3}\right) dv' \tag{44}$$

where $r_{ij} = |\mathbf{r}_i - \mathbf{r}_j|$. To find $\mathbf{B}$ as a function of the imposed field $\mathbf{B}_0$ we must have a relation between $\mathbf{M}$ and $\mathbf{B}_0$, or at least between $\mathbf{M}$ and $\mathbf{B}$. This relation depends on the properties of the magnetized material. For an isotropic material that is hysteresis-free,

$$\begin{aligned} \mathbf{H} &\equiv \frac{\mathbf{B}}{\mu_0} - \mathbf{M} \\ &\Longleftrightarrow \mathbf{M} = \frac{\mathbf{B}}{\mu_0} - \mathbf{H} = \frac{\mathbf{B}}{\mu_0} - \frac{\mathbf{B}}{\mu} = (1 - \upsilon_r)\frac{\mathbf{B}}{\mu_0} \end{aligned} \tag{45}$$

where the relative reluctivity υ_r is the inverse of the relative permeability $\mu_r = \mu/\mu_0$. Obviously this equation is only valid inside the magnetized material. Combining Equations

(44-45) we obtain

$$\mathbf{M}-\frac{1-\upsilon_r}{4\pi}\int_V \nabla\times\left(\frac{\mathbf{M}\times(\mathbf{r}_i-\mathbf{r}_j)}{r_{ij}^3}\right)dv' = \frac{1-\upsilon_r}{\mu_0}\mathbf{B}_0. \tag{46}$$

This equation must be solved numerically [56]. Dividing the volume V into N small finite elements ΔV_i an approximation of Equation (46) is obtained as

$$\mathbf{M}_i-\frac{1-\upsilon_r}{4\pi}\sum_{j=1}^{N}\nabla\times\left(\frac{\mathbf{M}_j\times(\mathbf{r}_i-\mathbf{r}_j)}{r_{ij}^3}\right)\Delta V_j = \frac{1-\upsilon_r}{\mu_0}\mathbf{B}_{0i} \tag{47}$$

where $i=1,2,\ldots,N$. Introducing a Cartesian coordinate system we have

$$M_{xi}-\frac{1-\upsilon_r}{4\pi}\sum_{j=1}^{N}\left(\alpha_{xij}M_{xj}+\beta_{xij}M_{yj}+\beta_{zij}M_{zj}\right)\Delta V_j = \frac{1-\upsilon_r}{\mu_0}B_{0xi} \tag{48}$$

$$M_{yi}-\frac{1-\upsilon_r}{4\pi}\sum_{j=1}^{N}\left(\beta_{xij}M_{xj}+\alpha_{yij}M_{yj}+\beta_{yij}M_{zj}\right)\Delta V_j = \frac{1-\upsilon_r}{\mu_0}B_{0yi} \tag{49}$$

$$M_{zi}-\frac{1-\upsilon_r}{4\pi}\sum_{j=1}^{N}\left(\beta_{zij}M_{xj}+\beta_{yij}M_{yj}+\alpha_{zij}M_{zj}\right)\Delta V_j = \frac{1-\upsilon_r}{\mu_0}B_{0zi}. \tag{50}$$

Note that the elements ΔV_i can have different volumes and shapes. For purposes of calculating the α and β coefficients, consider the dipole of each element to be located in the geometric center $[x_i, y_i, z_i]$ of ΔV_i. The coefficients for $i \neq j$ are

$$\alpha_{xij} = \frac{3(x_i-x_j)^2-r_{ij}^2}{r_{ij}^5} \tag{51}$$

$$\alpha_{yij} = \frac{3(y_i-y_j)^2-r_{ij}^2}{r_{ij}^5} \tag{52}$$

$$\alpha_{zij} = \frac{3(z_i-z_j)^2-r_{ij}^2}{r_{ij}^5} \tag{53}$$

$$\beta_{xij} = \frac{3(x_i-x_j)(y_i-y_j)}{r_{ij}^5} \tag{54}$$

$$\beta_{yij} = \frac{3(y_i-y_j)(z_i-z_j)}{r_{ij}^5} \tag{55}$$

$$\beta_{zij} = \frac{3(z_i-z_j)(x_i-x_j)}{r_{ij}^5} \tag{56}$$

where the distance r_{ij} between point i and point j is

$$r_{ij} = \sqrt{x_{ij}^2 + y_{ij}^2 + z_{ij}^2}. \tag{57}$$

Self-interaction, $i = j$, can be regarded as surface currents on the volume element, and one finds

$$\alpha_{xii} = \alpha_{yii} = \alpha_{zii} = \frac{8\sqrt{2}}{\Delta V_i} \tag{58}$$

$$\beta_{xii} = \beta_{yii} = \beta_{zii} = 0. \tag{59}$$

Equations (48-50) could be solved iteratively (Gauss-Seidel iteration) with the initial guess $\mathbf{M}_{guess} = (1 - \upsilon_r)/\mu_0 \mathbf{B}_0$, which is then used in the summation term to calculate a new value for $\mathbf{M}$. A more elegant method comes from realizing that the equations can be written in a matrix form and that the solution for $\mathbf{M}$ can be obtained with a single matrix inversion [56]. Equations (48-50) can be written as the matrix equation

$$\mathbf{E}_{3N\times 3N}\mathbf{M}_{3N} = \mathbf{G}_{3N} \tag{60}$$

where the $[x, y, z]$-components of the unknown magnetization vectors are

$$\mathbf{M}_{3N} = [M_{x1}, M_{x2}, \ldots, M_{xN}; M_{y1}, M_{y2}, \ldots, M_{yN}; M_{z1}, M_{z2}, \ldots, M_{zN}]^T \tag{61}$$

and the right hand side is

$$\mathbf{G}_{3N} = \frac{1 - \upsilon_r}{\mu_0} [B_{0x1}, B_{0x2}, \ldots, B_{0xN}; B_{0y1}, B_{0y2}, \ldots, B_{0yN}; B_{0z1}, B_{0z2}, \ldots, B_{0zN}]^T . \tag{62}$$

The $3N$ by $3N$ coefficient matrix in Equation (60) can be partitioned into nine sub-matrices

$$\mathbf{E}_{3N\times 3N} = \begin{bmatrix} \mathbf{E}_{11} & \mathbf{E}_{12} & \mathbf{E}_{13} \\ \mathbf{E}_{21} & \mathbf{E}_{22} & \mathbf{E}_{23} \\ \mathbf{E}_{31} & \mathbf{E}_{32} & \mathbf{E}_{33} \end{bmatrix} \tag{63}$$

where the N by N partitioned matrices are given by

$$\mathbf{E}_{11} = \delta_{ij} - \frac{1-\upsilon_r}{4\pi}\alpha_{xij}\Delta V_j \tag{64}$$

$$\mathbf{E}_{12} = -\frac{1-\upsilon_r}{4\pi}\beta_{xij}\Delta V_j \tag{65}$$

$$\mathbf{E}_{13} = -\frac{1-\upsilon_r}{4\pi}\beta_{zij}\Delta V_j \tag{66}$$

$$\mathbf{E}_{21} = -\frac{1-\upsilon_r}{4\pi}\beta_{xij}\Delta V_j \tag{67}$$

$$\mathbf{E}_{22} = \delta_{ij} - \frac{1-\upsilon_r}{4\pi}\alpha_{yij}\Delta V_j \tag{68}$$

$$\mathbf{E}_{23} = -\frac{1-\upsilon_r}{4\pi}\beta_{yij}\Delta V_j \tag{69}$$

$$\mathbf{E}_{31} = -\frac{1-\upsilon_r}{4\pi}\beta_{zij}\Delta V_j \tag{70}$$

$$\mathbf{E}_{32} = -\frac{1-\upsilon_r}{4\pi}\beta_{yij}\Delta V_j \tag{71}$$

$$\mathbf{E}_{33} = \delta_{ij} - \frac{1-\upsilon_r}{4\pi}\alpha_{zij}\Delta V_j \tag{72}$$

where δ_{ij} is the Kronecker delta.

Once we have inverted $\mathbf{E}_{3N\times 3N}$ and obtained the magnetization vectors, we can now obtain the total magnetic field, from both coil(s) and magnetized material, in any point $[x_k, y_k, z_k]$ as

$$B_{xk} = B_{0xk} + \frac{\mu_0}{4\pi}\sum_{j=1}^{N}\left(\alpha_{xij}M_{xj} + \beta_{xij}M_{yj} + \beta_{zij}M_{zj}\right)\Delta V_j \tag{73}$$

$$B_{yk} = B_{0yk} + \frac{\mu_0}{4\pi}\sum_{j=1}^{N}\left(\beta_{xij}M_{xj} + \alpha_{yij}M_{yj} + \beta_{yij}M_{zj}\right)\Delta V_j \tag{74}$$

$$B_{zk} = B_{0zk} + \frac{\mu_0}{4\pi}\sum_{j=1}^{N}\left(\beta_{zij}M_{xj} + \beta_{yij}M_{yj} + \alpha_{zij}M_{zj}\right)\Delta V_j. \tag{75}$$

2.4.3 Magnetized circuit design

With a mathematical tool at hand to deal with magnetized circuits, various designs of our horseshoe electromagnet could be numerically tested. The horseshoe-shaped magnetic cir-

cuit was divided into three parts - two parallel cylinders and a rectangular block, as depicted in Figure 7. Each of the three parts was divided into volume elements for the calculation of magnetization. This division can be done arbitrarily, although the results will, to some extent, depend on how the volume elements are chosen. The total magnetic field $\mathbf{B} = \mathbf{B}_0 + \mathbf{B}_m$ cannot be calculated accurately at a point that is much closer to one volume element than to that element's nearest neighbor, i.e., there is a limit on how close to the iron the magnetic field can be calculated accurately. A reasonable choice of elements is to use six elements in a ring around an innermost element in a hexagonal pattern. Continuing with the inner and outer radii of a second ring equal to the diameter of the innermost element, there will be ten elements in the second ring, etc. The angular orientation of each ring may be random. The height of each cylindrical slab, as well as each side of the volume elements of the rectangular block, is chosen as close as possible to the diameter of the innermost cylindrical elements. Our final choice of elements is shown in Figure 7. Due to computer limitations (IDL computer language on a 120 MHz Pentium personal computer), we were limited to two rings of elements, i.e., 17 volume elements, in each cylindrical slab.

The material of the magnetized circuit should have a low relative reluctivity to better "conduct" the magnetic field. We chose to use commercial iron ($\simeq$ 99% Fe), a low cost ferromagnetic material with a relative permeability of $\mu_r \simeq$ 200-6000 [44]. The range of values is due to the fact that iron is not a linear magnetic material. In fact, it is not hysteresis-free and consequently not isotropic, in apparent violation of Equation (45). This can be justified by noticing that in the equation we use $1 - \upsilon_r \equiv 1 - 1/\mu_r$ so that the exact size of μ_r is not important when $\mu_r \gg 1$.

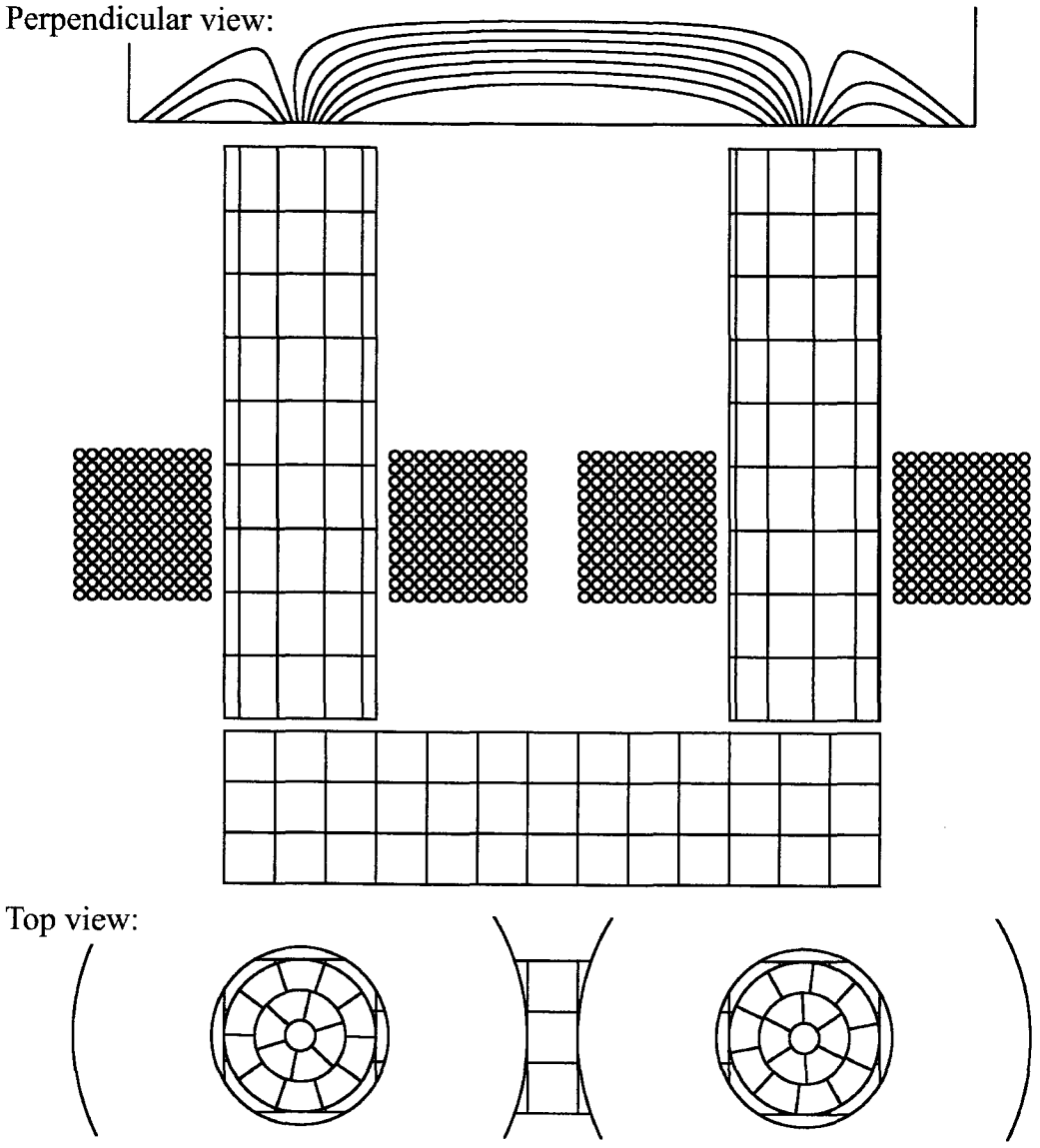

Figure 7: Design of horseshoe electromagnet for the bias magnetic field (one half scale). The iron core of the magnet consists of two parallel cylinders with a rectangular block connecting them (area hatched with rectangles). A small gap between cylinders and block allows each cylinder to be put at a different electric potential. The two coils of the electromagnet are shown in cross-section (area of small circles). Above the perpendicular view of the magnet, field lines of the calculated total magnetic field are shown. Field lines have only been drawn where they are inside the vacuum chamber, bounded to the left, right, and bottom by the vacuum port (tantalum disks will go in the gap between the top of the iron cylinders and the field lines; cf 2.2.3). There is a top view of the magnet beneath the perpendicular view. The hatch pattern of the iron core, in both perpendicular view and top view, represents the different volume elements used for calculations of the iron magnetization.

Around each cylinder was located a coil consisting of $n = LT$ turns of wire in L layers with T turns per layer. To calculate $\mathbf{B}_0$ provided by the coils, equations (116-117) were used for each turn. Note that for $L \gg 1$ and $T \gg 1$, L and T can be changed arbitrarily without significantly affecting $\mathbf{B}_0$, as long as we keep nI, the product of the number of turns and the current through each turn, constant.

After some numerical experimentation we settled on dimensions for the magnetic circuit and the coils. Note that the magnetization is a volume effect, so that the more iron, the stronger the field. However, the more iron used, the harder it gets to physically fit the coils, as well as other necessary parts such as vacuum seals, in the design. A diameter of 38.1 mm (1.5 in) was used for the iron cylinders, conveniently available in the form of iron rods, and also a size large enough to function as a magnetic circuit but small enough to leave room for the coils. The cylinders were located 127 mm apart, with each cylinder surrounded by a coil of inner radius 22 mm and outer radius 57 mm, located between 63 mm and 101 mm from the electrode surfaces. The chosen height of the cylinders was 143 mm, and the magnetic circuit was completed by a rectangular block with dimensions $38 \times 38 \times 165\,\mathrm{mm}^3$. A 3 mm gap was left between the rectangular block and each cylinder. The magnetic field for our final design is shown in Figure 7. The field strength along the axis between the two magnetic poles is plotted in Figure 8. Note that the field strength is given per current turn. The plot in Figure 8 was calculated using coils with $L = 11$ layers and $T = 12$ turns per layer, as indicated by the small circles in Figure 7, and a current per turn of $I = 1\,\mathrm{A}$. The magnetic field strength peaks at $\sim 5 \times 10^{-6}\,\mathrm{T}$ per current turn, so for the desired field strength of $B_{tor} \simeq 2\,\mathrm{T}$, the required current times turns product is $\sim 4 \times 10^5\,\mathrm{A}$.

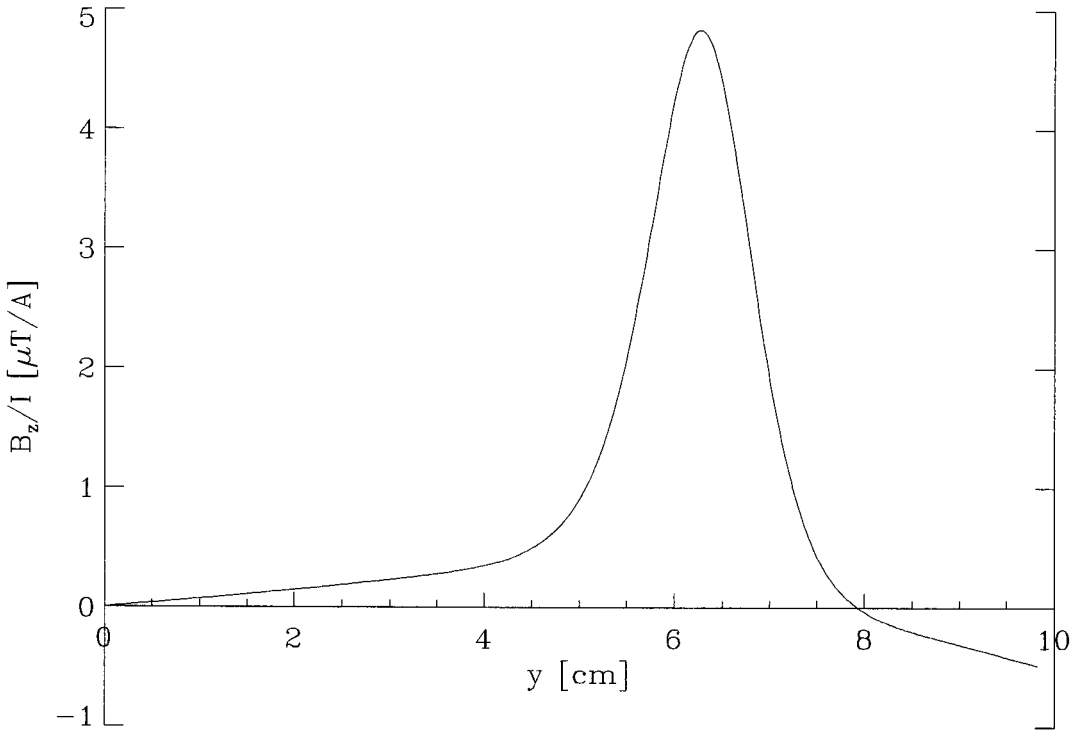

Figure 8: Toroidal magnetic field (component perpendicular to electrode surface) per current turn as a function of distance along the axis between the two magnetic poles. $y = 0\,\mathrm{cm}$ is midway between the magnetic poles, $y \simeq 9.8\,\mathrm{cm}$ is at the vacuum port.

2.4.4 Capacitor bank for toroidal magnetic field

The number of turns in the coils and what size capacitor bank that is needed, to drive the required current through the coils, must still be calculated. The self-inductance of a solenoid can be obtained by integration of Equation (125). Assuming that the length l of the solenoid is much larger than its diameter $2a$, then [57]

$$L_{11} = \pi\mu a^2 n^2 \left(\sqrt{l^2 + a^2} - a\right). \tag{76}$$

For the coils described above (see 2.4.3), use the inner radius for a because the relevant quantity is the linked magnetic flux, which will be dominated by the high permeability region of the iron cylinder. Thus, $a \simeq 22\,\mathrm{mm}$ and $l \simeq 38\,\mathrm{mm}$. The mutual inductance between the two coils must be between $L_{12} = 0$ and $L_{12} = \Phi/I$, depending on how well the magnetic circuit conducts the magnetic flux Φ. Both self- and mutual inductances can be calculated numerically, using our technique above (see 2.4.2), but for our purposes only a rough estimate is needed, so say that $L_{12} = \Phi/2I$. Connecting the two coils in parallel to the same capacitor bank C, the total inductance of the circuit is

$$L = \frac{\pi}{2}\mu a^2 n^2 \left(\sqrt{l^2 + a^2} - a\right) + \frac{\Phi}{4I} \tag{77}$$

where, in addition to l and a, we know that $\Phi \simeq 1$ mWb and that $nI \simeq 4 \times 10^5\,\mathrm{A}$. The resistance of the circuit is

$$R = \frac{1}{2}\frac{\rho n 2\pi a_R}{\pi b^2} = \frac{\rho n a_R}{b^2} \tag{78}$$

where the average radius of the coils $a_R \simeq 40\,\mathrm{mm}$, the resistivity of copper wire $\rho \simeq 1.7 \times 10^{-8}\,\Omega\mathrm{m}$, and where the wire radius b is known from $nb^2 \simeq 2l\,(a_R - a)$. The characteristic

L/R-time for the circuit is

$$t_{L/R} = \frac{L}{R} = \frac{l}{\rho}\left(1 - \frac{a}{a_R}\right)\left(\pi\mu a^2\left(\sqrt{l^2+a^2} - a\right) + \frac{\Phi}{2n\,(nI)}\right) \simeq \mu_r \times 41\,\mu\text{s} + \frac{1.2\,\text{ms}}{n}. \tag{79}$$

We have required $L \gg 1$ and $T \gg 1$ (cf 2.4.3) so $n = LT > 25$ would be reasonable. We know that $\mu_r \geq 200$. Consequently, the second term in Equation (79) is much smaller than the first term, so that the number of wire turns in our coils will not significantly affect the time response of the circuit. We used $2.7 \times 2.7\,\text{mm}^2$ square cross-section copper wire in 12 layers with approximately 13 turns per layer.

The total energy of the toroidal magnetic field is

$$W_{B_{tor}} = \frac{1}{2}LI^2 \simeq \frac{\pi}{4}\mu a^2\,(nI)^2\left(\sqrt{l^2+a^2} - a\right) \simeq \mu_r \cdot 1.7\,\text{J} \tag{80}$$

dropping the second term of (77) as it is much smaller than the first term. Assuming $\mu_r \approx 200$, we chose to use a capacitor bank $C = 9.9\,\text{mF}$ (designed by F.T. Cosso) that could be charged to $V_B = 600\,\text{V}$ to provide the necessary energy $\frac{1}{2}CV_B^2$ for the magnetic field. (The capacitor bank is rated to handle $V_B = 700\,\text{V}$, but as charging times get increasingly longer the higher the voltage, $V_B = 400$-$450\,\text{V}$ is the maximum voltage at reasonable charging times; we charged only a few times to $V_B = 600\,\text{V}$.)

2.4.5 Test of finished magnetic circuit

When testing the finished magnetic subsystem, the magnetic field strength was found to peak 7.5 ms after the system was triggered. Increasing the charging voltage on the 9.9 mF capacitor bank did not lead to a linear increase in peak magnetic field strength as expected. The magnetic flux and average magnetic field strength over the electrode surfaces are plotted as a function of charging voltage in Figure 9. The maximum obtained magnetic flux through the electrode surface was $\sim$ 0.50 mWb, as measured by a 100 turn pick-up coil

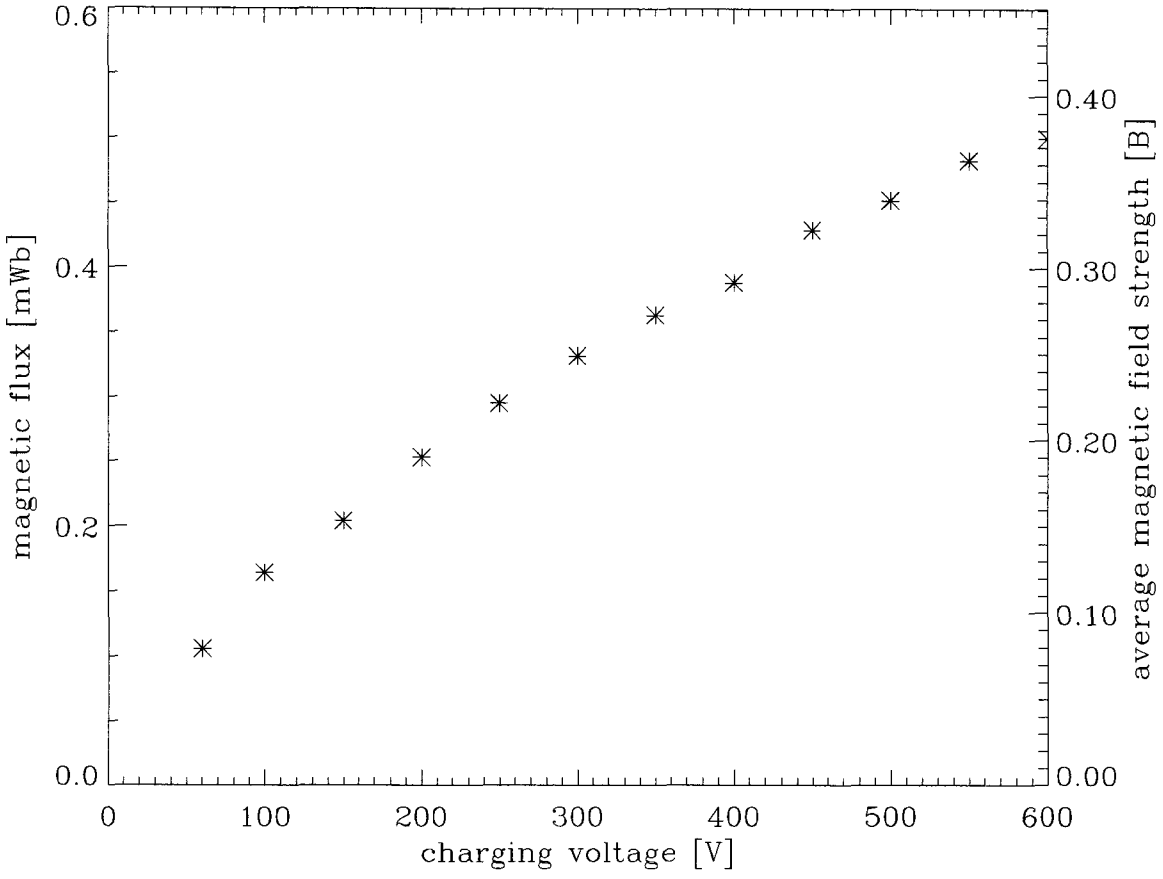

Figure 9: Toroidal magnetic flux and average magnetic field strength at the electrode surfaces of the first generation solar device (Mark I) as a function of charging voltage on the bias field capacitor bank.

with approximately the same diameter, 41 mm, as the electrodes. This corresponds to an average magnetic field strength of $\sim$ 0.38 T, which was deemed adequate as the magnetic profile calculation (cf Figure 8) indicates that the magnetic field should be somewhat stronger over the smaller cross-sectional area of the prominence. The non-linearity in Figure 9 was explained by looking more carefully at the magnetization of each individual element in the magnetic circuit calculation. Upon inspection, some elements should have been saturated, i.e., the magnetization of these elements exceeded the maximum possible magnetization of iron. The largest calculated magnetization was 3.7×10^6 A m^{-1}, while the maximum magnetization of iron is $M_0 = 1.7 \times 10^6$ A m^{-1} [44]. It is difficult to augment the matrix inversion technique to correct for saturation. Later calculations (Chapters 4-5) used a Gauss-Seidel iteration which included maximum magnetization limits. These calculations predicted the measured magnetic fields very well. The matrix inversion technique works very well in conditions when saturation does not occur.

2.5 The completed solar device

Using the principles and tests discussed in this chapter, the solar device depicted in Figure 10 was designed (by P.M. Bellan). It consists of a horseshoe electromagnet with an iron core and two coils providing a toroidal magnetic flux up to 0.50 mWb, a gas valve that can inject 1-10 μg of gas on a $\sim$ 100 μs time scale, and a low-inductance path for the toroidal current. The electromagnet is gapped by a Teflon insulator so that the two magnetic poles can act as electrodes for the toroidal current without being short-circuited. Electric insulation between electrodes and the vacuum chamber port is provided by two alumina tubes and two Macor rings. (Macor is a machinable ceramic, porcelain-like in appearance and composed of 55% fluorophlogopite mica and 45% borosilicate.) The coils were wound

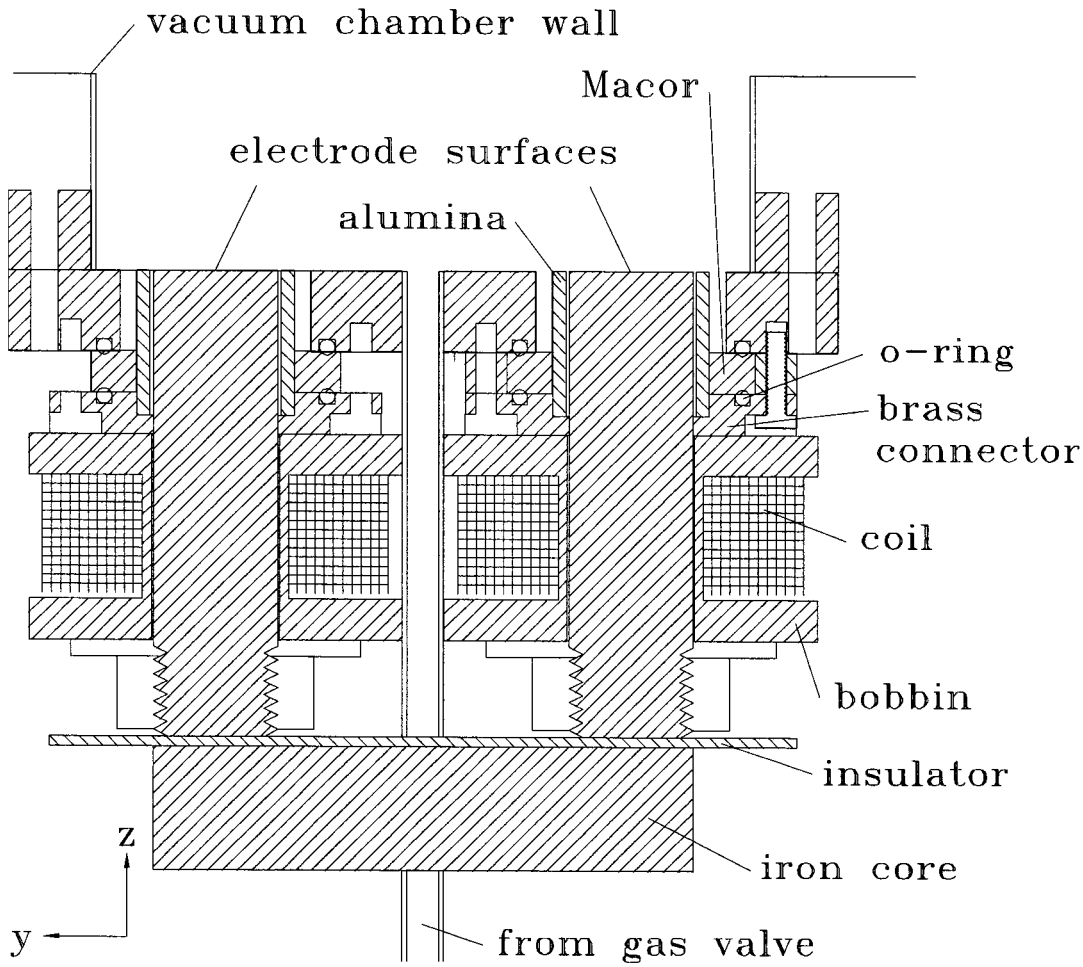

Figure 10: Schematic of first generation solar device (Mark I). A horseshoe electromagnet consisting of an iron core and two coils provides the toroidal magnetic field. Gas is injected from a gas valve (not shown) into the vacuum chamber (above the device) in the region of the magnetic field. The magnetic poles also act as electrodes for the toroidal current, connected via welded-on brass blocks to the coaxial cables (not shown) from the main capacitor bank. Electric short-circuiting is prevented by Lucite bobbins, alumina tubes, Macor rings, and an insulator gap in the horseshoe magnet. The vacuum seal is provided by a pair of o-rings between the vacuum port and the Macor rings and another pair between the Macor rings and the brass blocks.

on Lucite bobbins to insulate them electrically from the iron core. The vacuum seal is provided by o-rings between the vacuum port, the Macor rings, and brass blocks that are part of the low-inductance circuit.

Based on the same principles we also developed later generations of the experiment, as described in Chapters 4-5.

Chapter 3 First generation solar prominence experiment

This chapter presents the results from the first generation solar prominence experiment. The chapter consists of three sections. First, equipment and diagnostics will be described. Second, experimental results will be presented. Third, the results will be discussed and interpreted. The most important finding is that we can explain both prominence S-shapes and an observed plasma bifurcation using the force-free state equation $\nabla \times \mathbf{B} = \alpha \mathbf{B}$ (17). This supports the conjecture that solar prominences are in Woltjer-Taylor states (cf 1.2.1). Other important results include:

- Bright regions in images of the plasma are interpreted as current paths.
- The experiment confirmed the formation of S-shaped prominences when injecting positive helicity, and reverse S-shaped prominences when injecting negative helicity.
- The twist of a plasma, measured as a pitch angle, was confirmed to be larger for more unstable plasmas, smaller for more stable plasmas.

3.1 Equipment and diagnostics

3.1.1 Mark I solar device

The first generation solar device (Mark I) is described in detail in Chapter 2 and is shown schematically in Figure 10. In summary, it consists of two 38 mm diameter electrodes, located 127 mm apart, that are also the magnetic poles of a horseshoe electromagnet. A high speed gas valve pulsed by a 400 μF capacitor bank, charged to a voltage V_{valve} up to 700 V, injects a controlled amount of hydrogen gas (42) between the two electrodes. A

59 μF energy storage capacitor is used to apply an electrode voltage difference V_I of up to 12 kV that breaks down the gas. Once the plasma has formed, the capacitor drives a current through the plasma in the toroidal direction. This capacitor will be referred to as the main capacitor. A 9.9 mF electrolytic capacitor bank drives current through an electromagnet which generates the horseshoe-shaped magnetic field. This capacitor bank will be referred to as the bias field capacitor. The bias field capacitor can be charged up to $V_B = 600$ V and provides a magnetic flux of up to 0.50 mWb at the electrodes/magnetic poles. This corresponds to an average magnetic field strength of 0.38 T over the electrode surface area (cf Figure 9).

3.1.2 Timing sequencer

To trigger each subsystem of the solar device, as well as various diagnostics, a timing sequencer (designed by F.T. Cosso) with eight fiber-optic trigger outputs was used. (Fiber-optic triggering is desirable as it eliminates ground loops.) The timing sequencer consisted of four modules, each with one trigger input and two trigger outputs. The first trigger output of module N can be set to send out a trigger at $(1, 2, \ldots, 199) \cdot t_N$ after the input trigger. The second trigger output can be set to send out a trigger at $(1, 2, \ldots, 199) \cdot t_N$ after the first trigger output. The fixed incremental times for each module are $t_1 = 10$ ms, $t_2 = 10\,\mu$s, $t_3 = 1\,\mu$s, and $t_4 = 0.1\ \mu s$.

3.1.3 Vacuum chamber

The solar device was mounted on a 254 mm (10 in) port (port #17; cf Figure 4) of the large vacuum chamber described in Chapter 2. The chamber was pumped down to 5.5×10^{-5} Pa (4.1×10^{-7} torr) before operation of the solar device.

3.1.4 High voltage probe

A Tektronix high voltage probe model P6015 (maximum DC voltage 20 kV) was used to measure the voltage on one electrode (typically the cathode). The high voltage probe output was read by a 125 MHz LeCroy 9400 oscilloscope.

3.1.5 Rogowski coil

In order to measure the toroidal current, a Rogowski coil (cf A.2.15) was placed around the inner conductor of one of the four low-inductance cables connecting the main capacitor to the solar device. The coil was calibrated to $2.00 \times 10^{-5}\,\mathrm{V}\,/\,\mathrm{A}$. Taking into account the fact that the coil would only measure one quarter of the total toroidal current, assuming the current is symmetrically distributed among the four low-inductance cables,

$$I_{tor} = V_{Rogowski} \cdot 2.00 \times 10^{5}\,\mathrm{A}\,/\,\mathrm{V}\,. \tag{81}$$

Designed specifically for this experiment, the Rogowski coil was built to withstand high voltage and to include some special features that would reduce electronic noise. The coil was wound from 0.1 mm diameter magnet wire in 606 turns around a torus with minor radius $b = 2.4\,\mathrm{mm}$ and major radius $a = 19.1\,\mathrm{mm}$. The resistor of the integrating circuit was placed as close as possible to the coil (within a few millimeters) to reduce noise in the circuit. To further eliminate pick-up noise, the coil was wrapped in aluminium foil that was connected to the outer conductor (the shield) of a triaxial cable, while the lead from the coil was connected to the cable ground and the resistor was connected to the center conductor. One side of the foil was electrically insulated with electrical tape to prevent one layer of the wrapping foil to touch another layer, which would short out the signal that we want to measure. The entire coil assembly was placed in a machined groove in a slab of Lucite. Another slab of Lucite was glued on top of the first to completely encase the

coil in a high-voltage-proof material, and in that process any air pockets were removed by filling the groove with RTV. A hole in the Lucite allowed the center conductor of one of the low-inductance cables to pass through the center of the coil torus.

The Rogowski coil output was read by a 125 MHz LeCroy 9400 oscilloscope.

3.1.6 Photodiode

The light emitted by the plasma was measured by a simple photodiode located behind a quartz glass window (of vacuum port #1; cf Figure 2.1.1). The photodiode output was read by a 125 MHz LeCroy 9400 oscilloscope.

3.1.7 Cameras

A Xybion gated, intensified, charge-coupled-device (CCD) camera model ISG-250 was set up to take pictures of the plasma. The camera had a shutter speed of 80 ns and was triggered externally at a desired time after the plasma breakdown. The images were then captured by a frame-grabber card on a personal computer (66 MHz Intel 486), which displays the images on a monitor and stores these images for future use. Each image is 512 by 480 pixels in 256 grayscales (8 bits). The camera was mounted on a tripod oriented so that the camera would view the solar device through a 254 mm vacuum port equipped with a quartz window (vacuum ports #1, #6, and #14 in Figure 4). The technology of the camera was such that only one image per plasma discharge could be obtained, but it was our hope that the experiment would be sufficiently repeatable that it would be possible to assemble images from several discharges into pseudo-movies. Such high degree of reproducibility has been demonstrated in spheromak experiments [58], where magnetic probes were moved from shot to shot.

A prototype framing camera, on demonstration from Princeton Scientific Instruments, was also used in order to obtain multi-frame images from a single shot. The camera could take thirty images of a single discharge at a rate of one image every 2μs. Alternatively, the camera could take six series of five images each, with 1μs between each image and 2μs between the last image of one series and the first image of the subsequent series. The shutter speed of the camera was 1μs.

A second single image camera was obtained for demonstration purposes from Princeton Instruments. This camera was much more light-sensitive than the Xybion camera and could be fitted with various filters to study light in certain spectral lines. The image resolution was 576 by 384 pixels. The shutter speed was 10 ns.

3.1.8 Scintillation detector

To detect possible x-rays emitted by the plasma, a scintillation detector was positioned behind the quartz glass window of vacuum port #1 (cf Figure 2.1.1) and later behind a Mylar film of port #15. X-rays would be produced if some electrons accelerate long enough before colliding with plasma (impurity) ions or neutrals. The scintillation detector was covered with an aluminium foil to prevent detection of visible light, and was then calibrated with a ^{137}Cs source (γ-ray energy 661.64 keV). The detector output was 325 mV when exposed to a photon flux of $2 \times 10^3\,\mathrm{s}^{-1}\,\mathrm{cm}^{-2}$.

3.2 Results

3.2.1 Establishing nominal operating parameters

The following settings were used in the initial attempt to operate the solar device. The toroidal magnetic field was pulsed with a capacitor bank setting of $V_B = 400\,\mathrm{V}$, corresponding to a peak magnetic field of 0.35 T (cf Figure 9 above). The gas valve was sup-

plied with 274 kPa (25 psi over-pressure) hydrogen gas and pulsed with $V_{valve} = 350\,\mathrm{V}$, corresponding to an injected hydrogen mass of $0.45\,\mu\mathrm{g}$ using Equation (42). The chosen discharge voltage on the main capacitor was $V_I = 1.00\,\mathrm{kV}$.

The main capacitor was charged to a slightly higher voltage ($\sim 1.15\,\mathrm{kV}$) than the desired discharge voltage. When the Kaiser charging supply (cf 2.2.4) disengages, the voltage on the main capacitor started to drop slowly. After 10-15 seconds the voltage has dropped to the desired discharge voltage, as indicated by the control panel LED (cf Figure 5 above), and the timing sequencer was then manually triggered from a small handheld trigger-unit via an optical fiber. The timing sequencer was configured to send out trigger pulses as follows. First a pulse was sent to the bias field capacitor at time t_B. After a time delay of 7.0 ms, at time t_{valve}, a trigger pulse was sent to the gas valve supply. An additional $460\,\mu\mathrm{s}$ after that, at time $t_I \equiv 0$, a trigger pulse was sent to the main capacitor. The time delays were chosen so that B_{tor} peaks (7.5 ms after the bias field capacitor is triggered; cf 2.4.5) when the hydrogen gas is at the correct location in the vacuum chamber, after travelling at the speed of sound, $c_s \simeq 1.3\,\mathrm{km/s}$ (156), an approximate distance of 60 cm from the gas valve.

With these settings, the voltage on the main capacitor remained at 1.00 kV after the system was triggered, and we concluded that breakdown did not occur, i.e., no plasma formed. In order to satisfy the conditions of Paschen's law (41), the charging voltage on the main capacitor was increased to 4.00 kV, 6.00 kV, and 8.00 kV, still without achieving breakdown. Next the gas valve trigger time t_{valve} was changed as the estimate for t_{valve} could be far from optimum; either the bulk of the hydrogen gas is not given enough time to reach the region between the two electrodes, or the time is too long, so that most of the

gas has already passed through the region. Changing t_{valve} to $-10\,\mu$s, $-100\,\mu$s, $-200\,\mu$s, $-300\,\mu$s, ..., $-900\,\mu$s did not result in a gas breakdown, not even with the main capacitor charged to 8.00 kV. A repetition of these combinations with $V_{valve} = 500$ V to increase the total amount of injected gas also failed.

Suspecting that an insufficient amount of seed electrons (cf 2.2.5) were available in the vacuum chamber, t_I was synchronized with the discharge of a spheromak gun that was mounted on the opposite end dome of the vacuum chamber. A $10\,\mu$s delay was included to allow electrons to travel across the vacuum chamber. Not surprisingly, the main capacitor now discharged, sending a pink flash of light through the vacuum chamber viewports.

Operation with the solar device synchronized to a spheromak discharge provided repeatable discharges. However, we desired to discontinue this awkward mode of operation, as it left no available channels on the timing sequencer to trigger other equipment, such as diagnostics. A UV flashlamp was therefore installed to provide seed electrons (via the photoelectric effect; cf 2.2.5). A small shaft was drilled though one cylinder of the electromagnet iron core. A sapphire window with o-rings was installed at end of the shaft to provide a vacuum seal while allowing light through from the flashlamp, which was positioned against the window. The flashlamp was triggered from an available channel on the timing sequencer at $t_{flash} = -10\,\mu$s, accounting for a $4\,\mu$s delay in the flashlamp circuitry and another $6\,\mu$s for the light from the flashlamp to reach its peak as measured by the photodiode. Breakdown of the gas was not achieved with these settings. Changing t_{flash} from $0\,\mu$s to $-1\,\mu$s, $-2\,\mu$s, ..., $-15\,\mu$s, and $-23\,\mu$s, combined with variations in $V_I = 4.00$ kV, 5.00 kV, 6.00 kV, and variations in $t_{valve} = -320\,\mu$s, $-340\,\mu$s, ..., $-520\,\mu$s did not work either.

Equipment	bias field capacitor	gas valve capacitor	oscilloscope main capacitor	cameras
Operating parameters	$V_B = 400\,\mathrm{V}$	$V_{valve} = 550\,\mathrm{V}$ $p_{valve} = 7.9 \times 10^5\,\mathrm{Pa}\ (H_2)$	$V_I = 6.00\,\mathrm{kV}$	
Time	$t_B \simeq -7.91\,\mathrm{ms}$	$t_{valve} = -873\,\mu\mathrm{s}$	$t_I \equiv 0$	$t_{camera} = 0.1\text{-}30.0\,\mu\mathrm{s}$

Table 3: Nominal operating parameters for the first generation solar device (Mark I). The trigger time for each piece of equipment is relative to the trigger of the main capacitor.

As a next step the gas valve pulsing supply voltage and the hydrogen gas line pressure were increased to their maximum values, $V_{valve} = 700\,\mathrm{V}$ and $p_{valve} = 791\,\mathrm{kPa}$ (100 psi over-pressure) respectively, corresponding to an injected hydrogen mass of $8.3\,\mu\mathrm{g}$, or almost twenty times more than the previous amount. The gas valve timing was set to $t_{valve} = 443\,\mu\mathrm{s}$. With this amount of injected gas, breakdown was achieved for $V_I \gtrsim 5.85\,\mathrm{kV}$. Repeating the same procedure with the flashlamp activated (at $t_{flash} = -23\,\mu\mathrm{s}$), the hydrogen gas would break down at a slightly lower voltage, $V_I \gtrsim 5.83\,\mathrm{kV}$. (Further experimentation with the flashlamp did not produce more substantial effects than this.)

Keeping this setting for the gas valve ($8.3\,\mu\mathrm{g}$ of injected hydrogen), and triggering at $V_I = 6.00\,\mathrm{kV}$, a range of t_{valve} values were tested. Breakdown occurred when t_{valve} was between $-443 \pm 20\,\mu\mathrm{s}$ and $-1223 \pm 50\,\mu\mathrm{s}$. At an approximate midpoint of this range, $-873\,\mu\mathrm{s}$, breakdown occurred for $V_{valve} \gtrsim 4.75\,\mathrm{kV}$. From this information, we established the nominal operating parameters for the solar device as given in Table 3. (The trigger times for the cameras were chosen after obtaining the time profile of light emissions from the plasma; cf 3.2.3.)

3.2.2 Current and voltage profiles

For the established nominal settings of Table 3, the current through the plasma peaked around $t = 9.5\,\mu\mathrm{s}$ at some $72\,\mathrm{kA}$, as measured by the Rogowski coil. The current subse-

V_B [V] $\longrightarrow$	200		300		400	(nominal)
$\downarrow$ Event $\downarrow$	Time [μs]	Current [kA]	Time [μs]	Current [kA]	Time [μs]	Current [kA]
First peak	9.5	60	9.5	64	9.5	72
First zero	19.0	0	17.5	0	16.5	0
Second peak	24.0	-12	23.0	-14	22.0	-20
Second zero	31.0	0	30.0	0	27.5	0
Third peak	$\simeq$35	1	$\simeq$35	2	34.5	6
Third zero	$\simeq$41	0	$\simeq$41	0	$\simeq$40	0

Table 4: Current profile described in terms of peaks and the times when the current rang through zero, for different toroidal magnetic field strengths (expressed in charging voltage on bias field capacitor bank).

quently rang through zero twice. When the current reached zero a third time, it remained there. The current profile is summarized in Table 4.

The cathode voltage remained at $-6\,\mathrm{kV}$ until $4\,\mu$s after triggering, when breakdown occurred. The voltage then dropped to about $-1.2\,\mathrm{kV}$ within 0.1μs. The anode voltage remained at $0\,\mathrm{V}$ until breakdown, and then increased to $+1.2\,\mathrm{kV}$. After breakdown, the voltage was proportional to the derivative of the current, albeit with a small time lag (ringing through zero at $13\,\mu$s and $25\,\mu$s). The cathode voltage always equaled the negative of the anode voltage.

The voltage and current traces for a typical discharge at nominal settings is shown in Figure 11.

3.2.3 Light emissions

The photodiode registered light starting at $t \simeq 4\,\mu$s, indicating breakdown. The peak of the photodiode signal occurred at $t \simeq$ 8-9 μs.

3.2.4 Images

The Xybion camera was triggered at varying times, and images were obtained at times when the photodiode measured light emissions from the plasma. The camera took one picture of each plasma discharge. The discharge process and subsequent evolution of the

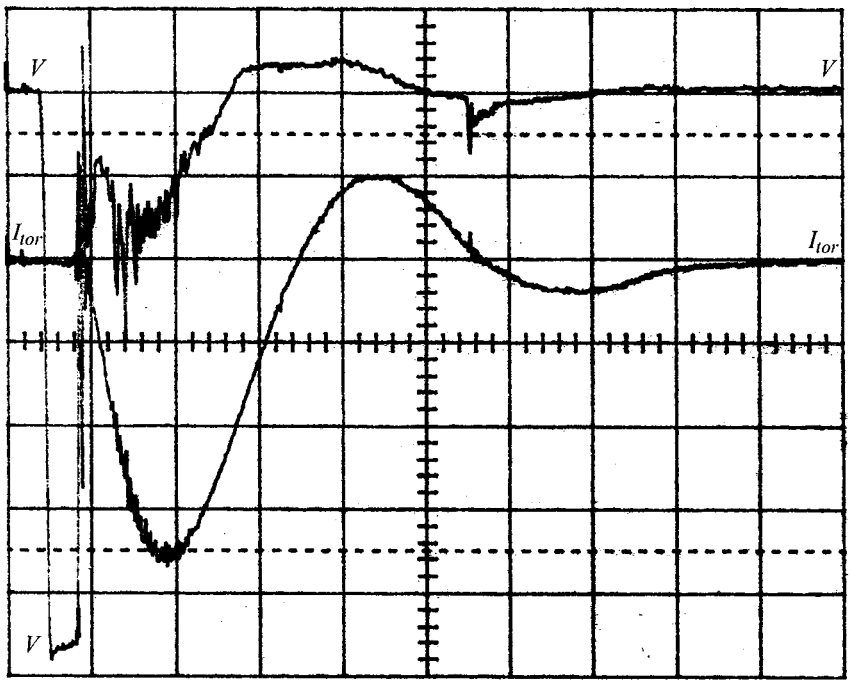

Figure 11: Oscilloscope traces of cathode voltage and toroidal current for a typical plasma discharge (Mark I device). Scales are $\simeq$ 0.9 kV/division for the cathode voltage V, and $\simeq$ 20 kA/division for the toroidal current I_{tor}.

plasma was quite reproducible. Taking several pictures with no change in any settings produced a set of images showing identical major features of the plasma. However, fine scale detail, $\lesssim 1$ cm, would differ from image to image. This high degree of reproducibility made it possible to assemble several series of time-ordered images showing the temporal evolution of the plasma. Figure 12 shows an example of such a sequence which was obtained using the settings listed in 3, with the camera located at vacuum port #1 (cf Figure 4). The sequence was displayed on a computer monitor as a pseudo-movie, a technique that turned out to be very helpful in learning about the plasma dynamics. At breakdown, the plasma forms a circular arc, shaped like a prominence, spanning the gap between the two electrodes. The arc describes approximately one quarter of a full circle. The arc brightens considerably in the next microsecond. About two microseconds after breakdown, the original arc starts to disappear, while two side arcs form. One microsecond later, the original arc is more or less gone, while the two side arcs grow in intensity and also expand outward. The side arcs exhibit a visible fine structure with a length scale of about one centimeter. The fine structure is not repeatable from image to image, but is always in the form of a helix. About four microseconds after breakdown, the two helical side arcs have expanded towards each other so that they touch and start to merge. The interaction is topologically complex, but can be summarized as a bright region of plasma being ejected from the solar device with more diffuse and less bright helical plasma trailing behind the brighter region and extending all the way down to the electrode surfaces. Eventually the bright region of the plasma leaves the field of view of the camera.

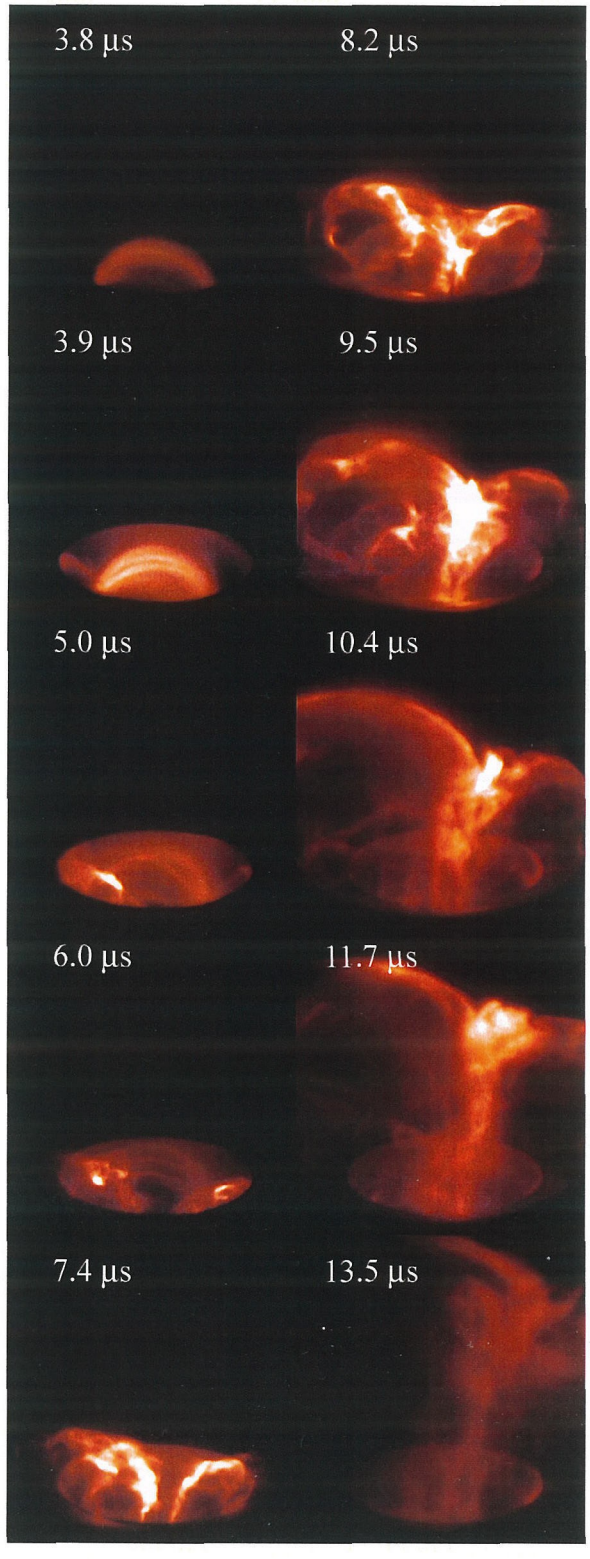

Figure 12: Evolution of plasma (Mark I device); perpendicular view. The increase in brightness was compensated for by closing the lens diaphragm; f-number 1.4 for $t \leq 3.9\,\mu$s; 2.0 for $t = 5.0\,\mu$s; 4.8 for $t \geq 6.0\,\mu$s.

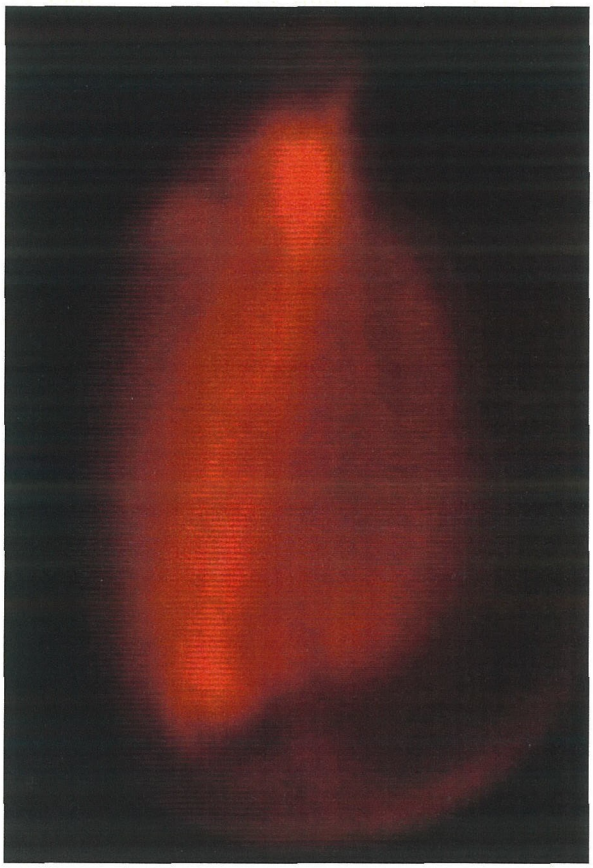

Figure 13: Top view of plasma (Mark I device). Image shows the main current channel at $t = 5.0\,\mu$s before the side arcs have grown significantly in intensity. Note the (reverse) S-shape.

Moving the Xybion camera to vacuum port #6 (cf Figure 4) provided images of the plasma from a "top" view. Figure 13 shows an example of such an image obtained at $t = 5.0\,\mu$s.

The Princeton Instruments camera was more light-sensitive than the Xybion camera and produced better quality images. Because of its high light-sensitivity, this camera was operated with the lens diaphragm set to f-number 22. The Princeton Instruments camera had threaded holes for a standard tripod mount on four sides (to allow either a 576:384 or a 384:576 aspect ratio by rotating the camera), and by attaching a flexible, threaded nylon rod to one of these holes, the Princeton Instruments and Xybion cameras were physically

connected in such a way that both cameras could be placed on the same tripod and view through the same vacuum port. Taking simultaneous pictures of the same discharge with both cameras allowed construction of stereographic images. Figure 14 is an example of such an image (obtained with the cameras at vacuum port #14). The stereographic images obtained this way were rather crude, since the cameras used different image formats, sizes, and dynamic ranges, and it was also difficult to trigger the cameras at exactly the same time.

The images obtained by the Princeton Scientific Instruments movie camera were rather blurry due to the long shutter times. The expansion speed of the plasma, measured at the center of the bright ejected region, was $56 \pm 15\,\mathrm{km\,/\,s}$.

3.2.5 Spectral line emissions

Due to mechanical forces in the device, one tantalum disk (cf 2.2.3) eventually came loose and fell to the bottom of the vacuum chamber. Since we lacked an easy way of accessing the interior of the vacuum chamber at this time, it was decided that operation would continue without the disk. The effect of eroded iron in the plasma was considered negligible [47], and damage to the device itself was ignored as a second generation device was already under construction. Inspection of the device upon removal revealed that a few hundred plasma discharges had removed iron from the circular edge of the exposed electrode, to a depth of approximately $2\,\mathrm{mm}$, corresponding to a volume of about $0.2\,\mathrm{cm}^3$. While the tantalum disk was absent, we took the opportunity to fit the borrowed Princeton Instruments camera with various filters (listed in Table 5 with associated transitions [44]), in order to study spectral line emissions of suspected impurities. The electromagnet core consists of low cost, commercial grade iron, so impurities would be not only iron, but possibly also

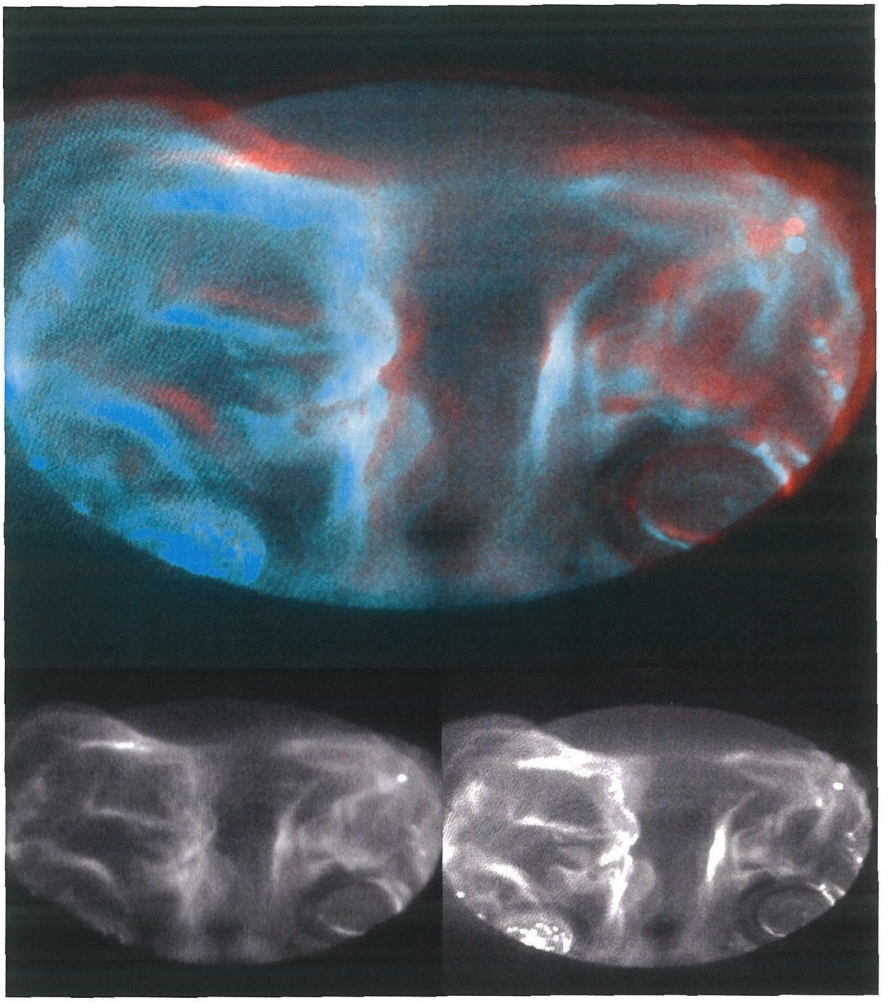

Figure 14: Stereographic image of plasma (Mark I device). Upper image shows the right eye view in red and the left eye view in blue-green (for use with red/blue glasses). The lower left image is the left eye image, and the lower right image is the right eye image (for black and white reproduction).

Wavelength	Bandwidth	Corresponding atom/ion
2300 Å	75 Å	Fe I, O II, C III
2800 Å	75 Å	Fe I, C II
4267 Å	80 Å	C II, Fe I, O II
6335 Å	110 Å	Fe II, O II (both weak)
6565 Å	12 Å	H I

Table 5: Filters used to study spectral lines in the plasma. Central wavelength and bandwidth of each filter is listed. Atoms or ions with a significant transition within each range are indicated.

carbon and oxygen. The lens diaphragm was set to f-number 1.8, thus letting in 2^7=128 times more light than when no filter was used. No light was registered when using the 2300 Å or the 2800 Å filters. With the 6335 Å filter a faint image of the plasma was obtained, and with the 4267 Å filter a fairly good image was obtained with the lens diaphragm set to f-number 11 ($2^5 = 32$ times more light than when no filter was used). The images obtained did not look in any qualitative way different than images from unfiltered light; they were merely dimmer. For comparison, images using an H_α-filter (6565 Å) were obtained. These images could barely be distinguished from unfiltered light images.

3.2.6 X-ray emissions

No x-rays were detected by the scintillation detector (within the limits of electronic noise, 25 mV). Improved x-ray emission results were obtained with later generation solar devices and will be presented in Chapters 4-5.

3.2.7 Other gases

Operation was attempted with gases other than hydrogen, namely deuterium and helium. The attempt was successful with deuterium (using otherwise nominal operating parameters; cf Table 3), and images of deuterium plasmas were obtained. No qualitative differences could be seen in these images compared to discharges in normal hydrogen. Plasma expansion was slowed somewhat, although this trend may have been due to statistical errors in measurements rather than a mass dependence. The deuterium expansion velocity was 49 ± 13 km / s, compared to 56 ± 15 km / s for hydrogen. Breakdown was not achieved when using helium (with $t_{valve} = -1773\,\mu$s to $-873\,\mu$s and otherwise nominal parameters).

Figure 15: Discharge with the background pressure in the vacuum chamber raised to 2×10^{-2} Pa (Mark I device).

3.2.8 Increased background pressure

Operation was attempted with the background pressure of the vacuum chamber increased. This was done by closing the gate valve to the APD cryo pump and pulsing the fast gas valve a fixed number of times until the desired chamber pressure was reached. The solar device was then operated normally. At background pressures of 10^{-3} Pa or higher, the prominence showed a dramatic increase in fine structure. Figure 15 shows an example of a discharge at a background pressure of 2×10^{-2} Pa.

3.3 Discussion

We will now discuss and interpret the results of this chapter. The most important finding is that we can explain both side arcs and S-shapes from the properties of the force-free state

equation $\nabla \times \mathbf{B} = \alpha \mathbf{B}$ (17). This supports the conjecture that solar prominences are in Woltjer-Taylor states (cf 1.2.1). Other results that will be discussed include:

- Bright regions in images of the plasma are interpreted as current paths. This is supported by both the local twisting of these paths and by noting that most of the observed light is H_α, presumably emitted by neutrals where these have been excited by collisions with ions and electrons, i.e., where current is flowing.

- The experiment confirmed the formation of S-shaped prominences when injecting positive helicity, and reverse S-shaped prominences when injecting negative helicity.

- The twist of a plasma, measured as a pitch angle, was confirmed to be larger for the more unstable side arcs, smaller for more stable main current channels.

- Electrode voltages and toroidal currents evolve in an explainable fashion, by regarding the plasma and the main capacitor as comprising an LRC-circuit. The plasma inductance increases as the plasma expands and grows larger.

3.3.1 Current and voltage profiles

The electrode voltages and the plasma toroidal current (cf Table 4) can be explained by regarding the plasma and the main capacitor as comprising an LRC-circuit. The stored energy in the capacitor is converted to magnetic energy, then back to energy in the capacitor again. The stored capacitor energy is zero when the voltage is zero (approximately when the current peaks), and the magnetic energy is zero when the current is zero (approximately when the voltage peaks). The plasma inductance increases as the plasma expands (cf the inductance for a current loop in A.2.4), causing a reduction in magnitude of subsequent

current peaks (minima or maxima) such that the total peak inductive energy remains the same. Similarly, lowering the toroidal magnetic field B_{tor} of a discharge, the reduced internal magnetic pressure allows a decrease in the plasma cross-section due to the pinch effect. A smaller cross-section means a slightly increased inductance, again leading to a smaller peak current.

Resistive losses cause the slight shift between the times of current peak and zero voltage, and vice versa, as well as additional reduction in peak current (and peak voltage) over time.

3.3.2 Images

We interpret the bright regions (strands, arcs) in the images as current paths in the plasma. This is supported by the observation of local twisting of these paths. Twists are created by the superposition of poloidal and toroidal magnetic fields. The poloidal field is created by the toroidal current (right-hand rule). The toroidal field is simply the bias magnetic field.

We expect current-carrying ions and electrons to excite neutrals via collisions. This agrees with observations of different spectral lines; most of the light has a wavelength of 6565 Å, corresponding to emission by hydrogen neutrals.

3.3.3 Side arcs

Here we make an important mathematical analysis that will prove useful for interpretation of both side arcs and S-shapes. The mathematical model is essentially a first order solution to the force-free state equation $\nabla \times \mathbf{B} = \alpha \mathbf{B}$ (17).

In the camera images, a prominence forms as expected as soon as the gas breaks down. However, as the current is ramped up, side arcs unexpectedly form and soon dominate the images ($t \gtrsim 6\,\mu$s in Figure 12). After carefully studying images of the discharges,

particularly the stereographic images, we conclude that the side arcs form between the electrodes and the copper gasket that is used to create the vacuum seal between vacuum port and solar device. This explains why our attempts to coat various surfaces with boron nitride failed to eliminate the side arcs; because of the geometry of the copper gasket and the area around it, the gasket cannot be fully coated.

After determining where the side arcs form, the next question is why they form. An analytic solution to the force-free state equation (17), relevant to our particular geometry [59], explains the formation of the side arcs. The basis of this solution is an assumption of uniform α throughout an infinite half-space. We shall see that the analysis will contribute significantly to our understanding of the plasma evolution.

A general solution to Equation (17) can be expressed in terms of a single scalar function $\psi(\mathbf{r})$ which is neither a potential nor a flux function, but has properties of both [20][60]. In cylindrical coordinates (r, ϕ, z) this general solution is

$$\mathbf{B} = -\alpha\hat{z} \times \nabla\psi - \nabla \times (\hat{z} \times \nabla\psi) \tag{82}$$

where $\hat{z}$ is a unit vector. Substituting this expression for $\mathbf{B}$ in Equation (17), we find that ψ must satisfy the Helmholtz equation

$$\nabla^2\psi + \alpha^2\psi = 0 \tag{83}$$

or, in cylindrical coordinates,

$$\frac{1}{r}\frac{\partial}{\partial r}\left(r\frac{\partial\psi}{\partial r}\right) + \frac{1}{r^2}\frac{\partial^2\psi}{\partial\phi^2} + \frac{\partial^2\psi}{\partial z^2} + \alpha^2\psi = 0. \tag{84}$$

Our geometry is an infinite half-space bounded by the plane of our electrodes. If we introduce cylindrical coordinates defined so that the electrode plane is $z = 0$, then we must specify the boundary conditions at $z = 0$ and require that all solutions $\psi \to 0$ as $z \to \infty$.

A solution that satisfies Equation (84) and the prescribed boundary conditions is the linear superposition of the modes

$$\psi_m(k,r,\phi,z) = \overline{\psi}_m(k)\, J_m(\kappa r)\, e^{-im\phi - kz} \tag{85}$$

where J_m is a Bessel function and $\kappa = \sqrt{k^2+\alpha^2}$. Combining equations (82) and (83), and including the exponential dependence on z, the magnetic field can be written as

$$\mathbf{B} = \nabla\frac{\partial\psi}{\partial z} + \alpha^2\psi\widehat{z} - \alpha\widehat{z}\times\nabla\psi = \underbrace{-k\nabla\psi}_{\text{potential field}} + \alpha^2\psi\widehat{z} - \alpha\widehat{z}\times\nabla\psi. \tag{86}$$

Using Equation (85), we get the specific components

$$B_r = -e^{-kz}\sum_{m=1}^{\infty}\overline{\psi}_m(k)\left(\frac{m\alpha}{r}J_m(\kappa r)\sin(m\phi) + k\kappa J_m'(\kappa r)\cos(m\phi)\right) \tag{87}$$

$$B_\phi = -e^{-kz}\sum_{m=1}^{\infty}\overline{\psi}_m(k)\left(-\frac{mk}{r}J_m(\kappa r)\sin(m\phi) + \alpha\kappa J_m'(\kappa r)\cos(m\phi)\right) \tag{88}$$

$$B_z = e^{-kz}\sum_{m=1}^{\infty}\overline{\psi}_m(k)\,\kappa^2 J_m(\kappa r)\cos(m\phi) \tag{89}$$

where $J_m'(\xi) \equiv dJ_m/d\xi$ and summation starts at $m=1$ since $m=0$ is not a physical mode in our geometry. This type of non-axisymmetric Woltjer-Taylor state (cf 1.2.1), based on Chandrasekhar-Kendall functions, has been previously suggested by Taylor to be relevant to solar prominences [61].

To pick our boundary conditions at $z=0$, consider the mode $m=1$. For this mode, any plane $z=$ constant will be divided into regions with alternating signs of B_z, bounded by separatrices where $B_z=0$, i.e., the line $\phi = \pm\pi/2$ (the x-axis), as well as all circles defined by the roots $J_1(\kappa r)=0$ (cf Figure 16). Between subsequent roots of $J_1(\kappa r)=0$, the regions are thus grouped in pairs with one $B_z>0$ region and one $B_z<0$ region, divided by the x-axis. Obviously, each region will have an extremum point for B_z at $J_1'(\kappa r)=0$ and $\phi=0$ or π (the y-axis). We will choose our boundary conditions

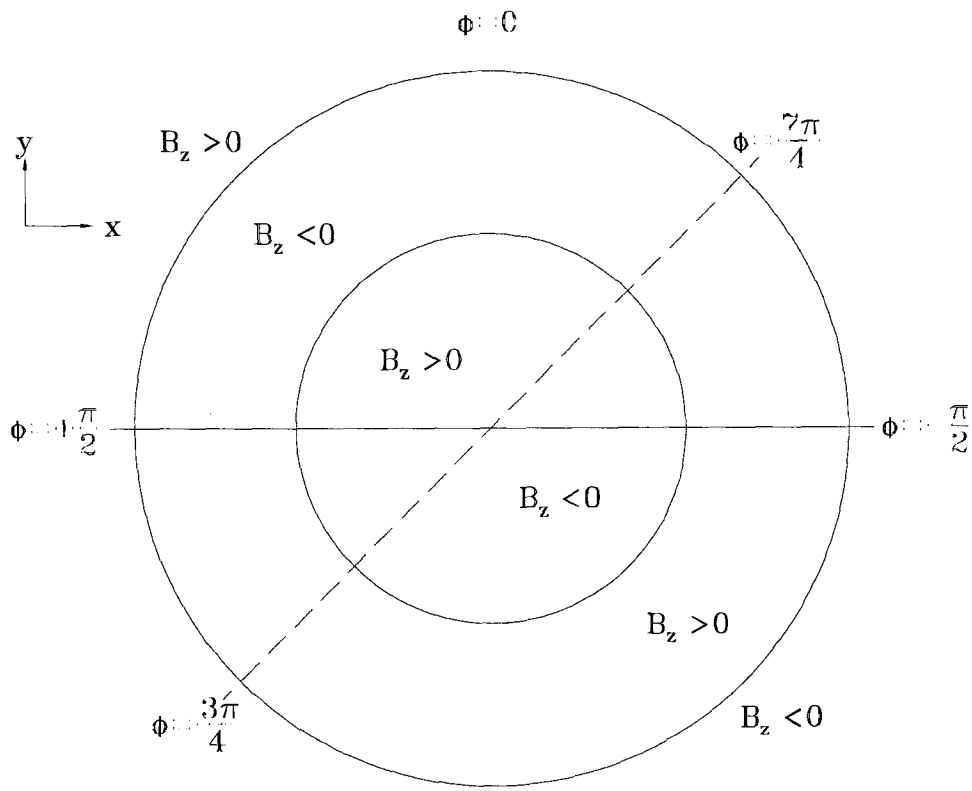

Figure 16: A representative z-plane (such as the electrode plane $z = 0$). The circles represent the first two roots to $J_1(\kappa r) = 0$. The solid line is the y-axis, where $\phi = 0$ or π. On the circles and the y-axis, the z-component of the bias magnetic field is zero, i.e., $B_z = 0$. The sign of B_z alternates between adjacent regions (areas bounded by the $B_z = 0$ separatrices).

such that the two extremum points of B_z corresponding to the first root of $J_1'(\kappa r) = 0$ (i.e., $\kappa y \approx \pm 1.8412$) will match the location of the two electrodes of the solar device, i.e., $y = \pm 127\,\mathrm{mm}/2 = \pm 63.5\,\mathrm{mm}$. Note that the mode $m = 1$ then gives a fairly accurate approximation of the actual boundary conditions at $z = 0$, as long as we only concern ourselves with the region that is inside the second root of $J_1(\kappa r) = 0$, i.e., inside $r = 63.5\,\mathrm{mm} \times 7.0156/1.8412 \simeq 24\,\mathrm{cm}$ [59]. This limit is well beyond the region of interest. For comparison, the inside radius of the vacuum port is $\simeq 10\,\mathrm{cm}$. For the remainder of this analysis, we shall disregard higher modes than $m = 1$.

Now consider the behavior of a magnetic field line in the prominence, initially extending from one electrode to the other, as the toroidal current is gradually increased from zero. The current is proportional to α (cf 1.2.3). Initially, there is no toroidal current, i.e., $\alpha = 0$, so that the magnetic field in Equation (86) is a potential field (since it is the gradient of a scalar) as expected. For $\alpha = 0$, the singular field line starting exactly at $\kappa y = 1.8412$ will simply extend upward, remaining at $\kappa y = 1.8412$ as $z \to \infty$. However, just inside this singular point, and for any $\kappa y < 1.8412$, the field line will bend towards the x-axis since $B_r < 0$. Eventually it will cross the x-axis (with no B_z-component) and follow a mirror image of the same path down to $\kappa y = -1.8412$. It is along some of these field lines that the laboratory prominence initially forms (visible in images $t \lesssim 6\,\mu\mathrm{s}$). A field line starting just outside $\kappa y = 1.8412$ will instead bend outwards since $B_r > 0$. Eventually it will cross the first root of $J_1(\kappa r) = 0$ (with no B_z-component) and then descend until it reaches $z = 0$, somewhere in the region between the first and second roots of $J_1(\kappa r) = 0$. These are the fringing field lines. The fringing lines can be seen in Figure 7 as the field lines that connect to the vacuum chamber wall rather than between electrodes. Also note that, in Figure 8, the

first root of $J_1(\kappa r) = 0$ would be at $y \simeq 8\,\mathrm{cm}$. If we now increase the toroidal current, i.e., make $\alpha > 0$, then $\mathbf{B}$ will no longer be a potential field as the two additional terms in Equation (86) are non-zero. These terms introduce additional curvature to the magnetic field. For example, in terms of a contour map of ψ, the term $-\alpha\hat{z} \times \nabla\psi$ points along a level contour of constant ψ. This means that trajectories of field lines no longer follow the gradient of ψ, from a hill to a valley, but will turn away from this path. In terms of the component equations for $\mathbf{B}$, $\alpha > 0$ makes $B_\phi \neq 0$ on the y-axis, so that the field line will turn away from the y-axis on its way from one electrode to the other. This corresponds to a twisting of the main current channel, as observed in camera images at $t \lesssim 6\,\mu\mathrm{s}$. Numerically integrating the path of a field line, the field line no longer ends up at its original location when descending to $z = 0$ in the $B_z < 0$ region. This has two implications [59]:

1. The often used concept of "line-tying" is flawed. This concept is often invoked as a means to inject helicity into a solar prominence by rotation of the prominence foot-points. Helicity injection by foot-point rotation is not proven invalid by our analysis, but one has to be careful if invoking line-tying. Simply asserting that magnetic field lines are tied to fixed spots on a rotating solar surface is incorrect. Instead one should obtain an electrostatic potential difference (that will drive a toroidal current) between the two foot-points using a $\mathbf{U} \times \mathbf{B}$-term [62]. However, note that our analysis demonstrates how helicity can increase in a prominence merely by increasing the toroidal current; no foot-point rotation is necessary.

2. If the toroidal current is increased sufficiently, then, for a certain α, the field line trajectory curves so much that the field line no longer will reach the $B_z = 0$ separatrix at the x-axis, but rather it reaches the circular $B_z = 0$ separatrix

corresponding to the first root of $J_1(\kappa r) = 0$. The field line will then descend to the $z = 0$ plane somewhere in the region between the first and second roots of $J_1(\kappa r) = 0$, similar to our original $\alpha = 0$ fringing field lines. In other words, we are presented with a bifurcation, as an infinitesimal increase in α leads to a change in the field line intersection with the $z = 0$ plane that is finite (and even qualitatively different). We propose that this bifurcation is the underlying reason behind the formation of the side arcs visible in camera images $t \gtrsim 5\,\mu$s.

A secondary consequence of the bifurcation is that the concept of magnetic flux tubes becomes unclear [59]. A magnetic flux tube is defined as the set of field lines that intersect some closed curve in space. It is trivial to choose this curve such that different field lines of the flux tube undergo the bifurcation at different values of α. When this happens, we cannot speak of a flux "tube" any more, but rather we must limit ourselves to the more fundamental concept of individual field lines.

Numerical integration of field lines that initially form a traditional flux tube is shown in Figure 17. Field lines start at a circle in the $z = 0$ plane, in the innermost region (inside the the first root of $J_1(\kappa r) = 0$) where $B_z > 0$, and the ribbon surface between each pair of field lines is plotted. The mirror image field lines of the first set are also plotted. (These mirror field lines start at different locations depending on α, chosen so that the field lines *always* end where the first set of field lines end *only when* $\alpha = 0$.) As discussed above, parts of the flux tubes eventually reach the $J_1(\kappa r) = 0$ circular separatrix as helicity is injected into the system, i.e., α is increased, and the flux tubes then become undefined as field lines end up in different regions. This happens for $|\alpha| = 0.65\kappa$-0.75κ in Figure 17. As α continues to increase, the flux tubes chosen for Figure 17 eventually become defined

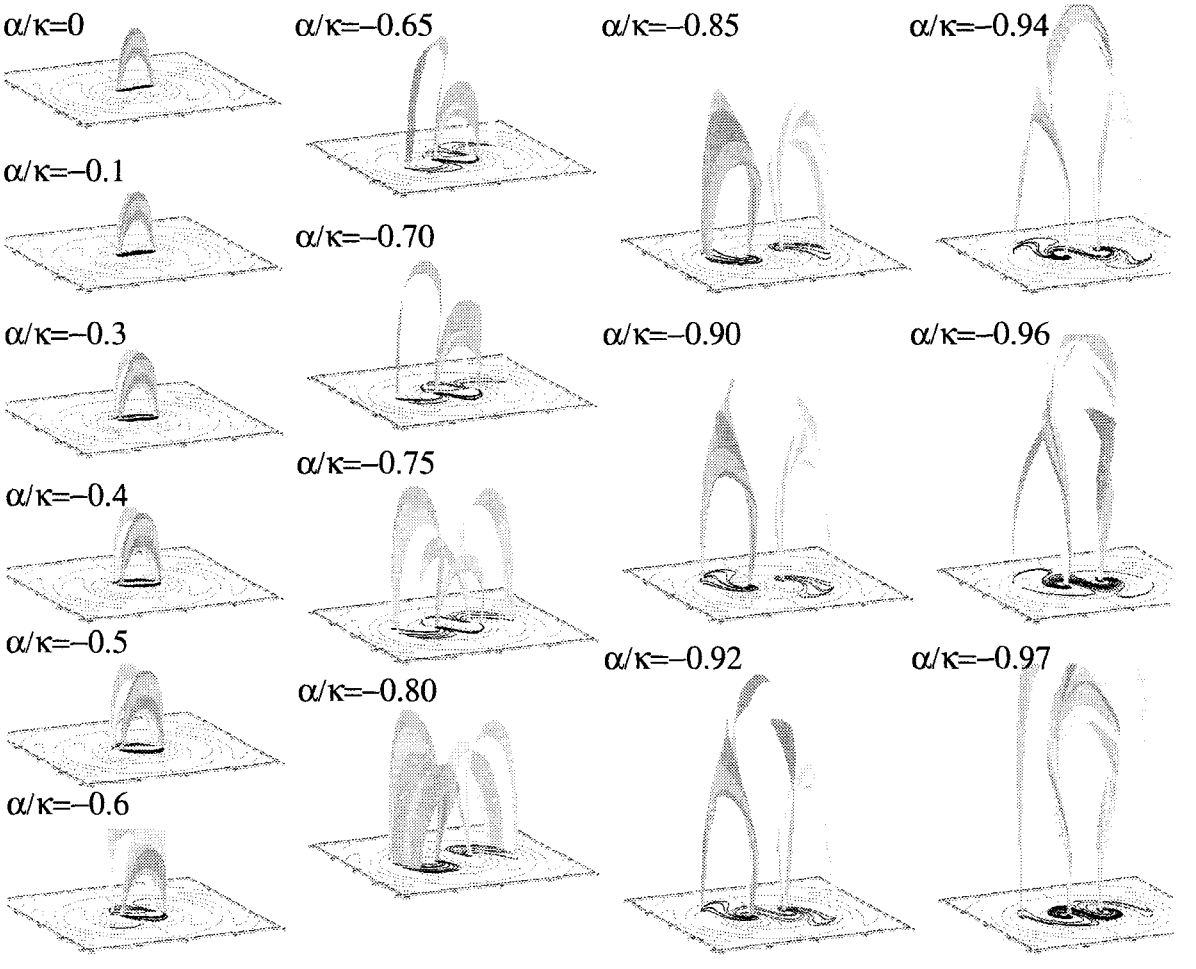

Figure 17: Magnetic field lines in $m = 1$ Chandrasekhar-Kendall function solution (plasma of Mark I device) for increasing values of α (normalized against κ). Contours of ψ have been drawn on the $z = 0$ planes, along with projections of the field lines.

again, with each flux tube going from an inner region (inside the first root of $J_1(\kappa r) = 0$) to an outer region (outside the first root of $J_1(\kappa r) = 0$), or vice versa ($|\alpha| = 0.80\kappa$-0.90κ in Figure 17). Curiously, for even larger amounts of injected helicity ($|\alpha| \geq 0.92\kappa$ in Figure 17) the field lines can again intercept the x-axis and then they will end up in the same region as they ended up when $\alpha = 0$.

3.3.4 S-shapes

Here we explain the characteristic S-shapes of prominences using the force-free state equation $\nabla \times \mathbf{B} = \alpha \mathbf{B}$ (17). The fact that both side arcs and S-shapes can be explained from the force-free state equation is an important indication that prominences are in Woltjer-Taylor states (cf 1.2.1).

The top-view images obtained of the laboratory prominence (cf Figure 13) show an S-shape similar to what has been observed on the Sun (cf 1.1.2). Magnetic cloud measurements [23] have *indirectly* linked S-shapes with positive helicity and reverse S-shapes with negative helicity (cf 1.1.4). The experiment verified this conclusion by producing S-shaped prominences when I_{tor} and B_{tor} were parallel (i.e., when injecting positive helicity) and reverse S-shapes with I_{tor} and B_{tor} antiparallel.

The S-shapes can be explained easily by tracing magnetic field lines using the mathematical model presented above (cf 3.3.3). As more helicity is injected, i.e., α increases, the projection of the flux tubes on the $z = 0$ plane (equivalent to the solar surface) changes from straight lines to increasingly curved shapes, and the sense of the projected curvature changes as B_z reverses. This can be seen directly from the force-free state equation $\nabla \times \mathbf{B} = \alpha \mathbf{B}$; a positive B_z means a positive z-component of the curl, and vice versa. Consequently, any field line or flux tube going between the two innermost regions (inside the

first root of $J_1(\kappa r) = 0$) must exhibit an S-shape. For reference, projections of the field lines onto $z = 0$ have been included in Figure 17.

3.3.5 Twists

On a finer scale, both the initial, main current channel and the subsequent side arcs consist of mixtures of brighter and darker strands of plasma. By observing how these strands cross each other, we can determine the handedness of each prominence in the same way as has been done for actual solar prominences [63]. Not surprisingly, prominences with the magnetic field B_{tor} parallel to the current I_{tor} were right-handed, and when B_{tor} was antiparallel to I_{tor} the prominences were left-handed.

3.3.6 Instability discussions

By looking carefully at the strands of the plasma in the camera images, we could also measure the pitch angle of both main current channels and side arcs. The pitch angle is analogous to the angle of the threads on a screw. We will actually look at the complement of the pitch angle, which is defined as

$$\varphi = \tan^{-1}(B_{pol}/B_{tor}) \tag{90}$$

where B_{pol} is the magnetic field due to the toroidal current I_{tor}, as indicated in Figure 3. For the main current channel, $\varphi = 0°$ initially and then increases steadily as the current is ramped up. When the side arcs appears, φ for the main current channel is about 15°-20°. The side arcs form twisted at $\varphi = 25°$-$45°$. From our discussion on the three roles of α (cf 1.2.3), we find that $\varphi \simeq 45°$ is an instability limit for a plasma in a Woltjer-Taylor state. Unfortunately, because the side arcs dominated the images, it was not possible to determine whether the main current channel would twist up to 45° and then go unstable. However, the

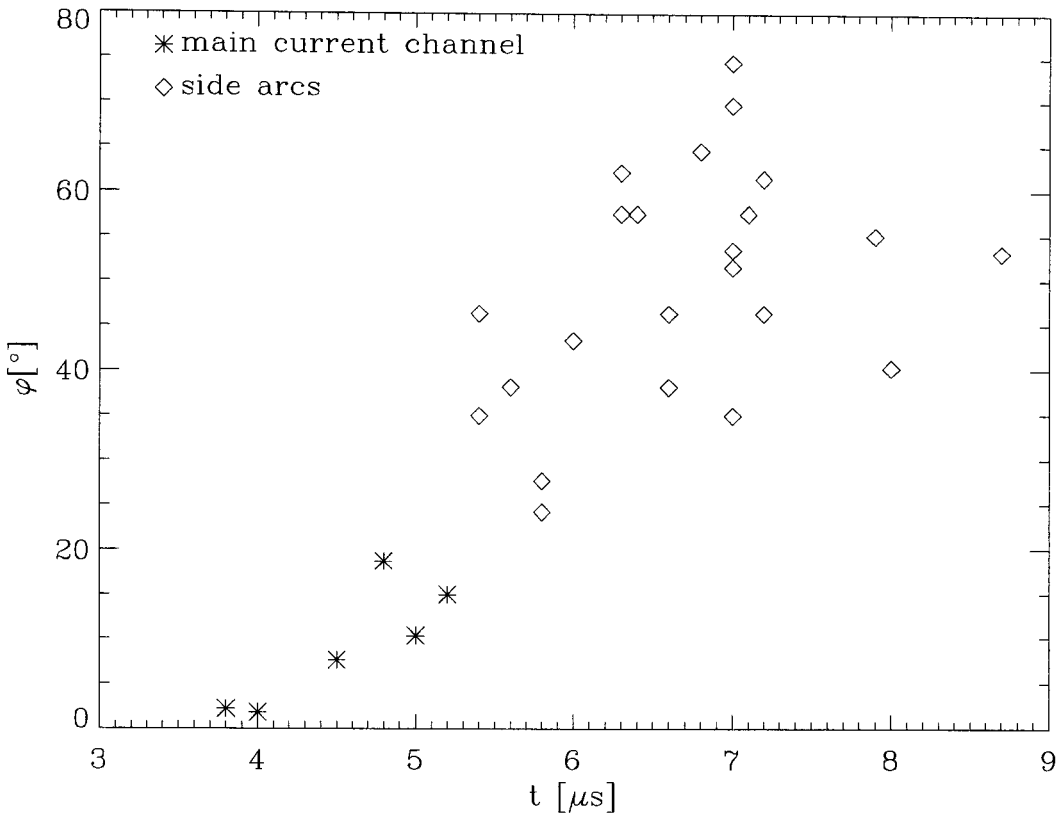

Figure 18: Measurements of the pitch angle complement φ, in main current channel and side arcs, as a function of time.

main current channel did appear stable when observable, while the side arcs would expand and erupt immediately. Measurements of φ are given in Figure 18.

Observations of solar prominences have shown that the angle between the magnetic field and the prominence axis (projected onto the solar surface) is on average $20° - 25°$ in quiescent prominences [64][65][12]. This would correspond well to an eruptive threshold of $\varphi \simeq 45°$ (assuming an even distribution of φ among quiescent prominences, then on average $\varphi = 45°/2 = 22.5°$). Also, measurements of the magnetic field with respect to the horizontal in solar prominences typically have shown angles of $< 30°$ for quiescent prominences, while active prominences can have much larger angles, even coming close

to having vertically oriented magnetic fields [65]. The angles measured in these cases are simply φ, which equals both the magnetic field angle to the horizontal and the angle to the prominence axis projected onto the solar surface. Later observations have indeed shown that $\varphi \gtrsim 45°$ for eruptive prominences [66] $\varphi < 45°$ for stable prominences [66][17]. All of these measurements lend support to the theory that solar prominences are in Woltjer-Taylor states and that they become unstable when the injected helicity exceeds a certain threshold.

Another instability criterion can be calculated using our mathematical analysis developed to understand side arc formation, although we shall see that this criterion is not very accurate. In the side arc analysis, there is no solution to Equation (86) for $\alpha \geq \kappa$, indicating that there is no stable, attached, force-free plasma configuration with this amount of injected helicity. To satisfy boundary conditions on the $z = 0$ plane, $\kappa L/2 \approx 1.8412$ (cf 3.3.3), where L is the footpoint distance. From our discussion on the three roles of α (cf 1.2.3), the toroidal current must be larger than $\alpha\Phi/\mu_0$ to form a detached spheromak-like plasma. Combining these expressions results in the following prominence instability limit with respect to toroidal current:

$$I_{tor} = \frac{\alpha\Phi}{\mu_0} = \frac{\kappa\Phi}{\mu_0} \simeq \frac{3.7\Phi}{L\mu_0} \tag{91}$$

In our case, the toroidal flux $\Phi \simeq 0.39$ mWb (cf Figure 9) and the footpoint distance $L = 127\,\mathrm{mm}$ (cf 2.4.3), and so the prominence is stable only for toroidal currents less than 8.8 kA. This is much less than the measured peak current of 72 kA, and also much less than our design criteria (cf 2.4.1). The reason for the difference lies in the different length scales used. The arguments made in the design process used a length scale on the order of the prominence minor radius, by arguing that pinch effects will limit the toroidal current to

a relatively small area. Equation (91) used the much larger length scale of the major radius. This is the only length scale there is in this case, because the analysis is based on a uniform α argument, requiring current to flow in constant proportion to the magnetic field strength in all space, i.e., no minor radius exists. The different choice of length scale should make Equation (91) a poor estimate of when instability occurs.

3.3.7 Pressure and gas estimate from breakdown analysis

It is possible to estimate the pressure and density of the laboratory prominence at the moment of breakdown using Paschen's law (41). For example, when injecting hydrogen mass of $8.3\,\mu$g ($V_{valve} = 700\,$V and $p_{valve} = 791\,$kPa), breakdown occurred for $V_I \gtrsim 5.85\,$kV. The corresponding pressure-distance product in Paschen's law is $pd \simeq 1.160\,$Pa m. The distance d can be calculated fairly accurately from the camera images. At breakdown the plasma forms a 90° circular arc with a radius of $127\,\text{mm}/\sqrt{2} \approx 90\,$mm, giving the distance d as the arc length: $d \simeq 141\,$mm. The gas pressure at the time of breakdown is then $p \simeq 8.2\,$Pa, which corresponds to a number density of $n_{H_2} \simeq 2 \times 10^{21}\,\text{m}^{-3}$ (assuming that the hydrogen gas was at room temperature before breakdown). The percent ionization of the hydrogen gas is unknown, but this analysis gives an upper bound on the plasma number density of $n_{i,e} \simeq 4 \times 10^{21}\,\text{m}^{-3}$.

Chapter 4 Second generation solar prominence experiment

This chapter presents the results from the second generation solar prominence experiment. The chapter consists of three sections. First, equipment and diagnostics will be described. Second, experimental results will be presented. Third, the results will be discussed and interpreted. The most important result that we present here is that a strapping field can inhibit the eruption of a prominence. The strapping field is a large scale vacuum magnetic field that straddles a prominence. We show quantitatively that prominence eruption is inhibited due to a $\mathbf{J} \times \mathbf{B}$-force between strapping field and the prominence toroidal current. Other important results are:

- More helical plasmas (larger φ) are produced with higher ratios of toroidal current to toroidal bias magnetic field.

- Properties of solar prominences are explained from experimental results. Explanations include the dip of a prominence above the neutral line, acceleration and other characteristics of disparitions brusque and sprays, and the large aspect ratio (length to height) of some prominences.

4.1 Equipment and diagnostics

4.1.1 Mark II solar device

The second generation solar device (Mark II) was designed along the same principles as its predecessor, the Mark I. These principles are presented in detail in Chapter 2. Here we

will give the parameters for the Mark II and point out major differences between the Mark II and the Mark I.

The Mark II is shown schematically in Figure 19. Like the Mark I, it consists of a horseshoe electromagnet with poles that also act as the electrodes for the prominence toroidal current. The Mark II electrodes are D-shaped, i.e., each electrode is roughly one half of a disk. Except for a 10 mm gap between them, the two electrodes together cover a circular area with a diameter of 178 mm (7 in). The size and shape of the electrodes are chosen to prevent side arcs (cf 3.3.3). The electrodes extend past the radius at which side arcs formed using the Mark I device. If side arcs are to form, they must do so beyond the radius of the electrodes, since there is no electric potential difference to drive a plasma current between two points on the same electrode. Other components of the Mark II were positioned so that the electrodes now lie in approximately the same plane as the vacuum chamber wall, thus better representing the solar surface.

Provisions were made to inject gas through a tube at the center of each leg of the horseshoe magnet. The gas would then be injected at the prominence footpoints, i.e., the location of the strongest magnetic field. This feature was introduced because operation with the Mark I took place at the right hand side of Paschen's curve (cf Figure 6). By injecting gas directly at the footpoints, a higher gas pressure in the region where the prominence will form allows gas breakdown at a lower voltage. (Another feature that was added provided the capability to break down the gas while it was still travelling through the tubes inside the horseshoe magnet. Since breakdown was very repetitive without this feature (cf 4.2.2), it was never used.) A specially constructed manifold that splits a (sonic) gas stream in two was connected to the gas valve exit. Since the two injection tubes through the horse-

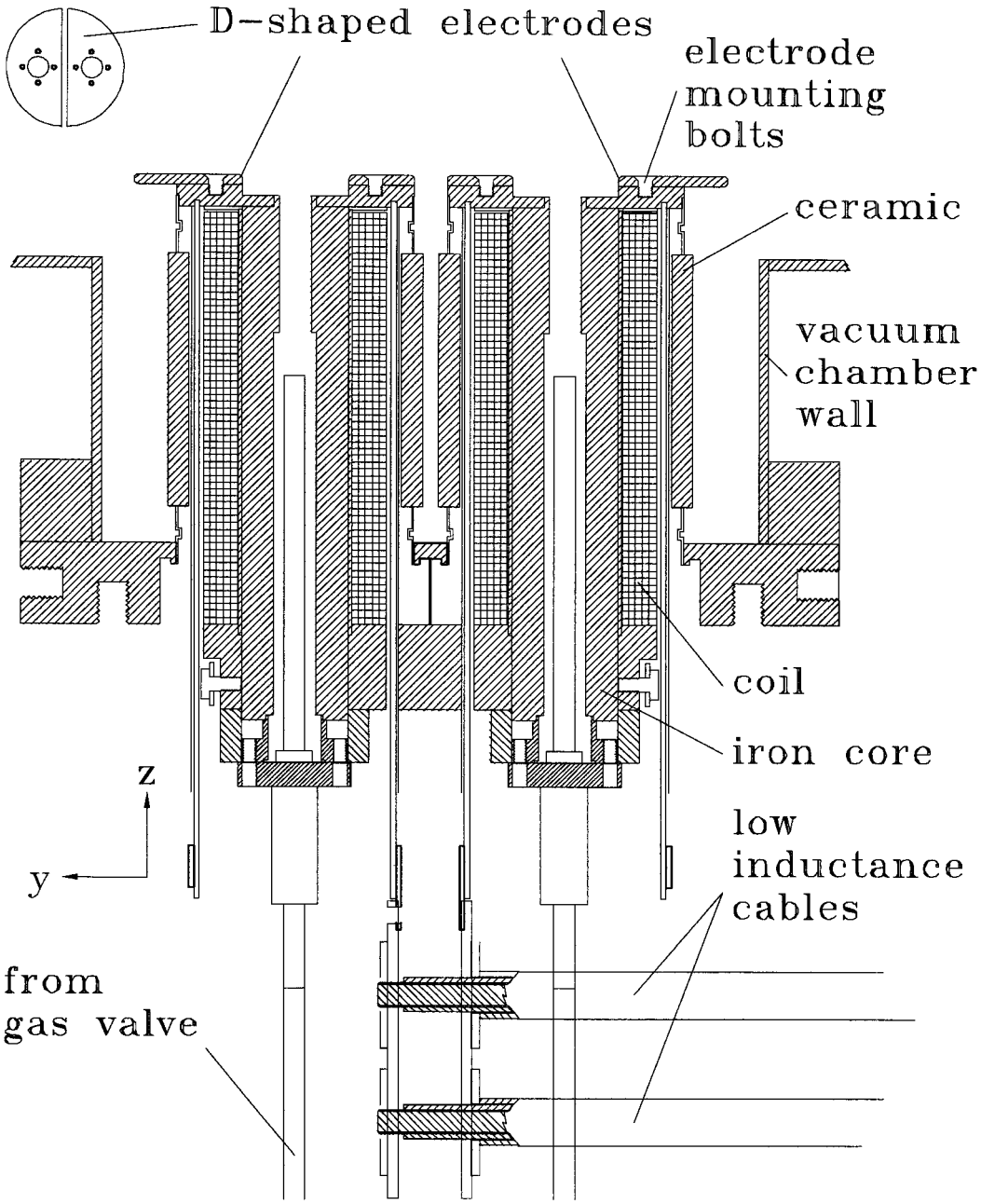

Figure 19: Schematic of second generation solar device (Mark II). The prominence forms in the region above the device. The D-shaped electrodes are also shown from a top view (upper left corner of figure in 1:5 scale compared to the rest of the schematic).

shoe magnet are at high voltage ($+V_I/2$ and $-V_I/2$, respectively) the gas valve must be electrically insulated from the injection tubes (and the two tubes must be insulated from each other). For this purpose, two pieces of Teflon tubing were added between the manifold and the injection tubes. The length of the Teflon tubes ($\sim 13\,\mathrm{cm}$ long) was calculated from Paschen's law (41), such that arcing through gas inside the tubes would be avoided. The distance between the gas injection points, i.e., the distance between the two magnetic poles, was 81 mm. (Means for injecting gas at the center of the device were retained, although the results were of little interest; a bright arc formed directly across the 10 mm gap between the two D-shaped electrodes and did not evolve further. The results reported in this chapter were obtained with gas being injected through the horseshoe magnet only.)

Other changes for the Mark II included the elimination of Macor parts for high voltage insulation and vacuum seal. Instead, Ceramaseal vacuum-tight ceramic electric breaks that could better withstand thermal and magnetic forces (cf B.3) were used. A special stand for the device was built. This stand was used when there was need to remove the device from the vacuum chamber. Also, the connectors between the device and the low inductance coaxial cables were improved, so that the connectors could disconnect and reconnect faster.

The gas valve and the capacitor banks used for the Mark II device were the same as for the Mark I. The high speed gas valve is pulsed by a $400\,\mu\mathrm{F}$ capacitor bank charged to a voltage V_{valve} between 0-700 V. A $59\,\mu\mathrm{F}$ capacitor can provide a voltage difference V_I of up to 12 kV to break down the gas between the two electrodes. Once the plasma has formed, this capacitor will drive a current I_{tor} through the plasma in the toroidal direction. (This capacitor will be referred to as the main capacitor.) An added 9.6 mF capacitor

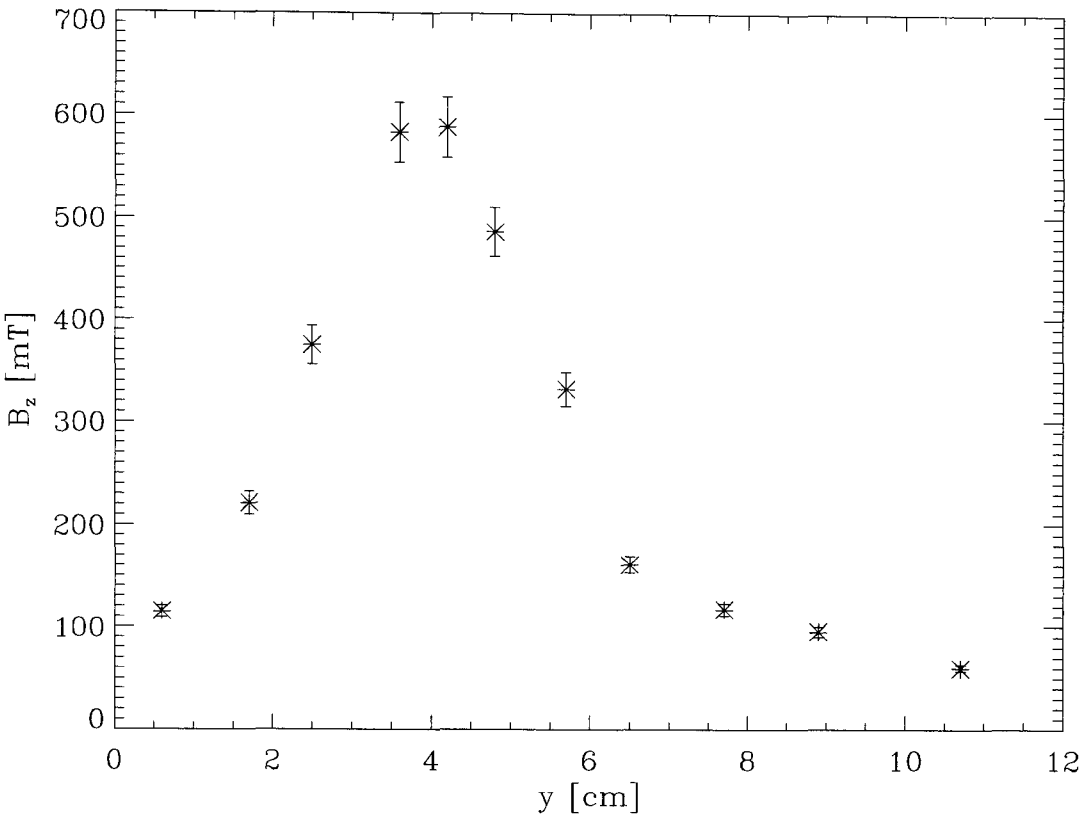

Figure 20: Toroidal magnetic field (B_z-component) of Mark II device for nominal settings (200 V charging voltage; cf 4.2.1) on a line between the two magnetic poles along the electrode surfaces (y-axis, i.e., $x = z = 0$ cm)

bank (maximum voltage 900 V; designed by F.T. Cosso) would, together with the existing 9.9 mF capacitor bank, create the toroidal bias magnetic field B_{tor} by driving current through the two coils of the electromagnet. (These capacitor banks will be referred to as the bias field capacitors.) Two separate banks were needed as the coils are no longer at ground potential, but instead each coil is at the voltage of its associated electrode (no room was available for high voltage insulation because the electrode surfaces were re-positioned to be flush with the vacuum chamber wall). The vacuum field B_{tor} was carefully mapped in the volume above the Mark II device using a Hall probe (calibrated to 250 V / T) and

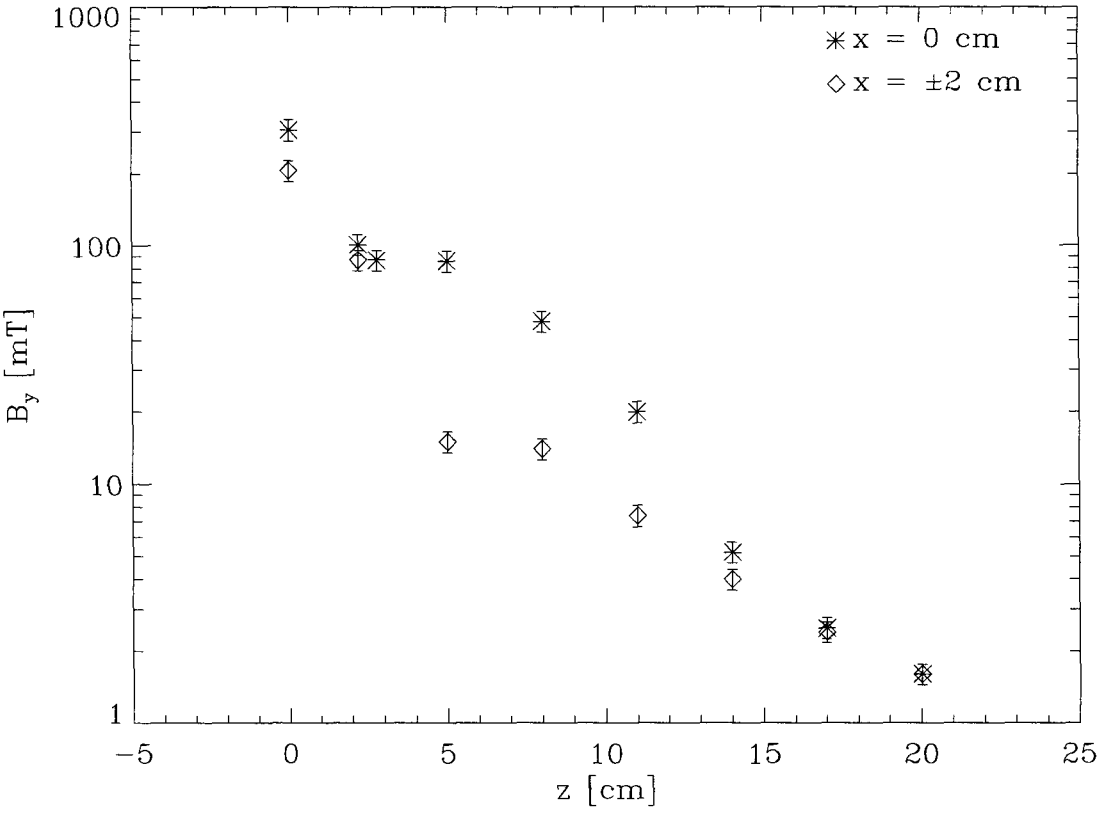

Figure 21: Toroidal magnetic field (B_y-component) of Mark II device for nominal settings (200 V charging voltage; cf 4.2.1) over the center of the device (z-axis, i.e., $x = y = 0\,\mathrm{cm}$) and along $x = 2\,\mathrm{cm}$, $y = 0\,\mathrm{cm}$.

a pick-up coil (200 μVs/T). Typical measurements are summarized in Figures 20-21. The B_z-component on the electrode surfaces is given in Figure 20 (note that gas is injected at $y \simeq 4\,\mathrm{cm}$). The B_y-component is given over the center of the device (z-axis) in Figure 21. Also indicated is the B_y-component a small distance ($x = 2\,\mathrm{cm}$) from the z-axis. Figures 20-21 show field strengths at peak magnetic fields (5.6 ms after the capacitor banks have been triggered). To speed up charging times, a fast charging unit (designed by F.T. Cosso) was added to each bias field capacitor bank. Each capacitor bank and its fast charging unit

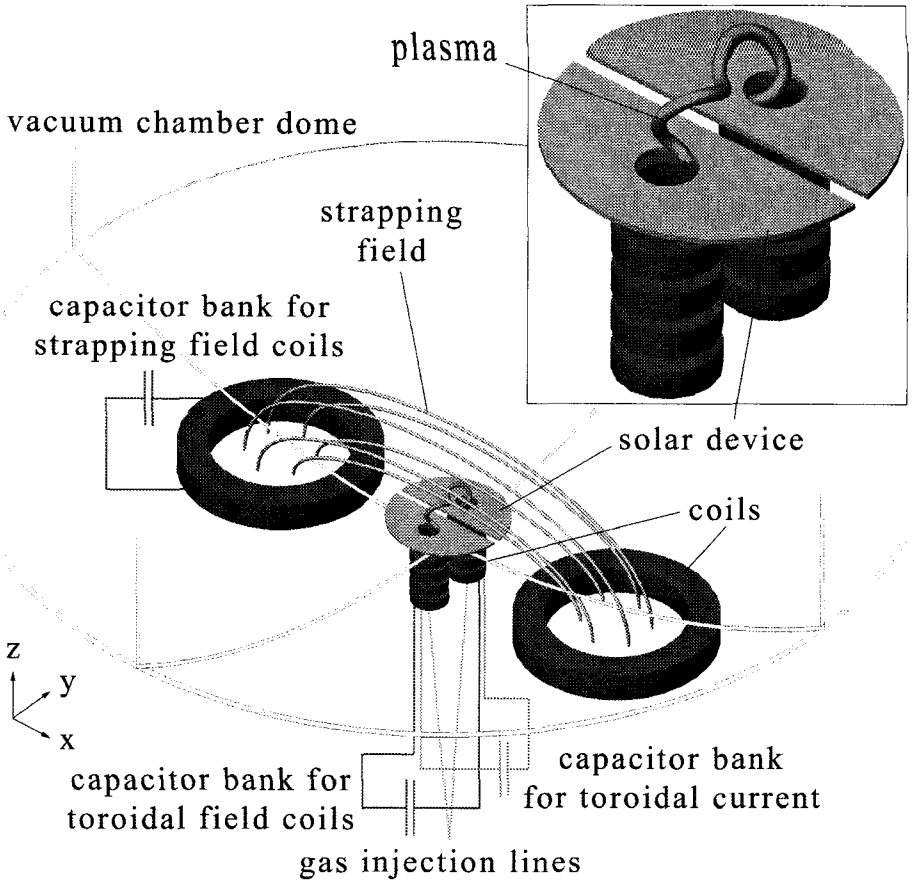

Figure 22: Two large coils on either side of the solar device generate a strapping field above the device and the plasma. Top right of figure shows a magnified inset of the Mark II device (D-shaped electrodes, toroidal magnetic field coils, and example of plasma).

were powered through a DEL Electronics transformer that provides up to 20 kV isolation between primary and secondary.

4.1.2 Strapping field coils and capacitor bank

It has been suggested that solar prominences form beneath much larger scale, overlying magnetic fields [67][17], often referred to as arcade or strapping fields. A strapping field is believed by some [68][69][21] to inhibit solar prominence eruption. A set of coils (cf Figure 22) were added to the experiment to simulate a strapping field B_{strap} and study its effect on the prominence. The coils were roughly circular (really a trapezoid with very rounded

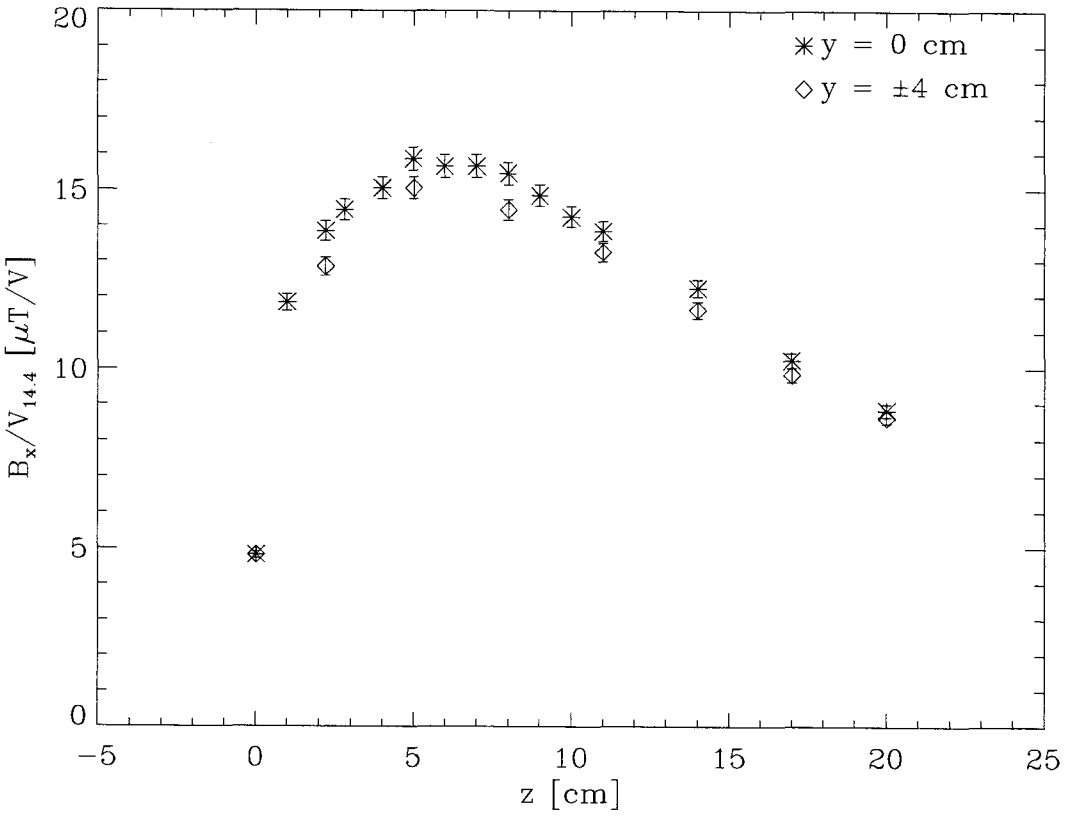

Figure 23: Strapping magnetic field (x-component) over the center of the Mark II device ($y = 0\,\mathrm{cm}$) and over the gas injection points ($y = \pm 4\,\mathrm{cm}$), normalized to capacitor bank voltage $V_{14.4}$, as a function of the height z above the electrode surfaces. This is the strapping field obtained with our first set of coils and capacitor bank.

corners) with inner radii of $13 - 16\,\mathrm{cm}$, outer radii of $16 - 19\,\mathrm{cm}$, and depths of $3\,\mathrm{cm}$. The coils were placed around the exterior of the vacuum ports adjacent to the solar device (ports #16 and #18 in Figure 4). The coils were connected in parallel to a $14.4\,\mathrm{mF}$ capacitor bank (maximum voltage $400\,\mathrm{V}$; designed by F.T. Cosso). The orientation of the magnetic field generated by the coils is shown schematically in Figure 22. B_{strap} was carefully mapped in the volume above the Mark II device using a Hall probe (calibrated to $250\,\mathrm{V}\,/\,\mathrm{T}$) and a pick-up coil ($200\ \mu\mathrm{Vs/T}$). The field strength over the device center ($x = y = 0\,\mathrm{cm}$) and over the gas injection points ($x = 0\,\mathrm{cm}$, $y = \pm 4\,\mathrm{cm}$) is plotted in Figure 23. The magnetic

field shown is the peak magnetic field (4.4 ms after the bank has been triggered) and has been normalized to the voltage $V_{14.4}$ on the 14.4 mF capacitor bank. At maximum charging voltage ($V_{14.4} = 400$ V) the peak magnetic field was $\simeq 6.3$ mT. Note that, like the toroidal bias magnetic field B_{tor}, the strapping field B_{strap} operates on a much slower time scale (milliseconds) than the toroidal current I_{tor} ramp-up time (microseconds), and can thus be regarded as effectively constant.

This set of coils and capacitor were later replaced when the effect on the plasma was found to be small (cf 4.2.3). A second set of coils was made by winding 2 AWG welding cable around vacuum ports #16 and #18. The circular coils had inner radii of ~ 10 cm, outer radii of ~ 15 cm, and depths of ~ 8 cm. Each coil was wound with 15 turns (3 layers of 5 turns each). The coils were connected in parallel to a 770 mF capacitor bank (maximum voltage 350 V; designed by F.T. Cosso). The field strength over the device center ($x = y = 0$ cm) as well as over four more points ($x = 0$ cm, $y = \pm 4$ cm and $y = \pm 9$ cm) is plotted in Figure 24. The magnetic field shown is the peak magnetic field (8.0 ms after the bank has been triggered) and has been normalized to the voltage V_{770} on the 770 mF capacitor bank. At maximum charging voltage ($V_{770} = 350$ V) the peak magnetic field was $\simeq 103$ mT.

4.1.3 Timing sequencer

A new timing sequencer was designed (by F.T. Cosso) for the Mark II device. This timing sequencer has twelve fiber-optic trigger outputs, and one trigger input. (fiber-optic triggering is desirable as it eliminates ground loops.) The timing sequencer was located in a slot in a CAMAC (Computer Automated Measurement And Control) crate and was controlled

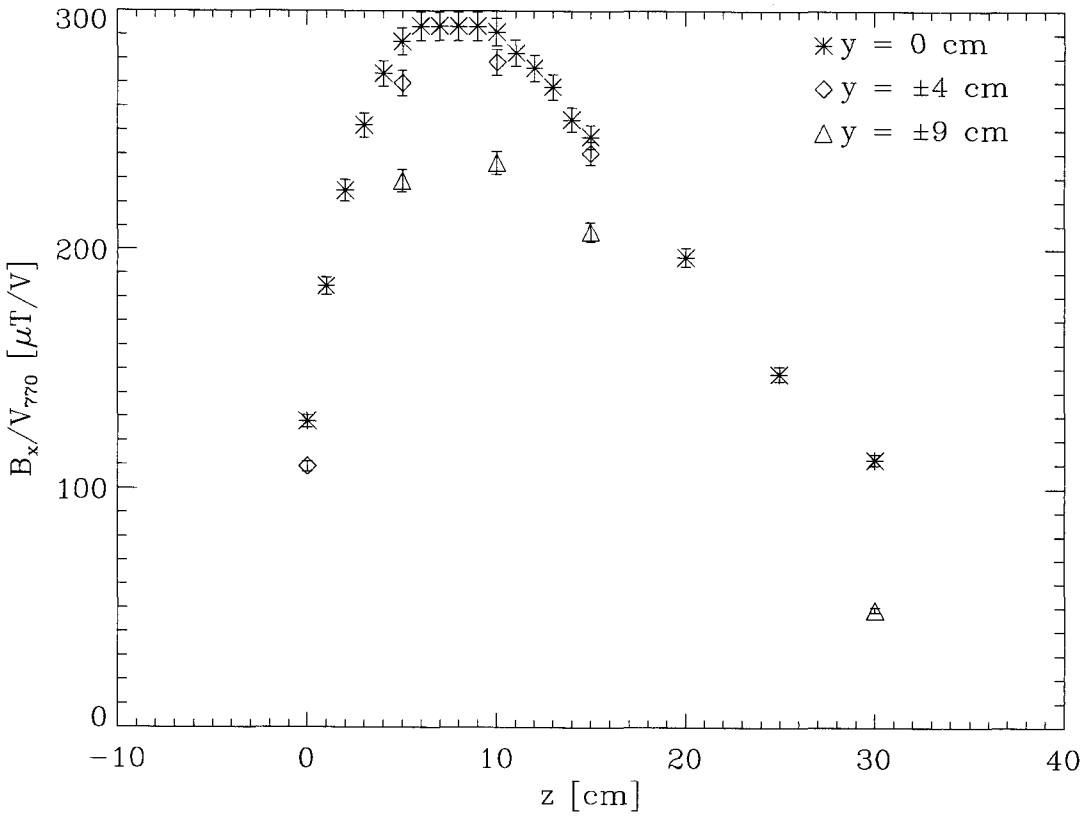

Figure 24: Strapping magnetic field (x-component) over the center of the Mark II device ($y = 0\,\mathrm{cm}$) as well as over four more points ($y = \pm 4\,\mathrm{cm}$ and $y = \pm 9\,\mathrm{cm}$), normalized to capacitor bank voltage V_{770}, as a function of the height z above the electrode surfaces. This is the strapping field obtained with our second set of coils and capacitor bank.

remotely by a personal computer (200 MHz Pentium). Each trigger output can be set to trigger between 20 ns and $2^{64} \times 20\,\text{ns} \approx 172\,\text{s}$ after the trigger input.

4.1.4 Vacuum chamber

The solar device was mounted on a 254 mm (10 in) port (port #17; cf Figure 4) of the large vacuum chamber described in Chapter 2. The chamber was pumped down to 2.8×10^{-5} Pa (2.1×10^{-7} torr) before operation of the solar device.

4.1.5 High voltage probe

A Tektronix high voltage probe (maximum DC voltage 20 kV) was used to measure the voltage on one electrode (typically the cathode). The high voltage probe output was transmitted via an analog fiber-optic link to a CAMAC crate, where the signal was read by a 10 MHz Aeon digitizer. The voltage profile of each discharge was uploaded and stored on a personal computer (120 MHz Pentium).

4.1.6 Rogowski coil

In order to measure the toroidal current, a Rogowski coil (cf A.2.15) was placed around one of the four bolts located at the corners of the main capacitor. Each of these bolts connects the capacitor to the copper sheet ground plane (cf 2.2.3), and hence carries one quarter of the total current. This was a desirable measurement location because all potentials were near ground. The coil was calibrated to $3.41 \times 10^{-6}\,\text{V}\,/\,\text{A}$. Taking into account the fact that the coil would only measure one quarter of the total toroidal current, assuming that the current is symmetrically distributed among the four bolts,

$$I_{tor} = V_{Rogowski} \times 1.17 \times 10^{6}\,\text{A}\,/\,\text{V}\,. \tag{92}$$

This Rogowski coil needed no special design to eliminate pick-up noise, as it was not located at the solar device. The coil output is available directly on the main cabinet control panel (cf Figure 5). From there the signal was transmitted via an analog fiber-optic link to a CAMAC crate, where it was read by a 10 MHz Aeon digitizer. The current profile of each discharge was uploaded and stored on a personal computer (120 MHz Pentium).

4.1.7 Cameras

Two gated, intensified, charge-coupled-device (CCD) Princeton Instruments cameras model ICCD-576-G/RB-E were set up to take pictures of the plasma. The cameras have very high quantum efficiencies, but are therefore susceptible to thermal noise. To reduce this noise, the CCD arrays must be electronically "cleaned" < 1 ms before they are used. Cleaning is performed through commands on two Princeton Instruments detector controllers model ST-1388. Also, the cameras are water-cooled, and the CCD arrays are kept moisture-free by a flow of dry nitrogen gas. The gating pulses are generated outside the actual cameras by two Berkeley Nucleonics pulser units model 310H. Gating pulses at -850 V with a duration of 10 ns were used to obtain 10 ns shutter speeds. The images are read by the controller units and passed on to dedicated cards in personal computers (120 MHz and 200 MHz Pentiums), which display the images on monitors and store these images for future use. Each image is 576 by 384 pixels in 65536 grayscales (16 bits).

A special camera mount was designed to allow both cameras a view of the plasma through the same 254 mm vacuum port. Because of the size of the cameras, one camera was mounted so that it viewed the plasma via a mirror. The mount allowed the cameras to slide along rails and could also adjust the effective angle between the cameras (by tilting the mirror) to obtain optimum parameters for stereographic photography. The camera mount

was in turn placed on a sturdy tripod head to allow adjustment of both camera viewing angles simultaneously. A dolly was built that allowed the cameras to be translated vertically or to be repositioned in the lab (e.g., at vacuum ports #1 and #14; cf Figure 4).

The lenses used for the Princeton Instruments cameras were a set of 17-28 mm wide-angle zoom lenses and a set of 28-105 mm telephoto zoom lenses.

An ultraviolet/x-ray camera was made from a 0.25 mm pinhole, an X-ray and Specialty Instruments micro-channel plate (MCP) and phosphor screen assembly, and a Meade Pictor CCD Imaging System (model 416 XT). The camera was located at vacuum port #15 (cf Figure 4). X-rays will pass through the pinhole to reach the MCP. The MCP was gated by one of the Berkeley Nucleonics pulser units (-900 V pulse for 100 ns duration). When gated, the MCP will output photo-electrons onto the phosphor, where they will be accelerated by a 3 kV (ungated) voltage. The phosphor screen then emits green light that can be observed directly or by a visual light camera, in our case the Meade Pictor CCD. The Meade camera was connected to a personal computer (120 MHz Pentium), which displays the images on a monitor and stores these images for future use. Each image is 768 by 512 pixels.

4.1.8 X-ray diode

An International Radiation Detectors bolometer x-ray diode was mounted inside the 69.9 mm vacuum port marked 'a' in Figure 4. This diode was expected to be sensitive to lower energy x-rays than the scintillation detector previously used (cf 3.1.8). The x-ray diode output was read by a 125 MHz LeCroy 9400 oscilloscope.

Equipment	B_{strap} capacitor	bias field capacitors	gas valve capacitor
Operating parameters	$V_{14.4} = 0\,\mathrm{V}$ $V_{770} = 0\,\mathrm{V}$	$V_B = 200\,\mathrm{V}$	$V_{valve} = 550\,\mathrm{V}$ $p_{valve} = 7.9 \times 10^5\,\mathrm{Pa}$ (H_2)
Time	$t_{14.4} = -4.4\,\mathrm{ms}$ $t_{770} = -8.0\,\mathrm{ms}$	$t_B = -5.6\,\mathrm{ms}$	$t_{valve} = -2.6\,\mathrm{ms}$

Equipment	Princeton Instruments camera: stop clean	Aeon digitizers oscilloscope main capacitor	cameras
Operating parameters		$V_I = 6.00\,\mathrm{kV}$	
Time	$t = -600\,\mu\mathrm{s}$	$t_I \equiv 0$	$t_{camera} = 0.1\text{-}30.0\,\mu\mathrm{s}$

Table 6: Nominal operating parameters for the second generation solar device (Mark II). The trigger time for each piece of equipment is relative to the trigger of the main capacitor.

4.2 Results

4.2.1 Establishing nominal operating parameters

Initial operating parameters were chosen based on experience with the Mark I device. The gas valve parameters were kept the same, except that t_{valve} was increased to account for the longer distance between gas valve and electrode surfaces (due to manifold, Teflon tubes, and the design of the device itself; cf 4.1.1). The Mark II device achieved gas breakdown with these gas settings and a charging voltage on the main capacitor as low as $V_I = 1.00\,\mathrm{kV}$ (the lowest voltage tested). For comparison with the Mark I device, however, the same nominal $V_I = 6.00\,\mathrm{kV}$ was kept. In response to some arcing problems in the electromagnet coils during initial operation, the nominal V_B was lowered by half, to $V_B = 200\,\mathrm{V}$. The nominal operating parameters are summarized in Table 6 along with the trigger sequence. Note that there is no strapping field when using the nominal settings. Camera settings are explained below (cf 4.2.3).

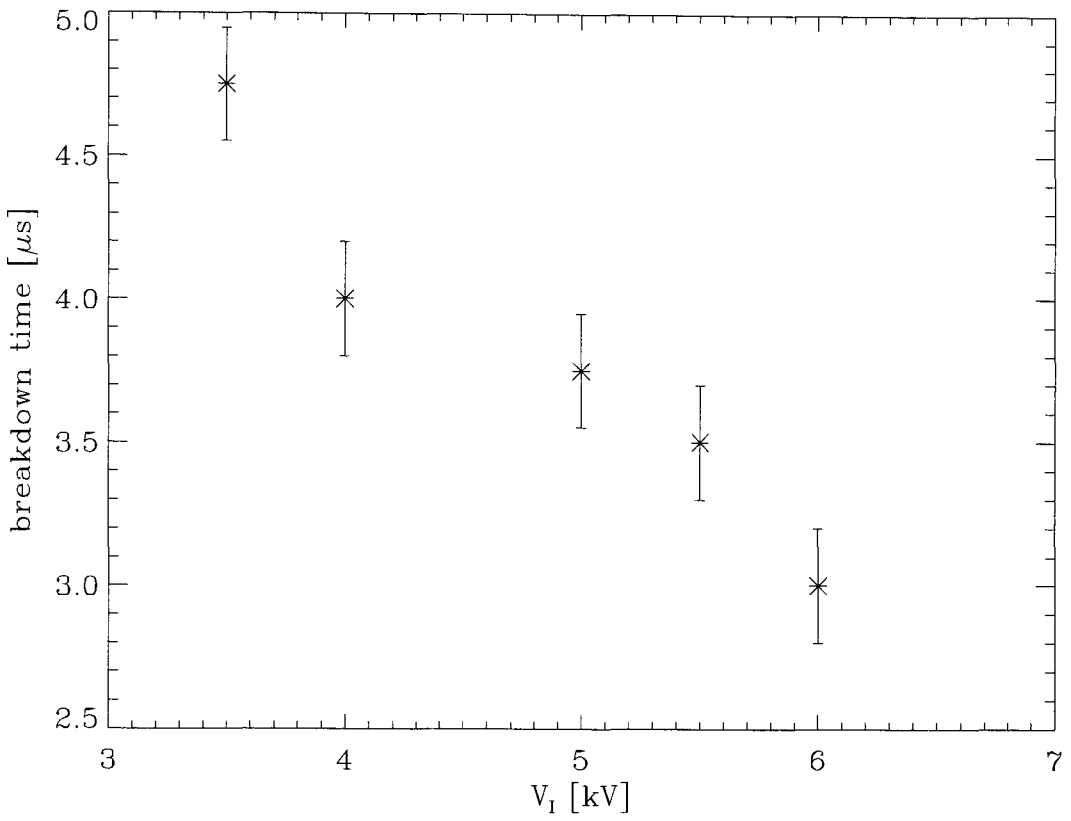

Figure 25: Breakdown time as a function of charging voltage V_I on the main capacitor (Mark II device).

4.2.2 Current and voltage profiles

The current and voltage profiles for the Mark II were very similar to those of the Mark I. Breakdown occurred very repetitively (as measured by the drop in electrode voltage) around $t = 3.0\,\mu$s for nominal settings. At lower main capacitor charging voltages, breakdown was slightly delayed as shown in Figure 25. For nominal settings, the peak current was $I_{tor} \simeq 74\,$kA at $t \simeq 6.5\,\mu$s. The peak current increased with increasing strapping field, as shown in Figure 26. The strapping field here was generated by the second combination of coils and capacitor bank (cf 4.1.2). The first combination of coils and capacitor bank produced only a marginal effect, as the maximum field was only 6.4 mT when the capac-

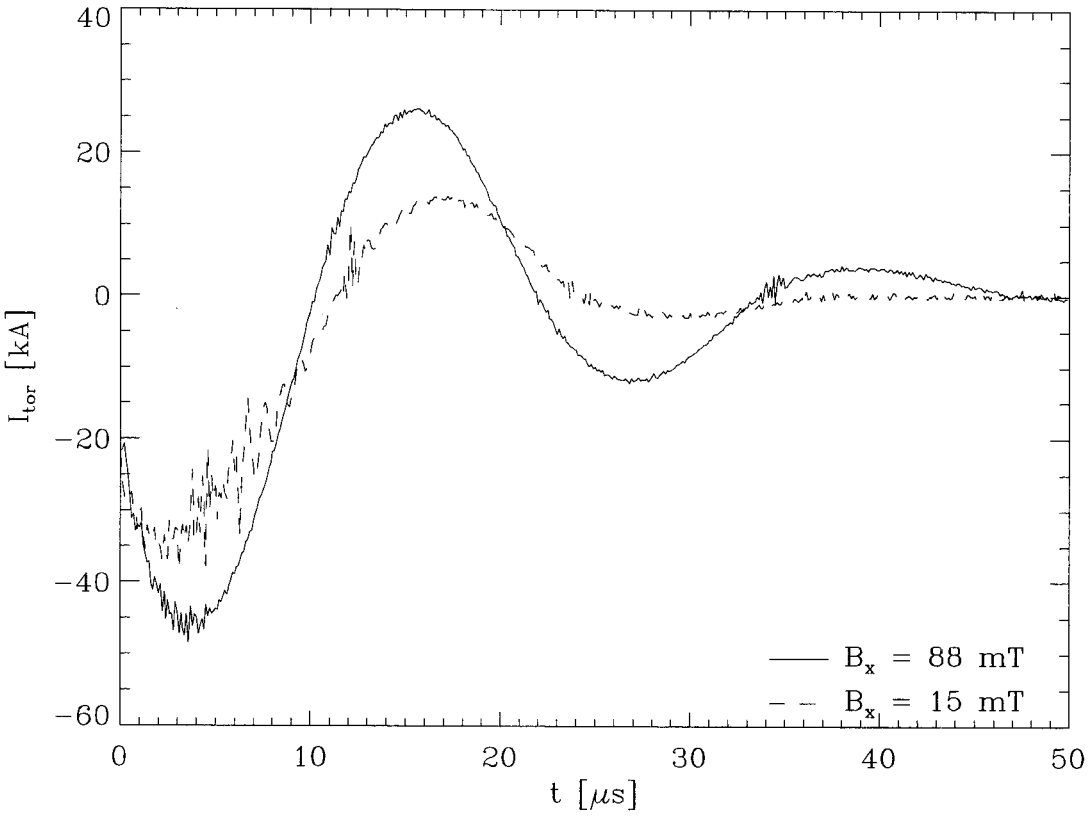

Figure 26: Toroidal current (Mark II device) as a function of time for two different values of the strapping field (x-component 15 mT and 88 mT, respectively). Charging voltage on the main capacitor was $V_I = 3.00$ kV.

itor was charged to maximum voltage $V_{14.4} = 400\,\mathrm{V}$. (During an intermediate period, the first set of coils were used in combination with the $770\,\mathrm{mF}$ capacitor bank, but this was inefficient due to ohmic losses; the time between trigger and peak field was $24\,\mathrm{ms}$.)

Polarity of the plotted I_{tor} is opposite in Figures 11 and 26, reflecting the change in location of the Rogowski coil (cf 4.1.6). The orientation of the electrodes has not changed (cathode is located at $y > 0$, anode at $y < 0$; cf 2.2.3 and Figure 19).

4.2.3 Images

The discharges were very reproducible, making it easy to construct temporal image sequences and pseudo-movies of the plasma evolution. A very low gain (50 on a scale from 0-1000) on the Princeton Instruments cameras was chosen to obtain best possible image qualities. Also, the Berkeley Nucleonics units were set to give the shortest possible camera shutter speeds ($10\,\mathrm{ns}$). With these settings, the lens diaphragms were set to f-number 4 to obtain an exposure that was neither under- nor over-exposed . Images obtained with these camera settings, and with nominal settings on the solar device, can be seen in Figure 27. Rotating the solar device by 45° led to the images in Figure 28. All of these images were studied in stereographic form. Two examples of stereographic images can be seen in Figure 29. Images were also obtained from a top view (cameras located at port #6 in Figure 4) of the device. These images were generally of a much lower quality because of a much longer distance to the plasma. Top view images can be seen in Figure 30.

Lowering the toroidal magnetic field B_{tor} produced plasmas that were more twisted. Figure 31 shows a plasma with the bias field capacitors uncharged, $V_B = 0$, so that there is no toroidal magnetic field (except possibly for some weak remaining magnetization of the solar device iron core). It is important to note that the plasma became more helical with

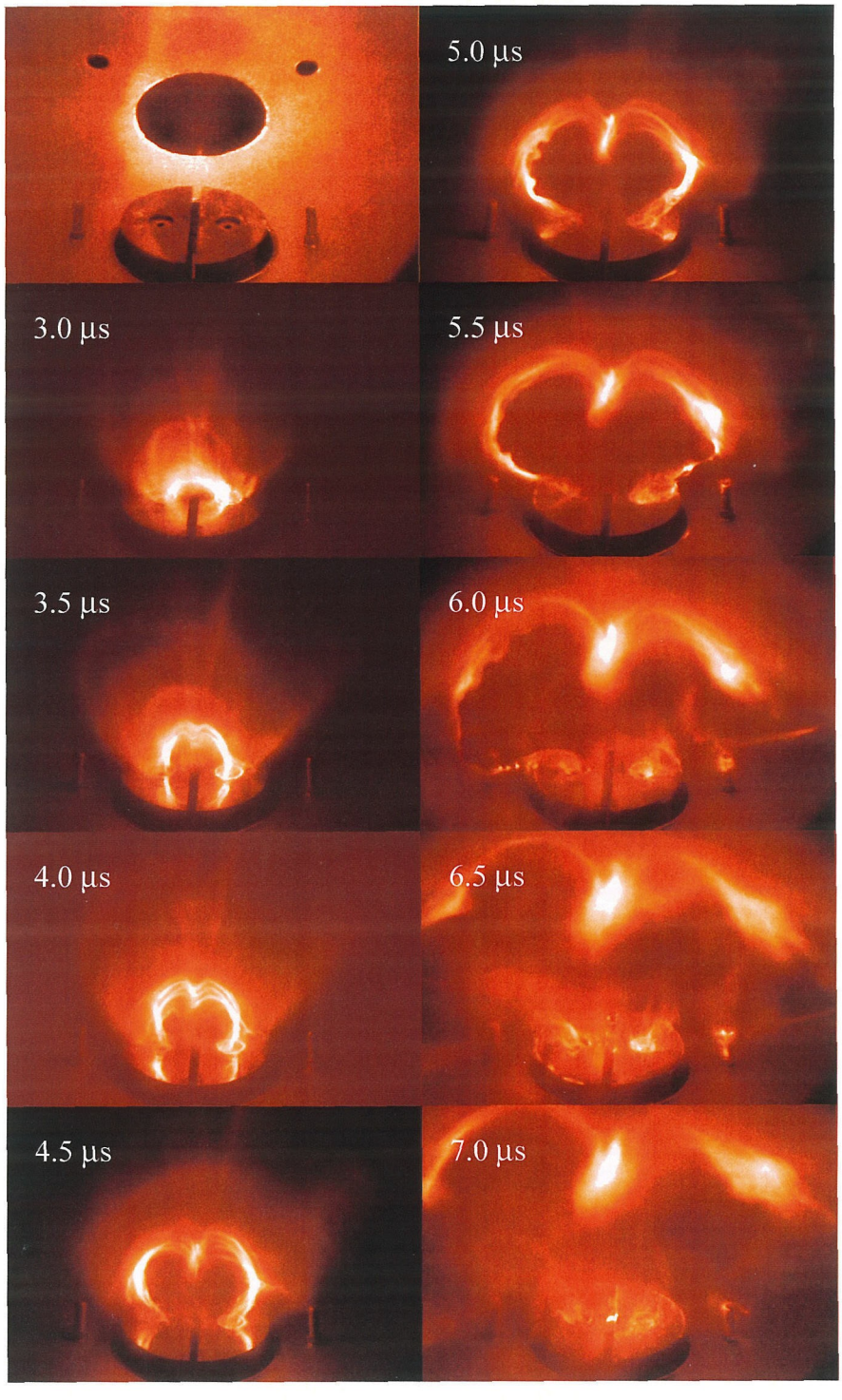

Figure 27: Evolution of plasma (Mark II device); perpendicular view. Top left image shows interior of vacuum chamber (D-shaped electrodes visible) before discharge.

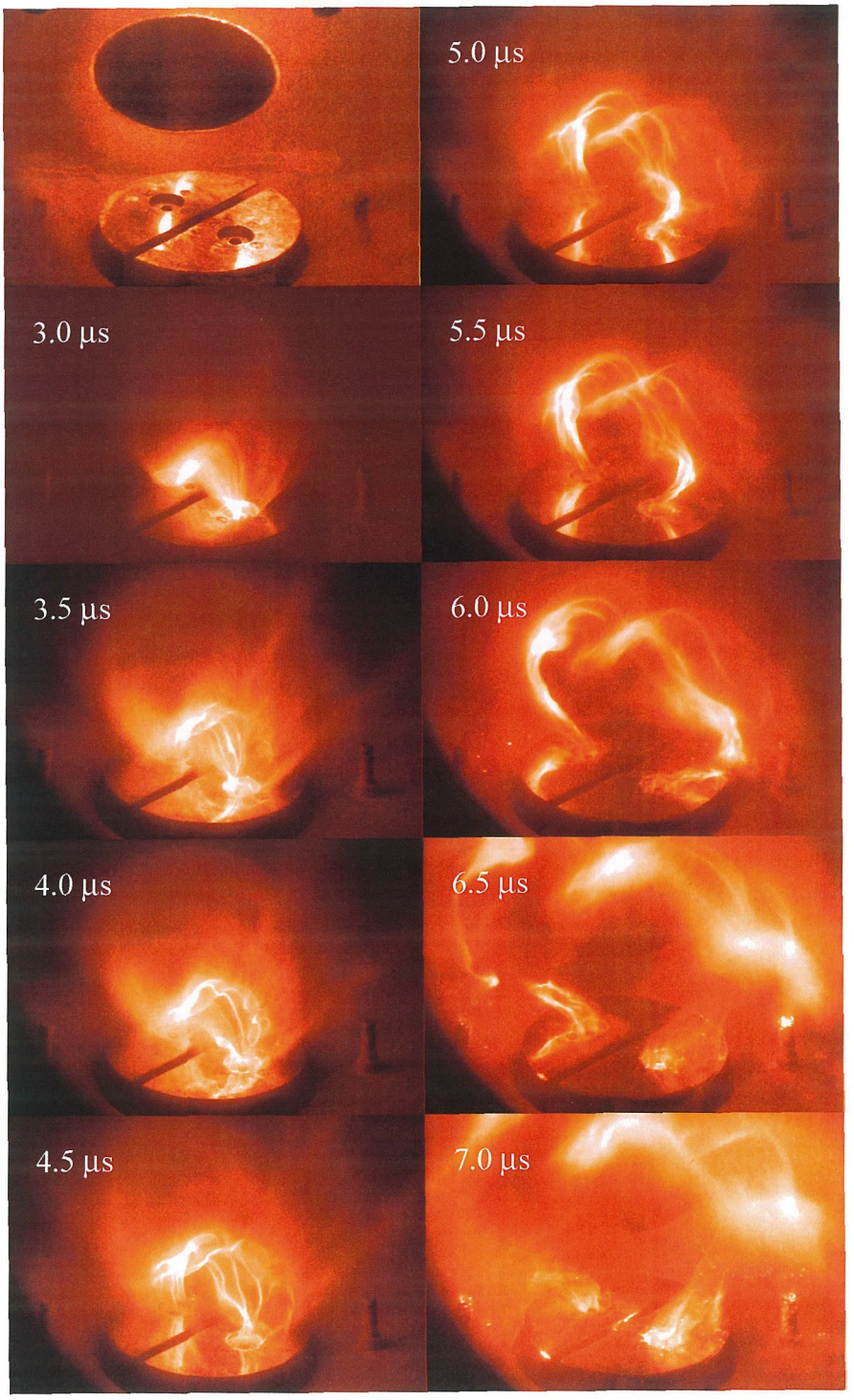

Figure 28: Evolution of plasma (Mark II device); 45° view. Top left image shows interior of vacuum chamber (D-shaped electrodes visible) before discharge.

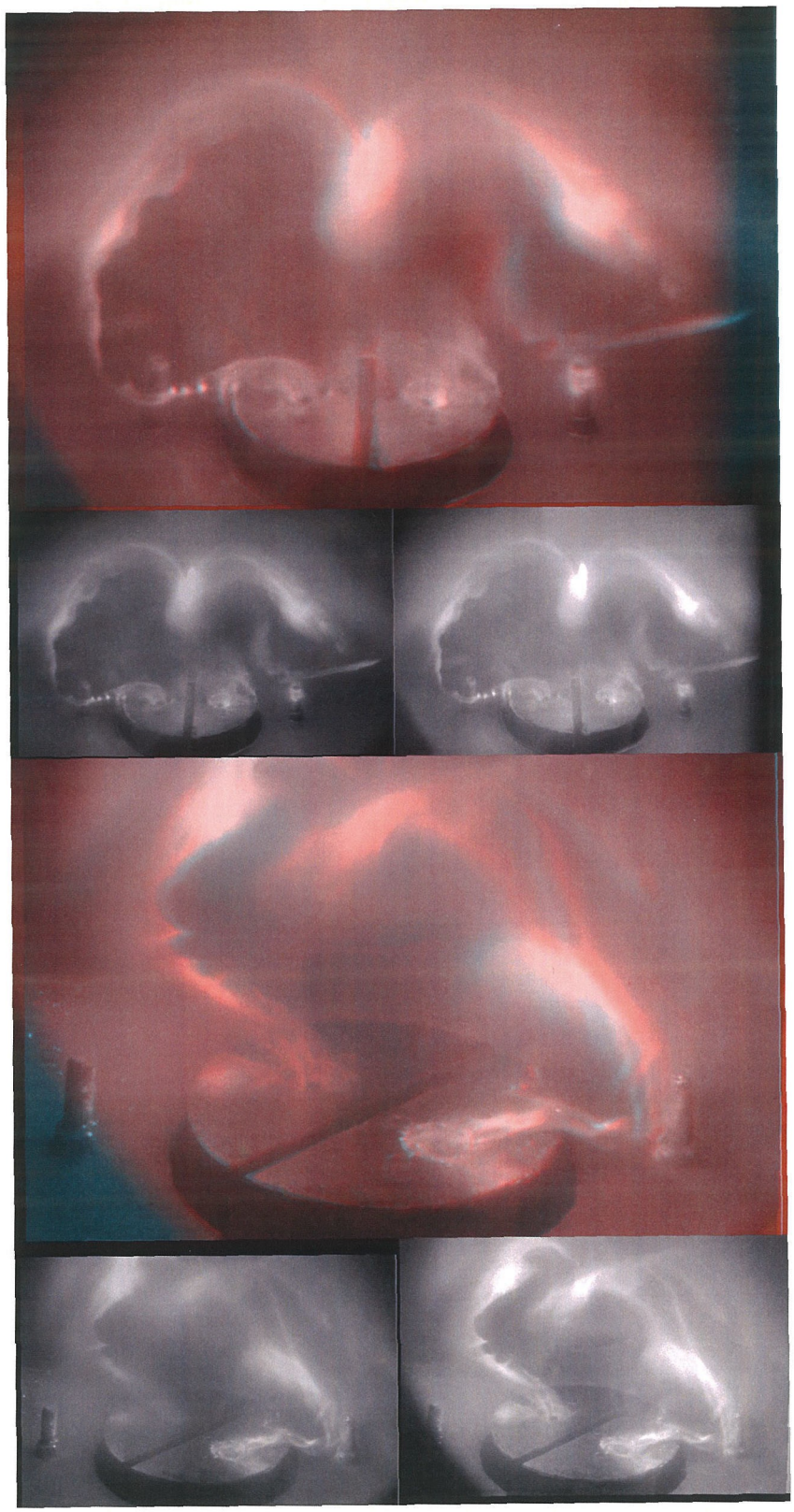

Figure 29: Stereographic images of plasma (Mark II device).

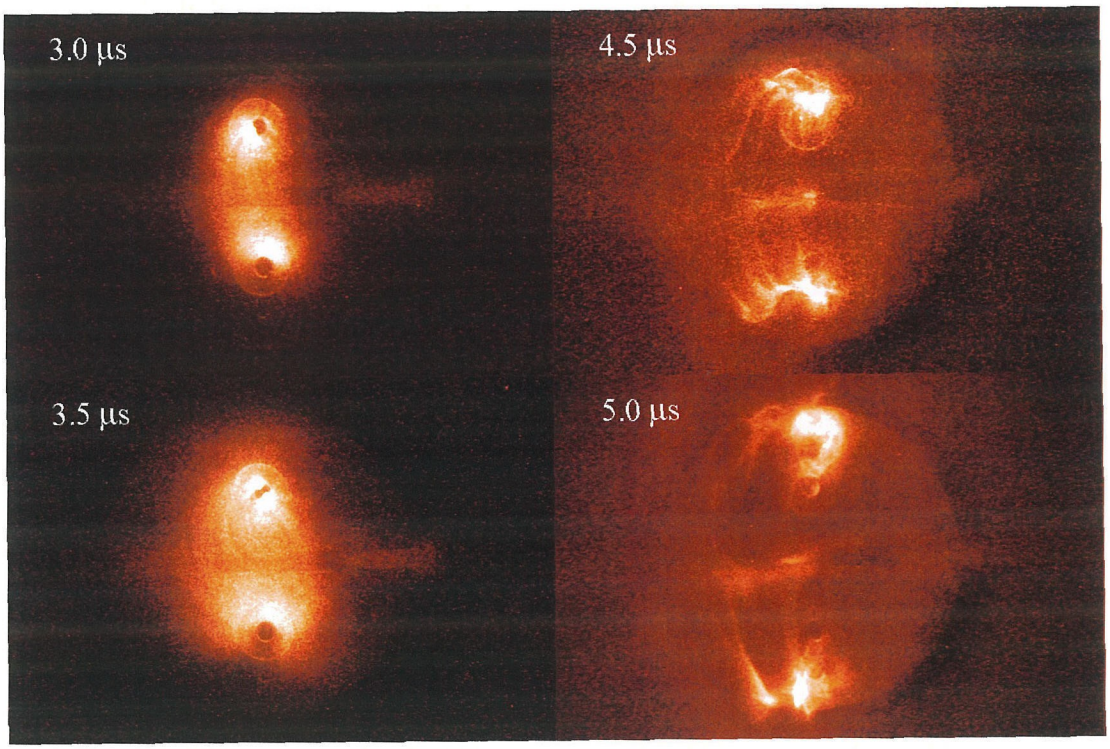

Figure 30: Images of the plasma (Mark II device) from a top view show S-shapes early in the discharge, and then a more complex shape later.

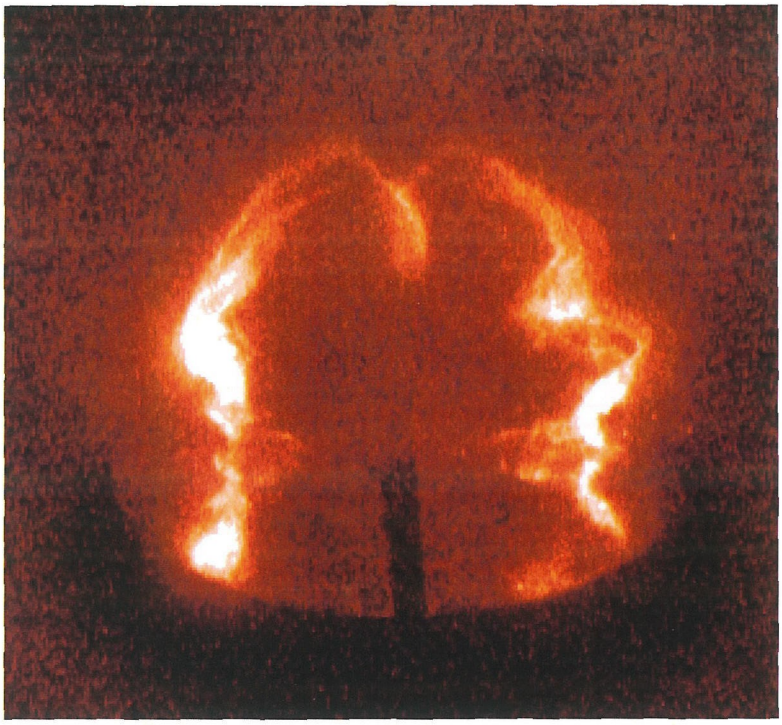

Figure 31: Example of plasma with a lower than nominal setting of the toroidal magnetic field. Note that the plasma writhes around the toroidal axis several times.

a lowered bias magnetic field. This fact will be used in the discussion section below to explain properties of a prominence erupting from a quiescent region.

Plasma evolution for various strapping field strengths can be seen in Figure 32. The strapping field slows prominence eruption or can inhibit it completely. This is the most important result of this chapter and will be discussed extensively below. (The strapping field here was generated by the second combination of coils and capacitor bank; cf 4.1.2 and 4.2.2.)

4.2.4 X-ray emissions

The x-ray diode produced a repeatable signal when the solar device was discharged. Unfortunately, the signal was bipolar, while x-ray photo-electrons should only generate a negative signal. Suspecting that energetic ions were impacting the diode, a grid was installed in

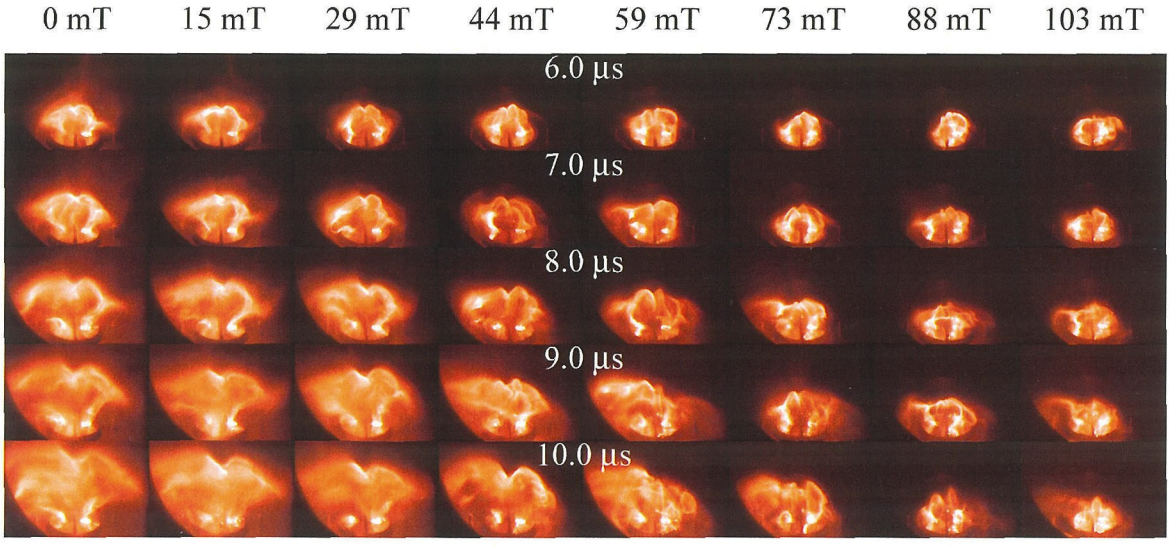

Figure 32: Plasma temporal evolution (Mark II device) for increasing strapping field strengths (maximum x-component of strapping field over center of device). The strapping field reduces both vertical and lateral expansion. Note that the expansion is completely inhibited for sufficiently strong strapping fields.

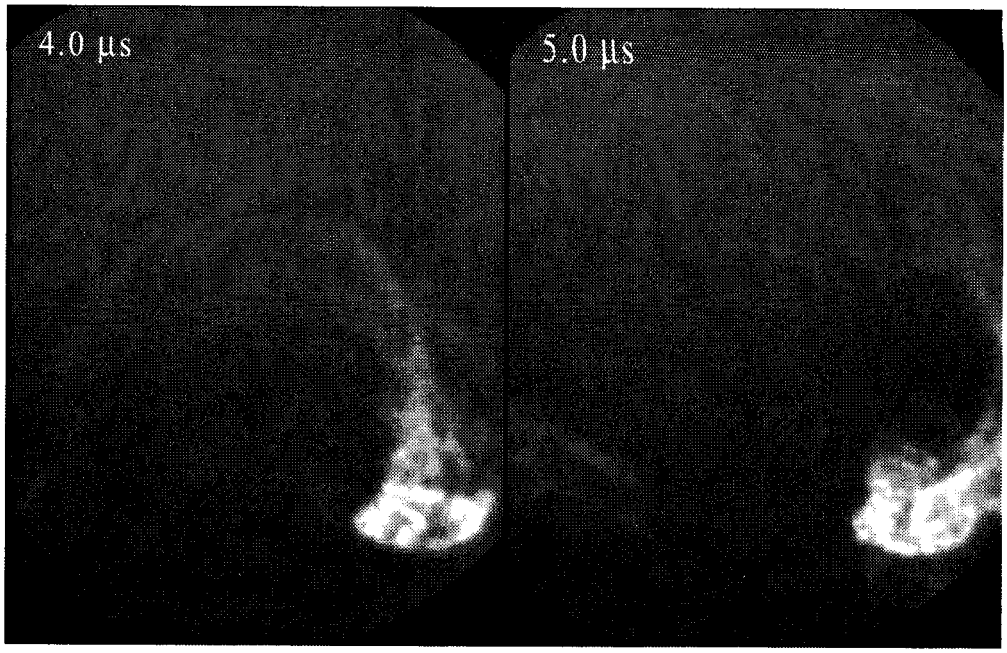

Figure 33: X-ray camera images of plasma (Mark II device). The cathode is to the right, the anode to the left.

front of the diode and biased to a positive voltage (10-200 V). This reduced the suspected ion signal somewhat, particularly for lower than nominal main capacitor charging voltages, $V_I \lesssim 5\,\mathrm{kV}$. Another possibility was that fast electrons were impacting the diode, or neutrals in the vicinity of the diode, creating secondary ions through some form of β-process (cf 2.2.5). Two sets of permanent magnets were positioned on either side of the vacuum port to divert electrons. The magnetic field strength was $\approx 50\,\mathrm{mT}$. Again, this reduced the positive peaks somewhat, but not entirely. Finally, we noted that a reverse bias on the x-ray diode, even as small as 1 V, helped in reducing the unwanted signal.

The x-ray camera successfully produced images of the plasma. Examples of two such images can be seen in Figure 33.

Improved x-ray emission results were obtained with a later generation solar device and will be presented and discussed in Chapter 5.

4.3 Discussion

We will now discuss and interpret the results of this chapter. The most important finding is that a strapping field can inhibit the eruption of a prominence. This is indicated both in toroidal current measurements and directly in images. A mathematical model explains the effect of the strapping field quantitatively and qualitatively. Prominence eruption is inhibited due to a $\mathbf{J} \times \mathbf{B}$-force between strapping field and the prominence toroidal current. Thus, the sign of the strapping field matters (contrary to models which rely on magnetic field line tension or magnetic pressure of the strapping field). The sign-dependence is verified experimentally. Other important results that will be discussed include:

- More helical plasmas (larger φ, the complement of the pitch angle) are produced with higher ratios of toroidal current to toroidal bias magnetic field.

- The dip of a prominence above the neutral line can be explained by the helical shape of the prominence.

- Acceleration duration and magnitude of disparitions brusque (a prominence erupting from a quiescent region) compared to a spray (a prominence erupting from an active region) can be explained by a proposition that quiescent regions on the Sun are subjected to stronger strapping fields than active regions. The proposition is supported by a comparison of the helical appearance of disparitions brusque to experiments producing plasmas with larger φ.

- The large aspect ratio (length to height) of some prominences can be the result of strong strapping fields.

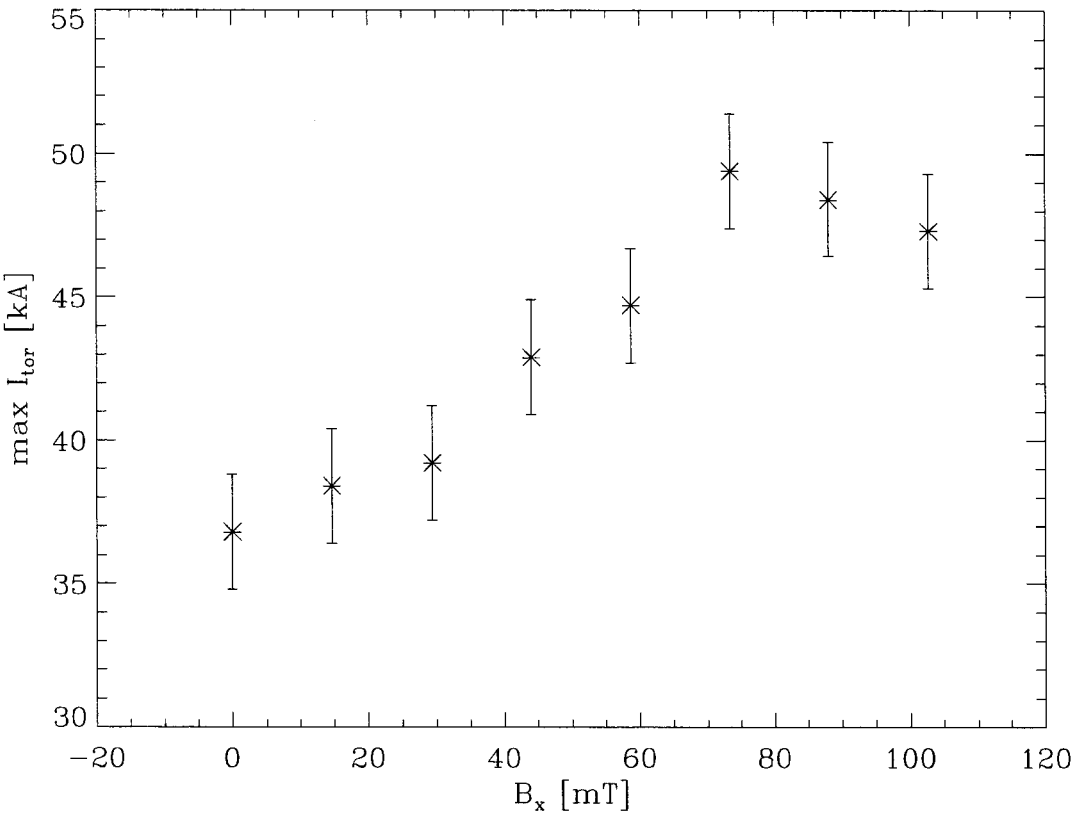

Figure 34: Peak toroidal current as a function of strapping field (maximum x-component over center of device).

4.3.1 Current traces

The increase in toroidal current as a function of increasing strapping field is shown in Figure 34. This increase can be explained by comparison to Figure 32. A strong strapping field slows the expansion of the plasma, i.e., slows the growth in inductance L (cf A.2.4). When all of the original energy $\frac{1}{2}CV_I^2$ on the main capacitor is in the form of inductive energy $\frac{1}{2}LI_{tor}^2$ in the plasma, the toroidal current I_{tor} must be higher when the plasma is strapped down.

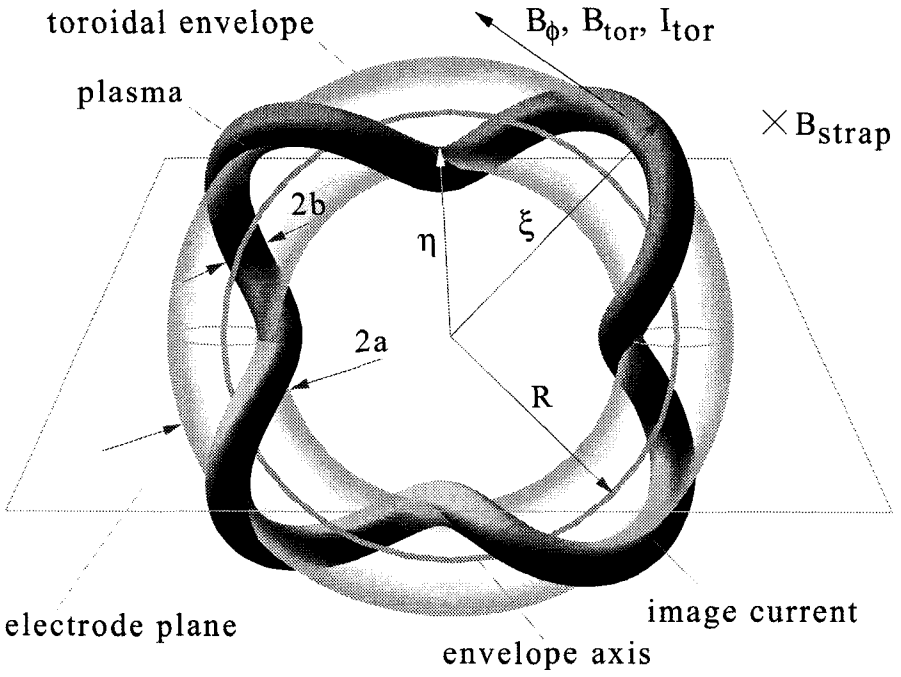

Figure 35: Geometric model of prominence. The plasma writhes around a fictitious toroidal envelope, circling the toroidal envelope axis (twice in this figure). Image currents in the electrode plane writhe the same number of turns around the toroidal envelope. Together, the plasma and its image writhe around the toroidal envelope N times ($N = 4$ in this figure).

4.3.2 Images

The camera images show that the plasma evolves through the following stages. First, initial breakdown forms a main current channel consisting of several strands of plasma, some darker, some brighter ($t = 3.0\,\mu$s in Figures 27-28). Second, the strands twist around each other ($t = 3.0$-$3.5\,\mu$s). The pinch effect begins to show at this stage; the plasma cross-section shrinks. Third, the entire plasma takes on a helical structure and expands outward ($t \geq 3.5\,\mu$s). Initially the helical structure is of mode $N = 4$ where $N/2$ is the number of turns the plasma makes around the toroidal axis, i.e., N is the combined number of turns that the plasma and its image current in the electrodes make around the toroidal axis (cf Figure 35). Fourth, the plasma twists up to $N = 8$ ($t \geq 6.5\,\mu$s). The three-dimensional

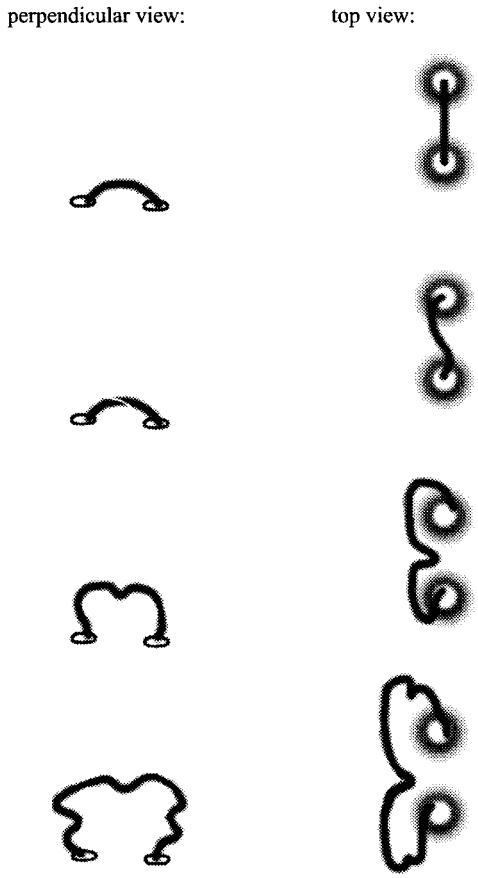

Figure 36: Plasma evolution stages for plasma (Mark II device) shown from perpendicular and top views. First, a main current channel forms between the two electrodes. Second, brighter and darker strands in the main current channel twist up. Third, the plasma takes on a helical shape and expands outward. Fourth, additional turns on the helix form during expansion.

aspect of the structure is verified by the stereographic images. The four stages can also be identified in the top view images. The plasma evolution stages are summarized in Figure 36.

It has often been suggested that a dip in the prominence magnetic field is necessary to prevent plasma from falling down to the solar surface (pulled by gravity along the magnetic field lines). The creation of such a dip has been explained by taking two prominences and reconnecting their field lines [70][65]. From Figure 27 we conclude that a *single* prominence can evolve a cusp-like dip. The dip is merely the projection of a three-dimensional

helical structure that occurs when the prominence toroidal current I_{tor} is sufficiently large. Observations show that dips on solar prominences occur only for large α [17], i.e., for large I_{tor}. Numerical models confirm the development of a dip when the prominence has become sufficiently "twisted" [71].

With a lower than nominal toroidal magnetic field B_{tor}, the plasma twists up beyond $N = 8$. This is a direct confirmation that bright regions (strands, arcs) in the plasma correspond to current paths (cf 3.3.2). A large N corresponds to a large pitch angle complement φ (cf Figure 3), which in turn corresponds to a large I_{tor}/B_{tor} ratio according to Equation (90). Note that $N = 8$ corresponds to three cusp-like dips. However, the plasma always develops a single dip (i.e., $N = 4$) before additional dips appear. The single dip always forms symmetrically between the electrodes. This symmetry also occurs on the Sun; observations show that when a dip forms, it is always above the "polarity inversion line," or neutral line between regions of opposite magnetic polarity [17].

4.3.3 Flux rope model of prominence and strapping field

The most important result in this chapter is that the demonstration that prominence expansion can be controlled by a strapping field. This is clearly shown in Figure 32. The strapping field slows the prominence expansion rate and a sufficiently strong strapping field even inhibits expansion altogether.

We quantified prominence expansion as follows. First, a reference point was defined in each image as the midpoint between the two visible orifices through which gas is injected. This is the origin $x = y = z = 0$ of the coordinate system previously used. Next, the central, cusp-like dip was identified, and the distance η (indicated in Figure 35) from the origin to the upper plasma-vacuum boundary (as apparent with a 5-95% brightness scaling

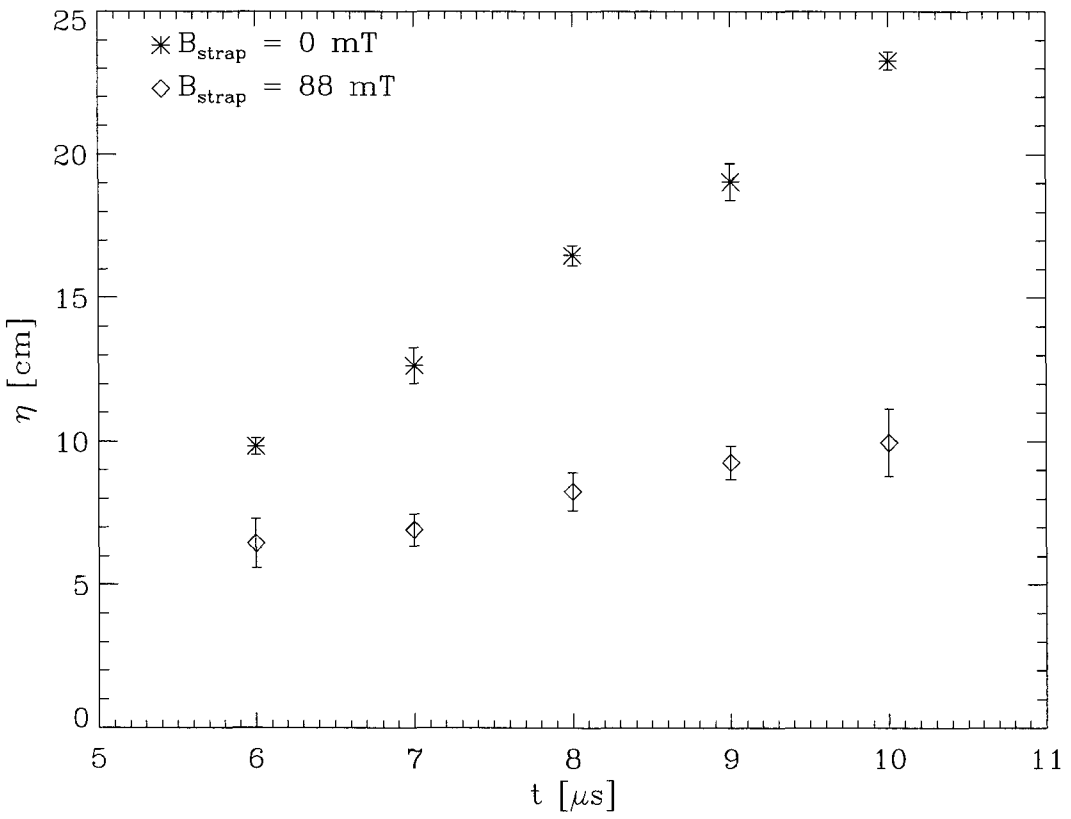

Figure 37: Expansion height η as a function of time with a 88 mT strapping field and with no strapping field.

of the image) at the dip was determined. The distance ξ from the origin to the "highest" point of the prominence, i.e., the longest distance from the origin to any plasma-vacuum boundary, was measured in a similar way. For times early in the evolution, before the prominence has taken on a helical shape and developed a dip, $\eta = \xi$. The filament radius b was also measured. Each distance, measured in pixels, was converted to actual length distance by scaling to known reference distances in the image.

Figure 37 shows the prominence height η versus time with and without an applied strapping field. Each data point corresponds to averaging over several discharges, and the error bars are the standard deviations. It is clear that the expansion rate, or velocity, is re-

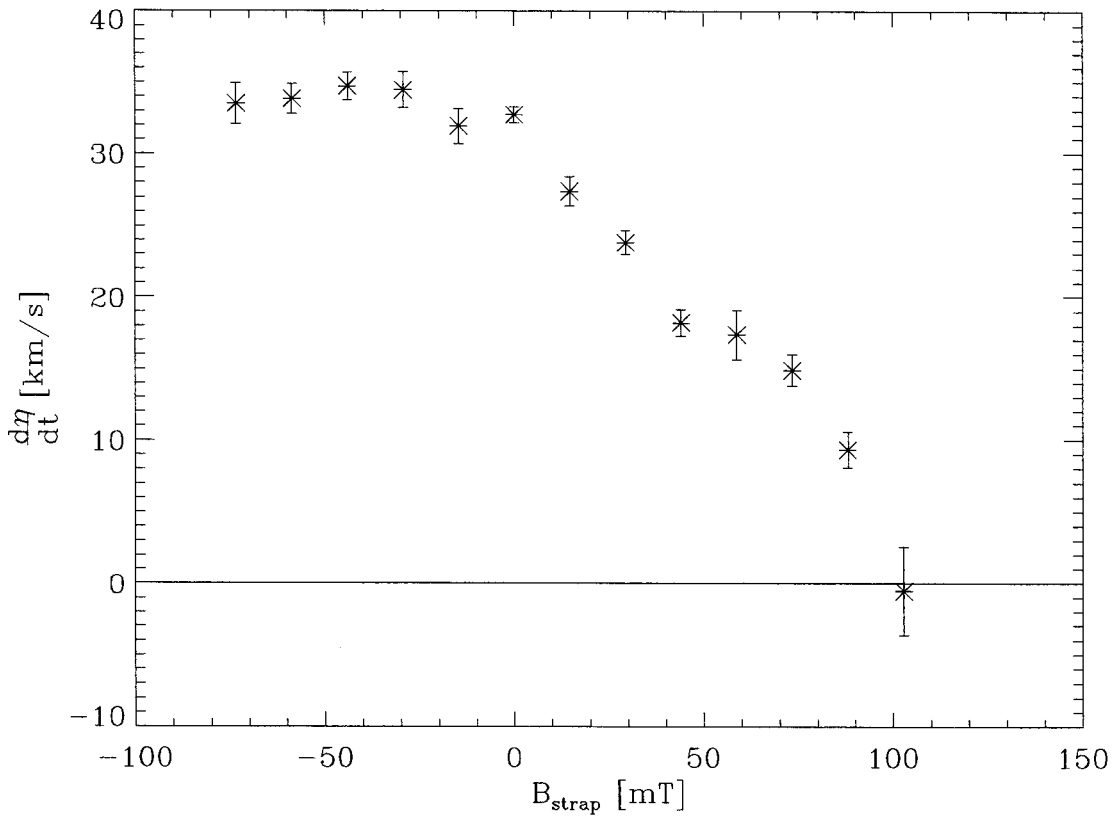

Figure 38: Expansion velocity $d\eta/dt$, as measured in camera images, as a function of strapping field stength (peak strength over center of Mark II device).

duced with increasing strapping field strength. For each value of the strapping magnetic field, the observed expansion velocity $d\eta/dt$ is nearly constant. This velocity is plotted in Figure 38 as a function of strapping field strength (peak strapping field strength on a line that is perpendicular to the electrode plane and goes through the origin). The velocity reduction is approximately proportional to the strength of the applied strapping field. Furthermore, if a negative strapping field is applied (i.e., a strapping field of reverse polarity) the expansion velocity exceeds that obtained with no applied strapping field at all. Note that, for sufficiently large strapping fields, the expansion is completely halted. In this situation, the prominence and its image (cf Figure 35) are in an equilibrium resulting from the

balancing of three distinct magnetic forces acting to change the envelope major radius R. The basis of these three forces can be seen as follows [72][73][74]:

1. The energy associated with the toroidal magnetic flux (relative to the vacuum field energy; cf 139) is:

$$W_{tor} = \int \frac{\left(B_\phi^2 - B_{tor}^2\right)}{2\mu_0} d^3r = \int \frac{\left(B_\phi^2 - B_{tor}^2\right)}{2\mu_0} 2\pi R dS \tag{93}$$

where B_ϕ is the toroidal magnetic field associated with poloidal current, and B_{tor} is the vacuum bias toroidal magnetic field. A virtual displacement along the major radius direction gives the tension along the magnetic field lines in the toroidal direction, B_ϕ, tending to decrease R:

$$F_{tension} = -\frac{\partial W_{tor}}{\partial R} = 2\pi \int \frac{1}{2\mu_o} \left(B_{tor}^2 - B_\phi^2\right) dS. \tag{94}$$

2. The energy associated with the toroidal current is:

$$W_{pol} = \frac{1}{2} L I_{tor}^2 = \frac{\left(L I_{tor}\right)^2}{2L} = \frac{\phi_{pol}^2}{2L} \tag{95}$$

where L is the circuit inductance associated with the toroidal current. This circuit inductance can be written as $L = \mu_0 R(\ln(8R/a) - 2 + l_i/2)$, where a is the envelope minor radius and l_i the internal inductance per unit length [72][73][74] (cf A.2.4). A virtual displacement, holding the poloidal flux ϕ_{pol} constant, along the major radius direction gives the poloidal hoop force associated with the toroidal current, I_{tor}, tending to increase R:

$$F_{hoop} = -\frac{\partial W_{pol}}{\partial R} = \frac{\phi_{pol}^2}{2L^2} \frac{\partial L}{\partial R} = \frac{1}{2} I_{tor}^2 \frac{\partial L}{\partial R}. \tag{96}$$

3. The force due to the interaction of the strapping field, B_s, and toroidal current, I_{tor}, tending to increase or decrease R depending on the polarity of the strapping field

is:

$$\mathbf{F}_{strap} = \int \mathbf{J}_{tor} \times \mathbf{B}_{strap} d^3r = \int \mathbf{J}_{tor} \times \mathbf{B}_{strap} 2\pi R dS = 2\pi R I_{tor} B_{strap} \hat{R}. \quad (97)$$

Thus, the force-balance equation is [72][73][74]:

$$2\pi R I_{tor} B_{strap} = 2\pi \int \frac{1}{2\mu_o} \left(B_{tor}^2 - B_\phi^2 \right) dS + \frac{1}{2} I_{tor}^2 \frac{\partial L}{\partial R}. \quad (98)$$

A similar force-balance equation for prominences has been suggested by Krall et al. [75].

The poloidal current can be determined by comparing images of the plasma with the geometric model in Figure 35. The experimental data in Figure 32 shows that the current channel spirals around the envelope axis twice on its path from one electrode to the other, or a total of four times around the envelope axis when we consider the image current in the electrode plane. Thus, the poloidal current is $I_{pol} = N I_{tor}$, where the number of poloidal turns is $N = 4$, and so the associated toroidal magnetic field due to prominence current is $B_\phi = \mu_0 N I_{tor} / 2\pi R$. Integrating B_ϕ over the entire envelope cross-section, πa^2, gives the strapping field required for force-balance:

$$B_{strap} = \frac{1}{2\mu_0 R I_{tor}} \int B_{tor}^2 dS - \frac{\mu_0 N^2 I_{tor} a^2}{8\pi R^3} + \frac{\mu_0 I_{tor}}{4\pi R} \left(\ln \frac{8R}{a} - 1 + \frac{l_i}{2} \right). \quad (99)$$

Using the measured values of $\eta = 51 \pm 2$ mm, $\xi = 62 \pm 2$ mm, $2b = 26 \pm 1$ mm (giving $R = (\xi + \eta - 2b)/2 = 43$ mm, and $a = (\xi - \eta + 2b)/2 = 19$ mm), $I_{tor} = 47.3 \pm 2.0$ kA, and a measured, average vacuum toroidal field over the envelope $B_{tor} = 0.12 \pm 0.02$ T, we can now calculate the required strapping field for force-balance, provided the internal inductance l_i is estimated. For this inductance we set $l_i = \frac{1}{2}$, corresponding to a uniform distribution of toroidal current over the cross-section of the envelope, a fair assumption considering that $2b \approx a$ (extreme values of l_i would be 0 or 1). Using these measured

values, the strapping field required for force-balance is calculated to be $B_{strap} = 82 \pm 5\,\mathrm{mT}$ (from measurement errors), $\pm 27\,\mathrm{mT}$ (from extreme values of l_i). This calculated value corresponds reasonably well to the field strength used to strap down the prominence in the actual experiment. The images indicated that expansion ceased for a strapping field between 88 mT and 103 mT (cf Figure 38). The peak toroidal current I_{tor} did not increase for strapping field $> 73\,\mathrm{mT}$ (cf Figure 34), another indirect indication that the prominence is strapped down.

We conclude that vacuum strapping fields can inhibit the eruption of solar prominences, and that force-balance arguments of the type presented here give a reasonable, quantitative description of strapping field effects on solar prominences. A sudden increase in prominence current, by mechanisms below the solar photosphere [76], can tip the balance and cause a prominence to become eruptive.

4.3.4 Comparison to earlier models

Here we review existing solar prominence models. There are two important differences between our model above and existing models. First, our model includes the important hoop force. Most existing models are two-dimensional and therefore cannot include a hoop force, which by nature is three-dimensional. Second, unlike most other models, we include a strapping field. The strapping field is very important as it can largely determine the fate of a prominence.

There are two classic magnetic field configuration models for quiescent prominences. Both of these models are two-dimensional (or 2.5 D), i.e., they model the prominence as an infinitely long tube at some distance above the solar surface. The first model was proposed by Kippenhahn and Schlüter [77] and consists of a prominence embedded in a magnetic

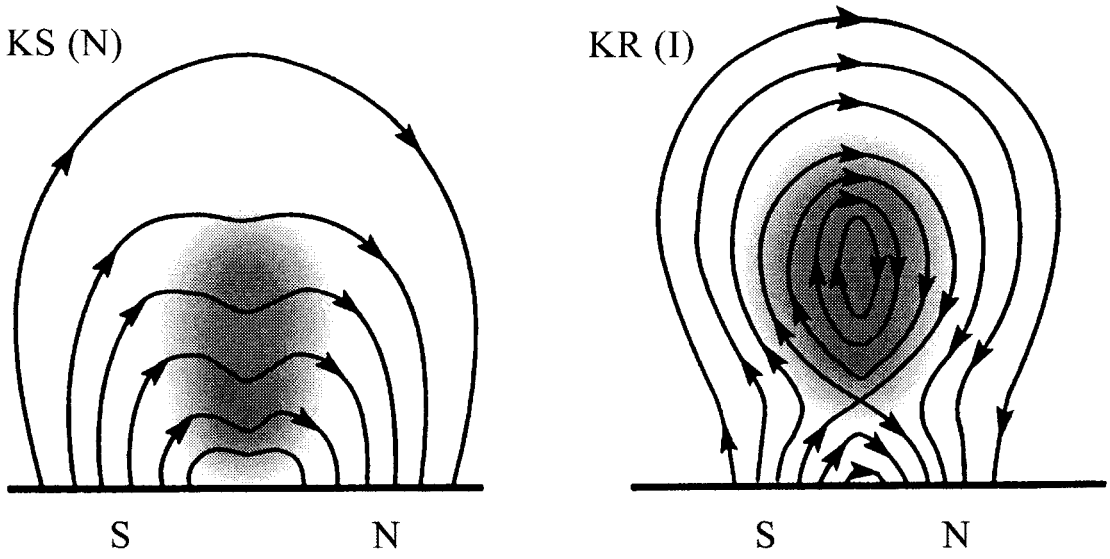

Figure 39: Kippenhahn-Schlüter (KS) and Kuperus-Raadu (KR) models of solar prominences. The shaded area indicates the prominence cross-section.

field perpendicular to the prominence but parallel to the solar surface (cf Figure 39). This model is called the Kippenhahn-Schlüter (KS) model or the normal (N) model. In the second model [78], magnetic field lines close to the prominence cross-section encircle the cross-section as shown in Figure 39. This model is called the Kuperus-Raadu (KR) model, after its developers [79], or the inverse (I) model. With our (three-dimensional) model of a solar prominence, it is not difficult to see that the difference between the normal model and the inverse model is simply that current is flowing along the prominence flux-rope. Again this is a case where we believe that sorting prominences into different categories is unnecessary. The current flowing along a prominence can have any of a continuum of values, or even change gradually from one value to another (including zero), so that a prominence can change from "normal" to "inverse," or vice versa.

Until recently, most models of a solar prominence as a magnetic flux rope have been either 2D or 2.5D [64][80][67] [81] like the Kippenhahn-Schlüter and Kuperus-Raadu

models. Three dimensional models have been presented only recently [68][17][21]. While some models include a strapping field, they differ on how the strapping field actually prevents prominence eruption. Some models explain the restoring force by tension in the magnetic field lines, requiring reconnection of the strapping field before the underlying prominence can erupt [69][82]. Others attribute the restoring force to the magnetic pressure $B^2_{strap}/2\mu_0$ in the strapping field. In either of these explanations, the sign of the strapping field does not matter. We have shown experimentally that it is neither the magnetic pressure nor the tension in the strapping field lines that inhibits eruption. The force that inhibits eruption is the $\mathbf{J} \times \mathbf{B}$-force between the prominence toroidal current and the strapping field, which is sign-dependent.

For completeness we would like to mention that other models do not rely on strapping fields to explain stability/instability. Some 2D models instead call for a sudden increase in resistivity, called anomalous resistivity, in regions around X-points (cf KR model in Figure 39) in the magnetic field topology, resulting in a sudden onset of instability [81]. An alternate explanation for how prominences are kept from erupting (derived from numerical models) claims that if a prominence becomes sufficiently twisted up, by $\sim 30\pi$ or 15 turns, then the twisted magnetic field lines form a higher pressure on the outside of the torus than on the inside [83]. This pressure is conjectured to balance the hoop force. If this model is otherwise correct, it is hard to see how the prominence could get this twisted up without a large toroidal current passing through it, thus increasing the hoop force even more.

4.3.5 Suggested relevance of strapping fields to other solar phenomena

We propose that solar regions with quiescent prominences (cf 1.1.1) are subjected to stronger strapping fields than regions with active prominences. We will combine this proposition with the experimental results obtained when lowering the toroidal magnetic field (cf Figure 31), to explain some observed characteristics of disparitions brusque and sprays.

The French term disparition brusque is used to describe a quiescent prominence that suddenly disappears. Before the disappearance, the prominence accelerates in a direction away from the solar surface, and is seen to develop an extremely helical structure accompanied by a spiraling motion of the prominence plasma. Some time after the disappearance, the prominence appears again, in its original position. Nearly one-half of all low-latitude prominences undergo a disparition brusque phase at least once, leading to a temporary disappearance [12]. It has been pointed out that the reappearing prominence should not necessarily be considered to be the same prominence, but rather a new prominence appearing in a magnetic field topology that has reverted back to the original topology after a reconnection process [84]. This interpretation is one that we share, and we believe that the ejected prominence becomes a magnetic cloud (cf 1.1.4).

A spray, i.e., a prominence being ejected from an active region, exhibits a larger acceleration than a disparition brusque, but for a shorter period of time. After the initial acceleration, both sprays and disparitions brusque attain a velocity of several hundred kilometers per second, typically about $4 \times 10^5\,\mathrm{m/s}$. This corresponds to the solar escape velocity at a height above the solar surface of $\sim 1 \times 10^8\,\mathrm{m}$. Prominences can be seen until they reach a height of at least $3 \times 10^8\,\mathrm{m}$, sometimes as much as $7 \times 10^8\,\mathrm{m}$ [12]. Thus, it is

fairly clear that, unless there is a retarding force other than gravity, the ejected plasma will travel outward through the solar system. Note that at the typical velocity, ejected plasma traveling in the correct direction will take 1 AU/4 $\times$ $10^5\,\mathrm{m\,s^{-1}} \approx 100\,\mathrm{h}$ to reach the Earth, which compares well with the $80\,\mathrm{h}$ travel time noted for magnetic clouds [23].

If an active prominence is subject to a relatively weak strapping field, as we propose, then a relatively weak hoop-force will cause it to erupt. Conversely, if a quiescent prominence is subject to a stronger strapping field, then a greater hoop-force will be required for eruption. Since the hoop force is proportional to the current flowing along the prominence, this current must be much larger in a disparition brusque (a prominence ejected from a quiescent region) than in a spray (a prominence ejected from an active region). As we have demonstrated experimentally, a larger current results in a much more kinked, or helical, prominence, in agreement with one of the characteristics of a disparition brusque. Also, a weaker strapping field over the spray explains why the spray accelerates faster than the disparition brusque. Assuming that the helicity injection rate does not depend on whether the prominence is quiescent or active, it would take a longer time for a disparition brusque to reach the toroidal current required for eruption (since this current is large), than it would for a spray (since the required current is small). This explains why sprays accelerate during a shorter time, than disparitions brusque. The distinction between sprays and disparitions brusque seems unnecessary, as the essential physics appears to be the same.

Finally, we also suggest that it is due to very strong strapping fields that prominences on the Sun can be seen to extend over relatively long distances compared to the prominence height. A strong, overlying strapping field inhibits vertical eruption but may allow some horizontal expansion. Solar prominences with these extreme length-to-height ratios often

develop characteristic barbs - intermediate locations along the length of the prominence where plasma filaments connect the prominence with the photosphere below. These barbs form because of local regions of opposite magnetic flux beneath the prominence, i.e., each such region causes a magnetic flux across the neutral line that is locally antiparallel to the general magnetic field direction [67][17].

4.3.6 Gravitational effects on a solar prominence

The force of gravity can be compared to the hoop force in our model. Consider a solar prominence with major radius R, minor radius a, typical magnetic field strength B, and density ρ. The hoop force (96) is

$$F_{hoop} = \frac{1}{2} I_{tor}^2 \frac{\partial L}{\partial R} = \frac{1}{2} I_{tor}^2 \mu_0 (\ln(8R/a) - 1 + l_i/2) \tag{100}$$

using $L = \mu_0 R(\ln(8R/a) - 2 + l_i/2)$. The toroidal current I_{tor} is associated with a poloidal magnetic field B_{pol}. From Ampère's law and Stoke's theorem, $I_{tor} = 2\pi B_{pol} a/\mu_0$. The hoop force accelerates a mass $M = \rho 2\pi R \pi a^2$. The acceleration due to the hoop force is

$$\begin{aligned} \frac{F_{hoop}}{M} &= \frac{I_{tor}^2 \mu_0 (\ln(8R/a) - 1 + l_i/2)}{2\rho 2\pi R \pi a^2} = \frac{(2\pi B_{pol} a/\mu_0)^2 \mu_0 (\ln(8R/a) - 1 + l_i/2)}{4\pi^2 \rho R a^2} = \\ &= \frac{B_{pol}^2 (\ln(8R/a) - 1 + l_i/2)}{\rho \mu_0 R} \end{aligned} \tag{101}$$

Assuming $R/a \simeq 10$, $l_i \simeq 0.5$, $B_{pol} \simeq B \simeq 8 \times 10^{-4}\,\mathrm{T}$ (cf Table 1), $\rho \simeq m_i n \simeq 2 \times 10^{-11}\,\mathrm{kg\,/\,m^3}$, and $R \simeq 3 \times 10^7\,\mathrm{m}$, then $F_{hoop}/M \simeq 3 \times 10^3\,\mathrm{m\,/\,s^2}$. Compare this to the gravitational acceleration on the surface of the Sun, $g \approx 3 \times 10^2\,\mathrm{m\,/\,s^2}$. Consequently, the force of gravity is negligible compared to the hoop force. Gravity cannot "hold down" a prominence (except a prominence with a very weak toroidal current), but some other effect must be responsible for this. We have shown that the presence of a strapping field can inhibit prominence eruption.

Chapter 5 Dual prominence experiment

On the Sun, prominences form from the emergence of magnetic flux ropes from the solar photosphere [54]. Some ropes are already twisted, or helical, when they appear [85]. It has been suggested that prominence eruptions, coronal mass ejections, and flares occur not because of a gradual build-up of magnetic energy and helicity in a single magnetic structure, but rather because two or more existing structures merge and the resulting structure is unstable [25][86][87]. In order to study this phenomena, a new generation of solar devices was developed. Two devices of this generation were built - one that is essentially the same as the Mark II device, and another that has four electrodes, each with a gas injection point and its own toroidal magnetic field coil. The first device (Mark III) is intended for future use in tandem operation with the Mark II device, creating two prominences that expand and interact in various geometries. For example, by mounting the Mark II and the Mark III on two different walls of the vacuum chamber, the two prominences can expand in directions perpendicular to each other and then "collide."

This chapter will describe experiments with the four electrode device (Mark IV), which is capable of creating two prominences side by side. The chapter consists of three sections. First, equipment and diagnostics will be described. Second, experimental results will be presented. Third, the results will be discussed and interpreted. The most important result of this chapter is that interaction between two prominences can cause one or both prominences to erupt sooner and at a higher velocity than a single prominence would. This can happen with two side-by-side prominences with opposite sign helicity (counter-helicity) via the destruction of toroidal magnetic flux, or with two side-by-side prominences

with same sign helicity (co-helicity) due to helicity transfer from one prominence to the other. Other important results include:

- Camera images show a bright region between two counter-helicity prominences. We suggest that this region is a reconnection layer in the form of a current sheet.
- X-ray emissions in a counter-helicity case can be more than an order of magnitude larger than in a similar co-helicity case or for a single prominence.
- A topology with more pronounced S-shapes is explained using the mathematical model of Chapter 3.

5.1 Equipment and diagnostics

5.1.1 Mark IV solar device

The Mark IV device has a double set of electrodes, horseshoe magnets with coils, etc., compared to the Mark II device. The electrodes are no longer D-shaped, but instead each forms one quarter of a circle with a radius of 127 mm. Gas is still injected through the centers of the toroidal magnetic field coils, with the gas injection points equally spaced, one on each electrode, so that they form the corners of a square with a side of 81 mm.

To take additional advantage of the square symmetry, the high voltage connectors between the solar device and the low inductance coaxial cables were redesigned. The new connectors were designed to be much more easily removed from and reattached to the device, while staying permanently mounted to the coaxial cables. On the device, the connectors mate to aluminium blocks that are clamped onto brass tubes welded to the electrodes. The aluminium blocks can be rotated by 90° (with the coaxial cables and connectors tem-

porarily removed). This means that the camera view (typically from vacuum port #1; cf Figure 4) is effectively rotated by 90°. Earlier, such a rotation would include the entire device, requiring its temporary removal from the vacuum chamber. To facilitate the change from a 0°-orientation to a 90°-orientation even further, ball valves were installed on each of the four gas injection tubes of the Mark IV device. These valves make it possible to switch between the 0°-orientation and the 90°-orientation without taking the vacuum chamber to atmospheric pressure.

Minor improvements of the Mark IV device included the removal of gas injection points at the center of the device, as this scheme of gas injection was of little value when operating the Mark II device (and the central gas feeds were awkwardly located when handling the device). Further, the diameter of the brass tubes (welded to the electrodes and part of the low inductance circuit) was somewhat reduced, to make it easier to insert insulating layers of Kapton between the tubes and the ceramic breaks.

The gas valve and the capacitor banks used for the Mark IV device were the same as for the Mark II. The high speed gas valve is pulsed by a 400 μF capacitor bank charged to a voltage V_{valve} between 0-700 V. A 59 μF capacitor can provide a voltage difference V_I of up to 12 kV to break down the gas between each pair of electrodes. Once plasma has formed, this capacitor will drive toroidal current I_{tor} through the plasma. We will refer to this capacitor as the main capacitor. Two electrolytic capacitor banks (9.6 mF and 9.9 mF) create the toroidal bias magnetic fields B_{tor} for the two prominences. One bank drives current through the two electromagnet coils on the high voltage side (i.e., the coils that are initially at the electrostatic potential V_I), the other bank the two ground side coils. (Consequently, each bank contributes to the toroidal magnetic fields of both prominences.)

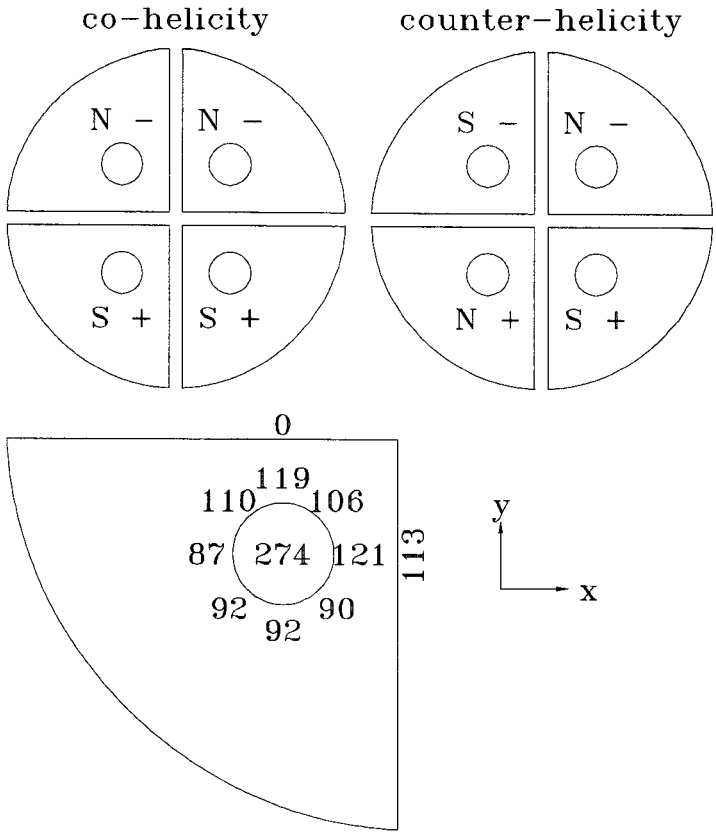

Figure 40: Top view of Mark IV electrodes. In the upper left, a co-helicity configuration is shown. In the upper right, a counter-helicity configuration. '+' indicates anodes, '-' cathodes, 'N' magnetic north poles, and 'S' magnetic south poles. In the bottom left, typical bias magnetic field strengths (z-component of B_{tor}) are shown at various locations on an electrode (bottom left electrode of co-helicity configuration) for a nominal charging voltage $V_B = 200\,\mathrm{V}$ on the bias field capacitor banks.

By swapping coil leads, the Mark IV device can be operated in either a co-helicity or a counter-helicity configuration (cf Figure 40). In co-helicity, both prominences are either right-handed or left-handed. In counter-helicity, one prominence is right-handed and the other is left-handed. Each capacitor bank (and its fast charging unit) were powered through a DEL Electronics transformer that provides up to 20 kV isolation between primary and secondary.

The toroidal magnetic fields B_{tor} were carefully mapped in the volume above the Mark IV device. Triggering the bias field capacitor banks at $V_B = 200\,\mathrm{V}$ produced a

toroidal magnetic field (z-component) $B_z = 281 \pm 13\,\mathrm{mT}$ at the gas injection points, 2 mm above the electrode surfaces, as measured by a Hall probe (calibrated to $250\,\mathrm{V}\,/\,\mathrm{T}$). The error indicates variation from electrode to electrode. The field (z-component) dropped to $\approx 100\,\mathrm{mT}$ at a distance 24 mm from the gas injection points. The magnetic field strength at some locations on a representative electrode are given in Figure 40.

5.1.2 Timing sequencer

A timing sequencer with twelve fiber-optic trigger outputs, and one trigger input, was used to trigger all capacitor banks and diagnostics. (Fiber-optic triggering is desirable as it eliminates ground loops.) The timing sequencer was located in a slot in a CAMAC crate and was controlled remotely by a personal computer (200 MHz Pentium). Each trigger output can be set to trigger between 20 ns and $2^{64} \times 20\,\mathrm{ns} \approx 172\,\mathrm{s}$ after the trigger input.

5.1.3 Vacuum chamber

The solar device was mounted on a 254 mm (10 in) port (port #17; cf Figure 4) of the large vacuum chamber described in Chapter 2. The chamber was pumped down to $2.5 \times 10^{-5}\,\mathrm{Pa}$ (1.9×10^{-7} torr) before operation of the solar device.

5.1.4 High voltage probe and Rogowski coil

The high voltage probe and Rogowski coil were the same as for the Mark II (cf 4.1.5 and 4.1.6). The signals from these diagnostics were transmitted via an analog fiber-optic link to 10 MHz Aeon digitizers in a CAMAC crate. The voltage and current profiles of each discharge were uploaded and stored on a personal computer (120 MHz Pentium).

5.1.5 Cameras

Two gated, intensified, charge-coupled-device (CCD) Princeton Instruments cameras model ICCD-576-G/RB-E were set up to take pictures of the plasma. Princeton Instruments detec-

tor controllers model ST-1388 handles electronic "cleaning" of the CCDs and image transfer from the cameras to personal computers (120 MHz and 200 MHz Pentiums). Gating pulses are generated outside the cameras by two Berkeley Nucleonics pulser units model 310H. Camera images are 576 by 384 pixels in 65536 grayscales (16 bits).

In addition to these still image cameras, two high speed framing cameras, one from Cooke and one from Hadland, were temporarily obtained (at different times) for demonstration purposes. The Cooke camera could take eight images of a plasma discharge. The minimum time between images was 2 ns, with the additional restriction that the minimum time between images #1 and #5 was 500 ns. The Hadland camera was similar to the Cooke camera but could take sixteen images of each plasma discharge.

The Princeton Instruments cameras were typically operated at a gain setting of 50 (on a scale from 0-1000), with 10 ns shutter speeds, and using zoom lenses set to 28 mm focal lengths and f-number 4. The cameras were triggered by -850 V pulses from the two Berkeley Nucleonics units. The Cooke camera was operated with 20 ns shutter speed and used a 28-105 mm telephoto zoom lens set to f-number 4. The Hadland camera was operated with 20 ns shutter speed with a variety of fixed focal length lenses set to f-number 2.

5.1.6 X-ray probe

A probe to measure x-ray radiation (designed by P.M. Bellan) was constructed around three International Radiation Detectors diodes. These diodes are sensitive to electromagnetic radiation from visible light to x-rays. Their quantum efficiency increases with increasing photon energies, and is approximately 10%/ eV, e.g., an incoming photon with an energy of 10 eV will produce one electron that can be detected by an external circuit connected to

the diode. To limit the sensitivity to a certain spectral range, diodes can be covered with thin metal foils. For our x-ray probe we used one diode without any foil (model AXUV-HS5), one diode with a 150 nm aluminium foil (model AXUV-HS5Al) making the diode sensitive only to ultraviolet radiation in the wavelength range 20-80 nm (equivalent to photon energies of 15-62 eV), and one diode with a 190 nm titanium foil (model AXUV-HS5Ti) passable only by x-rays with wavelengths < 15 nm (> 83 eV). (The terms ultraviolet light and x-rays are often interchangeable, particularly when speaking of "hard" UV or "soft" x-rays. In this chapter we will use the term UV to indicate a wavelength range of 20-80 nm and x-rays to indicate wavelengths < 15 nm.)

The x-ray probe was designed so that the diodes were located 1 cm behind a grid of nickel wires with a 127 μm spacing (or 200 wires per linear inch). Provisions were made to apply a bias voltage to this grid to repel high-energy ions. Furthermore, a set of neodymium-alloy permanent magnets were placed 2 cm in front of the grid to deflect both ions and electrons. The magnetic field strength in the spacing between magnets was ≥ 0.4 T, corresponding to an ion cyclotron radius of ~ 4 mm for an ion with a kinetic energy of 100 eV (and an even smaller radius for an electron of equal energy). The diodes, bias grid and magnets were enclosed in a metal probe head that allows photon entry to the diodes only through narrow channels passing the magnets and the bias grid. The diodes were connected to a private ground, electrically insulated from the probe head. A reverse bias voltage of 31.3 V was applied to the diodes to improve response times.

The probe was located at the 69.9 mm port marked 'c' in Figure 4. The diode outputs were AC-coupled to 10 MHz Aeon digitizers in a CAMAC crate. X-ray traces were uploaded and stored on a personal computer (200 MHz Pentium).

5.1.7 Triple probe

When a probe, electrically insulated except for a metal tip, is inserted into a plasma, it will collect ions and electrons depending on the difference in electric potential between the probe tip and the plasma. If the probe tip is at a potential V and the space potential of the plasma is V_s, then the total collected current is [88]

$$I = \begin{cases} -I_- e^{\frac{q_e(V-V_s)}{k_B T_e}} + I_+, & V < V_s \\ -I_-, & V > V_s \end{cases} \tag{102}$$

where q_e is the electron charge, k_B is Boltzmann's constant, T_e is the electron temperature. The electron and ion saturation currents are given by

$$I_- = \frac{1}{4} q_e n A_- \sqrt{\frac{8 k_B T_e}{\pi m_e}} \tag{103}$$

$$I_+ = e^{-\frac{1}{2}} A_+ q_e n \sqrt{\frac{T_e + T_i}{m_i}} \tag{104}$$

respectively, where n is the ion and electron number density, T_i is the ion temperature, m_e and m_i are the electron and ion masses, respectively, and A_- and A_+ are the electron and ion collection areas, respectively.

One method to extract information about plasma temperature and density is to insert a Langmuir probe into the plasma. By scanning the voltage on the probe tip and measuring the collected current, one can determine plasma temperature and density. The disadvantage of this method is the required time to scan the voltage. A triple probe with three probe tips can be used to overcome this time requirement. The first tip floats (i.e., collects no current) with respect to the plasma. A battery provides a constant voltage difference between the second and third tips. Designating the tip potentials with respect to V_s as V_1, V_2, and V_3,

respectively, then from Equation (102) we get the three equations

$$0 = -I_{-}e^{\frac{q_e V_1}{k_B T_e}} + I_{+} \tag{105}$$

$$-I = -I_{-}e^{\frac{q_e V_2}{k_B T_e}} + I_{+} \tag{106}$$

$$I = -I_{-}e^{\frac{q_e V_3}{k_B T_e}} + I_{+} \tag{107}$$

where I is the current collected by the third tip. Solve this system of equations for the electron temperature:

$$\frac{1}{2} = \frac{1 - e^{\frac{q_e(V_1 - V_2)}{k_B T_e}}}{1 - e^{-\frac{q_e V_{battery}}{k_B T_e}}} \tag{108}$$

where $V_{battery} = V_2 - V_3$, and for the ion saturation current:

$$I_{+} = I\frac{e^{\frac{q_e(V_1 - V_2)}{k_B T_e}}}{1 - e^{\frac{q_e(V_1 - V_2)}{k_B T_e}}}. \tag{109}$$

The voltage difference $V_1 - V_2$ can be measured, as can the current I, and so T_e can obtained implicitly from Equation (108), and then the ion saturation current from Equation (109). For $k_B T_e < q_e V_{battery}/2$ the electron temperature can be more readily obtained, as it is approximately a linear function of $V_1 - V_2$, namely

$$T_e \simeq \frac{q_e}{k_B}\frac{V_2 - V_1}{\ln 2} \tag{110}$$

Finally, the number density can calculated from Equation (104) using the known ion saturation current and some assumption regarding the ion temperature. In our case we use $T_i = T_e$. It seems it should also be possible to calculate the number density from Equation (103), and in this case without making assumptions regarding the ion temperature. In practice this does not work, except for situations involving very weak magnetic fields, as the electron collection area is unknown due to the small electron Larmor radius (much smaller than the typical length scale of the probe).

We mounted a triple probe (built by S. Hsu) at the 69.9 mm port marked 'b' in Figure 4, a distance 424 mm above the electrode surfaces of the solar device. The probe could be translated in and out through the port, i.e., translated in the plane $z = 424\,\mathrm{mm}$ at an angle $\phi_{probe} = 22.5°$ with respect to the x-axis, such that $x_{probe} = s_{probe}\cos\phi_{probe}$ and $y_{probe} = -s_{probe}\sin\phi_{probe}$, where s_{probe} is the translation distance of the probe from the symmetry axis of the vacuum chamber. The probe tip areas were $A_+ = 2.89\,\mathrm{mm}^2$, and a battery bias of $V_{battery} = 48\,\mathrm{V}$ was applied between the second and third tips. The probe outputs were read by 10 MHz Aeon digitizers in a CAMAC crate, as indicated in the probe electric circuit schematic in Figure 41. Time profiles of electron temperature T_e, ion saturation current I_+, and floating voltage V_1 were uploaded and stored on a personal computer (200 MHz Pentium).

5.2 Results

5.2.1 Establishing nominal operating parameters

The nominal operating parameters for the Mark IV device were simply carried over from its predecessor, the Mark II, with the exception of the charging voltage V_I on the main capacitor. As the Mark IV has four toroidal magnetic field coils, compared to the two of the Mark II, each bias field capacitor bank now operates two coils. To preserve the nominal operating ratio between toroidal magnetic field and peak toroidal current, either the bias field capacitor charging voltage V_B must be doubled, or the charging voltage V_I must be halved. Since doubling V_B from 200 V to 400 V would significantly increase charging time, as well as put unnecessary stress on the coils, it was decided to lower V_I from 6.00 kV to 3.00 kV. These settings worked with no need for further modifications. The settings are summarized in Table 7 along with the trigger times for each piece of equipment.

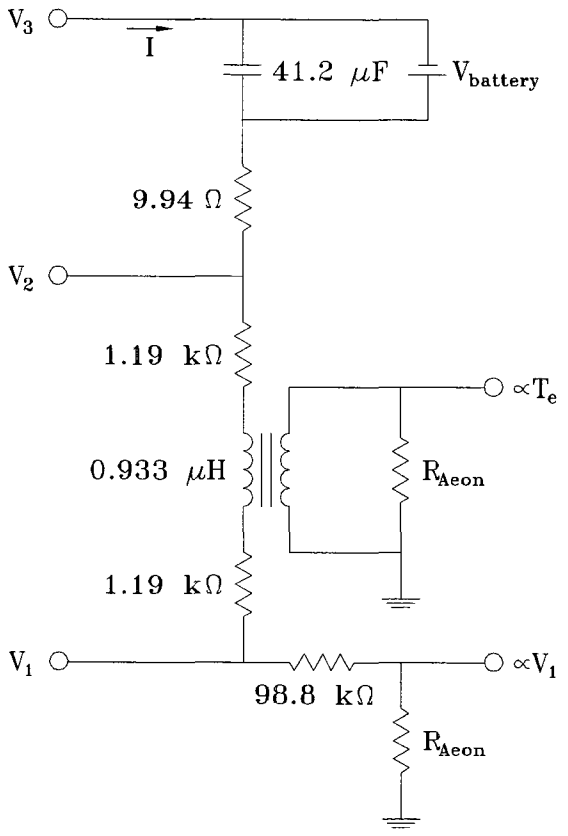

Figure 41: Electric circuit schematic of triple probe. The three probe tips are at voltages V_1, V_2, and V_3. The floating potential V_1 is output to an Aeon digitizer through a voltage divider (the input impedance of the digitizer is $R_{Aeon} = 1\,\mathrm{k}\Omega$). The voltage $V_2 - V_1$, proportional to the electron temperature T_e, is output to a digitizer via a transformer. The current I drawn by the third probe tip is measured by a Rogowski coil (located at arrow) and output to a third digitizer.

Equipment	bias field capacitors	gas valve capacitor	camera: stop clean	Aeon digitizers main capacitor	cameras
Operating parameters	$V_B = 200\,\mathrm{V}$	$V_{valve} = 550\,\mathrm{V}$ $p_{valve} =$ $= 7.9 \times 10^5\,\mathrm{Pa}$ (H_2)		$V_I = 3.00\,\mathrm{kV}$	
Time [ms]	$t_B = -5.6\,\mathrm{ms}$	$t_{valve} = -2.6\,\mathrm{ms}$	$t = -600\,\mu\mathrm{s}$	$t_I \equiv 0$	$t = 0.1$-$30.0\,\mu\mathrm{s}$

Table 7: Nominal operating parameters for the dual prominence experiment (Mark IV device) and trigger times for each piece of equipment.

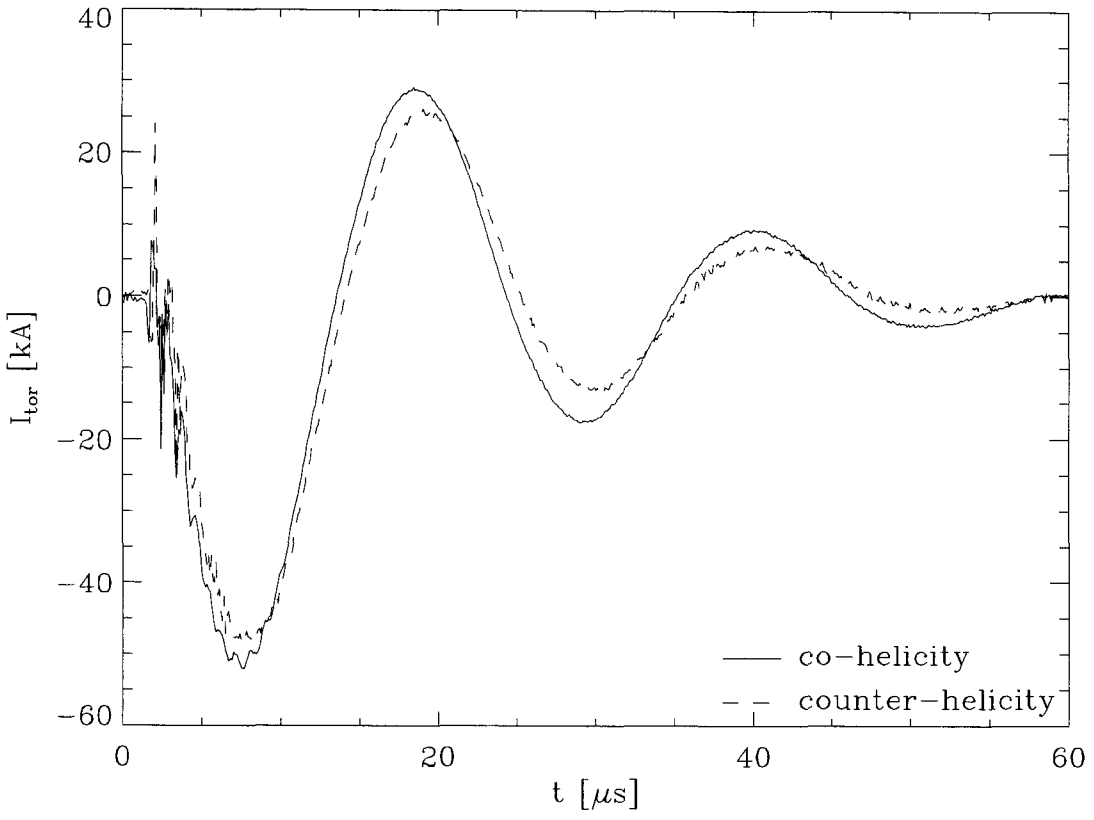

Figure 42: Toroidal current I_{tor} for co- and counter-helicity configurations as a function of time (obtained by averaging the traces from several (>100) discharges).

5.2.2 Current and voltage profiles

The current and voltage profiles for the Mark IV were similar to those of the Mark I and II. In the co-helicity configuration, the peak current was $I_{tor} \simeq 52\,\mathrm{kA}$ at $t \simeq 7.5\,\mu\mathrm{s}$ (using nominal settings). Subsequent current peaks (maxima or minima) occurred at $t \simeq 18\,\mu\mathrm{s}$, $29\,\mu\mathrm{s}$, $40\,\mu\mathrm{s}$ and $51\,\mu\mathrm{s}$ (cf Figure 42). In the counter-helicity configuration, the peak current was $I_{tor} \simeq 48\,\mathrm{kA}$ at $t \simeq 8.0\,\mu\mathrm{s}$ (using nominal settings). Subsequent current peaks (maxima or minima) occurred at $t \simeq 19\,\mu\mathrm{s}$, $30\,\mu\mathrm{s}$, and $41\,\mu\mathrm{s}$.

The voltage profile behaved differently in the counter-helicity case as compared to either the co-helicity case or the Mark I and II. When the voltage first reached $0\,\mathrm{V}$, it

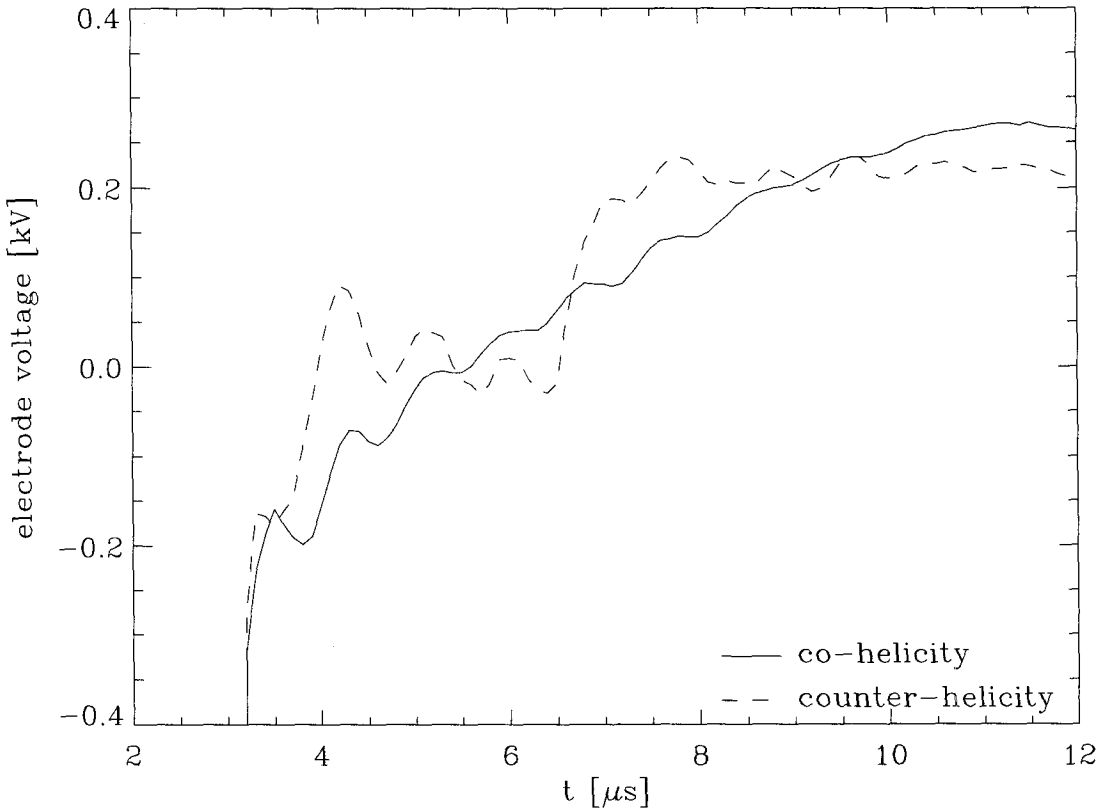

Figure 43: Electrode voltages for co- and counter-helicity configurations as a function of time. Note how the voltage temporarily remains at 0 V for the counter-helicity case (disregarding the superimposed high-frequency oscillations). These voltage traces were obtained by averaging the traces from several (>100) discharges.

temporarily plateaued at this level before continuing its oscillation. Figure 43 compares the co-helicity and counter-helicity voltage traces.

For both co- and counter-helicity, a small amplitude fast oscillation was superimposed on the voltage traces. The frequency of this oscillation was $\simeq$ 1 MHz, and the oscillation was damped out in $\lesssim 10\,\mu$s. This oscillation remained even when averaging over several (>100) discharges. This signal was initially suspected to be an artifact of oscillations on the ignitron trigger circuits, but the oscillation was not found there (on either the primary or the secondary; cf 2.2.2).

5.2.3 Images

The most important result of this chapter, that two interacting prominences can erupt sooner and with higher velocity than a single prominence, is based on camera images presented here. Just as for the Mark I and II, the reproducibility allowed for easy construction of temporal image sequences and pseudo-movies of the plasma evolution. Figures 44-49 shows the plasma evolution for the co- and counter-helicity cases from perpendicular, parallel, and top views.

From all viewing angles in the co-helicity case, it is evident that one prominence expands faster than the other. This is an important observation of a phenomena that could occur on the Sun. Which prominence expands faster depends on whether the prominences are both right-handed or both left-handed. In the top view, with the cathode oriented above the anode, the prominence to the right expands faster when both prominences are right-handed, while the prominence on the left expands faster when both prominences are left-handed. From the perpendicular and top views in the co-helicity case, it appears that the leading parts of the two prominences merge, at least at the resolution scale of the cameras. This merging is less apparent in the parallel view.

From all viewing angles in the counter-helicity case, a bright region is observable between the two prominences. The bright region appears at $t \simeq 5\ \mu$s. From the perpendicular view the bright region appears as a circular arc, approximately one quarter to one third of a full circle. The radius of this arc is larger than the major radius of each prominence (i.e., larger than the radius of a fictitious toroidal envelope enclosing a prominence). The arc endpoints do not appear to touch any of the electrodes or any part of the prominence plasmas. From the parallel view the bright region also appears as a roughly circular arc, albeit

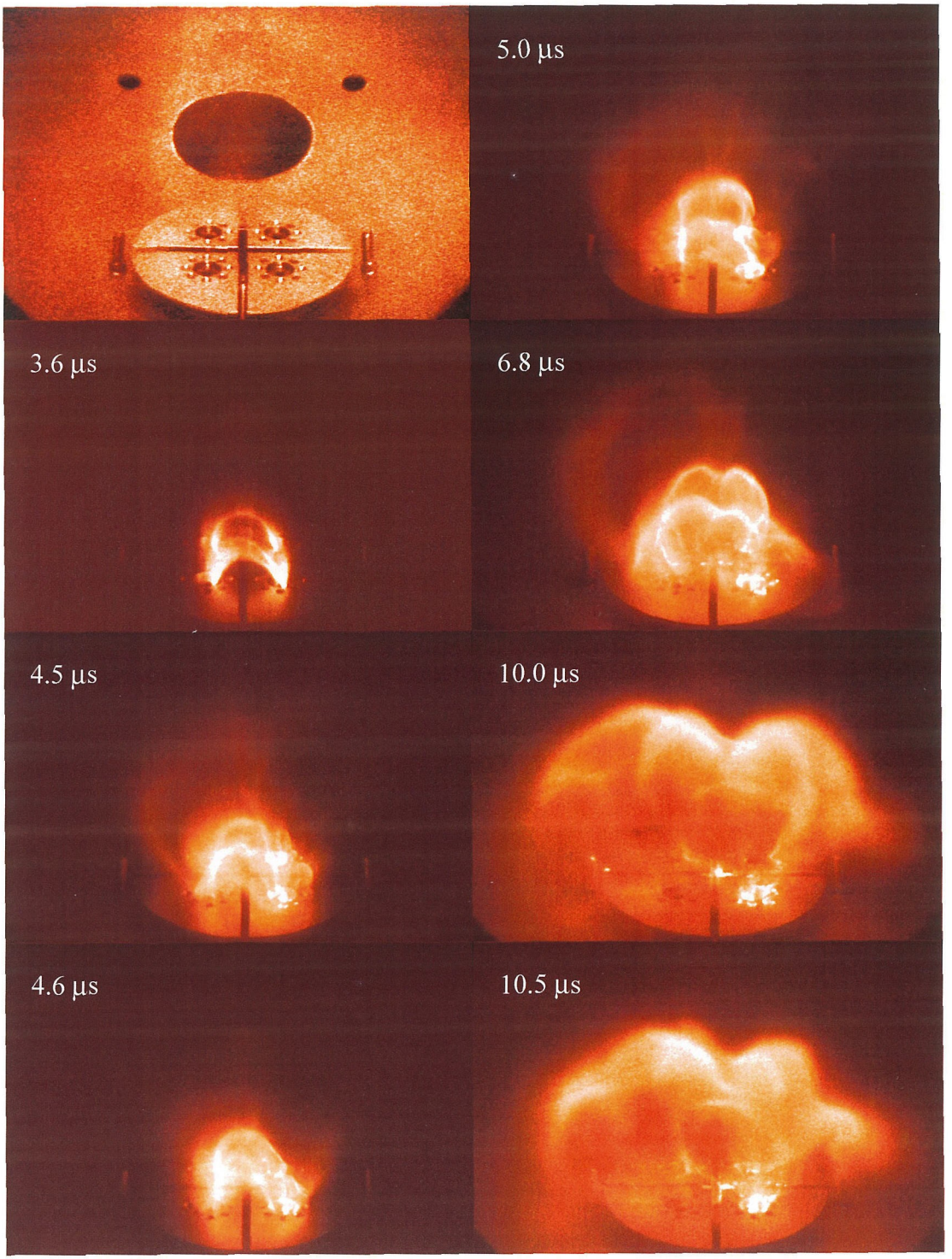

Figure 44: Co-helicity plasma evolution (perpendicular view).

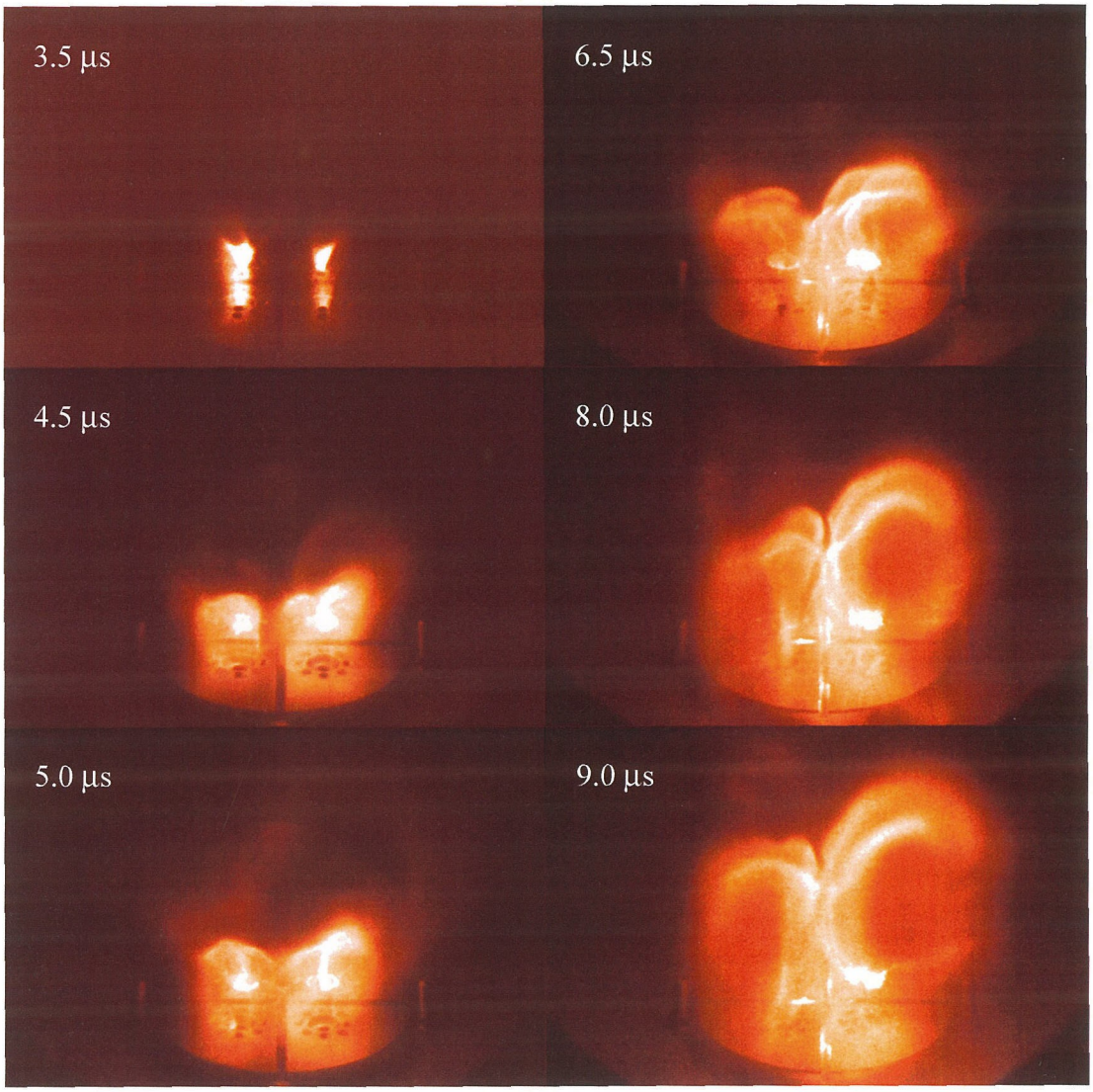

Figure 45: Co-helicity plasma evolution (parallel view).

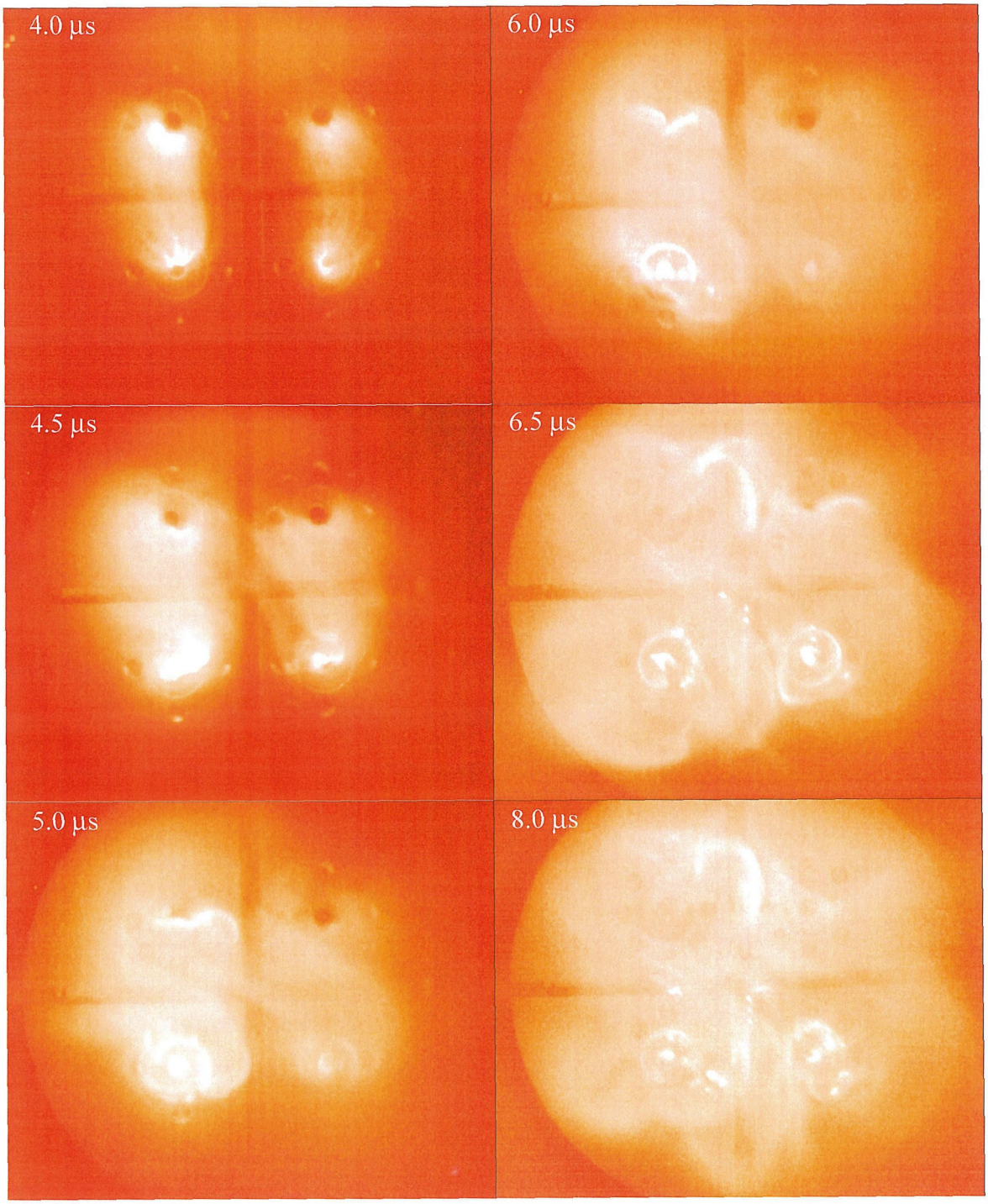

Figure 46: Co-helicity plasma evolution (top view).

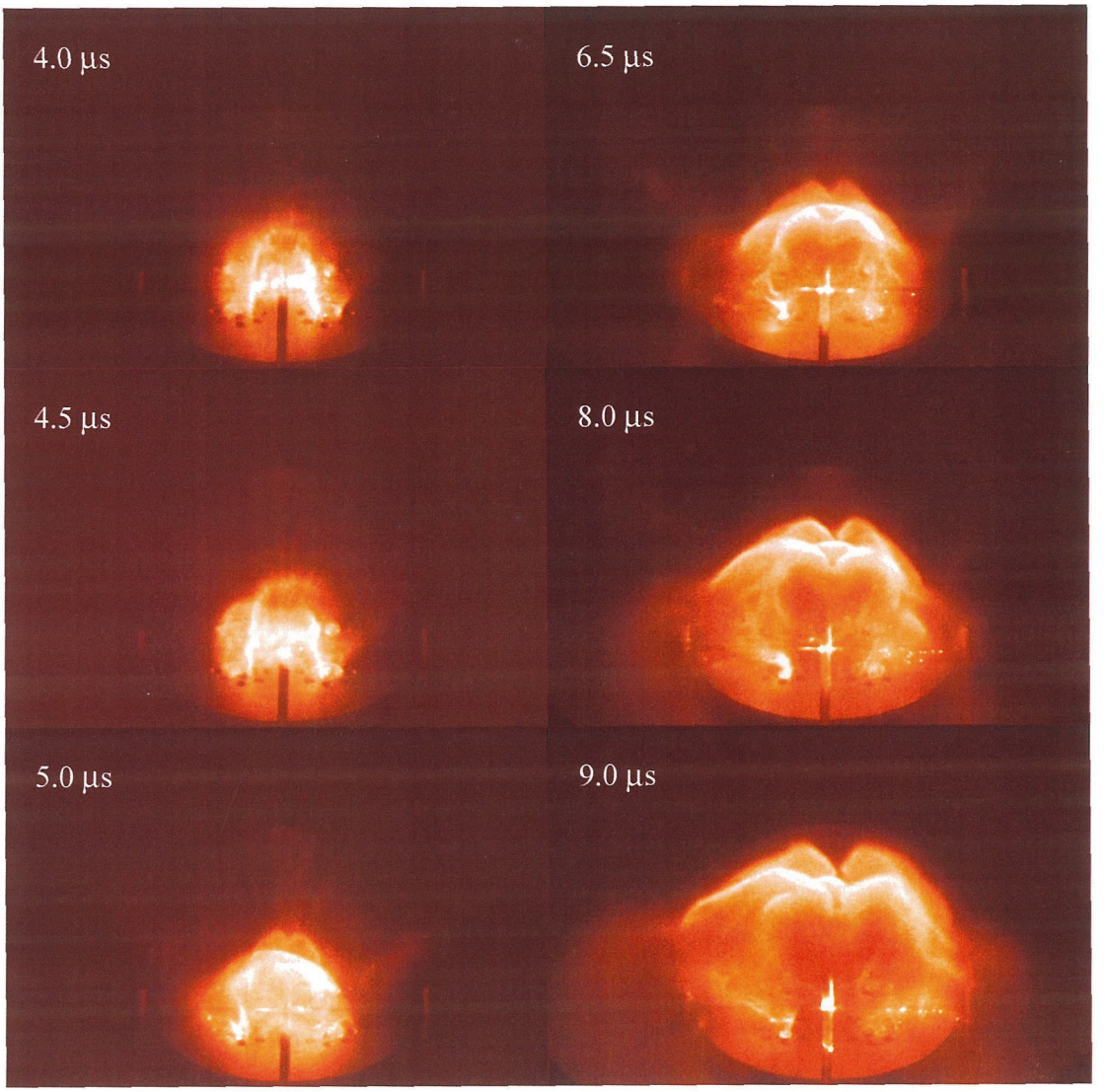

Figure 47: Counter-helicity plasma evolution (perpendicular view).

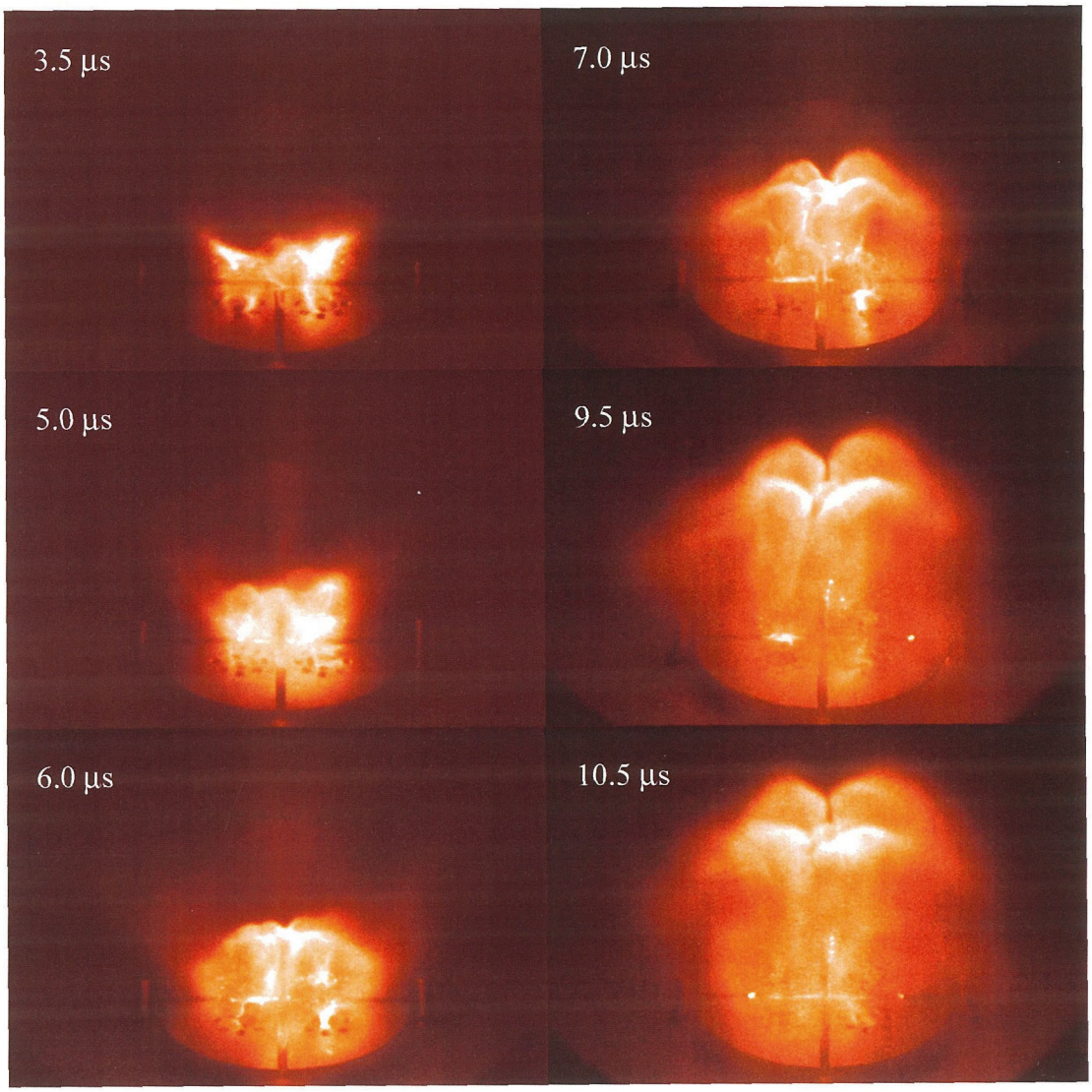

Figure 48: Counter-helicity plasma evolution (parallel view).

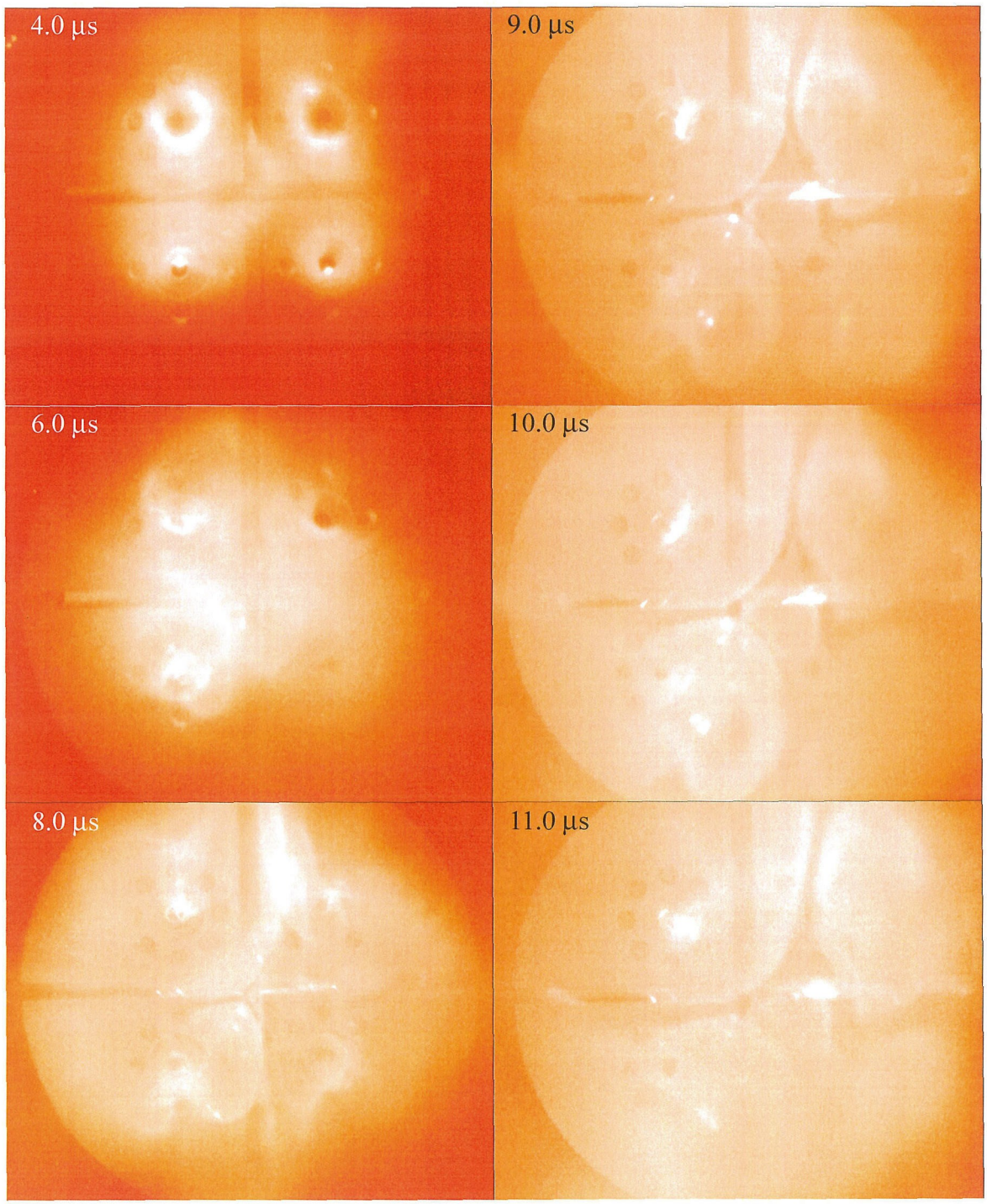

Figure 49: Counter-helicity plasma evolution (top view).

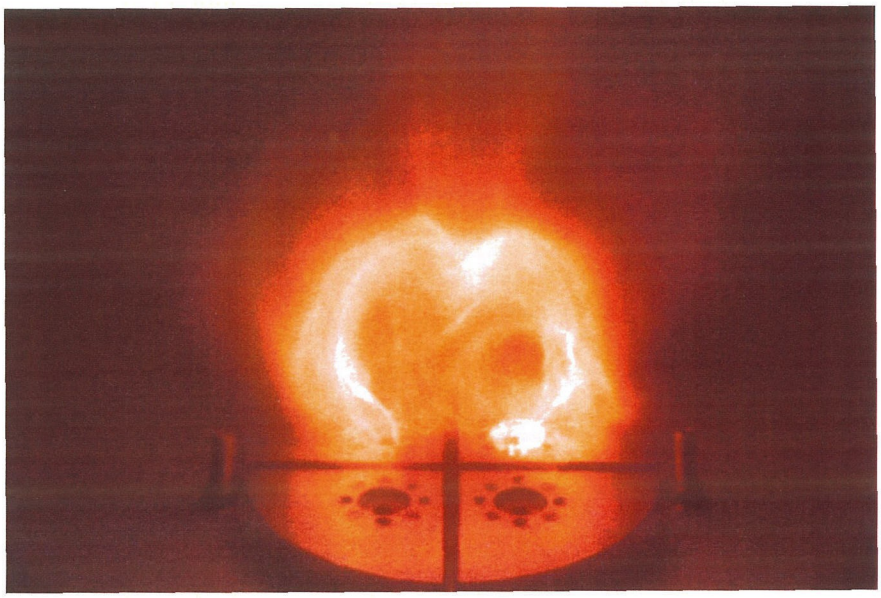

Figure 50: A single prominence (instead of two) is created by the Mark IV device by injecting gas through only one pair of electrodes.

with a much smaller radius, maybe a fourth or less of a prominence minor radius. From the top view the two prominences align such that the central cusp-like feature of each region points away from the neighboring prominence. The bright region almost fills the space between the cusps, leaving only a small gap between itself and each prominence. Also, note the unusually helical shape of the counter-helicity plasmas ($N \geq 12$ for times $t \gtrsim 9\,\mu$s). This important feature will be discussed below.

5.2.4 Selective gas injection

As a secondary benefit of installing the ball valves on the four gas feeds, gas can now be selectively injected through only some, instead of all, of the four electrodes. For example, one possible way to operate the Mark IV device is to valve off the gas for one prominence, not allowing any gas injection through either of its footpoints. The result is that only a single prominence forms, and in effect the Mark IV operates as the earlier Mark II (cf Figure 50). This demonstrates how the location of prominence footpoints in an experiment

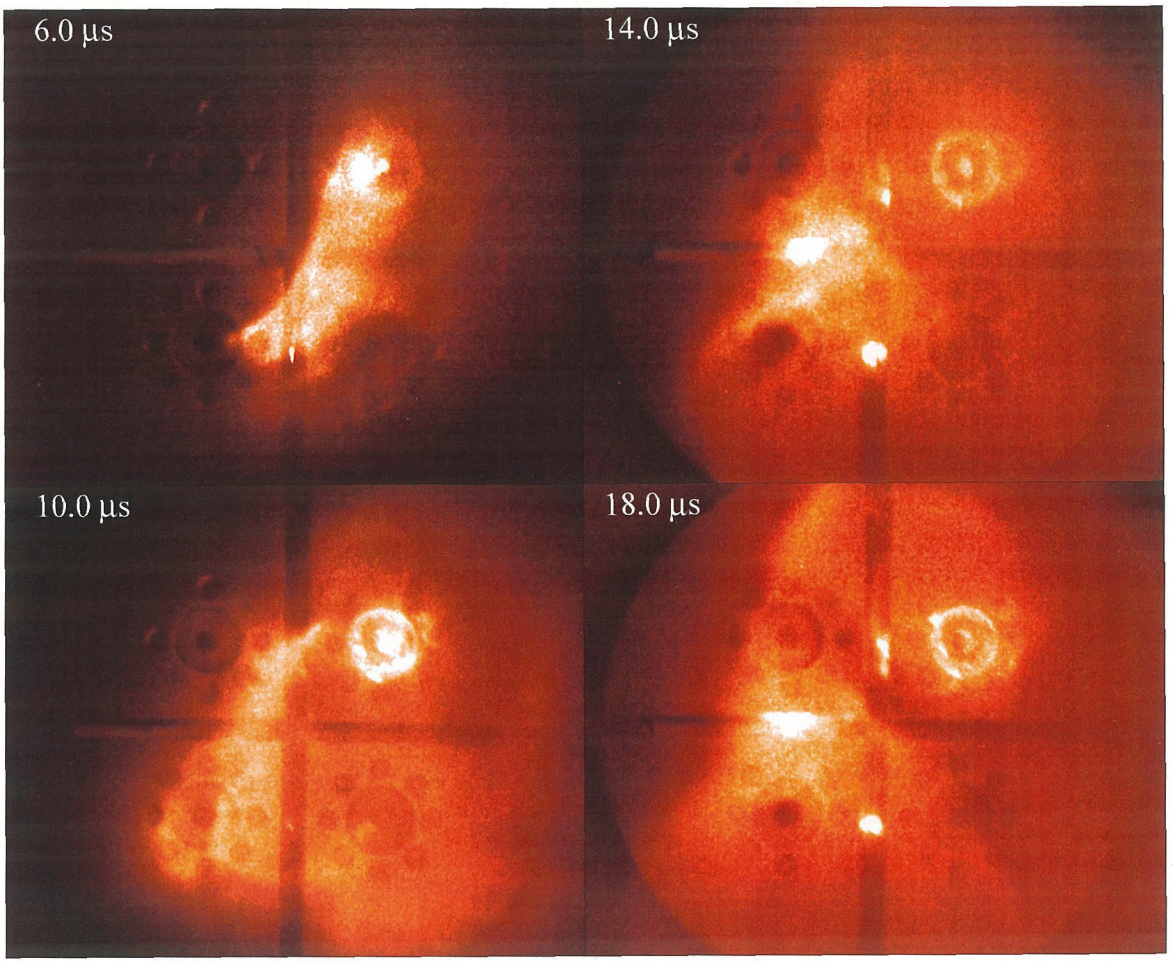

Figure 51: Plasma evolution when injecting gas through two diagonally opposite electrodes of Mark IV device (top view). Note S-shape.

can be controlled by the positioning of gas injection points.

Operation of the Mark IV is also possible when injecting gas through only two diagonally opposite electrodes. By injecting gas only through the electrodes along $\phi = 3\pi/4$ and $7\pi/4$ (cf Figure 16), while pulsing the bias field coils as we would for the co-helicity dual prominence case, the characteristic S-shape develops much further before the prominence assumes its typical $N = 4$ helical shape. Top view images in this configuration are shown in Figure 51. This observation will be discussed below, as it can explain conditions surrounding S-shapes on the Sun. Injecting gas only through the other two diagonally op-

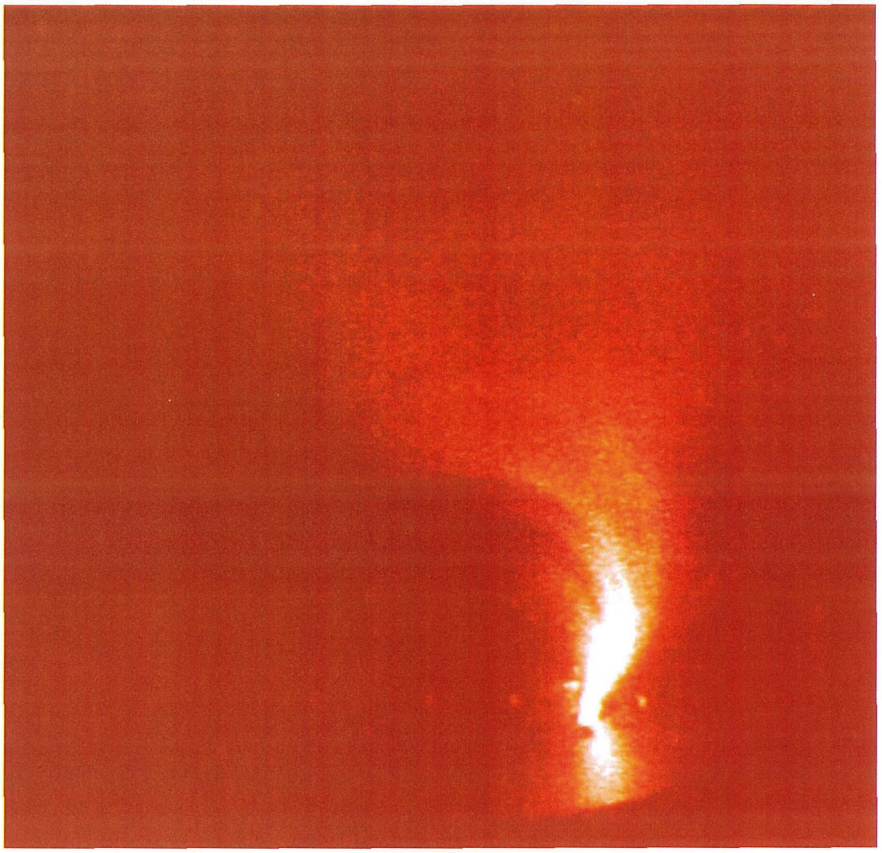

Figure 52: Streamer extending from cathode, curving left toward the anode.

posite electrodes ($\phi = \pi/4$ and $5\pi/4$) results in a plasma that is helical upon formation and rapidly twists up even more.

Another combination of open and closed ball valves injects gas through either the anodes or the cathodes, but not both. Breakdown was not achieved when injecting gas through only the anodes. Operation with gas injected through a single or both cathodes produced plasma striation and streamers. As the gas flow to the anodes was cut, breakdown would no longer occur on a sub-microsecond time scale. Rather, a streamer would extend further and further from the cathode, along the vacuum magnetic field lines (cf Figure 52). Only several microseconds later would the streamer touch the anode, thus completing the electrical circuit and allowing the prominence to evolve relatively normally from this time

Main capacitor voltage V_I [kV]	Single prominence radiation [mV]	Co-helicity radiation [mV]	Counter-helicity radiation [mV]
3.00	41 ± 12	33 ± 8	60 ± 25
4.00	111 ± 65	54 ± 17	235 ± 55
5.00	143 ± 75	93 ± 13	1130 ± 377
6.00	274 ± 170	129 ± 15	3247 ± 1406

Table 8: Radiation measured by the diode without foil for two prominences, in either co- or counter-helicity configuration, as well as for single prominences, as a function of charging voltage on the main capacitor. Radiation listed is peak emission at the first maximum.

on. Furthermore, wave-like patterns were present in camera images. These waves would form either along the streamer (cf Figure 53), or as circular waves around the cathode gas injection point (cf Figure 54), or both. Using the Cooke and Hadland high-speed framing cameras, the wavelength was determined to be $\simeq$ 1-3 cm, and the frequency $\simeq$ 1 MHz. The wavelength increased with increasing distance from the cathode, as indicated in Figure 55.

Rarely, wavelike patterns appear in images of discharges with normal gas injection. Figure 56 is an example.

5.2.5 X-ray emissions

Typical signals from the three diodes of the x-ray probe are shown in Figures 57-58. The main capacitor charging voltage was $V_I = 5.00\,\mathrm{kV}$ in these particular examples. Figure 57 shows the signals in a co-helicity case, Figure 58 in a counter-helicity case. The signal peaks around $t \simeq 7.5\,\mu\mathrm{s}$ in both cases. In general, co-helicity discharges would often show additional peaks around $18\,\mu\mathrm{s}$, $29\,\mu\mathrm{s}$ and $40\,\mu\mathrm{s}$. The second peak would occasionally be as large as the first. In the counter-helicity case, the second peak around $18\,\mu\mathrm{s}$ would sometimes be seen, but would be much weaker than the first peak.

The information of several discharges was quantized by looking at the peak value of the first emission maximum (around $t = 7.5\,\mu\mathrm{s}$). The radiation detected by the uncoated diode in the x-ray probe is summarized in Table 8. The errors are standard deviations from

Figure 53: Wave-like pattern along a streamer.

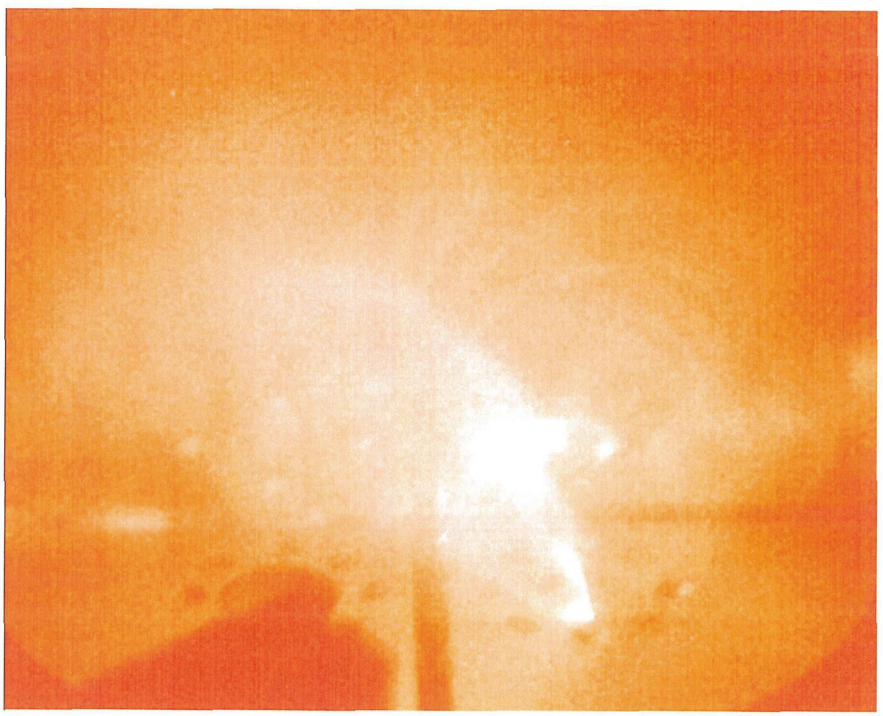

Figure 54: Circular wave-like pattern centered around the cathode gas injection point and magnetic pole.

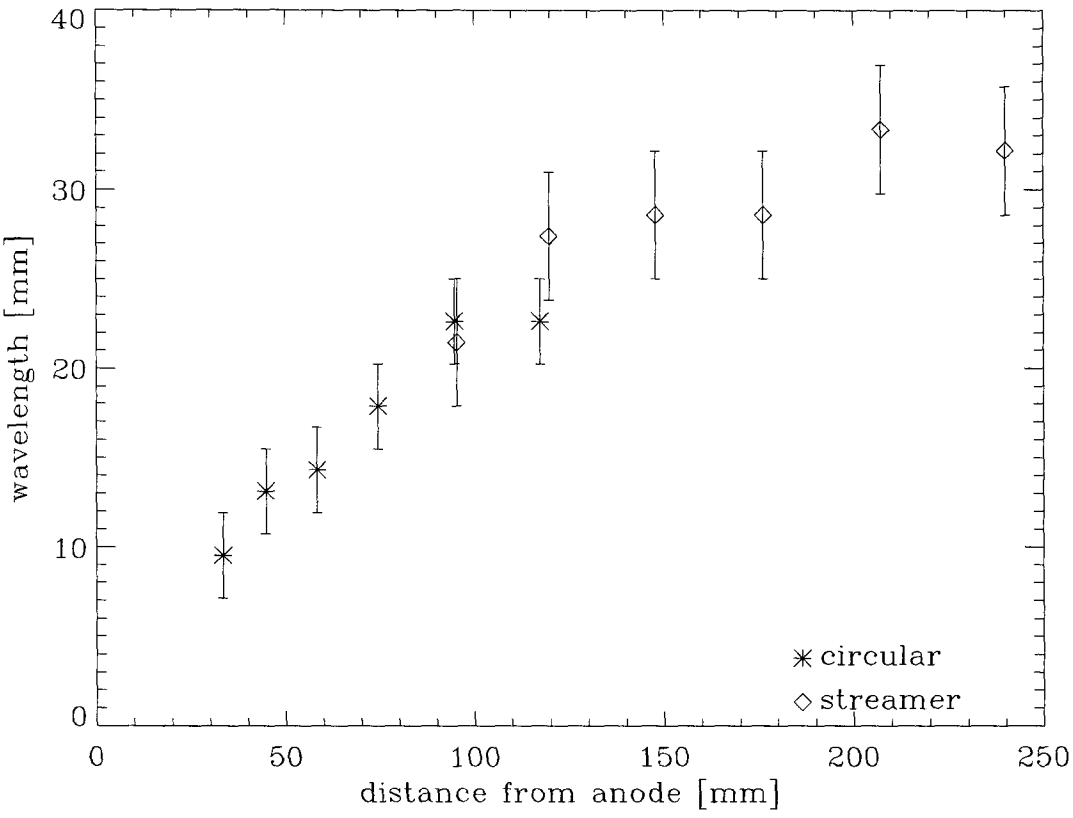

Figure 55: Wavelength of circular waves (centered around the cathode gas injection point and magnetic pole) and waves along streamers, as a function of the distance from the anode to the wave.

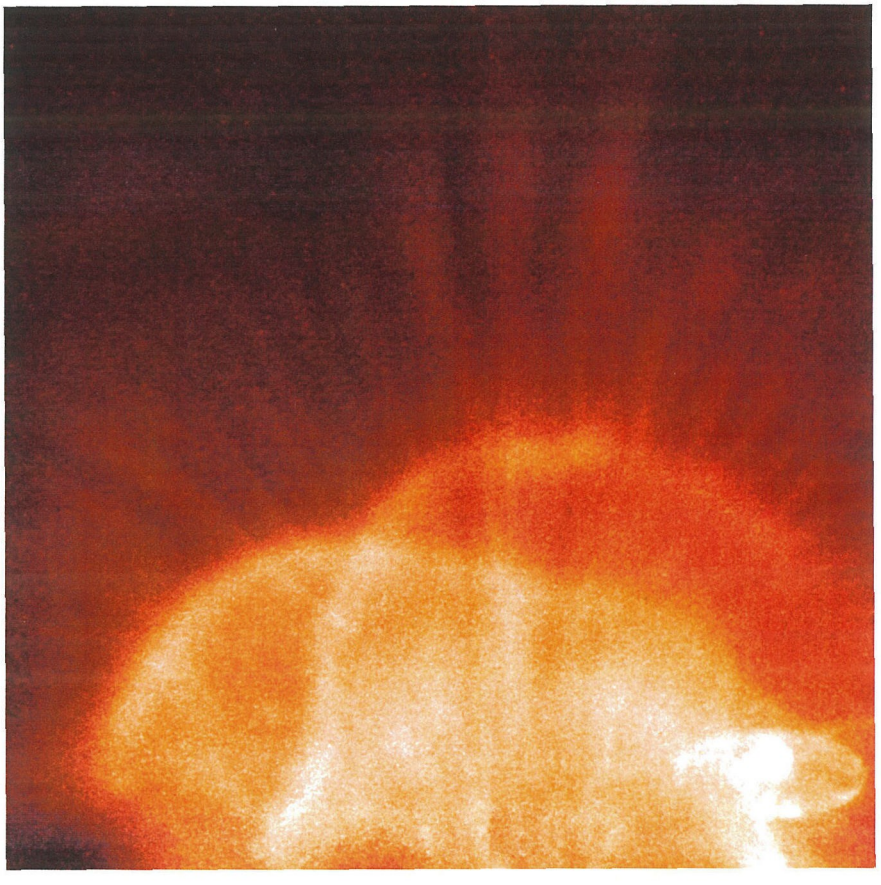

Figure 56: Wave-like pattern appearing in Mark IV discharge with regular gas injection.

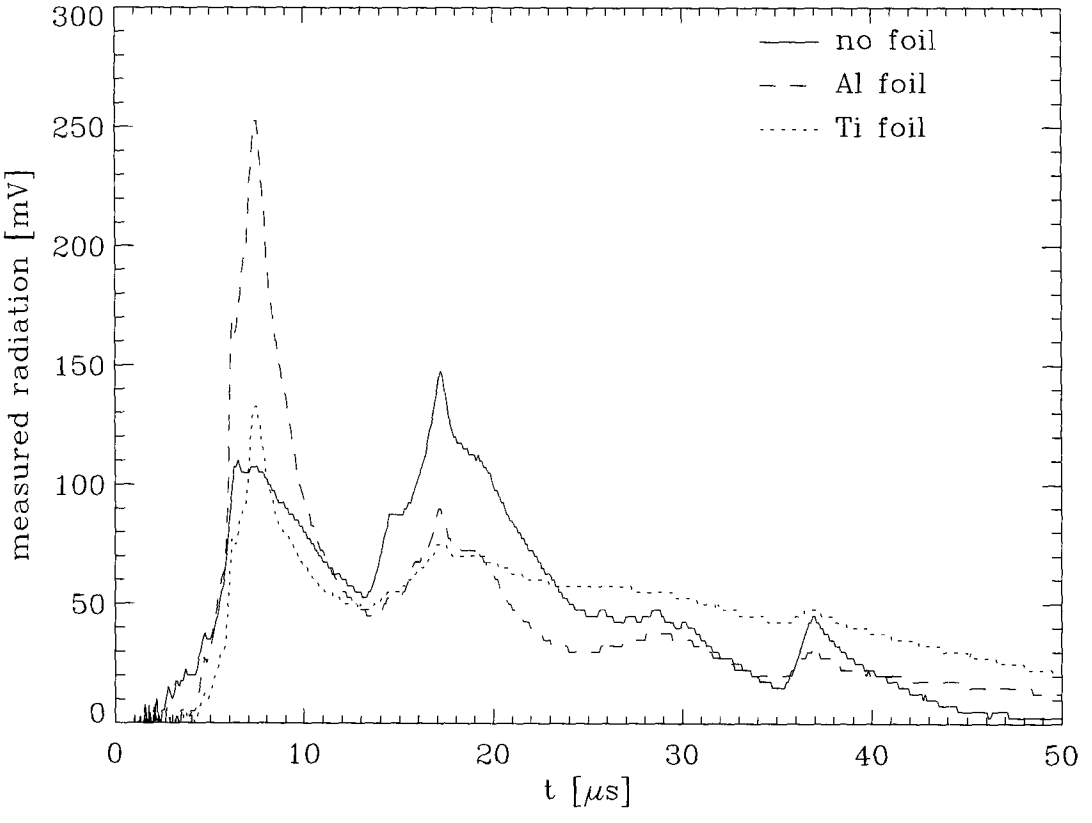

Figure 57: Radiation emission measured by the three diodes (without foil, with an aluminium foil, and with a titanium foil) of the x-ray probe for a typical co-helicity discharge, as a function of time. Main capacitor charging voltage $V_I = 5.00$ kV.

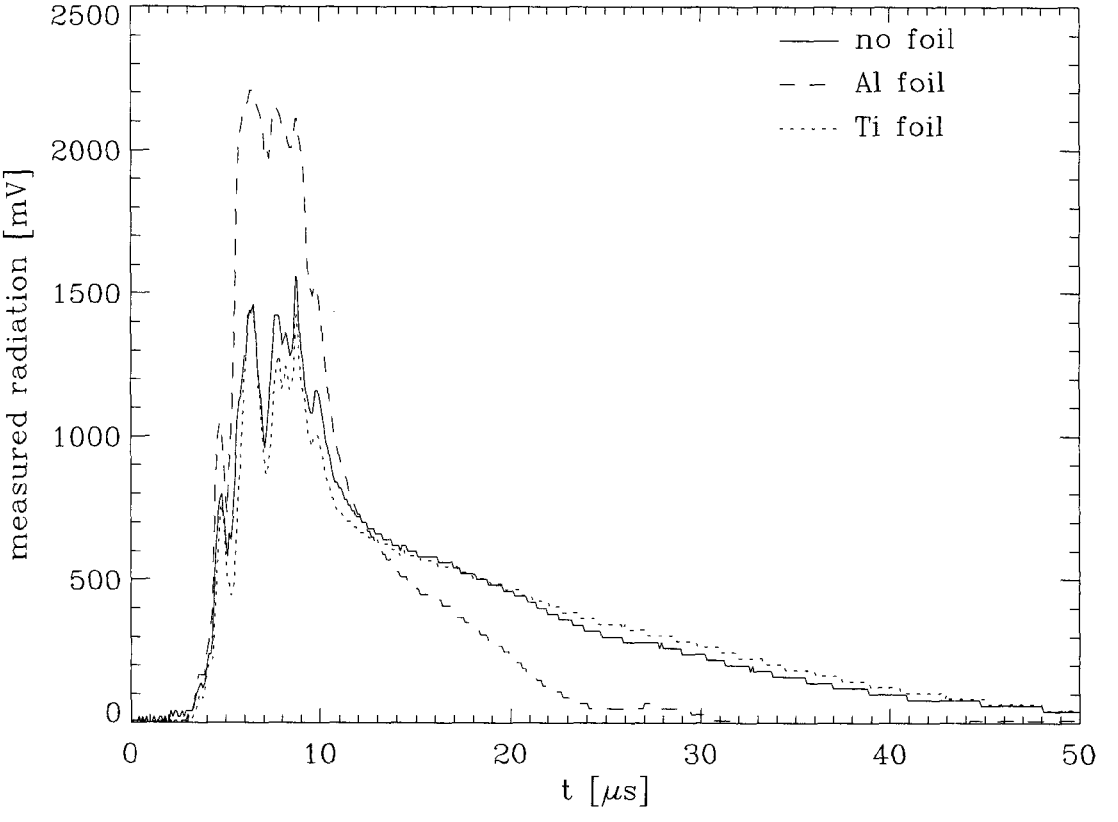

Figure 58: Radiation emission measured by the three diodes (without foil, with an aluminium foil, and with a titanium foil) of the x-ray probe for a typical counter-helicity discharge, as a function of time. Main capacitor charging voltage $V_I = 5.00$ kV.

Main capacitor voltage V_I [kV]	Single prominence UV emission [mV]	Co-helicity UV emission [mV]	Counter-helicity UV emission [mV]
3.00	30 ± 8	55 ± 27	102 ± 76
4.00	99 ± 75	65 ± 19	494 ± 209
5.00	168 ± 66	224 ± 65	1438 ± 449
6.00	357 ± 264	330 ± 17	3602 ± 1469

Table 9: Emission of 20-80 nm ultraviolet radiation as measured by the diode with an aluminium foil for two prominences, in either co- or counter-helicity configuration, as well as for single prominences, as a function of charging voltage on the main capacitor. Emission is peak emission at the first maximum.

averaging over several plasma discharges. The radiation increases with charging voltage V_I on the main capacitor. For a single prominence, the radiation increases by about a factor of eight when doubling V_I. For two prominences in a co-helicity configuration the increase is about a factor of four, while in a counter-helicity configuration the factor is above fifty.

Radiation in the more limited spectral range (UV) detected by the aluminium coated diode is summarized in Table 9. Again the radiation increases with V_I: a factor of twelve for the single prominence, a factor of six for two prominences in a co-helicity configuration, and a factor of more than thirty for the counter-helicity configuration, when doubling V_I.

Radiation in the x-ray spectral range detected by the titanium coated diode is summarized in Table 10. When doubling V_I, the radiation increases with a factor of seven for the single prominence, a factor of thirteen for two prominences in a co-helicity configuration, and a factor >140 for the counter-helicity configuration. The spectacular increase in (x-ray) emission in the counter-helicity case, compared to either the co-helicity case or a single prominence, is a very interesting result and will be discussed below.

The variation from discharge to discharge was fairly large, leading to the large standard deviations given in Tables 8-10. However, in a discharge with a large signal detected by one diode, the other two diodes would detect large signals as well. Therefore, to study

Main capacitor voltage V_I [kV]	**Single prominence x-ray emission** [mV]	**Co-helicity x-ray emission** [mV]	**Counter-helicity x-ray emission** [mV]
3.00	18 ± 2	18 ± 5	38 ± 25
4.00	43 ± 23	32 ± 8	203 ± 128
5.00	73 ± 36	120 ± 28	975 ± 360
6.00	134 ± 86	229 ± 26	5467 ± 1859

Table 10: Emission of <15 nm x-rays as measured by the diode with a titanium foil for two prominences, in either co- or counter-helicity configuration, as well as for single prominences, as a function of charging voltage on the main capacitor. Emission is peak emission at the first maximum.

Main capacitor voltage V_I [kV]	Single prominence fractional UV emission	Co-helicity fractional UV emission	Counter-helicity fractional UV emission
3.00	0.77 ± 0.18	1.65 ± 0.68	2.23 ± 0.69
4.00	0.86 ± 0.18	1.21 ± 0.17	2.10 ± 0.80
5.00	1.26 ± 0.36	2.40 ± 0.54	1.34 ± 0.36
6.00	1.33 ± 0.44	2.57 ± 0.19	1.11 ± 0.11

Table 11: Emission of 20-80 nm ultraviolet radiation divided by total radiation in all wavelengths in each plasma discharge, in either co- or counter-helicity configuration, as well as for single prominences, as a function of charging voltage on the main capacitor. Emission is peak emission at the first maximum.

radiation in one spectral range relative to another, the signals from the diodes covered with foils were divided by the signal from the diode with no foil. The results are summarized in Tables 11-12. Some of these ratios are larger than unity because of different internal capacitances of the photodiodes. This is a consequence of the diode manufacturing technique. It is also possible that the diodes view slightly different parts of the plasma and that their respective viewing angles are different due to imprecise machining of the probe head.

5.2.6 Triple probe measurements

The electron temperature T_e, ion saturation current I_+, and floating potential V_1 for a typical discharge are given in Figure 59. For all discharges, either single or dual prominence, the floating potential peaks (negative minimum) at t = 9-12 μs. The peak magnitude increased with main capacitor charging voltage V_I, while the rise time decreased. The electron temperature peaks once while the floating potential is dropping and once again as the floating potential is rising back to zero. Either or both of these electron temperature peaks are very large, typically 30-50 eV and sometimes as high as 150 eV (the maximum level sampled by the Aeon digitizers). This exceeds the range where the electron temperature is approximately a linear function of $V_1 - V_2$. The bias voltage $V_{battery}$ was temporarily increased from 48 V to 59 V and then to 98 V to remedy this problem. Fewer readings of

Main capacitor voltage V_I [kV]	Single prominence fractional x-ray emission	Co-helicity fractional x-ray emission	Counter-helicity fractional x-ray emission
3.00	0.45 ± 0.11	0.57 ± 0.09	0.59 ± 0.18
4.00	0.40 ± 0.06	0.59 ± 0.06	0.86 ± 0.51
5.00	0.53 ± 0.15	1.30 ± 0.33	0.85 ± 0.04
6.00	0.51 ± 0.13	1.78 ± 0.15	1.73 ± 0.26

Table 12: Emission of <15 nm x-rays divided by total radiation in all wavelengths in each plasma discharge, in either co- or counter-helicity configuration, as well as for single prominences, as a function of charging voltage on the main capacitor. Emission is peak emission at the first maximum.

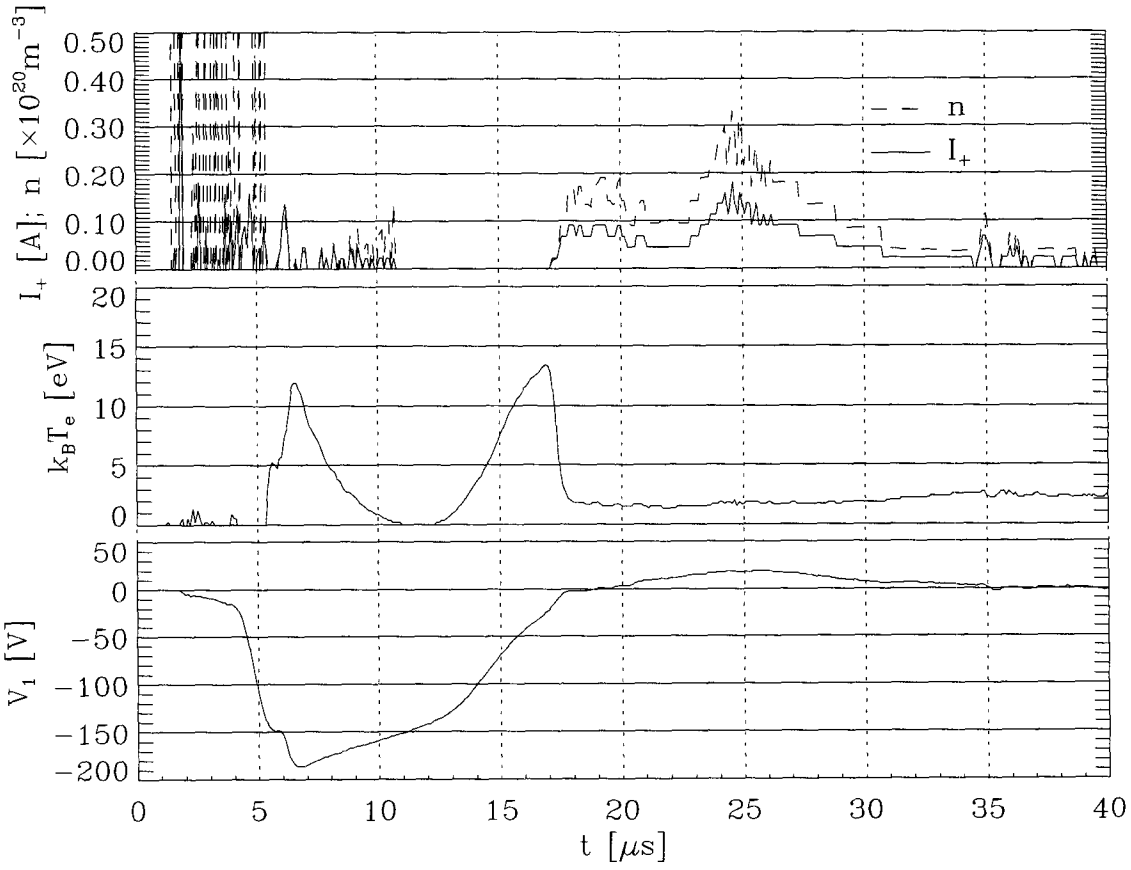

Figure 59: Measured time profiles for the ion saturation current I_+, electron temperature T_e, and floating potential V_1, for a typical discharge (co-helicity at $V_I = 5.00$ kV). The calculated density n is also given.

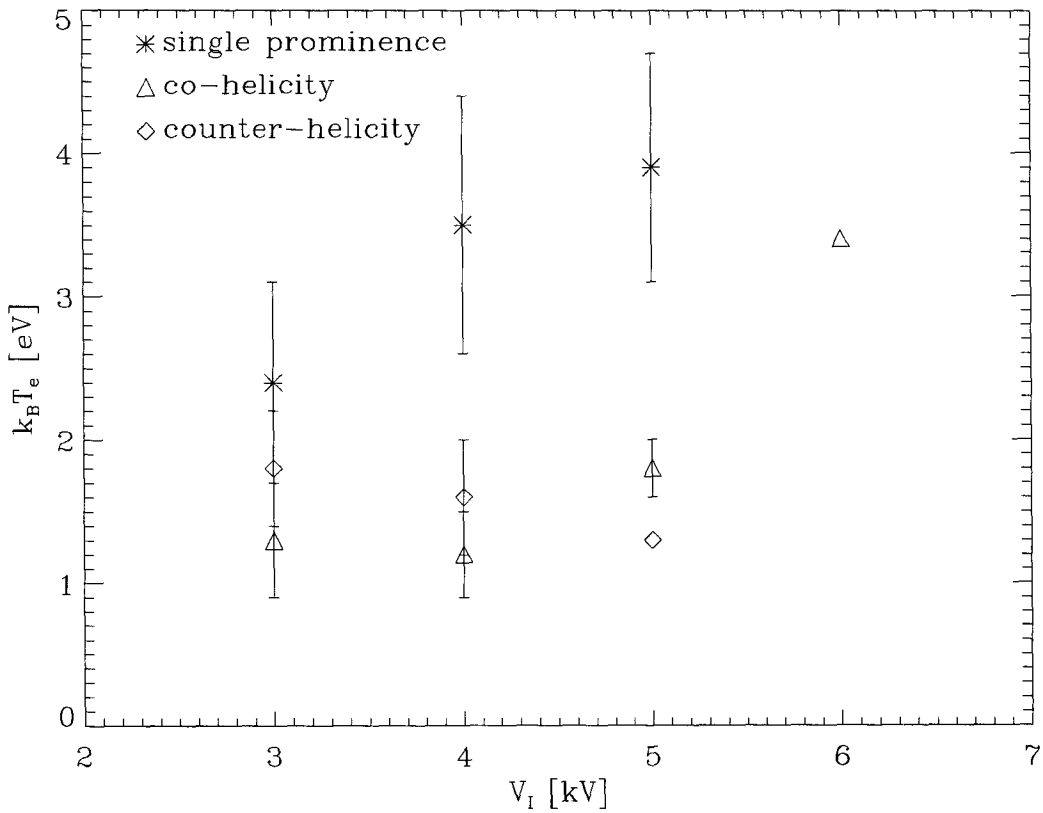

Figure 60: Electron temperature T_e for single and dual prominences (co- and counter-helicity) as a function of charging voltage V_I on the main capacitor.

$k_BT_e \geq 150\,\mathrm{eV}$ were registered with the increased $V_{battery}$, but still occurred. Moving the probe off center reduced the magnitudes of the two electron temperature peaks.

Later in time, typically around $t \simeq$ 23-28 μs, the ion saturation current rises to a small, local maximum. The electron temperature would rise very slightly at the same time. These readings are likely to come from the passing prominences; assuming that a typical laboratory prominence forms at a height $z = 40\,\mathrm{mm}$ at $t = 5\,\mu\mathrm{s}$ and then expands at a velocity of $20\,\mathrm{km}\,/\,\mathrm{s}$ toward the probe, the prominence should reach the probe around $t = 24\,\mu\mathrm{s}$. The readings are summarized in Figures 60-61. Error bars in these figures represent standard deviations from averaging over several shots. Occasionally, the ion

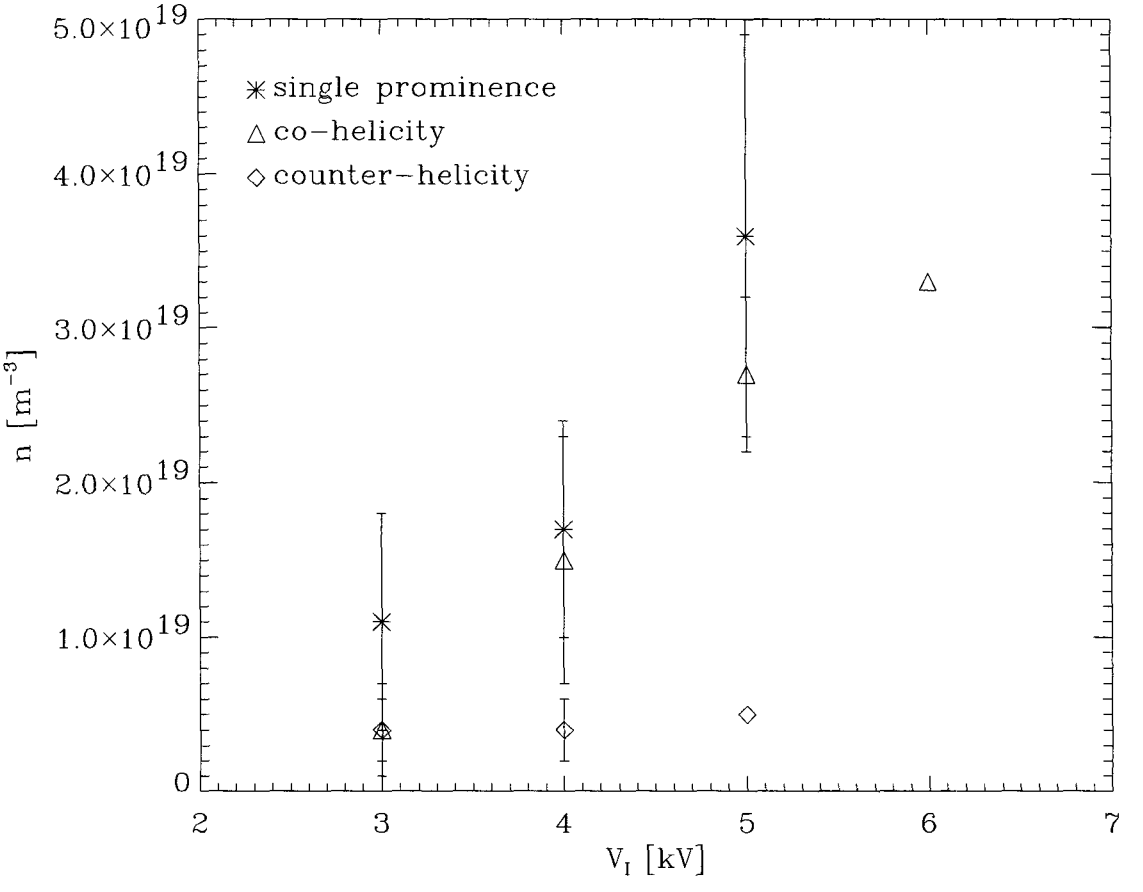

Figure 61: Plasma density n for single and dual prominences (co- and counter-helicity) as a function of charging voltage V_I on the main capacitor.

saturation current would "arc" around $t \simeq$ 23-28 μs; the probe would draw a very large current of 3 A or more (compared to the normal 0.3 A or less). Arcing would be more frequent at higher main capacitor charging voltages ($V_I \geq 5\,\mathrm{kV}$). These discharges were omitted from Figures 60-61 and are the reason behind missing data points (and missing error bars when only one discharge without arcing was recorded for a particular setting).

5.3 Discussion

We will now discuss and interpret the results of this chapter. The most important finding is that interaction between two prominences can cause one or both prominences to erupt sooner and at a higher velocity than a single prominence would. This can happen with two side-by-side prominences with opposite sign helicity (counter-helicity) via the destruction of toroidal magnetic flux, or with two side-by-side prominences with same sign helicity (co-helicity) due to helicity transfer from one prominence to the other. Other important results that will be discussed include:

- Camera images show a bright region between two counter-helicity prominences. We suggest that this region is a reconnection layer in the form of a current sheet.
- A topology with more pronounced S-shapes is explained using the mathematical model of Chapter 3.
- X-ray emissions from the plasma is shown to increase with current density.
- X-ray emissions in a counter-helicity case can be more than an order of magnitude larger than in a similar co-helicity case or for a single prominence.
- Striations and wave-like patterns are observed in the plasma.

- Plasma electron temperature is measured to be 1-4 eV. Plasma densities are measured to be on the order of $10^{19}\,\mathrm{m}^{-3}$. Electron temperature and plasma density increase with toroidal plasma current in the co-helicity case and for a single prominence.

5.3.1 Counter-helicity images

The two prominences carry parallel toroidal currents, causing them to attract each other. In the counter-helicity case, the prominences have oppositely directed toroidal magnetic fields, requiring the formation of a current sheet in the region between the main current channels. We suggest that electron-neutral and ion-neutral collisions in this current sheet cause the bright region between the prominences visible in Figures 47-49. Then this is a direct observation of the reconnection layer.

The destruction of toroidal magnetic flux is also evident from counting the number of turns N of the current channels around their respective toroidal envelope axes. For times $t \gtrsim 9\,\mu$s, the camera images (cf Figures 44-46) show $N \geq 12$, more turns than at comparable times for a solitary prominence. Larger N corresponds to larger I_{tor}/B_{tor} ratios (cf 4.3.2). Consequently, B_{tor} must be much less in the counter-helicity case than in the single prominence case. (By virtue of operating with two prominences, I_{tor} should be roughly one half of what it is in a single prominence case. In other words B_{tor} must be less than half of what it is for a single prominence.) This means that each prominence is more unstable than it would be if it were alone. This is important as it means that two interacting counter-helicity prominences on the Sun may erupt sooner than non-interacting prominences would.

The plasma evolution in the counter-helicity case is summarized in Figure 62. First,

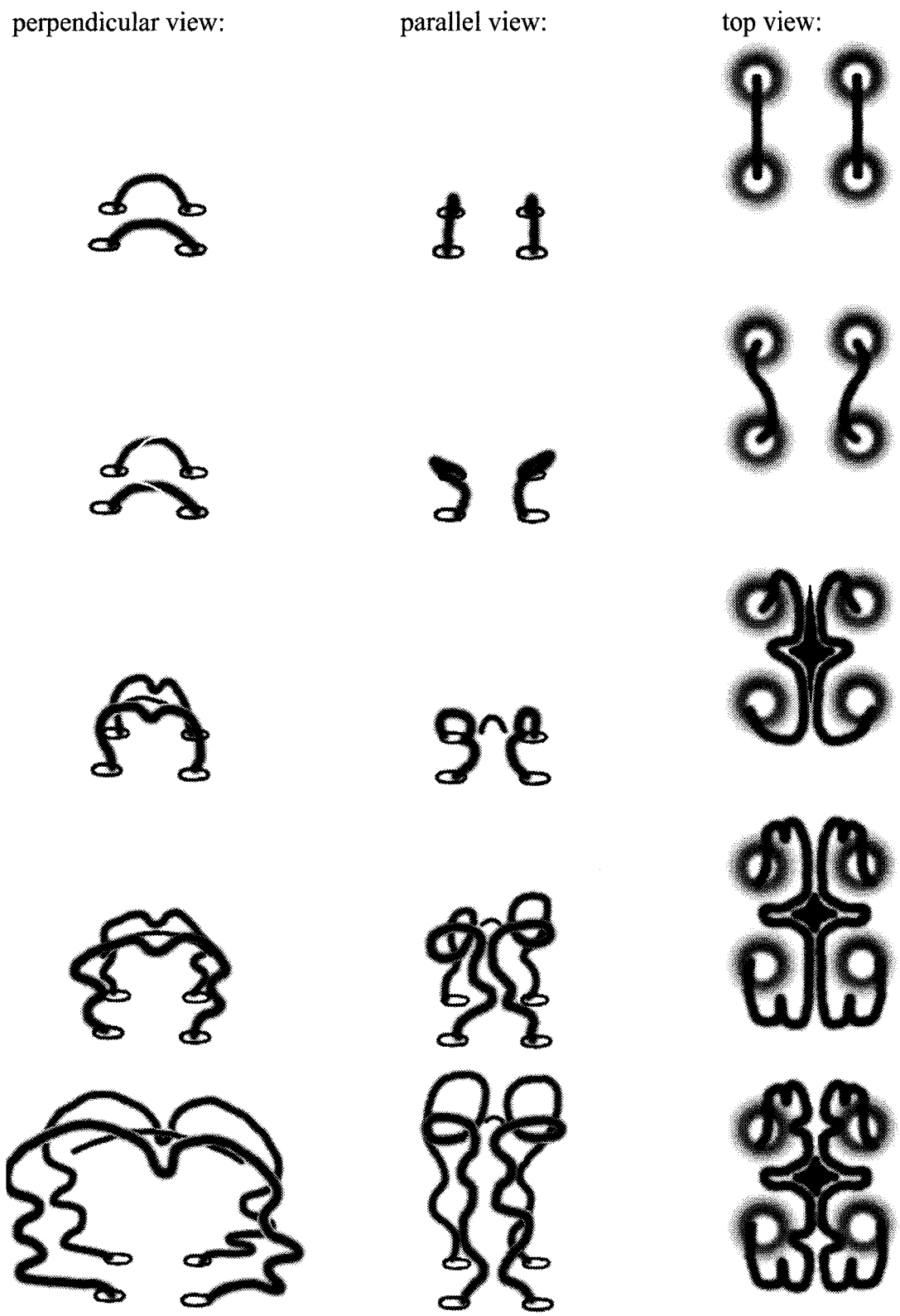

Figure 62: Plasma evolution in the counter-helicity case. Refer to text.

two main current channels form between each electrode pair (cf $t = 4.0\,\mu$s in Figure 47). Second, brighter and darker strands in the main current channels twist up. From both parallel and top views, the characteristic S-shapes are distinguishable at this time (cf $t = 3.5\,\mu$s in Figures 48-49). Third, the plasmas take on helical shapes and expand outward. A bright region between the two prominences becomes visible (cf $t > 5.0\,\mu$s in Figures 47-49). Additional turns on the helices form during expansion. The number of turns are more than in a single prominence case.

5.3.2 Co-helicity images

Other experiments have studied the interaction between two spheromaks in co- and counter-helicity configurations [89][90][91]. These spheromak plasmas are fairly uniformly distributed across the cross-section of the toroidal envelope discussed in Chapter 4. When two of these identical toroidal flux-ropes are forced together in a co-helicity configuration (typically by running the toroidal currents in parallel), the magnetic field lines in the boundary region "meet" at an angle. (The angle is 2φ, where φ is the complement of the pitch angle of each spheromak; cf Figure 3.) This means that a current sheet must form between the two spheromaks, and that any merging will be preceded by a reconnection of field lines at the boundary.

In our case, the main current channel spirals in a helix around the toroidal envelope (cf Figure 35). The plasma is not uniformly distributed across the toroidal cross-section but is mainly located to the current channel. Assuming that the plasma is governed by the force-free state equation (17), the main current channel is already aligned with the magnetic field. If the current channels of two prominences, or sections thereof, somehow align themselves with each other, their field lines will already be parallel and thus they are free

to merge with no reconnection necessary. It appears that at $t \simeq 7\,\mu$s the leading parts of the Mark IV prominences merge. Some magnetic reconnection, specifically between the relatively tenuous plasmas outside the main current channels, is necessary before this can happen. However, judging from images (as well as x-ray emissions and voltage traces) this reconnection process is not particularly dramatic compared to the counter-helicity reconnection.

Before the apparent merging, there already appears to be some interaction between the two prominences, explaining why one prominence expands faster than the other. In some images (e.g., $t = 5.0\,\mu$s in Figures 45-46), a strand of plasma can be seen connecting one prominence with the other. This means that some current initially flowing through one prominence is now flowing in the other. A larger toroidal current means a larger hoop-force and a faster expansion. This is important for solar prominences, as it means that one of two neighboring prominences may erupt sooner than a solitary prominence would. Our experimental observation may predict which of the two prominences will erupt sooner; in an image with the toroidal currents flowing toward the top of the image, the prominence to the right erupts first if the prominences are right-handed, the one to the left if the prominences are left-handed.

The plasma evolution in the co-helicity case is summarized in Figure 63. Initially the evolution is similar to the counter-helicity case; main current channels form (cf $t = 3.6\,\mu$s in Figure 44), twist up to S-shapes (cf $t = 5.0\,\mu$s in Figure 45 and $t = 4.5\,\mu$s in Figure 46), and take on helical shapes. However, one prominence becomes S-shaped slightly earlier than the other (cf $t = 4.5\,\mu$s in Figure 45 and $t = 4.0\,\mu$s in Figure 46), and the same prominence also becomes helical slightly earlier (cf $t = 5.0\,\mu$s in Figures 44 and 46). As

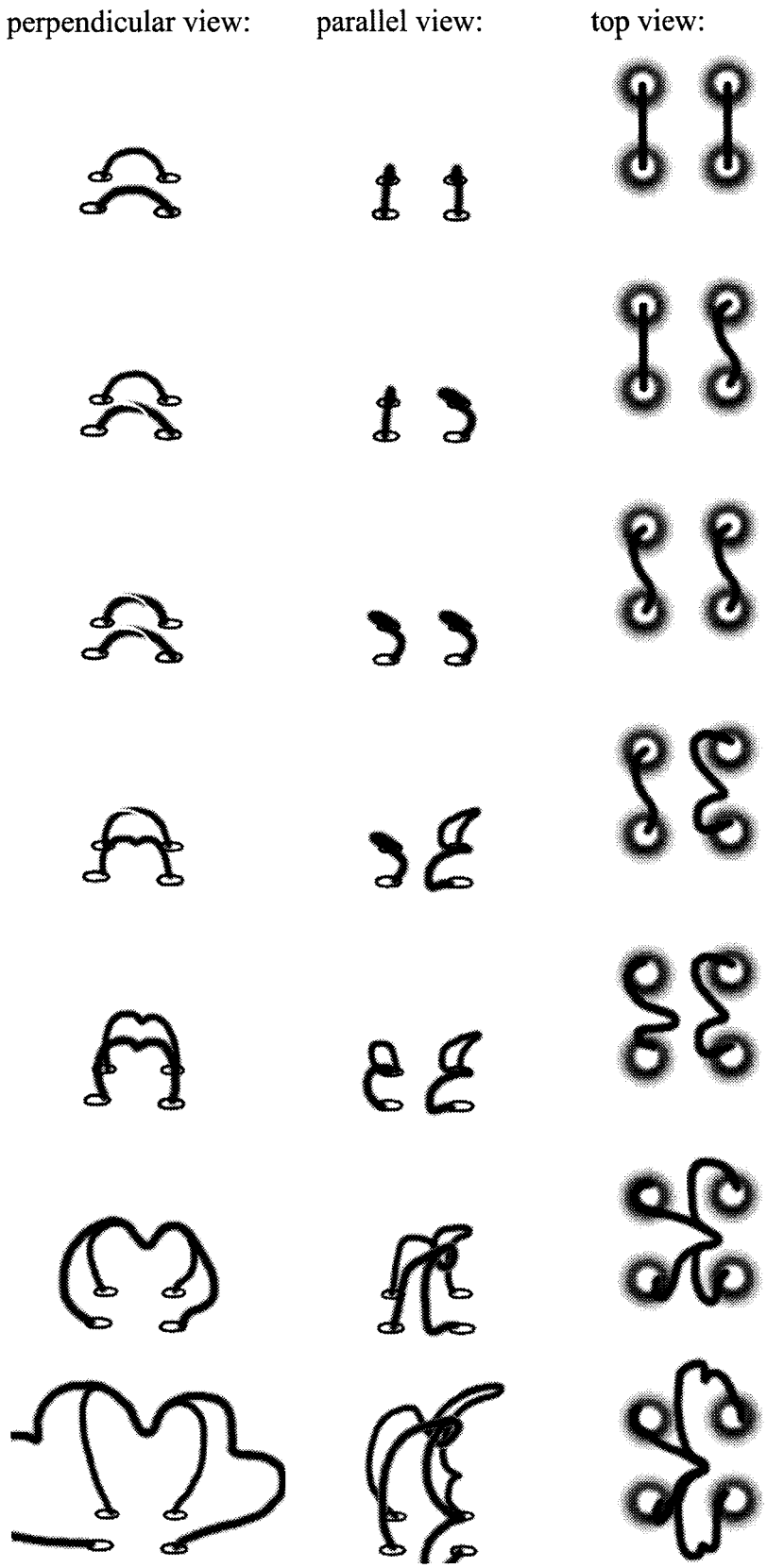

Figure 63: Plasma evolution in the co-helicity case. Refer to text.

the prominences expand, the leading edges appear to merge (cf $t \geq 6.8\,\mu$s in Figures 44 and 46). One prominence expands faster and takes on the $N = 8$ helical shape earlier (cf $t = 10.5\,\mu$s in Figure 44, $t = 9.0\,\mu$s in Figure 45, and $t = 8.0\,\mu$s in Figure 46).

Finally, we note that a parallel view image of a laboratory prominence strongly resembles a plage filament on the Sun [65].

5.3.3 Voltage traces

The unique plateau in the counter-helicity voltage traces occurs at the same time as the bright region in the images appears. Interpreting the bright region as a current sheet, it is likely that the voltage plateau is a consequence of the current sheet formation. If the initial current sheet temporarily provides a low inductance path between the electrodes, then this would explain the plateau.

5.3.4 X-ray emissions

The peak x-ray (and UV) emissions increased with charging voltage V_I on the main capacitor. X-ray production is thus a function of toroidal current. In fact, the toroidal current time profile matches the x-ray trace very well; each of the peaks in the x-ray trace corresponds to a peak (minimum or maximum) in the toroidal current.

The most spectacular x-ray probe result is the large x-ray (and UV) emission in the counter-helicity case. The diode measuring overall radiation also registered a large difference between the co- and counter-helicity cases, but as the cameras did not register a significant difference in overall plasma brightness, we conclude that it is the UV and x-ray emissions that are different. We suggest that the additional x-rays are produced in conjunction with the counter-helicity reconnection process. Toroidal magnetic fields are associated with poloidal currents, so the current sheet is essentially the superposition of the poloidal

current of each prominence. As the prominences are forced together, the current density in the sheet increases. It has already been shown that larger currents correspond to greater x-ray production. The tremendous increase in x-ray emission as a function of V_I is a measure of the increased current density in the reconnection layer caused by the increased attraction between the parallel toroidal currents.

Comparing the co-helicity case with the single prominence, we find that some additional x-ray production occurs also for the co-helicity case. In a single prominence, the toroidal current density is roughly twice as large, so some mechanism not present in the single prominence case must be behind the increased x-ray production. Again this is likely to be reconnection, albeit in the more tenuous plasma outside the main current channels (cf 5.3.2).

The fractional emissions of Tables 11-12 reinforce what has already been said. Table 12 clearly shows that a mechanism absent in the single prominence case is responsible for the increased x-ray production with increasing V_I. In the counter-helicity case, Tables 11-12 show that the increase in total radiation with increasing V_I is dominated by the increase in x-rays, not UV.

5.3.5 Triple probe data

For a single prominence and two prominences in the co-helicity case, the increase in plasma density n with charging voltage V_I on the main capacitor is consistent with the pinch effect. The toroidal current (at a given time) is proportional to V_I, and a larger current will pinch down the plasma cross-section, increasing the plasma density. The electron temperature T_e also appears to increase with V_I in these two plasma configurations (although the trend may be due to statistical errors).

It is unclear why neither density nor electron temperature increase with V_I in the counter-helicity case. One possibility is that plasma is escaping along open field lines in the reconnection region.

The peak in the floating potential V_1 and the two associated peaks in T_e are possibly related to fast electrons emitted during the breakdown process. These readings are too early in time to be associated with prominence plasma passing the probe. Also, the rise time in V_1, just like the breakdown time (cf Figure 25), decreases with increasing V_I.

5.3.6 S-shapes

The regime with pronounced S-shapes can be explained using the mathematical analysis of Chapter 3, although on two points this needs to be justified:

1. The boundary conditions at the electrode plane $z = 0$ for the Mark IV device are not a good match to the $m = 1$ boundary conditions in the model (cf 3.3.3). The $B_z > 0$ region now has two local B_z maxima and is not bounded by the circle $J_1(\kappa r) = 0$. However, it still *is* a $B_z > 0$ region, and the $z-$component of $\nabla \times \mathbf{B}$ still has the same sign throughout this region. The same goes for the $B_z < 0$ region on the opposite side of the $\phi = \pm\pi/2$ separatrix.

2. The $m = 1$ model does not describe the plasma after it has assumed its typical $N = 4$ helical shape. However, *before* the plasma becomes helical, both the Mark II and IV plasmas behave according to the $m = 1$ model.

The gas injection points are the initial footpoints of the prominence. Injecting gas through two diagonally opposite electrodes is analogous to commencing field line integration at two points along the line $\phi = 3\pi/4$ or $7\pi/4$ (cf Figure 16). In the $m = 1$ model,

starting at these points would allow for a longer, curved field line, and consequently a more pronounced S-shape, before passing over the x-axis $B_z = 0$ separatrix (at $x = y = 0$).

It is interesting to note when the $m = 1$ model no longer accurately describes the plasma and the $N = 4$ helical shape forms. It appears that this happens when a critical angle between the prominence axis (at $x = y = 0$) and the direction of the bias magnetic field has been exceeded. From images (cf Figures 30 and 51) we find this angle to be approximately 45°. Injecting gas at two points along $\phi = 3\pi/4$ or $7\pi/4$ means that the prominence axis (at $x = y = 0$) can turn an additional $\pi/4$ or 45° before the helical shape forms, creating a more pronounced S-shape. The existence of a critical angle means that observations of S-shaped solar prominences could provide some information on the local vacuum magnetic field surrounding the prominence.

5.3.7 Streamers and waves

A streamer is an ionization front, the speed of which can reveal certain properties of the gas and its environment, such as gas pressure and applied electric field [92]. Studies of streamers in oil and other commercial insulators continues to be an important subject for the power industry [93]. For our purposes, we note that it has been suggested that streamers grow step-wise [94]. (This has been recently demonstrated [95].) Instabilities in the ionization front can lead to striation or ionization waves [96][97]. These waves occur in regimes of large ionization gradients and are due to ionization diffusion oscillations [97]. The waves detected in our experiment, when only injecting gas through the cathodes, could be ionization waves. In the systematization of different types of two-dimensional ionization waves by Pekarek [97], these ionization waves would possibly be of the type F_D^-, a type that has been previously identified in hydrogen. However, in top-view images, our ioniza-

tion waves are approximately planar waves extending similar distances in both dimensions perpendicular to the general direction of the streamer. Thus they do not necessarily fit in a two-dimensional classification. Three-dimensional ionization waves [98] do not yet have a well-developed classification scheme.

It is unclear whether or not streamers associated with ionization and their related ionization waves would appear in the solar corona, as observations indicate that solar prominences form from the emergence of magnetic flux ropes from the solar photosphere [54][85] and not as a part of an ionization process. Oscillatory behavior associated with prominences has however been abundantly observed [65]. An alternate explanation to our observed waves could be some sort of ion acoustic wave, similar to what has been suggested would occur on the Sun [99]. Such slow magnetoacoustic waves would display a structure of bands centered about certain magnetic field lines and would move along these magnetic field lines [99]. This is similar to our observation of circular waves moving away from the cathode magnetic pole.

The wave-like pattern observed in a few discharges with normal gas injection curiously resembles a solar phenomenon known as a helmet streamer.

Chapter 6 Summary

We have demonstrated how solar prominences can be simulated in laboratory experiments. Through careful scaling of terms in the two-fluid electron equation of motion, the experiments preserve the essential physics of solar prominences. The experiments provide valuable insights into the evolution of solar prominences. Most important among these insights are how strapping fields can inhibit prominence eruption, how two interacting solar prominences affect each other, and how certain aspects of prominence shapes can be explained using the force-free state equation $\nabla \times \mathbf{B} = \alpha \mathbf{B}$.

In Chapter 3 we explained both prominence S-shapes and an observed plasma bifurcation using the force-free state equation $\nabla \times \mathbf{B} = \alpha \mathbf{B}$. This supports the conjecture that solar prominences are in Woltjer-Taylor states. We interpreted bright regions in images of the plasma as current paths, based on both the local twisting of these paths and by noting that most of the observed light is H_α. (H_α is emitted by hydrogen neutral atoms after they have been excited by collisions with ions and electrons. This is more likely to occur where current is flowing.) This important interpretation was the basis of other results derived partly from camera images. We experimentally confirmed the formation of S-shaped prominences when injecting positive helicity, and reverse S-shaped prominences when injecting negative helicity. Also, we confirmed that the twist of a plasma is larger for more unstable plasmas, smaller for more stable plasmas.

In Chapter 4 we demonstrated that a strapping field can inhibit the eruption of a prominence. The strapping field magnitude required to completely inhibit prominence eruption was found to be in good agreement with a theoretical model which takes into account the full three-dimensional magnetic topology. Prominence eruption is inhibited

due to a $\mathbf{J} \times \mathbf{B}$-force between strapping field and the prominence toroidal current. Thus, the sign of the strapping field matters (contrary to models which rely on magnetic field line tension or magnetic pressure of the strapping field), and this sign-dependence was verified experimentally. We also showed that more helical plasmas are produced with higher ratios of toroidal current to toroidal bias magnetic field. Finally, we explained various aspects of solar prominences based on our experimental observations. The dip of a prominence above the neutral line can by explained by the helical shape of the prominence. Acceleration duration and magnitude of disparitions brusque (a prominence erupting from a quiescent region) compared to a spray (a prominence erupting from an active region) can be explained by a proposition that quiescent regions on the Sun are subjected to stronger strapping fields than active regions. The proposition is supported by a comparison of the helical appearance of disparitions brusque to experimentally produced plasmas. The large aspect ratio (length to height) of some prominences can be the result of strong strapping fields.

In Chapter 5 we found that interaction between two prominences can cause one or both prominences to erupt sooner and at a higher velocity than a single prominence would. This can happen with two side-by-side prominences with opposite sign helicity (counter-helicity) by the destruction of toroidal magnetic flux, or with two side-by-side prominences with same sign helicity (co-helicity) because of helicity transfer from one prominence to the other. We also found that x-ray emissions in a counter-helicity case can be more than an order of magnitude larger than in a similar co-helicity case or for a single prominence, and that x-ray emissions increase with current density. We suggested that a bright region between two counter-helicity prominences, appearing in camera images of the laboratory plasma, is a reconnection layer in the form of a current sheet. We explained a topology

with more pronounced S-shapes using a mathematical model based on the force-free state equation $\nabla \times \mathbf{B} = \alpha \mathbf{B}$. Finally, we explored a regime where striations and wave-like patterns are observed in the plasma.

Bibliography

[1] Secchi, A. *Le Soleil* (Gauthier-Villars, Paris, 1875-77).

[2] Young, C. A. *The Sun* (D. Appleton, New York, 1896).

[3] Pettit, E. *Publ. Yerkes Obs.* **3,** 205 (1925).

[4] Pettit, E. *Ap. J.* **76,** 9 (1932).

[5] Severny, A. B. *Dokl. Akad. Nauki* **73,** 475 (1950).

[6] Severny, A. B. and Khoklova, V. L. *Izv. Krymsk. Astrofiz. Obs.* **10,** 9 (1953).

[7] Menzel, D. H. and Evans, J. W. *Acad. Naz. Lincei. Conv. Volta* **11,** 119 (1953).

[8] de Jager, C. *Handbuch der Physik* **52,** 80 (1959).

[9] Zirin, H. *The Solar Atmosphere* (Blaisdell-Ginn, Waltham, Massachusetts, 1966).

[10] Hale, G. E. and Ellerman, F. *Publ. Yerkes. Obs.* **3,** 3 (1903).

[11] Deslandres, H. *Ann. Obs. Paris-Meudon.* **4,** 1 (1910).

[12] Tandberg-Hanssen, E. *The Nature of Solar Prominences* (Kluwer Academic, Dordrecht, 1995).

[13] Hirayama, T. *Solar Phys.* **100,** 415 (1985).

[14] Martin, S. F., Marquette, W. H., and Bilimoria, R. in *The Solar Cycle* (ed., K. L. Harvey), ASP Conf. Series **27,** 53 (1992).

[15] Gigolashvili, M. *Solar Phys.* **60,** 293 (1978).

[16] Pevtsov, A. A., Canfield, R. C., and Metcalf, T. R. *Astrophys. J.* **440,** 109 (1994).

[17] MacKay, D. H., Longbottom, A. W., and Priest, E. R. *Solar Phys.* **185,** 315 (1999).

[18] Mikić, Z., Barnes, C., and Schnack, D. D. *Astrophys. J.* **328,** 830 (1988).

[19] Mikić, Z. and Linker, J. A. *Astrophys. J.* **430,** 898 (1994).

[20] Nakagawa, Y., Raadu, M. A., Billings, D. E. & McNamara D. *Sol. Phys.* **19,** 72 (1971).

[21] Amari, T. and Luciani, J. F. *Astrophys. J.* **515,** L81 (1999).

[22] Jackson, B. V. and Howard, R. *Sol. Phys.* **148,** 359 (1993).

[23] Burlaga, L. F. *J. Geophys. Res.* **93,** 7217 (1988).

[24] Rust, D. M. *Geophys. Res. Lett.* **21,** 241 (1994).

[25] Rust, D. M. and Kumar A. *Solar Phys.* **155,** 69 (1994).

[26] Taylor, J. B. *Phys. Rev. Lett.* **33,** 1139 (1974).

[27] Bellan, P. M. *Spheromaks* (Imperial College Press, London, 2000).

[28] Woltjer, L. W. *Proc. Nat. Acad. Sci. (USA)* **44,** 490 (1958).

[29] Woltjer, L. W. *Proc. Nat. Acad. Sci. (USA)* **44,** 833 (1958).

[30] Lust, R. and Schluter, A. *Z. Astrophys.* **34,** 353 (1954).

[31] Rosenbluth, M. N. and Bussac, M. N. *Nucl. Fusion.* **19,** 489 (1979).

[32] Barnes, C. W., Fernandez, J. C., Henins, I., Hoida, H. W., Jarboe, T. R., Knox, S. O., Marklin, G. J., and McKenna, K. F. *Phys. Fluids* **29,** 3415 (1986).

[33] Brown, M. R. and Bellan, P. M. *Phys. Rev. Lett.* **64,** 2144 (1989).

[34] Alfvén, H., Lindberg, L., and Mitlid, P. *J. Nucl. Energy C* **1,** 116 (1960).

[35] Jarboe, T. R., Henins, I., Hoida, H. W., Linford, R. K., Marshall, J., Platts, D. A., and Sherwood, A. R. *Phys. Rev. Lett.* **45,** 1264 (1980).

[36] Wysocki, F. J., Fernandez, J. C., Henins, I., Jarboe, T. R., and Marklin, G. J. *Phys. Rev. Lett.* **65,** 40 (1990).

[37] Fernandez, J. C., Wright, B. L., Marklin, G. J., Platts, D. A., and Jarboe, T. R. *Phys. Fluids B* **1,** 1254 (1989).

[38] Loewenhardt, P. K., Brown, M. R., Yee, J., and Bellan, P. M. *Rev. Sci. Instrum.* **66,** 1050 (1995).

[39] Yee, J. *Experimental investigations in spheromaks: injection into a tokamak and formation in an unbounded environment.* California Institute of Technology thesis (2000).

[40] Durance, G., Jessup, B. L., Jones, I. R., and Tendys, J. *Phys. Rev. Letters* **48,** 1252 (1982).

[41] Hugrass, W. N. *J. Plasma Phys.* **28,** 369 (1982).

[42] Gekelman, W., Leneman, D., Maggs, J., and Vincena, S. *Phys. Plasmas* **1,** 3775 (1994).

[43] Stamper, J. A. and Ripin, B. H. *Phys. Rev. Letters* **34,** 138 (1975).

[44] Bolz, R. E. and Tuve, G. L., Eds. *CRC Handbook of Applied Engineering Science* (CRC, Cleveland, Ohio, 1970).

[45] Smithells, C. J., Ed. *Metals Reference Book* (Plenum, New York, 1967).

[46] Chapman, B. *Glow Discharge Processes* (Wiley, New York, 1980).

[47] Brown, M. R., Bailey, A. D., and Bellan, P. M. *J. Appl. Phys.* **69,** 6302 (1991).

[48] Chen, F. F. *Introduction to plasma physics and controlled fusion* (Plenum Press, New York, New York, 1984).

[49] Brown, S. C. *Basic Data of Plasma Physics: The Fundamental Data on Electrical Discharges in Gases* (American Institute of Physics, New York, New York, 1994).

[50] Ling, Y.-M. and Zhu, W. *Jpn. J. Appl. Phys.* **34,** 3671 (1995).

[51] Githens, Jr., S. *Phys. Rev.* **57,** 822 (1940).

[52] Lisovsky, V. A. and Yegorenkov, V. D. *J. Appl. Phys.* **27,** 2340 (1994).

[53] von Engels, A. *Ionized gases* (Oxford University Press, Oxford, 1965).

[54] Zirin, H. *Sol. Phys.* **14,** 328 (1970).

[55] Thomas, J. C., Hwang, D. Q., Horton, R. D., Rogers, J. H., and Raman, R. *Rev. Sci. Instrum.* **64,** 1410 (1993).

[56] Karmaker, H. C. and Robertson, S. D. T. *IEEE Trans. Power Apparatus and Systems* **92,** 815 (1973).

[57] Smythe, W. R. *Static and Dynamic Electricity* (McGraw-Hill Book Company, New York, New York, 1950).

[58] Chin-Fatt, C., de Silva, A. W., Goldenbaum, G. C., Hess, R., Coté, C., Filuk, A., Gauvreau, J.-L., and Hwang, F. K. *Phys. Fluids B* **5,** 1816 (1993).

[59] Bellan, P. M. and Hansen, J. F. *Phys. Plasmas* **5,** 1991 (1998).

[60] Finn, J. M., Manheimer, W. M., and Ott, E. *Phys. Fluids* **24,** 1336 (1981).

[61] Taylor, J. B. *Rev. Mod. Phys.* **58,** 741 (1986).

[62] Tokman, M. *Magnetohydrodynamic Modeling of Solar Magnetic Arcades Using Exponential Propagation Methods.* California Institute of Technology thesis (2001).

[63] Chae, J. *Astrophys. J.* **540,** L115 (2000).

[64] Leroy, J. L., Bommier, V., and Sahal-Bréchot, S. *Astron. Astrophys.* **131,** 33 (1984).

[65] Priest, E. R., Ed. *Dynamics and Structure of Quiescent Solar Prominences* (Kluwer Academic, Dordrecht, 1989).

[66] Vrsnak, B., Ruzdak, V., and Rompolt, B. *Solar Phys.* **136,** 151 (1991).

[67] Aulanier, G. and Démoulin, P. *Astron. Astrophys.* **329,** 1125 (1998).

[68] Chen, J. *J. Geophys. Res.* **101,** 27499 (1996).

[69] Antiochos, S. K. *Astrophys. J.* **502,** L181 (1998).

[70] Pneuman, G. W. *Solar Phys.* **88,** 219 (1983).

[71] DeVore, C. R. and Antiochos, S. K. *Astrophys. J.* **539,** 954 (2000).

[72] Shafranov, V. D. *Re. Plasma Phys.* **2,** 103 (1966).

[73] Bateman, G. *MHD Instabilities* (MIT Press, Cambridge, Massachusetts, 1978).

[74] Miyamoto, K. *Plasma Physics for Nuclear Fusion* (MIT Press, Cambridge, Massachusetts, 1976).

[75] Krall, J., Chen, J., and Santoro, R. *Astrophys. J.* **539,** 964 (2000).

[76] Pevtsov, A. A., Canfield, R. C., and McClymont, A. N. *Astrophys. J.* **481,** 973 (1997).

[77] Kippenhahn, R. and Schlüter, A. *Z. Astrophys.* **43,** 36 (1957).

[78] Kuperus, M. and Tandberg-Hanssen, E. *Solar Phys.* **2,** 39 (1967).

[79] Kuperus, M. and Raadu, M. A. *Astron. Astrophys.* **31,** 189 (1974).

[80] Emonet, T. and Moreno-Insertis, F. *Astrophys. J.* **458,** 783 (1996).

[81] Magara, T. and Shibata, K. *The Hot Universe (Proc. IAU 188th symposium)*, 207 (1998).

[82] Antiochos, S. K., DeVore C. R., and Klimchuk J. A. *Astrophys. J.* **510,** 485 (1999).

[83] Emslie, A. G. and Wilkinson, L. K. *Astrophys. J.* **431,** 873 (1994).

[84] Hiei, E., Hundhausen, A. J., and Sime, D. G. *Geophys. Res. Lett.* **20,** 2785 (1993).

[85] Tanaka, K. *Sol. Phys.* **136,** 133 (1991).

[86] Feynman, J. and Martin, S. F. *J. Geophys. Res.* **100,** 3355 (1995).

[87] Pevtsov, A. A., Canfield, R. C., and Zirin, H. *Astrophys. J.* **473,** 533 (1996).

[88] Ji, H., Toyama, H., Yamagishi, K., Shinohara, S., Fujisawa, A., and Miyamoto, K. *Rev. Sci. Instrum.* **62,** 2326 (1991).

[89] Yamada, M., Ji, H., Hsu, S., Carter, T., Kulsrud, R., Bretz, N., Jobes, F., Ono, Y., and Perkins, F. *Phys. Plasmas* **4,** 1936 (1997).

[90] Ono, Y., Inomoto, M., Okazaki, T., and Udea, Y. *Phys. Plasmas* **4,** 1953 (1997).

[91] Brown, M. R. *Phys. Plasmas* **6,** 1717 (1999).

[92] Bayle, P., Bayle, M., and Caumes, G. *J. Phys. D: Appl. Phys.* **16,** 2449 (1983).

[93] Lundgaard, L., Linhjell, D., Berg, G., and Sigmond, S. *IEEE Transactions on Dielectrics and Electrical Insulation* **5,** 388 (1998).

[94] Pekárek, L. and Krejčí, V. *Czech. J. Phys. B* **12,** 296 (1962).

[95] Aleksandrov, N. L. and Bazelyan, E. M. *Journal of Experimental and Theoretical Physics* **91,** 724 (2000).

[96] Nedospasov, A. V. *Sov. Phys. Usp.* **11,** 174 (1968).

[97] Pekárek, L. *Sov. Phys. Usp.* **11,** 188 (1968).

[98] Ohe, K. Naito, A., and Kimura, T. *Phys. Fluids B* **3,** 3302 (1991).

[99] Oliver, R., Hood, A. W., and Priest, E. R. *Astrophys. J.* **461,** 424 (1996).

[100] Abramowitz, M. and Stegun, I., Eds. *Handbook of mathematical functions with formulas, graphs, and mathematical tables* (U.S. Govt. Print. Off., Washington, District of Columbia, 1972).

[101] Cheng, D. K. *Field and Wave Electromagnetics* (Addison-Wesley Publishing Company, Reading, Massachusetts, 1989).

[102] Pfister, H. and Gekelman, W. *Am. J. Phys.* **59,** 497 (1991).

[103] Goldston, R. J. and Rutherford, P. H. *Introduction to Plasma Physics* (Institute of Physics Publishing, Bristol and Philadelphia, Pennsylvania, 1995).

[104] Gundersen, M. University of Southern California. Private communication (1996).

Appendix A: Formulae

A.1 Mathematical formulae

A.1.1 Complete elliptic integrals

The complete elliptic integral of the first kind is

$$K(k) = \int_0^{\pi/2} \frac{d\theta}{\sqrt{1 - k^2 \sin^2 \theta}}. \tag{111}$$

The complete elliptic integral of the second kind is

$$E(k) = \int_0^{\pi/2} \sqrt{1 - k^2 \sin^2 \theta} d\theta. \tag{112}$$

Numerically, the integrals can be approximated as [100]

$$\begin{aligned} K &\simeq 1.3862944 + 0.1119723\eta + 0.0725296\eta^2 + \\ &\quad - \left(0.5 + 0.1213478\eta + 0.0288729\eta^2\right) \ln \eta \end{aligned} \tag{113}$$

$$E \simeq 1 + 0..4630151\eta + 0.1077812\eta^2 - \left(0.2452727\eta + 0.0412496\eta^2\right) \ln \eta \tag{114}$$

where $\eta = 1 - k^2$.

A.2 Physical formulae

A.2.1 Alfvén waves

A multitude of different waves can propagate through a plasma. One of these waves is the Alfvén wave. The propagation speed of the Alfvén wave, often used as a representative speed for the fastest phenomena in an MHD plasma, is

$$v_A = \frac{B}{\sqrt{\mu_0 n_i m_i}} \tag{115}$$

where B is the magnetic field strength, n_i is the ion number density, and m_i is the ion mass.

A.2.2 Boltzmann's constant

Boltzmann's constant $k_B = 1.3807 \times 10^{-23}\,\mathrm{J}\,/\,\mathrm{K}$ relates temperature T with its associated thermal energy $k_B T$. To compare thermal energies to electrostatic potentials, it is useful to remember that $1/k_B = 11604\,\mathrm{K}\,/\,\mathrm{eV}$.

A.2.3 Circular current loops

In cylindrical coordinates, the magnetic field from a loop with radius a conducting a current I is [57]

$$B_\rho = \frac{\mu I}{2\pi} \frac{z}{\rho\sqrt{(a+\rho)^2 + z^2}} \left(-K(k) + \frac{a^2 + \rho^2 + z^2}{(a-\rho)^2 + z^2} E(k) \right) \tag{116}$$

$$B_z = \frac{\mu I}{2\pi} \frac{1}{\sqrt{(a+\rho)^2 + z^2}} \left(K(k) + \frac{a^2 - \rho^2 - z^2}{(a-\rho)^2 + z^2} E(k) \right) \tag{117}$$

where the K and E are complete elliptic integrals of the first and second kind (cf A.1.1) with the argument k defined by

$$k^2 = \frac{4a\rho}{(a+\rho)^2 + z^2}. \tag{118}$$

On the axis of the loop, i.e., $\rho = 0$ we have

$$B_\rho = 0 \tag{119}$$

$$B_z = \frac{\mu I}{2} \frac{a^2}{(a^2 + z^2)^{3/2}}. \tag{120}$$

In spherical coordinates, we can approximate

$$B_r \simeq \frac{\mu I}{4} \frac{a^2}{r^2} 2\cos\theta \tag{121}$$

$$B_\theta \simeq \frac{\mu I}{4} \frac{a^2}{r^2} \sin\theta \tag{122}$$

when $r^2 \gg a^2$, i.e., far from the loop [101].

The force F between two parallel concentric circular current loops with radii a_1 and a_2 carrying currents I_1 and I_2, respectively, is [57]

$$F = -\frac{\mu I_1 I_2 d}{\sqrt{(a_1+a_2)^2+d^2}}\left(-K(k)+\frac{a_1^2+a_2^2+d^2}{(a_1-a_2)^2+d^2}E(k)\right) \tag{123}$$

where d is the separation distance between the loops and with the argument k now given by

$$k^2 = \frac{4a_1a_2}{(a_1+a_2)^2+d^2}. \tag{124}$$

A.2.4 Inductance

Faraday's law implies that if we try to change the magnetic flux flowing through a closed electrical circuit, a voltage will be generated in the circuit, creating a current that seeks to maintain the original magnetic flux. Our method of changing the flux is irrelevant; if we try to change the current flowing through an electrical circuit, the change will be opposed by a voltage LdI/dt where the inductance L depends on the circuit topology.

The mutual inductance between two concentric circular loops of radii a_1 and a_2, respectively, can be derived by integrating the magnetic flux from one loop (117) linking the other [57]:

$$L_{12} = \int_{S_1} \mathbf{B}_2 \cdot \mathbf{n} dS_1 = \frac{2\mu\sqrt{a_1a_2}}{k}\left(\left(1-\frac{k^2}{2}\right)K(k)-E(k)\right) \tag{125}$$

where the K and E are complete elliptic integrals of the first and second kind (cf A.1.1) with the argument k defined by

$$k^2 = \frac{4a_1a_2}{(a_1+a_2)^2+d^2} \tag{126}$$

where d is the distance between the loops.

The self-inductance of any conductor can be expressed in two parts, one that treats the inside of the conductor, and one that treats the outside. If the conductor is thin, e.g.,

like a wire, the internal self-conductance per unit length is

$$\frac{dL'_{11}}{da} = \frac{\mu'}{8\pi} \tag{127}$$

where μ' is the permeability inside the conductor. Adding (125) with $k \rightarrow 1$ and (127) gives the self-inductance of a circular loop, i.e., a torus, as [57]

$$L_{11} = a\left(\mu\left(\ln\frac{8a}{b} - 2\right) + \frac{\mu'}{4}\right) \tag{128}$$

assuming the major radius a is much larger than the minor radius b.

Finally, we note that the total inductance of a collection of closely packed concentric circular loops with the same radii scales with the square of the number of loops. This can be generalized to a coil of wire of any geometry, such that if we change the number of turns n per unit area, the total inductance changes as n^2.

A.2.5 LRC-circuit

Many, if not all, circuits used in the solar prominence experiment consist of a capacitor bank, a switch, and a load that is resistive and inductive. When the switch is closed, the capacitor bank and the load are in series with each other, and we can write this mathematically as:

$$L\frac{dI}{dt} + IR + \frac{Q}{C} = 0 \tag{129}$$

where L and R are the inductance and resistance, respectively, of the load, I is the current through the load, C is the capacitance of the capacitor bank, and Q is the charge on the capacitor bank. Furthermore, the current I deposits charge in the capacitor bank:

$$Q(t) = Q_0 + \int_0^t I(\tau)\, d\tau \tag{130}$$

where the charge on the capacitor bank at time zero is $Q_0 = CV_0$, the product of the capacitance and the charging voltage, V_0. If we take the time derivative of Equation (129),

we get a second order differential equation with solution

$$I(t) = I_1 e^{r_1 t} + I_2 e^{r_2 t} = e^{\alpha t}\left(I_1 \cos(\beta t) + I_2 \sin(\beta t)\right) \tag{131}$$

where the roots $r_1 = \alpha + i\beta$ and $r_2 = \alpha - i\beta$, with $\alpha = -R/2L$ and $\beta = \sqrt{\alpha^2 - 1/LC}$. In all cases we are interested in, no current flows through the circuit at time zero, so $I_1 + I_2 = 0$.

In the special case where the system is over-damped, so that the roots r_1 and r_2 are well separated, we get

$$I = -\frac{V_0}{R}\left(e^{-\frac{t}{RC}} - e^{-\frac{Rt}{L}}\right) = \left[\text{for } t \gg \frac{L}{R}\right] = -\frac{V_0}{R} e^{-\frac{t}{RC}}. \tag{132}$$

We can obtain the maximum current in this special case from

$$\frac{d}{dt}\left(e^{-\frac{t}{RC}} - e^{-\frac{Rt}{L}}\right) = 0 \tag{133}$$

which integrates to give

$$\frac{1}{RC} e^{-\frac{t}{RC}} = \frac{R}{L} e^{-\frac{Rt}{L}} \tag{134}$$

or

$$t_{\max} = \frac{\ln\left(\frac{R^2}{L/C}\right)}{\frac{R}{L} - \frac{1}{RC}} \simeq \frac{L}{R} \ln\left(\frac{R^2}{L/C}\right) \tag{135}$$

which inserted into the expression for the current gives

$$\begin{aligned} I_{\max} &= -\frac{V_0}{R}\left(e^{-\frac{t_{\max}}{RC}} - e^{-\frac{Rt_{\max}}{L}}\right) = -\frac{V_0}{R}\left(\frac{R^2}{LC} - 1\right) e^{-\frac{Rt_{\max}}{L}} \simeq \\ &\simeq -\frac{V_0}{R}\frac{R^2}{LC} e^{-\frac{Rt_{\max}}{L}} \simeq -\frac{V_0}{R}. \end{aligned} \tag{136}$$

A.2.6 Lundquist number

The Lundquist number is simply the magnetic Reynold's number (144) with the velocity U taken as the Alfvén velocity v_A (equation 115):

$$S = \frac{v_A L \mu_0}{\eta}. \tag{137}$$

Thus, the Lundquist number is the ratio of the diffusive time scale to the convective time scale, and provides a measure of how well a magnetic field is frozen to the plasma.

A.2.7 Magnetic dipole

Far from an electric dipole and far from a small current loop (cf A.2.3), the electric field lines from the dipole and the magnetic field lines of the loop are geometrically identical. This motivates the introduction of a magnetic dipole $\mathbf{m} = \pi b^2 I \hat{z}$, where b is the loop radius, I the current, and $\hat{z}$ a unit vector along the loop axis. In the far field, the magnetic field from this magnetic dipole is obtained from the vector potential

$$\mathbf{A} = \frac{\mu_0 \mathbf{m} \times \mathbf{R}}{4\pi R} \tag{138}$$

where $\mathbf{R}$ is the vector from the dipole to the point where we want to know the vector potential.

A.2.8 Magnetic energy

The magnetic energy in a volume V is

$$W = \int_V \frac{B^2}{2\mu_0} d^3r \tag{139}$$

A.2.9 Magnetic helicity

Magnetic helicity is defined as

$$K = \int_V \mathbf{A} \cdot \mathbf{B} d^3r \tag{140}$$

and is a measure of the linking of magnetic flux tubes with each other. This can be shown by considering two linked magnetic flux tubes of volumes V_1 and V_2 and magnetic flux Φ_1 and Φ_2, respectively. For simplicity, say that the magnetic field is $\mathbf{B}$ inside the tubes and

zero outside. Then $K = K_1 + K_2$, where

$$K_1 \equiv \int_{V_1} \mathbf{A} \cdot \mathbf{B} d^3 r \tag{141}$$

and K_2 is defined analogously. The volume element $d^3 r = d\mathbf{l} \cdot d\mathbf{S}$, where $d\mathbf{S}$ is the normal vector to an infinitesimal surface element on the cross-section of a flux tube, and $d\mathbf{l}$ is an infinitesimal vector element parallel to $d\mathbf{S}$. Then

$$K_1 \equiv \int_l \int_S \mathbf{A} \cdot \mathbf{B} d\mathbf{l} \cdot d\mathbf{S} = [\mathbf{B} \| d\mathbf{l}] = \int_l \int_S \mathbf{A} \cdot d\mathbf{l} \mathbf{B} \cdot d\mathbf{S} = \underbrace{\int_S \mathbf{B} \cdot d\mathbf{S}}_{=\Phi_1} \int_l \mathbf{A} \cdot d\mathbf{l} = \Phi_1 \int_{S_1} (\nabla \times \mathbf{A}) \cdot d\mathbf{S} \tag{142}$$

where we have used Stoke's theorem, and where S_1 is the area circumscribed by flux tube #1, i.e., the area of the hole through the torus that is flux tube #1. The only flux passing through this hole is Φ_2. Thus, from the definition of the vector potential we get $K_1 = \Phi_1 \Phi_2$, so that

$$K = 2\Phi_1 \Phi_2 \tag{143}$$

Consequently, magnetic helicity is additive. Using "Christmas ribbons," or Möbius strips, one can show in a more intuitive fashion how magnetic helicity is related to flux tube linking, and why magnetic helicity is conserved during magnetic reconnection [102].

A.2.10 Magnetic Reynold's number

The magnetic Reynold's number R_M is the ratio between the MHD $\mathbf{U} \times \mathbf{B}$ convective term, and the $\eta \mathbf{J}$ resistive term, or

$$R_M = \frac{UL\mu_0}{\eta} \tag{144}$$

where U is the MHD (center of mass) velocity, L is a typical length scale, and η is the Spitzer resistivity (equation 166).

A.2.11 Magnetohydrodynamics (MHD)

In MHD, electrons and ions are not treated separately, but rather velocities are averaged to the center of mass velocity

$$\mathbf{U} = \frac{\sum_{\sigma} m_s q_s \mathbf{u}_s}{\rho} \tag{145}$$

where the density

$$\rho = \sum_{\sigma} m_\sigma n_\sigma \tag{146}$$

and the subscript σ denotes the different particle species.

The MHD equations are the MHD equation of continuity $\partial\rho/\partial t + \nabla \cdot (\rho \mathbf{U}) = 0$, Faraday's law, Ampère's law in the form $\nabla \times \mathbf{B} = \mu_0 J$, the MHD Ohm's law (149), and the MHD equation of motion

$$\rho \frac{D\mathbf{U}}{Dt} = \mathbf{J} \times \mathbf{B} - \nabla \cdot \mathbf{P} \tag{147}$$

where the convective derivative

$$\frac{D}{Dt} = \frac{\partial}{\partial t} + \mathbf{U} \cdot \nabla \tag{148}$$

and the tensor pressure $\mathbf{P}$ is reduced to the regular scalar pressure $P = nk_BT$ in the single adiabatic regime where collisions equilibrate both parallel and perpendicular pressures and temperatures, i.e., these quantities are isotropic and not a function of angle with respect to the magnetic field.

A.2.12 Ohm's law

The MHD Ohm's law is

$$\mathbf{E} + \mathbf{U} \times \mathbf{B} = \eta \mathbf{J}. \tag{149}$$

A.2.13 Plasma β

The plasma β is the ratio of the thermal pressure p to the magnetic pressure $B^2/2\mu_0$:

$$\beta = \frac{p}{\frac{B^2}{2\mu_0}}. \tag{150}$$

A.2.14 Plasma frequency

The ion and electron plasma frequencies are

$$\omega_{p\sigma} = \sqrt{\frac{n_\sigma q_\sigma^2}{\varepsilon_0 m_\sigma}} \tag{151}$$

where n_σ is the particle number density, q_σ and m_σ are the particle charge and mass, respectively, and σ denotes the ions (i) and electrons (e), respectively. Note that

$$\frac{\omega_{pe}^2}{\omega_{pi}^2} = \frac{m_i}{Z^2 m_e} \tag{152}$$

where $Z = q_i/q_e$, so that the electron cyclotron frequency is significantly larger than the ion cyclotron frequency, e.g., for hydrogen $\omega_{pe}/\omega_{pi} \approx 43$.

A.2.15 Rogowski coil

A toroidal coil (a coil wound around a torus) can be used to measure the current I in a conductor passing through the center hole of the coil. The magnetic field from the conductor is

$$B_\phi(r) = \frac{\mu_o I}{2\pi r} \tag{153}$$

and has only an azimuthal component if we assume that the conductor is infinitely long and straight. If the torus major radius is $r = a$ and the minor radius is b, then the magnetic flux through a cross-section of the torus is

$$\Phi_{torus} = \pi b^2 B_\phi(a). \tag{154}$$

If the coil has N turns, then the total linked flux through the coil is $\Phi = N\Phi_{torus}$. From Faraday's law we know that a change in the magnetic flux, i.e., a change in current in the conductor through the hole, will generate a voltage

$$V = \frac{d\Phi}{dt} = \frac{N\mu_0 b^2}{2a}\frac{dI}{dt}. \tag{155}$$

If we integrate this voltage we obtain the current I flowing in the conductor. Integration can be performed numerically by an oscilloscope or by a computer, although traditionally integrating RC-circuits have been used.

A.2.16 Speed of sound in a gas

The adiabatic speed of sound in a gas, c_s, is given by

$$c_s^2 = \frac{dp}{d\rho} = \gamma\frac{k_B T}{M} \tag{156}$$

where the result for derivative of the pressure p with respect to the density ρ holds true for any gases of interest, and where k_B is Boltzmann's constant, T is the temperature, M is the molecular weight, and $\gamma = 1 + 2/d$ where d is the dimensional freedom of the gas molecules, e.g., 3 for argon or atomic hydrogen, 5 for molecular hydrogen.

A.2.17 Spitzer resistivity

The electrical resistivity of a plasma can be estimated from an analysis of electron-ion collisions. In a plasma subjected to an electrical field $\mathbf{E}$, electrons and ions are constantly being accelerated in opposite directions by the field. Collisions between electrons and ions provide drag - a force that balances the acceleration due to the electric field. If electron-ion collisions occur at a frequency ν_{ei}, then we can write the force balance relation as

$$0 = -\frac{q_e}{m_e}\mathbf{E} - \nu_{ei}\left(\mathbf{u}_e - \mathbf{u}_i\right) \tag{157}$$

where $\mathbf{u}_e$ is the average electron velocity and $\mathbf{u}_i$ is the average ion velocity. Now the current density in the plasma is

$$\mathbf{J} = q_e \left(n_i \mathbf{u}_i - n_e \mathbf{u}_e\right) = \left[n_i = n_e\right] = -q_e n_e \left(\mathbf{u}_e - \mathbf{u}_i\right) \tag{158}$$

with n_e electron (and ion) density. We now recognize an expression similar to Ohm's law from electrical circuit theory:

$$\mathbf{E} = \eta \mathbf{J} \tag{159}$$

with the resistivity

$$\eta = \frac{m_e \nu_{ei}}{n_e q_e^2} \tag{160}$$

Next, consider the collision frequency ν_{ei}. In a plasma with density n_e, where the cross-sectional area for electron-ion collisions is σ and the incident velocity (the velocity at infinite distance) between colliding particles is v_0, collisions will occur at a frequency

$$\nu_{ei} = n_e \sigma v_0. \tag{161}$$

In Rutherford scattering problems, the angle of deflection θ of the scattered particle is a function of the impact parameter b_θ, which is the perpendicular distance between the tangent of the incoming particle's trajectory at infinite distance from the target particle, and the target particle:

$$\tan\left(\frac{\theta}{2}\right) = \frac{q_{\sigma 1} q_{\sigma 2}}{4\pi\varepsilon_0 b \mu v_0^2} \tag{162}$$

where $q_{\sigma 1}$ and $q_{\sigma 2}$ are the charges of the scattered particle and the target particle, respectively, v_0 is the velocity of the scattered particle when at infinite distance from the target particle, and the reduced mass $\mu = 1/\left(m_{\sigma 1}^{-1} + m_{\sigma 2}^{-1}\right)$. In particular, the impact parameter for 90° collisions is

$$b_{\pi/2} = \frac{q_{\sigma 1} q_{\sigma 2}}{4\pi\varepsilon_0 \mu v_0^2}. \tag{163}$$

Using Equations (162-163) we can calculate the cross-sectional area for collisions as

$$\sigma = \int_{b_{\pi/2}}^{\lambda_D} 2\pi \left(\theta\left(b\right)\right)^2 bdb \simeq \frac{1}{2\pi}\left(\frac{q_e^2}{\varepsilon_0 \mu v_0^2}\right)^2 \ln\left(\frac{\lambda_D}{b_{\pi/2}}\right) \tag{164}$$

where we have used $\tan\left(\theta/2\right) \simeq \theta/2$ to simplify equation 162 for small angles.

Finally, make the expression more general by allowing for ion charges of $-Zq_e$, approximate $\mu \simeq m_e$ and $v_0 \simeq v_{Te}$, and we arrive at an estimate for the parallel electrical resistivity of a plasma

$$\eta = \frac{Zq_e^2}{2\pi m_e \varepsilon_0^2 v_{Te}^3} \ln\left(\frac{\lambda_D}{b_{\pi/2}}\right) \tag{165}$$

where Z is the ion valence, $\lambda_D = \sqrt{\varepsilon_0 k_B T_\sigma / n_{0\sigma} q_\sigma^2}$ is the Debye length, q_e and m_e are the electron charge and mass, respectively, $b_{\pi/2}$ is the impact parameter for electron-ion collisions with the velocity at infinity equal to the electron thermal velocity $v_{Te} = \sqrt{3k_B T_e / m_e}$.

A higher order effect that causes electrons with higher speed to accelerate more readily in the electric field than electrons with lower speed modifies the equation above [103]. For a hydrogen plasma, an estimate of the resistivity that includes this higher order effect is known as the Spitzer resistivity:

$$\eta = \frac{1}{3}\frac{q_e^2}{2\pi m_e \varepsilon_0^2 v_{Te}^3} \ln\left(\frac{\lambda_D}{b_{\pi/2}}\right) = \frac{6 \times 10^1\, \Omega\,\mathrm{m\,K}^{3/2}}{T^{3/2}} \ln\left(\frac{\lambda_D}{b_{\pi/2}}\right). \tag{166}$$

A.2.18 Vacuum magnetic field

A vacuum magnetic field, also known as a curl-free field or a potential field, is the magnetic field inside a volume V entirely generated by sources (currents) outside of V. More specifically, the vacuum field is the magnetic field configuration with the lowest possible energy that satisfy a prescribed magnetic field boundary condition on the surface of V. Consequently, any perturbation to the vacuum magnetic field (that does not change the boundary

conditions) must increase the magnetic energy, and can be visualized as a stretching of the magnetic field lines.

Appendix B: Additional information on subsystems and configuration variations

This appendix describes the testing or monitoring of certain subsystems and configuration variations used in the solar prominence experiment.

B.1 Puff gas valve

This section describes how a prototype gas valve was built and tested and the improvements made for and testing of the actual gas valve used in the experiment.

B.1.1 Prototype gas valve testing

From the order of magnitude analysis (cf 2.3.1) we designed a prototype gas valve with a 36.5 mm diameter, 0.76 mm thick aluminium disk and a matching diameter electromagnet with 10 turns of 0.89 mm diameter wire. A 341 μF capacitor bank (maximum voltage 990 V) and a small charging supply were built to test the valve. The capacitor bank was connected via a thyristor switch to the gas valve. A 125 MHz LeCroy 9400 oscilloscope connected to a Rogowski coil (cf A.2.15) with a simple RC-integrator was used to measure the current in the positive lead between the capacitor bank and the gas valve. Pulsing the circuit with a 100 V initial voltage on the capacitor bank, the total inductance and resistance of the circuit were determined to be 2.0×10^{-6} H and 180 mΩ, respectively (129-136). Repeating the procedure with the gas valve short-circuited gave 1.3×10^{-6} H and 120 mΩ for the circuit, and thus the coil in the gas valve itself has an inductance of 0.7×10^{-6} H and a resistance of 60 mΩ. Some 7.4% of the energy in the capacitor bank went into magnetic energy in the coil.

Next, the spring and the half of the gas valve body that supports the spring were removed. The remaining half that holds the electromagnet coil was oriented with the aluminium disk on top and horizontal. Pulsing the gas valve in this configuration, with 600 V on the capacitor bank, the disk to flew some $30 - 40$ cm upwards. Calculating the mass of the disk using the density of aluminium, 2.70×10^3 kg / m^3, and the dimensions given above, note that some 0.006% of the energy in the capacitor bank, or only 0.08% of the energy in the magnetic field, went into the 2.1 g disk in the form of kinetic energy.

Despite the low energy efficiency, we proceeded to test-fire the gas valve into a small vacuum chamber. The volume of the chamber was 3.1×10^{-2} m^{-3}, and it was pumped down by a mechanical pump to a base pressure of about of $2 - 4$ Pa ($15 - 30$ mTorr) as measured by a thermocouple gauge. A capacitance manometer was used to measure incremental pressure changes in the vacuum chamber with the pump temporarily valved off. A fast ionization gauge was used to measure the time profile of the gas puff. The fast ionization gauge works just like a regular ionization gauge; it consists of a hot filament that emits electrons, an anode that collects the electrons, and a cathode that collects ions created by the electrons colliding with any neutral atoms that happen to be present, for instance from our injected gas puff. For the ion gauge to work, the mean free path of the electrons must be greater than the filament-anode distance, which presents a problem at very high pressures, such as in the gas puffs from our gas valve. The solution to this problem is to make the ion gauge smaller. We built the fast ionization gauge with two electrodes of shim stock steel, 5×7 mm^2 in area and 127 μm thick, and a tungsten wire filament 11 mm long and 127 μm in diameter. The two electrodes were placed 11 mm apart on a vacuum probe head, each 5 mm from the filament. The ion gauge was mounted on the vacuum chamber such

that it could be moved toward and away from the point where the gas valve would puff gas into the chamber. A 27 V bias voltage was applied to the anode and -9 V to the cathode using batteries, while a 2 A current was driven through the filament using a constant current power supply. The ion current through the cathode was amplified by an op-amp circuit and fed to a second channel on the LeCroy oscilloscope.

For safety reasons we chose to use argon rather than hydrogen. The test commenced with an argon pressure of 136 kPa (5 psi pressure above atmospheric pressure). The minimum voltage on the capacitor bank at which the gas valve operated was $300 - 350$ V, but at 360 V the gas valve would let in a double puff of gas, as recorded by the fast ion gauge on the oscilloscope. We interpret the double puff as the result of the aluminium disk bouncing as it settles back onto the o-ring. The total duration of the gas puff as registered by the ion gauge was about 240 μs. From incremental pressure measurements using the manometer, the mass of gas admitted to the chamber by each pulse was deduced to be $3.4 - 6.1$ μg, not varying consistently with changes in either gas feed pressure or capacitor bank voltage. Moving the fast ion gauge to different distances from the gas valve, the speed of the front of the expanding argon gas was determined to be 0.47 km / s, while the peak density of the gas puff would move at 0.42 km / s. This is comparable to either the thermal velocity (atom rms-speed) in argon, which at room temperature is $v_{rms} = \sqrt{3k_BT/m_{Ar}} = 0.43$ km / s, or to the speed of sound (156) in argon, $c_s = 0.32$ km / s at room temperature.

To resolve the problem of the bouncing disk, a rather soft aluminium spring in the gas valve was replaced with a stiffer spring of a beryllium copper alloy. The test proceeded using different gas pressures in the argon gas feed and a variety of charging voltages on the capacitor bank. We found a clear correlation between argon pressure and the minimum

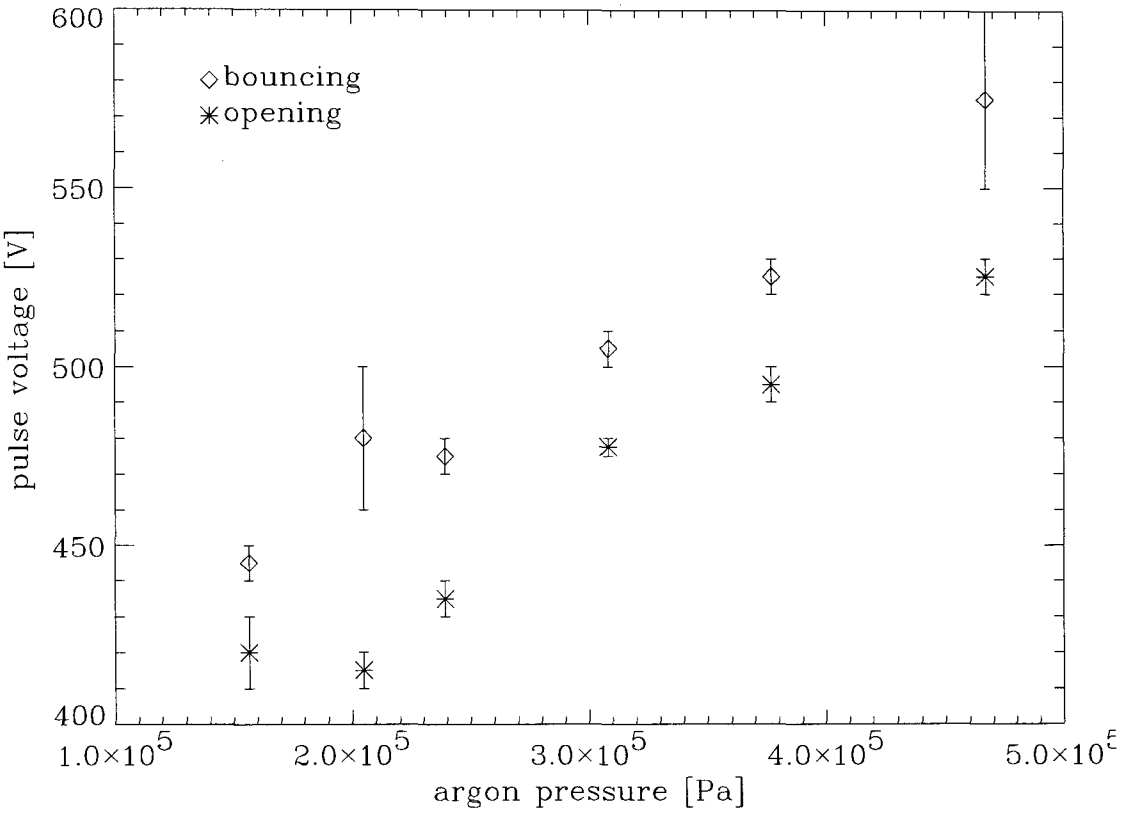

Figure 64: Voltage on gas valve capacitor bank required for valve to open, and the voltage at which the gas valve aluminium disk starts to bounce, as a function of gas line pressure. The gas used was argon.

voltage at which the gas valve would open, as well as between the argon pressure and the voltage at which the disk would bounce, leading to a double pulse registered by the fast ion gauge. The results are summarized in Figure 64. It can be seen that both opening and bouncing voltages monotonically increase with argon pressure. Testing was terminated at 467 kPa (53 psi over-pressure) when the beryllium-copper spring, which has a length comparable to its diameter, happened to turn itself sideways inside the valve.

B.1.2 Gas valve for prominence experiment

While the tests performed on the prototype gas valve were very encouraging, we decided to add a few extra features to the final gas valve that was constructed for the solar prominence experiment. To prevent the bouncing behavior of the disk in the prototype valve, a small metal skirt was added onto the disk. The skirt was supplemented with a plenum in the gas valve, so that the plenum and skirt would act together to more precisely determine the volume of gas let into the vacuum chamber when the gas valve is operated. The valve body between the electromagnet coil and the disk was made thinner (0.79 mm), to increase the amount of energy converted into disk kinetic energy by reducing the volume of metal where parasitic image currents appear. The beryllium-copper spring was replaced by a tapered spring in the same material that, unlike its predecessor, will be correctly oriented inside the gas valve under any operating circumstances. Finally, provisions were made to measure the capacitance between the metal disk and the rest of the gas valve, thus providing a direct method of observing disk location as a function of time.

Repeating the test with the back part of the gas valve removed and allowing the valve to shoot the disk straight up in the air showed that reducing the valve body thickness had improved gas valve performance. The old disk from the prototype valve would fly higher than 2.5 m when the new valve was pulsed at 600 V. A variety of disks with different diameters and thicknesses, and of different materials were tested at this point, and we concluded that the disk with the skirt would perform adequately. A 2 m long transmission line, necessary for the real experiment, was added between valve and capacitor bank. This addition reduced the kinetic energy of the disk by 40%.

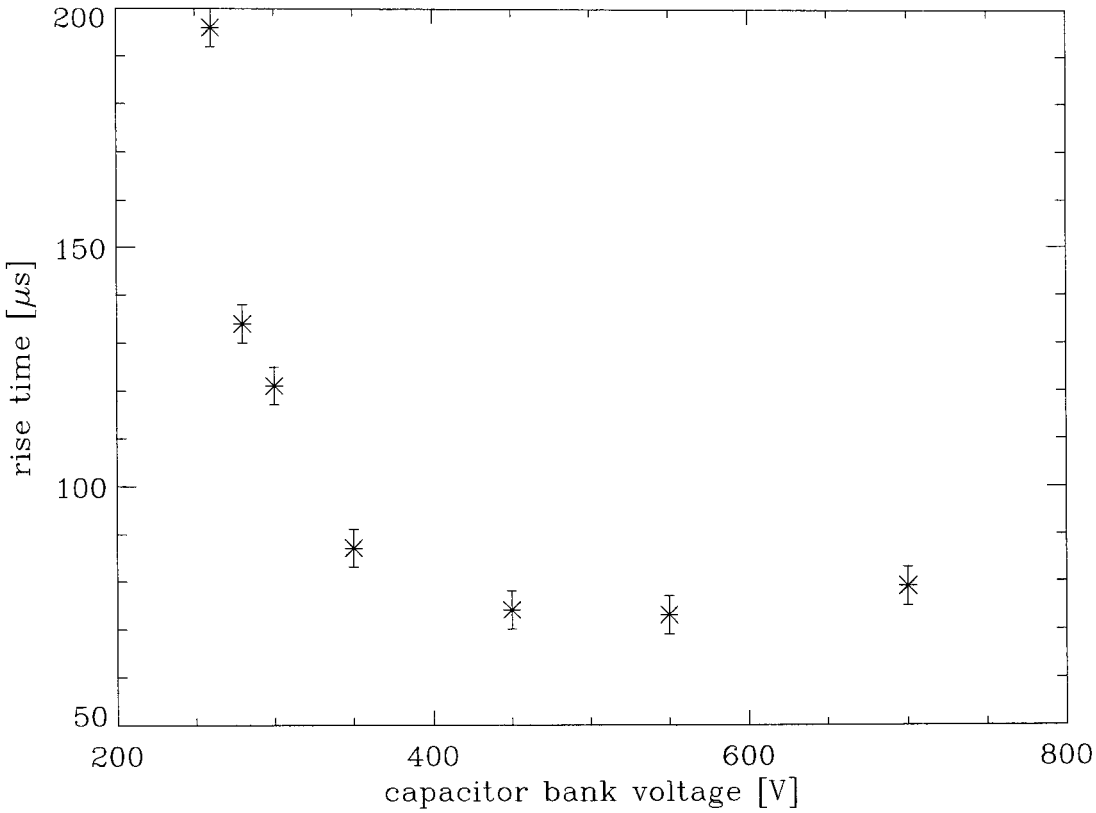

Figure 65: Gas puff rise time as a function of gas valve capacitor bank voltage.

The rise time of the gas puff, as a function of voltage on the 341 μF capacitor bank, was determined. While this was somewhat erratic for the prototype valve, the new plenum valve showed that rise times decrease with increasing voltage. For very high voltages of 700 V or more, the decrease in rise time stops or even reverses. This indicates that at some voltage, probably around 550 V, the kinetic energy of the disk is enough to substantially compress the tapered spring, and that a higher voltage on the capacitor bank merely makes the valve stay open slightly longer, thus letting in more gas and delaying the peak time of gas density.

The indication that the capacitor bank stores more energy than necessary suggests a reduction of the bank capacitance, thus making the electrical circuit faster. The current pulse, as measured by the Rogowski coil, had a duration of 112 μs with the original 341 μF capacitor bank. Reducing the bank capacitance, to 201 μF, led to a current pulse duration of 84 μs. Repeating the measurement of rise time as a function of voltage now led to a 10 μs faster rise time than before, when operating the valve at moderate to high voltages (over 550 V). At lower voltages the rise times significantly increased, which is expected since there is less energy in the capacitor bank. A slight increase in rise time as a function of voltage was still observed for very high voltages. Further reduction of the capacitance, to 133 μF, led to no additional gains in terms of smaller rise times, but instead, as indicated by gas puff durations, the valve would briefly be stuck open.

Reverting to the 201 μF configuration, gas valve performance as a function of argon pressure was measured. A change in rise time as a function of gas pressure was not detected. However, the gas valve would close faster with higher gas pressure, and thermocouple measurements indicated that a slightly larger amount of gas would be let into the chamber at lower pressures than at higher. At 239 kPa (20 psi over-pressure) the valve would let 15.2 μg of argon into the chamber, while at 515 kPa (60 psi over-pressure) it would let in 13.9 μg.

The capacitance between disk and gas valve was calibrated to 24 pF with a 1.0 mm gap between disk and valve, and 20 pF with a 1.5 mm gap. Unfortunately, the capacitance measurements were inconclusive, since during operation the disk apparently would not only touch the spring, which was accounted for, but would also short-circuit against some other part of the valve. Interestingly, shorts would occur for several milliseconds after

each discharge, indicating a vibration in the disk that nevertheless does not let gas into the vacuum chamber. This indicates that there is some asymmetry in the disk motion that eventually leads to a rocking motion when the disk has settled on the o-ring. This rocking motion can cause the skirt on the disk to briefly get jammed in the plenum, and is possibly what happened during operation with the capacitance reduced to 133 μF.

Several of the tests discussed above were briefly repeated using helium instead of argon. Another 20 V was added to the anode voltage on the fast ion gauge to account for the larger ionization potential of helium. The test results for helium agreed with those for argon.

B.2 Configuration variations

This section describes how the Mark I and II devices were modified to test ideas for future generation devices (Mark II and IV, respectively).

B.2.1 Configuration variations of the Mark I device

Here we describe our efforts to eliminate the formation of side arcs. Few scientific results were obtained from this exercise, but it provided ideas on how to construct a second generation experiment (cf Chapter 4).

To prevent the formation of side arcs, we modified the configuration of the Mark I solar device. Five different configurations were investigated for this purpose. These configurations are summarized in Table 13, including the provisions made for the flash lamp and the accidental configuration change due to the absent tantalum disk. The first attempt to eliminate the side arcs (configuration 'D'), consisted of coating the inside of the vacuum port on which the device was mounted (port #16 in 4), as well as to the vacuum chamber wall (the end dome) within 5-10 cm of this port, with boron nitride. The idea

Configuration	Description	Side arcs?
A	Original	Yes
B	Shaft and window for flash lamp	Yes
C	Missing tantalum disk	Yes
D	C + coated vacuum port and wall	Yes
E	D + coated vacuum flange of device	Yes
F	E + ceramic tube inserted in port	Yes
G	E + electrodes and alumina tubes extended	No
H	F + G + gas injection tube extended	No

Table 13: Configuration changes on first generation solar device (Mark I). Side arcs were inhibited only when the electrodes were extended some 117 mm.

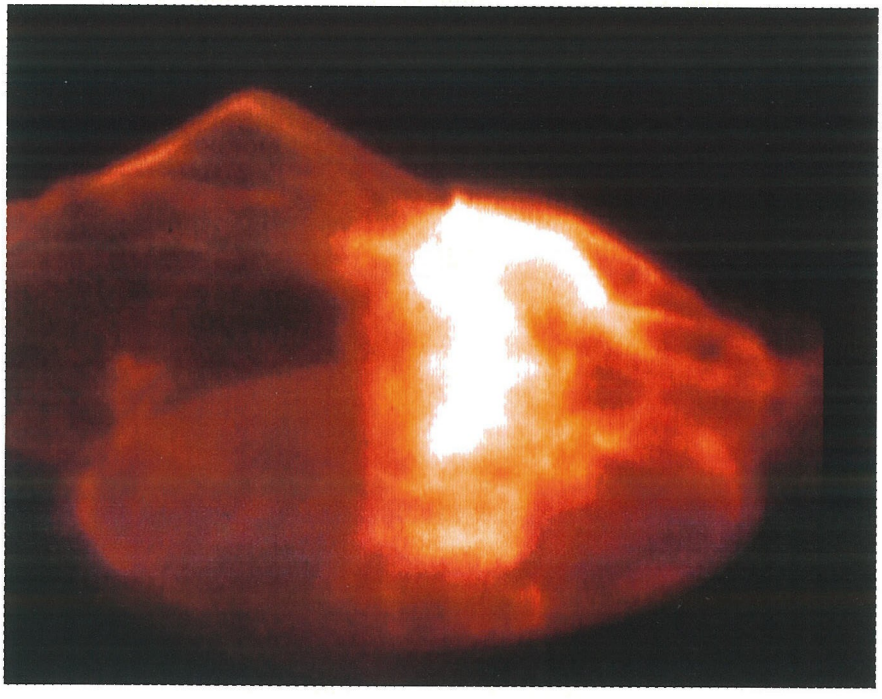

Figure 66: Example of plasma in one of the unsuccessful configurations of the Mark I device (for which the side arcs still appeared). Note that the ceramic tube inserted into the vacuum port has an effect on the plasma; the side arc has developed a sharp bend.

was to electrically insulate this part of the vacuum chamber to prevent flow of the side arc currents. In particular it was thought that the side arcs were connecting to the 90° corner between the vacuum port and the end dome wall. The coating had no effect, and so the remainder of the configuration variations listed in Table 13 were tried. Figure 66 shows an example of an image obtained in configuration 'F', which included a ceramic tube (184 mm inner diameter) inserted into the port. Only when by extending the electrodes 117 mm (into the vacuum chamber) were the side arcs eliminated (configuration 'G'). This extension was done by removing the one remaining tantalum disk and using the existing threaded holes available on the iron core surfaces (cf Figure 10). At the same time, the alumina tubes were replaced by tubes that were 111 mm longer. As this moved the electrode surfaces away from the gas injection point, the effective gas pressure was lowered, causing

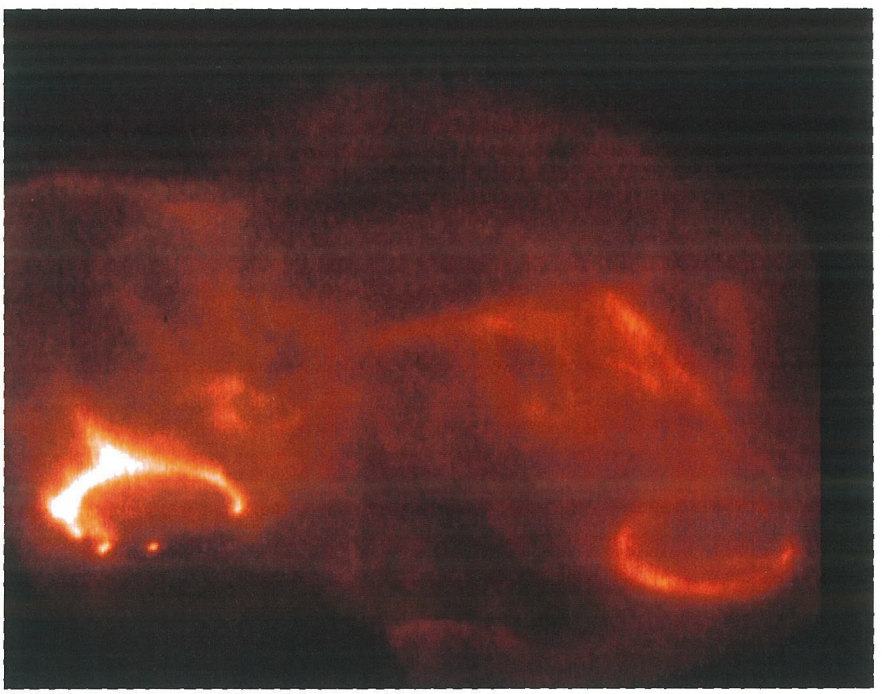

Figure 67: Plasma discharge with the electrodes of the Mark I device extended. The main current channel becomes strongly twisted (no side arcs form).

breakdown problems. Most attempts to break down the gas would fail, and at other times the breakdown time would be highly irreproducible, varying randomly between 12-61 μs. Obtaining images of the plasma under these conditions was difficult. Extending also the gas injection tube (with a glass tube), repeatability was slightly improved. The image in Figure 67 was obtained in this configuration ('H').

Before configuration 'G', we also made a change to the cabinet with the main capacitor. An extra circuit was added (cf Figure 5) to temporarily disconnect a heavy, braided wire that grounded the vacuum chamber to the capacitor. A current equal to a small fraction ($<10\%$) of I_{tor} would flow in this wire, and it was suspected that it could affect the side arc formation. However, no observable effect was noted when the experiment was operated

with the grounding wire temporarily disabled. Also, no effect was noticed on either anode or cathode voltage traces. Operation with the grounding wire disconnected was suspended.

B.2.2 Configuration variations of the Mark II device

The plasma consists of mixtures of brighter and darker strands of plasma, a property that can be used to estimate how helical the plasma is (cf 3.3.5). Making a slight configuration change to the Mark II device, we attempted to control both the number of strands and their points of origin on the electrodes. The configuration change consisted of replacing any or all of the eight flat-headed electrode mounting bolts (cf Figure 19) with sharp-tipped bolts. The idea was that the resulting local increase in electric fields around the bolts would lead to gas breakdown at the bolt tips instead of at the gas injection points. The attempt was not successful; the plasma formed and evolved qualitatively identically in discharges with or without sharp-tipped bolts.

Another Mark II configuration variation was aimed at studying the interaction between two prominence-like plasmas (cf Chapter 5). Before designing a new generation solar device for this purpose, we wanted to know whether or not the formation of two prominence-like plasmas by the same device and in close vicinity to each other was possible. For this purpose, a pair of V-shaped electrode extensions were mounted on the Mark II device. The extensions were made from iron, to split the magnetic flux in two equal parts, and holes were drilled to guide and split the gas flow. The extensions were successful; two prominences formed simultaneously (cf Figure 68). However, the distance between the prominences was too large for any visible interaction to occur.

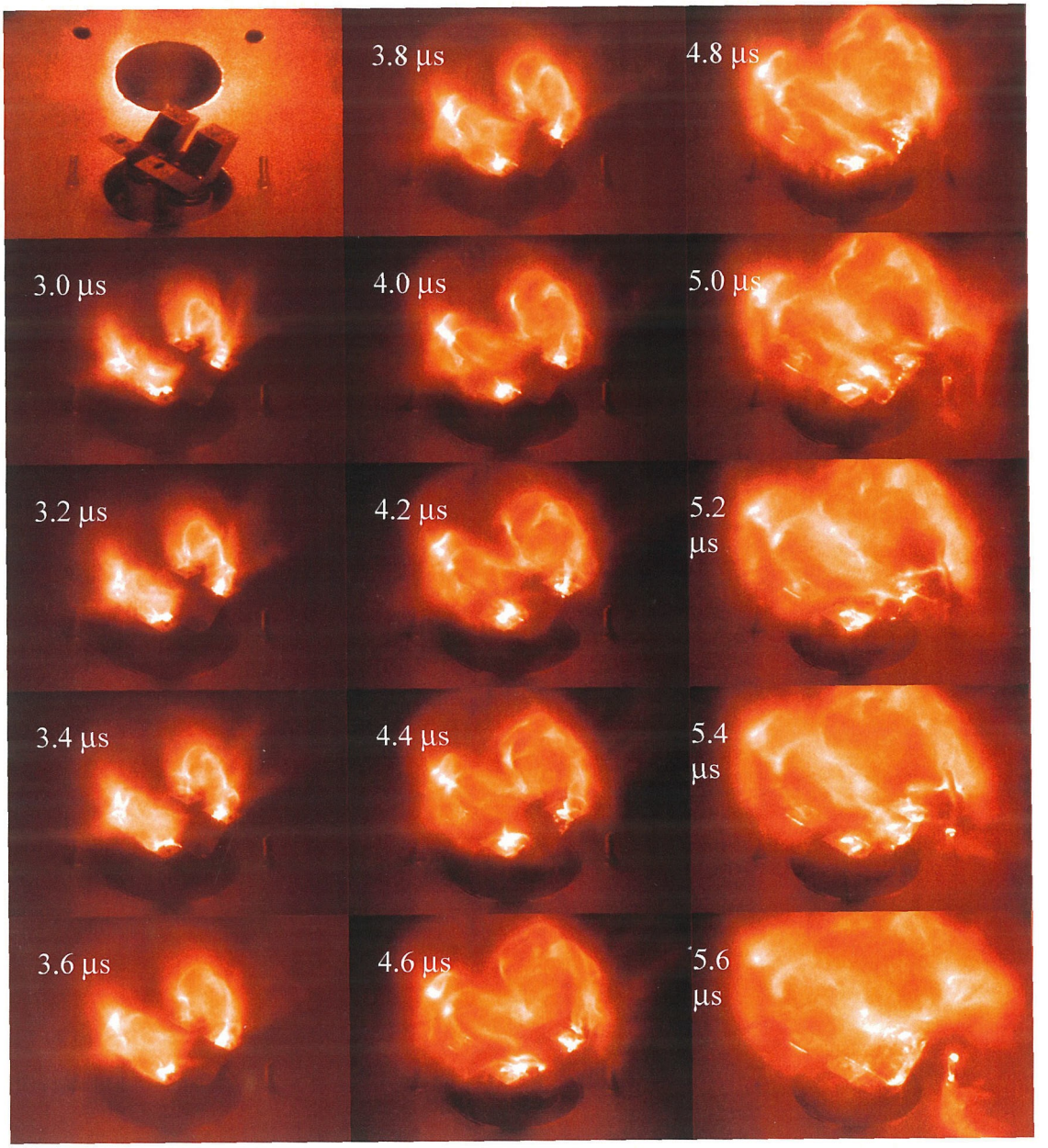

Figure 68: Plasma evolution with V-shaped extensions on the Mark II device. Two prominences form simultaneously. Because of the low toroidal magnetic fields, both prominences become highly twisted. Top left image is an image before the discharge, showing the two V-shaped electrodes sticking out of the vacuum port.

Since it was easy to do, we also attempted a few discharges with the D-shaped electrodes removed and with no other extensions added. No visible effect on the plasma was noted.

B.3 Equipment temperature increases

The temperature of the Mark I solar device was monitored during the first few days of operation. Temperature was measured using an Omega Engineering infrared temperature transducer model OS-500C. Much of the energy in the bias field capacitor banks is converted to heat in various parts of the toroidal magnetic field subsystem, e.g., in the electromagnet coils (due to ohmic resistance) and in the iron core (due to hysteresis loss, i.e., friction encountered during domain-wall motion and domain rotation in a ferromagnetic material). The temperature increase during approximately two hours of normal operation is shown in Figure 69. The increase is fairly dramatic, often 20 °C or more. To investigate whether this gradual temperature increase has an effect the experiment, data were collected in such a way that, when mapping the dependence of a certain parameter, that parameter would be changed in a randomized fashion until all desired values had been sampled. For example, when making the pseudo-movies (cf 3.2.4) pictures would be taken in an order such as t_{camera} = 4, 11, 5, 6, 9, 8, 7, 12, 10 μs, instead of t_{camera} = 4, 5, 6, 7, 8, 9, 10, 11, 12 μs. No effect on the experiment, due to the temperature increase, was found.

Stress due to either thermal expansion or electromagnetic forces, or more likely due to both, once resulted in a catastrophic failure during operation with high voltage settings (10 kV) on the main capacitor. Stress on one electrode's Macor ring and alumina tube caused fractures in both. The event produced an explosive sound as these parts cracked, air

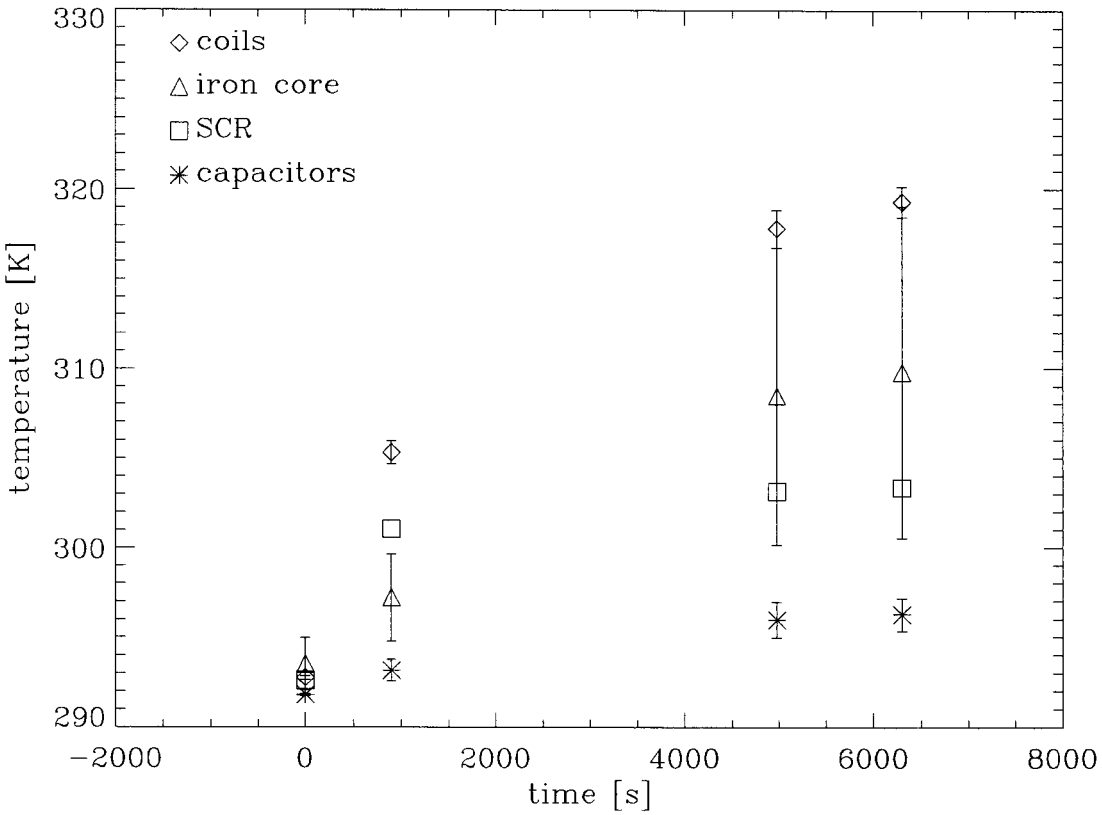

Figure 69: Temperature increase of various parts of the toroidal magnetic field subsystem of the first generation solar device (Mark I) as a function of time during normal operation. Error bars indicate lowest and highest temperature on any part of a piece of equipment. Due to its small size, the SCR had a homogenous temperature and therefore no error bars are marked.

rushed into the chamber, and many alumina fragments were scattered around the vacuum chamber.

B.4 Flashlamp

The fact that the UV flashlamp did not significantly affect plasma breakdown characteristics is possibly attributable to the work function of the type of metal that was illuminated. Flashlamps have been used successfully by researchers using molybdenum metal surfaces [104]. In our case, the UV flashlamp illuminates an iron surface. The work function of iron is 4.63 eV, while for molybdenum it is 4.13 eV. It is possible that our experiment would have benefitted from coating the shaft through the iron core with molybdenum or another similar metal. Metals with work functions similar to molybdenum include tantalum and zirconium, both easy to work with. (Uranium and thorium have even lower work functions, 3.45 eV and 3.47 eV, respectively.)